NUMERICAL STUDIES OF URBAN HEAT ISLAND IN GREATER KUALA LUMPUR, MALAYSIA: FROM SURFACE AND BOUNDARY LAYER CONDITIONS TO LOCAL AIR POLLUTION

OOI CHEL GEE

DEPARTMENT OF CIVIL ENGINEERING
UNIVERSITY OF NOTTINGHAM
MALAYSIA CAMPUS

2017

NUMERICAL STUDIES OF URBAN HEAT ISLAND IN GREATER KUALA LUMPUR, MALAYSIA: FROM SURFACE AND BOUNDARY LAYER CONDITIONS TO LOCAL AIR POLLUTION

OOI CHEL GEE

THESIS SUBMITTED IN FULFILMENT OF THE REQUIREMENTS FOR THE DEGREE OF

DOCTOR IN PHILOSOPHY

DEPARTMENT OF CIVIL ENGINEERING
UNIVERSITY OF NOTTINGHAM
MALAYSIA CAMPUS

2017

ABSTRACT

Rapid urbanization of cities has greatly modified the thermal and dynamic profile in the urban boundary layer. This thesis attempts to study the effect of urban heating on the local climate and air quality for a tropical coastal urban agglomeration, Greater Kuala Lumpur (GKL) in Malaysia. A state-of-art numerical model, Weather Research and Forecast Model (WRF) is used to identify the influence of urbanization through modification of urban surfaces. In order to thoroughly study the environmental impact of land use change in GKL, this thesis begins with the local urban heating on the surface layer before extending to the influence on the boundary layer circulation and its atmospheric composition.

The WRF model is tested for its applicability to reproduce the urban heating condition. The model verification hence incorporates sensitivity analysis of physics pertinent to the simulation of land surface and boundary layer dynamics condition, namely the land use map, urban canopy model (UCM) and planetary boundary layer (PBL) physics options. Result shows that the urban surface representation and parameterization models in WRF are of great importance for the high resolution urban climate in the region. The locally calibrated land use map and urban parameters have substantially improved the near-surface weather and urban heating prediction. The local PBL scheme also predicts a generally good agreement for the studied region in terms of near-surface environment and vertical profile during the morning and evening transitional period.

Incorporating the optimum physics settings, the control study found that urbanization due to land use change has induced a modelled daily mean urban heat island intensity (UHII) of 0.9 °C with a more severe heating of 1.9 °C at night. The heating condition induces urban thermal circulation that interacts with the local topographic flow, namely sea/land breeze and downhill/uphill breeze for the coastal urban agglomeration sheltered by the mountain ranges on the other side. Depending on the cloud cover and prevailing synoptic flow, the immense heat forcing on the surface accelerates/decelerates the moisture-bearing sea breeze during the day. It also induces vertical lifting which creates a conducive environment for convective precipitation on the upwind region.

The subsequent control study with chemical weather prediction model (WRF-Chem) shows that the urban heating condition reduces the ground ozone level by around 20 ppbv throughout the day. Analysis shows that the reduced ozone level is closely correlated to the stronger horizontal sea breeze front (SBF) advection in the morning and urban-enhanced vertical mixing during the night which disperse the ground ozone and its precursors. Despite the reduction of ozone level, the air quality monitoring result identifies GKL as NO_x-sensitive region which is prone to higher level of ozone with the continuous expansion of urban.

The thesis explores the ability of WRF software to reproduce the high resolution urban climate. The model evaluation has realistically discovered that WRF is able to produce good approximation of the near-surface weather condition and fairly reasonable vertical boundary layer profiles. However, the atmospheric chemistry composition of the local surface pollutants is greatly underestimated. Continuous effort is required to improve the regional prediction on the chemistry weather prediction tool.

ACKNOWLEDGEMENTS

I would like thank the Ministry of Science Technology and Innovation (MOSTI) of Malaysia for providing financial support for this research work. This work is partly sponsored under contract number 06-02-12-SF0346. I would also like to thank University of Nottingham Malaysia Campus for awarding a research scholarship and the access to the University of Nottingham High Performance Computing Facility in UK.

I would like to express my sincere gratitude to my supervisors, Professor Andy Chan and Dr Lau Phei Li for the continuous support and guidance. Andy is an accountable and encouraging person that I can always turn to whenever I encounter problems. I am truly grateful to have you as my supervisor and wish you all the best in the new life event.

Besides, I would like to express my gratitude to my colleagues. They are, Mr. Muhammad Yaasiin Oozeer, Dr. Kenobi Isima Morris and Dr. Matthew Ashfold from University of Nottingham Malaysia Campus, and Mr. Kumarenthiran Subramaniam from Malaysian Meteorological Department who have helped with the data and provided their valuable input and suggestion to continuously improve my thesis. Also a big thank you to my friends who keep me accompanied and take good care of me whenever I am working around the clock: Ms. Lim Chang Nong, Ms. Jessica Lim and the unnamed heros and heroines in BSS, NLG03 and Ph.D who are also striving hard with research now. Thank to everyone who has helped me in any form during the research.

Last but not the least, a big hearty thank to my beloved family members, 妈，爸，姐，伟，嫂，欣，宁. Without the understanding, support and trust from you, I would not be able to focus and endure the hardship during the course of the research. This includes a special thanks to Mr Kon Kee Jun for the unconditional support and dearly love which keeps me motivated at all times.

TABLE OF CONTENTS

LIST OF FIGURES

LIST OF TABLES

LIST OF ABBREVIATIONS AND SYMBOLS

Chapter 1

UHI	:	Urban Heat Islands
SEA	:	South East Asia
LU	:	Land Use
USA	:	United States of America
GKL	:	Greater Kuala Lumpur
UN	:	United Nations
MC	:	Maritime Continent
WRF; WRF/ARW	:	Weather Research and Forecast Software with ARW core
NWP	:	Numerical Weather Prediction
NCAR	:	National Centre for Atmospheric Research
ARW	:	Advanced Research WRF
MMM	:	Mesoscale and Microscale Meteorology Division
CTM	:	Chemical Transport Model
CWP	:	Chemical Weather Prediction
MODIS	:	Moderate Resolution Imaging Spectroradiometer satellite
AVHRR	:	Advanced Very High Resolution Radiometer sensor
UCM	:	Urban Canopy Model
LSM	:	Land Surface Model
OSULSM	:	Oregon State University Land Surface Model
MM5	:	The fifth generation of Mesoscale Model
BEP	:	Building Effect Parameterization
BEM	:	Building Energy Model
UBL	:	Urban boundary layer
PBL	:	Planetary boundary layer
GIS	:	Geographical Information System

Chapter 2

NWM	:	North-East monsoon
SWM	:	South-West monsoon
TRMM	:	Tropical Rainfall Measuring Mission data

ERA-interim : ECMWF reanalysis data
WPS : WRF Pre-processing System
NETCDF : Network Common Data Form
NCL : NCAR Command Language
GRIB : General Regularly-distributed Information in Binary form
RDA : NCAR’s Research Data Achieve
MYT : Malaysian local time
ECMWF : European Centre for Medium-Range Weather Forecasts
CFL : Courant–Friedrichs–Lewy condition
RRTM : Rapid Radiative Transfer Model
BMJ : Betts-Miller-Janjić cumulus scheme
MMD : Malaysian Meteorological Department
DOE : Department of Environment Malaysia
ST : Weather stations
LDR : Low density residential
HDR : High density residential
COM : Commercial/ industrial region
LO : Original WRF LU map (MODIS)
LN : Updated LU map with 1 urban class
LN3 : Updated LU map with 3 urban classes
KLIA : Kuala Lumpur International Airport
CBL : Convective boundary layer
SBL : Stable boundary layer
UHII : UHI Intensity
noURB : WRF model case without urban grids in LU map
CAT : LU categories, refer to Table 3.2

Chapter 3

JPBD : Jabatan Perancangan Bandar dan Desa (Selangor Town and Country Planning Department)
noUCM : (Case settings for UCM) Noah LSM
bUCM : (Case settings for UCM) bulk UCM
SLUCM : (Case settings for UCM) default single layer UCM
calSLUCM : (Case settings for UCM) calibrated single layer UCM

JKR : Jabatan Kerja Raya (Public Works Department Malaysia)

Chapter 4

YSU : Yonsei University scheme
ACM2 : Asymmetric Convective Model version 2
MRF : Middle Range Forecast model
Eta : Janjić Eta Monin-Obukhov surface layer parameterization scheme

Chapter 5

SBOS : Synoptic flow flowing in the same direction with sea breeze
SBF : Sea breeze front

Chapter 6

RETRO : REanalysis of TROpospheric emission data
EDGAR : Emission Database for Global Atmospheric Research emission data
POA : Primary Organic Aerosols
CDP : Community Data Portal
MEGAN : Model for Emissions of Gases and Aerosols from Nature
EF : Emission factor
LAI : Leaf area index
PFT : Plant functional types

Chemical Species (according to alphabetical order)

BVOC : Biogenic volatile organic compound
CH_4 : Methane
CO : Carbon monoxide
CO_2 : Carbon dioxide
GHG : Greenhouse gases
HNO_3 : Nitric acid
HO_2 : Hydroperoxy radical
HONO : Nitrous acid
ISOP : Isoprene
N_2 : Nitrogen molecule/ gas

N_2O_5 : Dinitrogen pentoxide

NO : Nitrogen oxide/ nitric oxide

NO_2 : Nitrogen dioxide

NO_x : Nitrogen oxides

O : Oxygen atom

O_2 : Oxygen molecule/ gas

O_3 : Ozone

OH : Hydroxyl

OH· : Hydroxyl radicals

PM10 : Particulate Matter (<10 microns)

RH : Long hydrocarbon chain

RO_2 : Organic peroxy radical

SO_2 : Sulphur dioxide

VOC : Volatile organic compound

NMHC : Non-methane hydrocarbon

THC : Total hydrocarbon

Symbols (according to appearance)

C_h : Surface exchange coefficient of heat

κ : Von Kármán constant

z_a : Height of the lowest computational level above ground

$z_{0,m}$: Roughness length of momentum

$z_{0,t}$: Roughness length of heat

z : Height of model level

ψ_m : Stability dependent function of momentum

ψ_t : Stability dependent function of heat

L : Monin-Obukhov length scale

C : General term for prognostic mean variables

t : Time

$\overline{w'c'}$: Flux variance of prognostic variables c

$\overline{w'e'}$: Vertical divergence of vertical transport of TKE by w’

$\overline{w'u'}$: Vertical divergence of vertical transport of velocity u by w’

$\overline{w'v'}$: Vertical divergence of vertical transport of velocity v by w’

$\overline{w'\theta'}$: Vertical divergence of vertical transport of θ by w’

K_c : Diffusivity profile

η : Sigma-pressure vertical coordinate in WRF-ARW

p : Pressure

p_{hs} : Pressure of dry atmosphere at the surface

p_{ht} : Pressure of dry atmosphere at the top atmosphere layer

p_0 : Reference pressure (100 hPa)

μ : Mass of dry air per unit area within column in model domain

x : Horizontal coordinate in x-direction

y : Horizontal coordinate in x-direction

$\vec{u}$, u Velocity in x direction

$\vec{v}$, v Velocity in y direction

$\vec{w}$, w Velocity in η direction

U : u-vector (x direction) in flux form

V : v-vector (y direction) in flux form

W : w-vector (η direction) in flux form

$\vec{V}$: 3 directional vector field

$\nabla \cdot \vec{V}$: Divergence of continuously differentiable vector field

m : (in flux form) map factor

ϕ : Geopotential

ϕ_x : Geopotential in x direction

ϕ_y : Geopotential in y direction

ϕ_η : Geopotential in η direction

g : Gravity acceleration

θ : Potential temperature

θ_m : Potential temperature of moist air

Θ : Potential temperature under dry air condition

q_m : Mixing ratio of moisture

Q_m : Mass mixing ratio of moisture

α : Specific volume of air

α_d : Specific volume of dry air

q_v : Mixing ratio of water vapor

q_c : Mixing ratio of cloud water

q_i : Mixing ratio of ice

R_d : Gas constant of dry air

R_v : Gas constant of wet air

γ : Specific heat ratio (C_p/C_v)

C_p : Specific heat capacity of air under constant pressure

C_v : Specific heat capacity of air under constant volume

MAE : Mean Absolute Error

RMSE : Root Mean Square Error

FAE : Fractional Averaged Error

NMAE : Normalized Mean Absolute Error

M_{ni} : Measured data at n^{th} station at i^{th} hour

O_{ni} : Observed data at n^{th} station at i^{th} hour

N : (in error statistics) total number of stations

t : (in error statistics) total number of hours

T_j : Total number of j^{th} (0-23) daily hour within the simulation period

T2 : 2-meter temperature

RH2 : 2-meter relative humidity

TSK : Skin surface temperature extracted from WRF output

Q2 : 2-meter mixing ratio

uv10 : 10-meter wind speed

wdir10 : 10-meter wind direction

LST : Land surface temperature extracted from satellite imageries

Q_v : Vertical mixing ratio of water vapor

uv_h : Horizontal wind speed

PBLH/ h : Planetary boundary layer height

θ_v : Virtual potential temperature

TKE/ e : Turbulent Kinetic Energy

F_{urb} : Impervious fraction in an urban grid

F_{veg} : Vegetated fraction in an urban grid ($1-F_{urb}$)

Q_H : Sensible heat fluxes from surface

Q_{Hurb} : Sensible heat fluxes from urban surface

Q_{Hveg} : Sensible heat fluxes from vegetated surface

H_a : Heat exchange between urban architecture and urban canopy environment

H_{can} : Heat exchange between urban canopy environment and atmosphere above the canopy top

H_r : Sensible heat fluxes from building top

H_w : Sensible heat fluxes from wall

H_g : Sensible heat fluxes from ground

l_t : Normalized length of roof

l_r : Normalized length of canopy/ road width

l_w : Normalized length of wall/ building height

ε : Dissipation term

ρ : Density

K_c : Eddy diffusivity coefficient

l : Mixing length

S_c : Proportionate coefficient

γ_c : Counter-gradient term of local diffusion equation

M_u : Upward mixing fluxes from the top of the first model layer

M_{d_i} : Downward fluxes transport to a layer below

$M_{d_{i+1}}$: Downward fluxes transport to a layer above

C_l Prognostic variables at the top of the first model layer

f_{conv} : Fraction of non-local fluxes to total fluxes near surface

u_* : Friction velocity

K_a : Molecular thermal diffusivity of air

z_l : Height at the lowest level where turbulent heat transfer mechanism becomes important

Re : Reynolds number

υ_a : Kinematic viscosity of air

C_{zil} : Empirical constant in Eta scheme

h_c : Height of the canopy

RAINNC : Non-convective precipitation amount produced in WRF result

RAINC : Convective precipitation amount produced in WRF result

LIST OF APPENDICES

CHAPTER 1: INTRODUCTION

1.1 Background and motivation

1.1.1 Urban heating

Among the 3.9 billion global urban inhabitants, more than half settle in Asia, one of the less urbanized region in the world [*United Nations*, 2014]. These cities are projected to expand by 16% before 2050 to accommodate the urban rush. The demographic shift from country-sides to cities has caused the overcrowded metropolitan to be ubiquitously hotter than countryside [*Oke*, 1973, 1976]. The "Urban Heat Island" (UHI) is temperature upswing of metropolitan area compared to its rural vicinity as a result of continuous urban development [*Oke*, 1995]. The urban canopy warming effect is first documented in London [*Howard*, 1833] and receives growing interest in other cities, such as New York [*Bornstein*, 1968], Seoul [*Kim and Baik*, 2002], Taipei [*Lin et al.*, 2008], Thessaloniki [*Kantzioura et al.*, 2012], Shanghai [*Geng et al.*, 2011]. The warming phenomenon becomes one of the central topic of urbanization effect due to the continuous rise of UHI intensity over the years [*Kataoka et al.*, 2009]. Depending on the city size, local climate and urban fabric, UHI is recorded around 4 °C hotter than its surrounding rural for Asian cities [*Roth*, 2007; *Santamouris*, 2015]. The cities in South East Asia (SEA) records higher population growth rate compared to the other East Asian cities [*The World Bank*, 2017]. The urban heating rate is logarithmically proportionate to the population count [*Oke*, 1976; *Jauregui et al.*, 1992], hence expectedly, these countries experience one of the highest urban heating rate over the past 40 years [*Akbari et al.*, 1992; *Kataoka et al.*, 2009].

1.1.2 Importance of urban land use (LU) change

Urban region is delineated as area with intensive land use (LU) development to accommodate human activities. Attempts to overcome limitation and efficiency of spaces have led to ideas of maximizing the functionality of land use by replacing the under-utilized natural surfaces with man-made structures. The transformation of surface land cover alters the surface moisture and overall heat budget of the soil, near surface and boundary layer of the city. The formation of urban heating effect primarily stems from the introduction of impervious man-made surface and structure made up of engineered material with dissimilar thermal and radiative characteristics [*Oke,* 1987; *Jusuf et al.*, 2007]. These strong and durable man-made materials, especially concrete and asphalt are of high thermal conductivity to absorb and store massive heat during the day [*Oke and Maxwell*, 1975; *Akbari et al.*, 2008]. Unlike mature vegetated surfaces, the limited moisture content in urban surface impedes latent heat dissipation causing the ground to cool down at a slower rate [*Dimoudi and Nikolopoulou*, 2003; *Gao and Jia*, 2013].

1.1.2.1 Local circulation

As the height of buildings in urban increases, overall roughness length of the urban surface increases. This leads to the rising of the surface vicious layer that greatly reduces the air flow within the canopy layer. The long-wave solar radiation released then increases the nocturnal temperature within the densely-packed urban canopy (layer from ground up to average height of the buildings) with low sky-view factor [*Grossman-Clarke et al.*, 2008]. Urban surfaces with high thermal inertia topped up with anthropogenic heat emission retains intense heat within narrow urban canyons and bolsters the turbulent instability within the boundary layer especially after sunset [*Oke*, 1995; *Miao et al.*, 2009; *Giovannini et al.*, 2013]. The pressure depression induced by the UHI draws surrounding air towards the urban core forming the urban breeze [*Miao et al.*, 2009]. The warm air continues to rise and diverges near the top of the atmospheric layer to complete the thermal circulation. The formation of the complete urban heat circulation is particularly intense during the weak synoptic period under clear sky and calm condition [*Lai and Cheng,* 2009; *Santamouris,* 2015]. The severity of UHI is often amplified by the local topographic circulation [*Steyn*, 1996; *Lin et al.*, 2008; *Giovannini et al.*, 2013] and synoptic weather condition [*Morris et al.*, 2001; *Chow and Roth*, 2003; *Lai and Cheng*, 2009]. The urban forcing is found to displace and weaken/strengthen the topographic circulation depending on the location of urban, i.e. human settlement which situates within valley region sheltered by mountains or close to water body for protection, resources availability and accessibility [eg. *Freitas et al.*, 2006; *Thompson et al.*, 2007; *Ryu and Baik*, 2013; *Von Glasow et al.*, 2013].

1.1.2.2 Precipitation

Surface forcing driven by land surface of various characteristics has greatly influenced the flux dynamics of the atmospheric boundary layer, including its structure and associated clouds formation and precipitation processes [*Sertel et al.*, 2009; *Zhang et al.*, 2011; *Giovannini et al.*, 2013; *Li and Bou-Zeid*, 2014]. Evidences shows that surface characteristics of the urban have altered the rainfall and thunderstorm pattern within and around the city [*Shepherd*, 2005; *Von Glasow et al.*, 2013; *Han et al.*, 2014]. The urban surface is favorable for accumulating surface sensible heat fluxes and are known to enhance the precipitation intensity through formation of convective cells [*Thielen et al.*, 2000; *Kusaka et al.*, 2014; *Pathirana et al.*, 2014]. The surface dynamic drag developed at the urban agglomeration characterized by high roughness further leads to atmospheric instability and amplification of the buoyant movement of air parcel [*Thielen et al.*, 2000; *Carraca and Collier*, 2007; *Zhong and Yang*, 2015].

1.1.2.3 Air quality

Excessive gaseous pollutants and aerosols are emitted into the urban dome as a result of human activities including transportation, industrial and domestic energy usage [*Lin et al.*, 2008; *Salamanca et al.*, 2011]. Although the thermal forcing of the urban surface generates higher mixing height, the pollutant dilution is case-sensitive and highly susceptible to the topographic circulation with urban-induced alteration. In certain circumstances, the pollutants may eventually circulate back to the emission source of pollutant [*Lo et al.*, 2006; *Thompson et al.*, 2007] or transport to the adjacent sub-urban region that is generally calmer and hence more conducive to the formation of urban smog [*Sarrat et al.*, 2006; *Ji et al.*, 2013]. Under episodes of severe pollution, the radiation forcing is likely to attenuate and thereby reducing the amount of net radiation heat received by ground [*Rosenfeld*, 2000; *Quan et al.*, 2013]. The excessive aerosol would positively suppress the urban perturbation and the diffusion of the air constituent within the boundary layer, leading to more polluted scenario.

1.1.2.4 Future projection

Future projection of alteration of land use and cover results in major implication on surface environment and urban air quality but also overall energy budget of the boundary layer [*Mahmood et al.*, 2010; *Pielke et al.*, 2011]. *Foley et al.* [2005] has emphasized the implication of anthropogenic land use conversion in modern years and described UHI as "an extreme case of how land use modified regional climate". The land use conversion, for urbanization and agriculture, has heavily contributed to the reduction of diurnal temperature variation as well as surface warming up to 0.27 °C in the United States of America (USA) [*Kalnay and Cai*, 2003]. The urban-induced moisture convergence in lower atmosphere significantly is found to alter the regional hydrological cycle and involves in cases of intensive downfall and flooding [*Thielen et al.*, 2000; *Shepherd*, 2005; *Huong and Pathirana*, 2013]. Expansion of urban land use change in few large urban agglomerations has similarly discovered that increment of the daily temperature eventually leads to higher nocturnal ground ozone (O_3) and carbon monoxide (CO) concentration within the rapid years of urbanization [*Wang et al.*, 2007; *Jiang et al.*, 2008; *Yu et al.*, 2012; *Ryu et al.*, 2013a; *Li et al.*, 2014]. The continual thermal stress is estimated to stimulates an additional emission of isoprene [*Sanderson*, 2003; *Guenther et al.*, 2006].

Isoprene increment has apparently increased O_3 in isoprene sensitive region, especially the urban [*Wu et al.*, 2012; *Silva et al.*, 2016].

As discussed, the modification of land use has demonstrated a remarkable environmental impact on different scale and aspect. The urban-induced heating on near-surface environment leads to the adaptation and change of local circulation and convection on the boundary scale. The atmospheric pollutant composition in the urban and its surrounding region is also susceptible to the warming and interaction of urban and topographic-induced flow circulation. Hence, the research project attempts to scrutinize the effect of land use change in the urban compound for the intended study region.

1.1.3 Case study site: Greater Kuala Lumpur (GKL), Malaysia

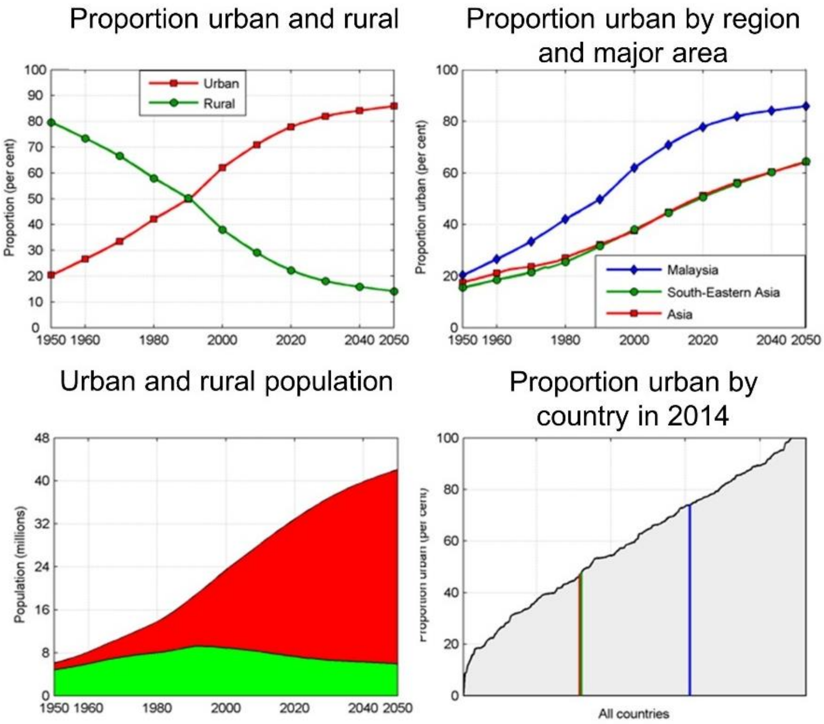

Figure 1.1: Urban population statistic in Malaysia, from United Nations **[2014]**

The Department of Statistics Malaysia has defined the concept of urban area as of 2010 as “*Gazetted areas with their adjoining built-up area which had a combined population of 10,000 or more. Built up areas were defined as areas contiguous to a gazetted area* *and had at least 60% of their population (aged 15 years and over) engaged in non-agricultural activities*" [*Department of Statistics*, 2011a]. With reference to the definition, the United Nations (UN) census statistics reported that the urban population in Malaysia has exceeded 60% of the national population and stayed ahead of the average condition of SEA and Asia countries (see Figure 1.1). Such adverse growth of population in the urban has swiftly posed threat to the continuous expansion of urban land use. Among which, Greater Kuala Lumpur (GKL) is the most urbanized conurbation of Malaysia [*Department of Statistics*, 2011b]. The urban agglomeration, also known as Klang Valley, covers the country's capital, Federal Territory of Kuala Lumpur, Federal Territory of Putrajaya, alongside with its surrounding satellite cities within the state of Selangor as shown in Figure 1.2. The population and housing census have shown that both Federal Territories recorded the highest urbanization rate of 100% and still counting [*Department of Statistics*, 2011b]. It is interesting to note that 27% of the population converges to 2% of the national land and the continuous urban population growth renders GKL one of the most vulnerable region for UHI implication.

Past studies report that the urban core of GKL experienced higher temperature up to 5.5 °C than its rural park and this city is on average 3.9 °C hotter than other cities in Malaysia [*Sani*, 1986; *Ng et al.*, 2005; *Elsayed*, 2012]. Lake Garden, once the heat sink of Kuala Lumpur region, is no longer exerting a low temperature along with the expansion of surrounding developing area [*Sani*, 1984]. Recent urban study in GKL has focused on the Putrajaya, the new administration of Malaysia. It is planned and built from scratch by embracing the concept of green garden city [*Ho*, 2006]. The measurement study observed the surface air temperature (~ 2 °C) is highest at night near the urban core (boulevard) compared to the urban park [*Ahmed et al.*, 2014]. The numerical effort agrees with the latter but with a slightly higher intensity for having the pre-urbanized form as the reference for the urbanized change [*Morris et al.*, 2015]. The fact that the surface air temperature increases with a lower rate (~ 1.4 °C) over a decade (1999 – 2011) has shown that proper planning is possible to improve the urban heating but not eradicate it [*Morris*, 2016b]. GKL is located within tropical wet climate regime with high humidity and sunshine all-year round based on the Köppen classification [*Roth*, 2007]. Under such hot and humid climatic condition, thermal stress experienced for the same amount of urban heat is much intense in tropics compared to the temperate region [*Akbari et al.*, 1992; *Zhao et al.*, 2014].

Disediakan dan diterbitkan oleh Jabatan Perangkaan Malaysia, 2010
Prepared and published by Department of Statistics, Malaysia, 2010

Figure 1.2: *Location of Klang Valley covering Kuala Lumpur, Putrajaya and surrounding administrative districts, extracted from Department of Statistics* [2011c]

Sitting at the heart of Maritime Continent (MC), weather of GKL is complicated by the heterogeneity of land-sea mask [*Oki and Musiake*, 1994; *Fujita et al.*, 2010; *Teo et al.*, 2011]. The large composition of water body within the scattered land surface complicates the weather and hydrological cycle in the region. GKL is well shaded by the central backbone of the peninsula, Titiwangsa mountain range and the Sumatra island as shown in Figure 2.4 in next chapter [*Oki and Musiake*, 1994; *Varikoden et al.*, 2010]. The geographical location of GKL forms a contrasting precipitation profile compared to the other states in Malaysia. The orientation of coast being perpendicular to the prevailing monsoonal wind causes such an out-of-phase climatic behavior more pronounced compared to the rest of the MC region [*Ding and Chan*, 2005]. The local weather of GKL is further discussed in the background weather (Section 2.2).

1.2 Effect of urbanization for sheltered coastal city

GKL lies in the Selangor state, a flat valley to the east of the Straits of Malacca. The region is identified as the land-side coastal tropical precipitation regime that features great influence of land-sea breezes [*Kikuchi and Wang*, 2008]. The mutual interactions of strong urban thermals with natural topographic flow are observed especially in valley and coastal cities such as São Paulo, Seoul, Pearl River Delta, New York, etc. [*Freitas et al.*, 2006; *Lo et al.*, 2006; *Thompson et al.*, 2007].

The differential heating rate of land surface and sea water body creates the thermal gradient between the surfaces and induces sea (land) breeze during the day (night). Urbanization has two different influences on the sea breeze flow propagation towards the urban cities. The high physical roughness of the urban surface produces larger surface friction and drag that decelerate the flow passing the coastal urban surface [*Freitas et al.*, 2006; *Chen et al.*, 2011a; *Ryu and Baik*, 2013]. In such case, the arrival of sea breeze front at the urban core is delayed due to the horizontal wind shear and lifting of the frontal head. This is observed in cities including New York [*Thompson et al.*, 2007], Greater Beijing [*Zhong and Yang*, 2015] and Toulouse [*Hidalgo et al.*, 2008]. This dynamical effect is also observed in Tianjin [*Miao et al.*, 2015], Athens [*Dandou et al.*, 2009], Houston [*Chen et al.*, 2011a] but it is limited to the initiation stage of sea (land) breeze flow in the morning (evening) near the upwind of coastal region (urban core). This occurs when the differential heating of urban is less significant [*Kang et al.*, 2014]. Therefore, as soon as the thermal gradient between the urban and water is established to counter the dynamical drag, the sea breeze passage starts to accelerate towards the urban heat center in the noon.

Studies have also found influences of sea breeze passage on the urban heat circulation. Strong sea breeze has weakened the urban thermal and displaces the UHI around 5 km to 10 km downwind of the city, especially in cities located near to the water body [*Gedzelman et al.*, 2003; *Dandou et al.*, 2009]. The UHI returns to the urban center following the dissipation of sea breeze at night [*Chemel and Sokhi*, 2012]. The delicate balance of the sea breeze-urban breeze system is subjected to the synoptic level condition. The strong prevailing synoptic condition has a suppressive effect on the urban heat circulation [*Seasman et al.*, 1988; *Lemonsu and Masson*, 2002]. The influence of synoptic condition on the topographic flow is usually directional; the landward (seaward) synoptic flow enhances the sea (land) breeze during the day [*Gedzelman et al.*, 2003; *Lai and Cheng*, 2009]. Conversely, when synoptic flow prevails in the opposite direction of sea breeze, sea breeze front is developed and more prone to the accumulation of secondary pollutant in the rear of the front.

For cities bounded by elevated grounds like GKL, the orographic movements such as up-, down- and cross-valley flows complicate the sea breeze-urban breeze circulation system. During the daytime, the air from the valley blows uphill and weakens urban breeze on the hill-side which flow in the opposing direction [*Ryu and Baik*, 2013; *Miao et al.*, 2015]. The valley/ up-mountain breeze has enhanced the sea breeze passage unlike the flat plain region that stagnates the sea breeze before the city [*Ohashi and Kida*, 2002]. However, the UHI tends to suppress the night inversion which weakens the down-valley flow and prolongs the duration of lake/sea breeze periods [*Giovannini et al.*, 2013; *Miao et al.*, 2015]. The displacement or weakening/strengthening of these currents has significantly altered the rainfall patterns [*Thielen et al.*, 2000; *Dixon and Mote*, 2003; *Kusaka et al.*, 2014] and pollutant level within and around the city [*Thompson et al.*, 2007; *Ji et al.*, 2013]. It is also found that a city located within a valley region with a crossing water body is more prone to pollutant accumulation due to re-circulation of air back to the land as observed in the Pearl River Delta and the Straits of Malacca [*Lo et al.*, 2006; *Fujita et al.*, 2010].

This greatly emphasizes the potential effect of urban-induced thermals on the topographic flows in the GKL region and vice versa. Comparative study also discovers that its valley-like topography has made it more vulnerable to the accumulation of heat and pollutants than the neighboring Singapore located within the same climatic zone [*Tso*, 1996]. Such a unique topography of GKL therefore intrigues the effect of urban heating on the local climatic conditions especially the topographic land/sea flow. In this context, a research tool with the ability to map the effect of terrain height and land-sea mask is essential to dissect the influence of urbanization.

1.3 Effect of urbanization on ozone emission

The implication of land surface re-characterization does not refrain to alteration of physical and thermal properties, but also the chemical constituents of the atmosphere [*Foley et al.*, 2005; *Mahmood et al.*, 2010; *Pielke et al.*, 2011]. Excessive gaseous pollutants and aerosols are emitted into the urban dome as a result of human activities including transportation, industrial and domestic energy usage [*Lin et al.*, 2008; *Salamanca et al.*, 2011]. Under the presence of sunlight, the anthropogenic emission of the urban pollutant, nitrogen oxides (NO_x) contributes great amount of tropospheric oxidizing radicals to the photochemical reaction and eventually forms ground O_3. O_3, a component in urban smog is well related to the aggravation of human health, crops production and ecosystems [*Chameides et al.*, 1988; *Bell et al.*, 2004; *Lacour et al.*, 2006]. On top of that, O_3 together with some of its precursors, including carbon dioxide (CO_2), methane (CH_4), and NO_x are greenhouse gases (GHG) with ability to heat up the air temperature. The GHG absorb the incident solar radiation, emit long wave radiation towards the ground and absorb long wave radiation re-emitted from the ground. The engulfment of radiation within the boundary layer can create inversion layer that suppress movements of rising air from being cooled and thus prevent the dispersion of these pollutants [*Taha et al.*, 1998]. The retention of heat-containing pollutants prevents the dissipation of heat produced or accumulated near the region and leading to larger heat built-up.

The urban environment is usually characterized with less favorable atmospheric condition for the dispersion of produced pollutant and heat. The higher nocturnal O_3 concentration in few large urban agglomerations is associated to urban-induced warming [*Wang et al.*, 2007; *Jiang et al.*, 2008; *Yu et al.*, 2012]. Photochemical ozone production is limited during the night hence the O_3 level is determined through the chemical loss rate of ozone (Equation 6.3). The warmed environment at night induces atmospheric instability which aids the dispersion of primary pollutant such as nitrogen oxide (NO) and hence the depletion of ozone [*Ryu et al.*, 2013a; *Li et al.*, 2014]. Ambient humidity is known to reduce to ozone level by terminating the chain reaction of the photochemical reaction and more significantly through the wet scavenging of nitrogen dioxide (NO_2) into nitrous acid (HONO) and nitric acid (HNO_3) [*Valuntaite et al.*, 2012; *Ono et al.*, 2014]. This also explains the higher ozone level that often observed in the dry urban environment with less vegetation cover [*Romero et al.*, 1999; *Civerolo et al.*, 2000; *Jiang et al.*, 2008]. The calm wind condition within the urban region is one of the contributing factor to the accumulation of O_3 precursors and O_3 exceedance [*Civerolo et al.*, 2000; *Duenas et al.*, 2002]. Frequently, the pollutant trapped during calm night causes the morning exceedance of pollution level [*Wang et al.*, 2007; *Lai and Cheng*, 2009]. The surface heat forcing from the urban surfaces driven by urban land surface has greatly influenced the flux dynamics of the atmospheric boundary layer and influence the pollutant transportation [*Civerolo et al.*, 2007; *Sertel et al.*, 2009; *Zhang et al.*, 2011]. It is also noted that the continual urban warming is likely to stimulate additional emission of isoprene (ISOP) from natural vegetation to counter the thermal stress [*Sanderson*, 2003; *Guenther et al.*, 2006]. The major natural emitters of this biogenic volatile organic compound (BVOC) is the evergreen forest and palm plantations that presence in abundance in the tropical region [*Misztal et al.*, 2011; *Guenther et al.*, 2012; *Miettinen et al.*, 2014]. More importantly, ISOP reacts actively with hydroxyl radicals (OH·) to produce peroxy radical and enhances the oxidation process of the NO for further ozone production. Such ozone forming mechanism is usually observed in the urban region where ISOP concentration is the limiting condition [*Wu et al.*, 2012; *Silva et al.*, 2016].

1.3.1 Ozone level in Klang Valley

Previous studies in Malaysia has shown that the daily maximum of ozone level is approximately 50±20 ppbv [*Banan et al.*, 2013; *Silva et al.*, 2016]. The highest ozone concentration and prolonged exceedance (>100 ppbv [*Department of Environment*, 2013]) are often recorded at stations located near the residential region with close proximity to the highly developed urban cluster or industrial area [*Latif et al.*, 2012; *Ahamad et al.*, 2014]. The study also shows that ozone level is generally the highest during the transition of winter monsoon into spring (November to March) and the lowest is observed during summer (June to August). The regional ozone level is highly correlated to the NO_x concentration and humidity level compared to the other air pollutants (CO_2, SO_2, PM_{10}) [*Ahamad et al.*, 2014]. Most previous work on effect of urbanization on local climate and air quality is conducted through analytical work of air quality recorded from ground measurement stations. Although it provides a valuable local information, it has the generic difficulty to scrutinize the sole spatio-temporal influence of urbanization. The ozone formation in the region is correlated with meteorological condition and primary pollutants while the role of imperative role of ISOP in ozone formation is thus far neglected [*Ahamad et al.*, 2014; *Tan et al.*, 2014]. Seeing that the ozone formation is subjected to the concurrent factors involving the emission from urban sources, the current effort to identify the effect of urbanization in the region on the air quality condition is still not well established.

1.4 Research approach

Most UHI work conducted in Malaysia has reported the statistical profile of near-surface ground parameters obtained from stationary measuring stations [*Ling et al.*, 2010; *Ishak et al.*, 2011; *Elsayed*, 2012]. Traversing sampling device was deployed to record the cross-sectional heating profile in the industrial plot of Johor Bahru, the southernmost city of the peninsula [*Kubota and Ossen*, 2009]. Comprehensive study on the implication of land use change on urban heating requires knowledge of on the spatial extent, hence in-situ measurement approach with their inherent limitation on spatial distribution is a less preferable alternative [*Mirzaei and Haghighat*, 2010; *Santamouris*, 2015]. Although, remote sensing approach is also adopted to study the spatial distribution of UHI [*Ahmad et al.*, 2009; *Salleh et al.*, 2013], the quality of satellite imageries vary greatly due to the cloud coverage and time lag in data collection [*Sohrabinia et al.*, 2012]. Nevertheless, it provides a sufficiently reliable surface reflectance data for time-invariant data such as land use cover [*Miettinen et al.*, 2014].

Despite the established urban canopy models incorporated to the weather models [*Grimmond et al.*, 2011], not until very recent that more simulation work on urban study are conducted in the SEA tropical region [*Roth*, 2007]. An ensemble study is conducted for the island city, Singapore to discuss the importance of anthropogenic heat emission and evapotranspiration of the urban surfaces on the urban wind field and precipitation pattern [*Li et al.*, 2013b, 2016]. Several efforts have verified the feasibility of garden city concept in the new administration center of Malaysia, Putrajaya which the urban heating is offset by the heterogeneous mixing of vegetation cover within the city [*Morris et al.*, 2015; *Morris*, 2016b]. Although the numerical weather prediction (NWP) model used is well verified with measured data in most of these studies, it is noted that the scientific ground of some essential parameterization physics is not given much attention. The application of the model physics remains an issue of reliability due to the lack of site-specific evidence and support, especially for case studies at high resolution urban scale of few kilometers [*Grimmond et al.*, 2011; *Liao et al.*, 2014]. The model sensitivity analysis and evaluation therefore become more pressing with the rapid growth of NWP application despite being in its induction stage in Malaysia.

1.4.1 Modelling tool

To resolve the detailed interactions of urban land surface with local atmospheric condition, high resolution NWP Advanced Research core of the Weather Research and Forecast (WRF-ARW) system version (3.6.1) is deployed [*Wang et al.*, 2015]. Weather Research and Forecast software (WRF), developed by National Centre for Atmospheric Research (NCAR) is a free software package for simulation of regional and global weather pattern. Advanced Research WRF (ARW) core developed by Mesoscale and Microscale Meteorology Division (MMM) of NCAR for research purposes is chosen for the simulation of historical local weather pattern to define the phenomenon of UHI in GKL; hereafter referred as WRF. The solver runs with non-hydrostatic Eulerian Mass dynamical cores with run time hydrostatic option [*Skamarock et al.*, 2008]. Mass-based vertical coordinate of atmospheric layer has abided by terrain-following hydrostatic coordinate. The governing equations are given in the methodology (refer to Chapter 2.3). WRF uses Arakawa C horizontal finite-difference grid to discretize equation and allows several map projections including Lambert-conformal, Mercator, Polar stereographic and rotated latitude and longitude. Owing to the elliptical shape of the Earth, all fully compressible non-hydrostatic equations are expressed in curvature terms. The solver applies a 3rd order Runge-Kutta scheme for time integration while 2nd to 6th order options are available for both horizontal and vertical advection scheme. Lateral boundary conditions are specified with relaxation for real cases while upper boundary conditions are open to rigid or absorbing to increase horizontal diffusion. Full physics options provided include microphysics, cumulus convection, atmospheric and surface radiation, land-surface specification etc.

The NWP tool is able to integrate a full online chemistry transportation model (CTM). The Chemical Weather Prediction (CWP) is known as WRF-Chem [*Grell et al.*, 2005] to account the non-linearity of the ozone formation process. The online mass continuity mechanism of gaseous chemistry accounts for the chemistry transportation, advection and reaction system, including dry and wet deposition, gas-phase chemical mechanisms, photolysis reaction, direct and indirect aerosol feedback interactions [*Peckham et al.*, 2014a]. Most CWPs adopt offline modelling system that performs calculation of chemical components separately from the weather model. The WRF-Chem model has a bidirectional feedback system for the simulated weather information and chemical module. It provides atmospheric processes that closely resemble the actual result to the chemical model. Although this method might take a longer computational power to generate different chemical transportation case for each weather set, the continuous simulation has prevented the potential information loss in atmospheric data which has a smaller time scale, especially in cases of highly-demanded fine resolution [*Grell et al.*, 2005; *Kukkonen et al.*, 2012]. WRF-Chem spearheads the development of online CWP with sophisticated system which integrates both NWP and CTM into each other at each allocated time step. Initial and boundary conditions are required to input emission packages to initiate and compute the biogenic emissions, biomass burning emissions, anthropogenic emissions and the background emissions such as dust, DMS and sea salt [*Peckham et al.*, 2014b].

The versatility of WRF model allows the different physical properties of land use to be investigated for their respective contribution to the urban heating, for example impervious fraction of surface [*Grimmond et al.*, 2011; *Giovannini et al.*, 2013; *Li et al.*, 2013a], roughness length [*Carraca and Collier*, 2007; *Loughner et al.*, 2012; *Zhong and Yang*, 2015], urban morphology and building materials [*Grimmond et al.*, 2011; *Giovannini et al.*, 2013; *Sharma et al.*, 2016a]. The powerful NWP model comes with complete source code that allows the communal effort of software developer and users to debug and improve the model. Such environment is especially conducive and beneficial to kick start the modelling effort in developing countries. To this end, this work attempts to scrutinize the effect of urban heating phenomenon as a result of urbanization in GKL by using a numerical modelling tool, WRF.

1.5 Evaluation of WRF performance in GKL

1.5.1 WRF Land Use (LU) Data

Terrestrial boundary data in numerical weather model including land use, soil texture and vegetation fraction map characterize the basic thermal and hydraulic properties of the land surfaces. These geological data governs the albedo, surface roughness, surface emissivity and thermal inertia that considerably affect the surface meteorological fields and overall energy budget of the boundary layer [*Lo and Quattrochi*, 2003; *Kumar et al.*, 2014]. Ensemble evaluation of the data suggested that correct representation of land use has significantly improved the surface fluxes and evolution of boundary layer [*Kumar et al.*, 2014]. Better approximation of vegetation fraction and leaf area index data have also successfully partitioned both the latent and sensible heat fluxes through radiation budget model [*Hong et al.*, 2009; *Kumar et al.*, 2014]. The evaluation of land use map is therefore essential to improve the model performance [*Mahmood et al.*, 2010].

WRF software supplies two land use classification maps by default. They are MODIS-20 captured by TERRA Moderate Resolution Imaging Spectroradiometer (MODIS) satellite in 2003-2004 and USGS-24 captured by Advanced Very High Resolution Radiometer (AVHRR) sensor in 1992-1993 [*Strahler et al.*, 1999; *Food and Agriculture Organization*, 2000]. They are compared in Table 1.1.

Figure 1.3 shows that MODIS manages to identify the dominant forest, evergreen broadleaf forest in Selangor while USGS misclassifies them as the irrigated cropland and pasture and deciduous broadleaf forest. Besides, MODIS is able to identify the urban and built-up land for the economic and administrative hub, GKL but USGS only locates 8% of this region as built-up area. The fully urbanized federal administration center, Putrajaya is located at 2°52’ to 2°59’ latitude and 101°40’ to 101°44’ longitude, marked by the circle in the same figure. MODIS classifies the administration center dominantly as cropland and shrubland with small patch of urban area on the north-east direction; while, USGS categorizes Putrajaya as deciduous broadleaf forest and irrigated cropland and pasture. None of the maps is able to identify the urban land use and reserved wetland in Putrajaya area. The misclassification of land use especially urban is similarly observed especially for assessment outside the USA [*Bai*, 2010; *Cheng et al.*, 2012; *Gao and Jia*, 2013].

Table 1.1: *Comparison of two WRF default land use classification maps: MODIS-20 and USGS-24*

Aspects	**MODIS-20**	**USGS-24**	**Reference**
Sensor	Terra MODIS	AVHRR	*Bai* [2010]
Data collection period	Jan 2003 - Dec 2004	Apr 1992 - Mar 1993	
Classification technique	Supervised decision-tree classification	Unsupervised with post-classification refinement	
Validation	High resolution images and other ancillary data	Other satellite images	
Category	20	24	Refer to official document
Official document	*Strahler et al.* [1999]	*Food and Agriculture Organization* [2000]	

The misclassification of urban land as vegetation in the model regulates excessive surface heat from the urban energy system to atmosphere through evapotranspiration and vaporization of soil moisture [*Lo and Quattrochi*, 2003; *Denman et al.*, 2007]. In turn, if the urban land is falsely located, the lower daytime surface temperature estimated might lead to lower boundary layer height and hence affects the diurnal sea/land breeze propagation for the coastal city [*Freitas et al.*, 2006; *Lin et al.*, 2008; *Sertel et al.*, 2009]. The major implication of misclassified land use and land cover highlights the need to feed appropriate land use map into the WRF model to reasonably simulate the effect of urbanization on local surface wind circulation. The generic representation of default land use map has prompted modelers to produce their own local land use map for in-depth investigation of the urban environment and planning strategies [*Ching et al.*, 2009; *Leung et al.*, 2010; *Meng et al.*, 2011].

1.5.2 Urban Canopy Model (UCM) in WRF

Together with other geographical information provided, the Land Surface Model (LSM) in WRF subsequently derives the surface forcing conditions from the thermal and physical features of different land use and soil classes [*Skamarock et al.*, 2008]. Noah

LSM inclusively covers the fundamental soil heat and moisture transfer processes for vegetation surfaces. It is originally the Oregon State University land surface model (OSULSM) designed to couple with the preceding mesoscale model of WRF, the fifth generation Mesoscale Model (MM5) [*Chen and Dudhia*, 2001]. The Environmental Modelling Center of NCAR named the Noah LSM[1] after several collaborators to recognize their contribution [*Mitchell et al.*, 2005]. The current Noah LSM incorporates new features such as diurnally dependent Penman potential evaporation model, 4-layer soil model, canopy moisture resistance formulation and surface runoff scheme [see *Chen and Dudhia*, 2001]. The scheme also accounts for the transpiration effect of vegetation for derivation fluxes instead of direct soil evaporation.

---

[1] Full name of NOAH acronym is N: **N**ational Centers for Environmental Prediction (NCEP); O: **O**regon State University; A: U.S. **A**ir Force; H: Office of **H**ydrologic

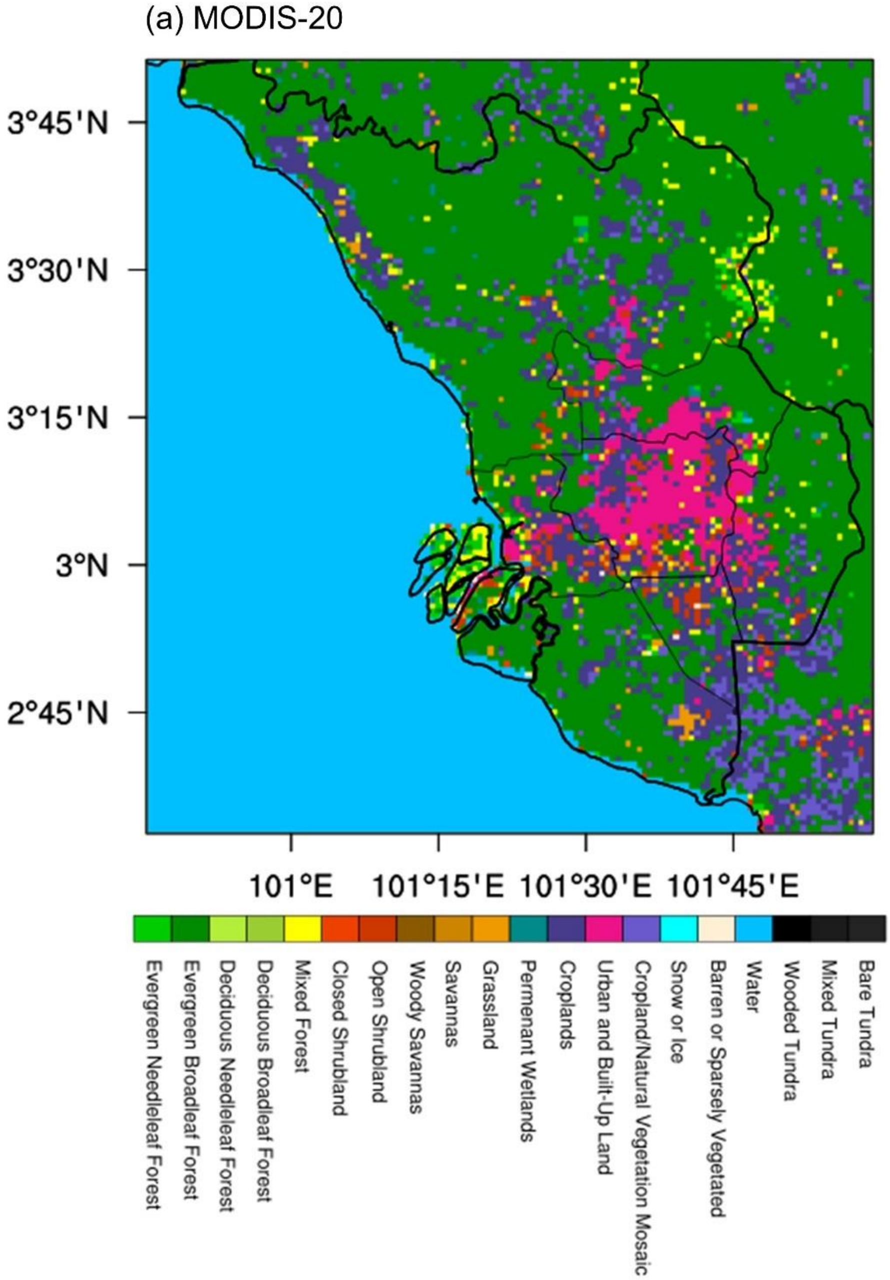

Figure 1.3: (a) WRF MODIS land use classification at 1 km resolution. The circle marks the location of Putrajaya.

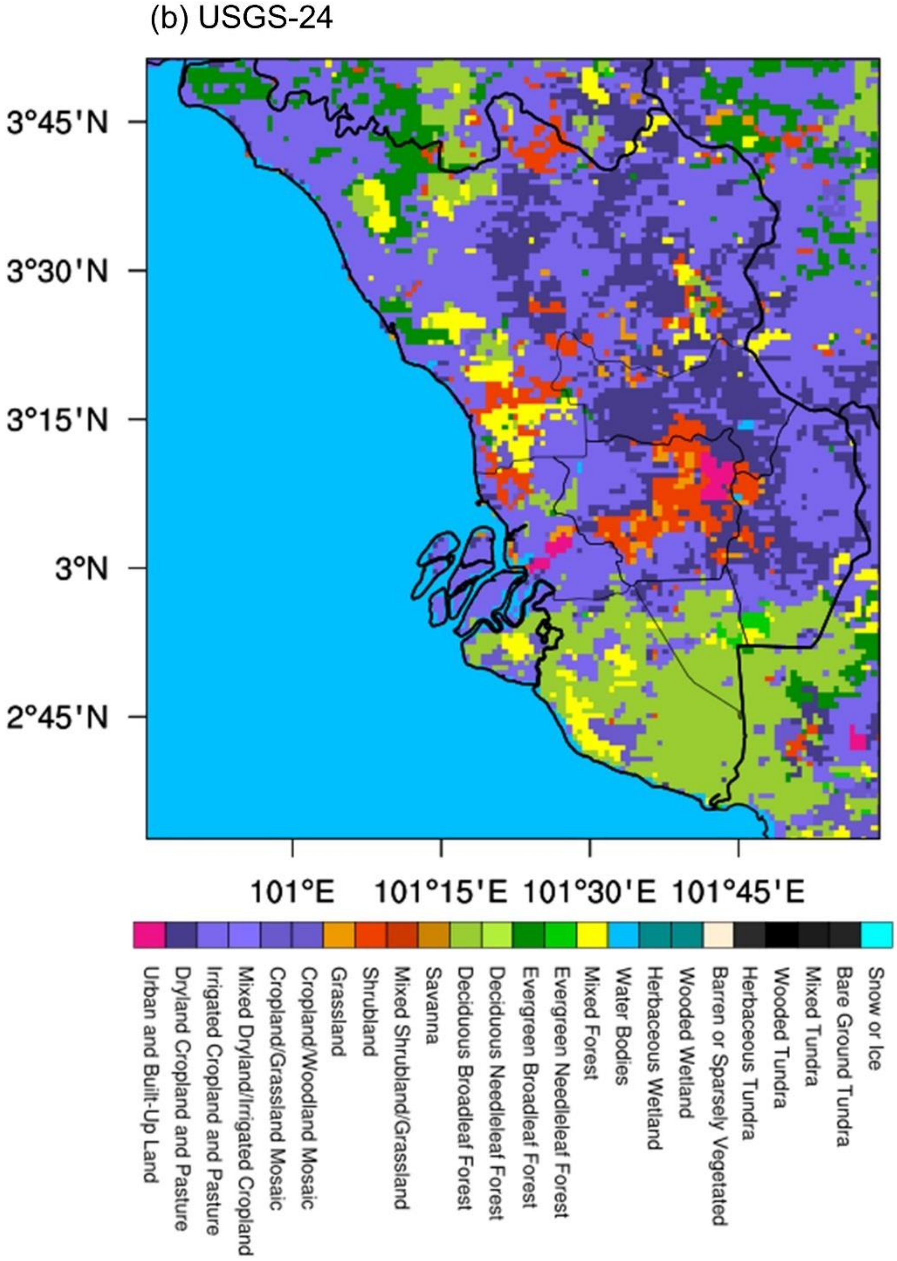

Figure 1.3 (cont.): (b) WRF USGS land use classification at 1 km resolution.

Urban canopy model (UCM) is an option coupled into the LSM model to parameterize the sub-grid scale interaction of localized urban surface texture and near-surface atmospheric condition [*Chen et al.*, 2004b; *Mirzaei and Haghighat*, 2010]. It bridges the gap between mesoscale atmospheric model and microscale transport to accurately capture the momentum, heat and moisture fluxes produced on urban canopy scale, resolvable at horizontal grid resolution of 500 m [*Chen et al.*, 2011b]. The urban surface dynamics could be better predicted with additional heterogeneous thermal and physical information of the urban canopy, especially with increasing demand for high resolution down-scaling studies [*Chen et al.*, 2004b]. Single-layer UCM is another UCM alternative that incorporates the shadowing, reflection and trapping of radiation fluxes within street canyons composing of roof, building and street surfaces [*Kusaka and Kimura*, 2004; *Chen et al.*, 2011b]. Also, there is a more sophisticated UCM, building effect parameterization (BEP) which accounts the three-dimensional building feature on multilayer interaction [*Salamanca et al.*, 2011]. With the introduction of simple building energy model (BEM), the multilayer UCM is able to incorporates the energy exchange function between the indoor and outdoor environment of buildings.

The original set of WRF urban canopy parameters is mainly compiled in the mid-latitude cities and therefore its applicability elsewhere often requires detailed evaluation [*Chen et al.*, 2011b]. *Chen et al*. (2004a) discovered that incorporation of the single-layer UCM to Noah LSM in Houston metropolitan manages to capture fine-scale UHI distribution according to the heterogeneity of the urban surfaces. An effort during Texas Air Quality Study 2006 summer field campaign further proves that the single-layer UCM compares better with the measured boundary layer height by realistically partitioning the latent and sensible heat fluxes of urban surface [*Lee et al.*, 2011]. However, the model fails to reproduce the near-surface temperature for commercial land use with the original urban parameters. The BEP+BEM scheme resolves the anthropogenic heat explicitly.

Hence, the multilayer scheme successfully improves the prediction of nocturnal UHI effect by supplying detailed indoor building energy data [*Sharma et al.*, 2016b]. *Grimmond et al.* [2011] has compared 32 offline UCMs (not limited to UCM in WRF) and showed that none of the model predicts all energy and radiation fluxes well. This is mainly attributed to few factors including the derivation of individual radiative fluxes through closure equation, physical interaction between the surface and atmospheric conditions, accurate representation of urban parameters and complexity of the model. For instances, the simple slab model is empirically designed to reproduce variables that is commonly used for verification, but it might not be true for the detailed energy and radiation budget when it is required. On the other hand, multi-layer UCM is able to include more details to reproduce the urban environment on a finer scale. However, its overall performance is highly susceptible to the quality of input data. Studies of UCM schemes in Baltimore-Washington, Yangtze River Delta and London also agree with the fact that each UCMs has its respective edges and weaknesses which the user needs to be mindful of [*Chemel and Sokhi*, 2012; *Li et al.*, 2013a; *Liao et al.*, 2014].

1.5.3 Boundary layer parameterization in WRF

The effect of uneven solar heating, land mask and terrain height contribute to the turbulent instability and hence the increment of mixing height of the urban boundary layer (UBL) [*Cooper and Eichinger*, 1994; *Lemonsu and Masson*, 2002; *Kang et al.*, 2014]. The urban-induced vertical air movements essentially determine the development and the structure of the boundary layer where fluxes of heat, moisture and component interacts between the land surface and the atmosphere. However, such eddies are unable to be resolved using conventional mesoscale numerical model and therefore have to be parameterized through the planetary boundary layer (PBL) model and surface layer model. In WRF, each PBL is bonded to a specified surface layer scheme. Therefore, discussion will focus on the comparison of PBL scheme while surface layer scheme is only briefly covered.

Surface layer parameterization provides exchange coefficients of surface heat, momentum and moisture to determine the amount of these fluxes between land surface and PBL. This routine serves as a bridge between LSM and PBL model. Radiative forcing and precipitation terms from PBL are passed to LSM together with the surface coefficient. Calculation of LSM then returns the value of surface heat and moisture fluxes back to PBL scheme for calculation of boundary layer flux convergence. The latter step has hence updated the information for atmospheric temperature and precipitation tendencies. The surface exchange coefficient of heat (C_h) in the heat surface flux is formulated according to the Monin-Obukhov Similarity Theory [*Monin and Obukhov*, 1954] as,

Equation 1-1: Monin-Obukhov Similarity Theory

$$C_h = \frac{\kappa^2}{\left[ln\left(\frac{z_a}{z_{0m}}\right) - \psi_m\left(\frac{z}{L}\right)\right]\left[\left(ln\frac{z_a}{z_{0t}}\right) - \psi_t\left(\frac{z}{L}\right)\right]}$$

where κ is von Kármán constant as 0.4, z_a and z is the height of the lowest computational level above ground and the calculated model level respectively, ψ_m and ψ_t is the stability dependent function of momentum and heat respectively, $z_{0,m}$ and $z_{0,t}$ is the momentum and thermal roughness length and L is Monin-Obukhov length scale,. C_h can also be applied to the mixing ratio and other passive scalar. Parameterization of the thermal roughness length is the major difference of each surface layer scheme.

In the weather simulation context, PBL physics resolve the subgrid-scale vertical interaction of surface heat, moisture and air constituent flux within the atmospheric environment bounded under the free atmosphere layer. It is around 500 m to 3000 m from

Earth surface [*Jacobson*, 2005; *Skamarock et al.*, 2008]. The general equation of boundary layer diffusion with assumption of gradient transport theory (K-theory) is

Equation 1-2: Vertical diffusion

$$\frac{\partial C}{\partial t} = -\frac{\partial}{\partial z}\overline{w'c'} = \frac{\partial}{\partial z}(K_c \frac{\partial C}{\partial z})$$

where C is prognostic mean variables (u, v, θ, q), $\overline{w'c'}$ is the flux variance, K_c is diffusivity profile. From which, K profile has to be determined as well as practical issues affecting the planetary boundary layer. Two methods are generally used to close the boundary layer turbulence problem. They are the local closure approach that estimates the turbulent fluxes at each point from the mean properties of its adjacent points and non-local treatment which determines the fluxes from the depth of boundary layer. Details are given in Section 4.2.

Comparative studies in the south-central USA have confirmed that local schemes produce closer agreement of vertical profile and near-surface variables under stable condition [*Hu et al.*, 2010; *Shin and Hong*, 2011]. Nevertheless, it is prone to overestimate the moisture content during summer. Non-local schemes excel in reconstructing the PBL height and estimating the lower boundary lapse rate even during the extreme cold episode which is pertinent to the prediction of pollution distribution [*Bossioli et al.*, 2009; *Xie et al.*, 2012; *Balzarini et al.*, 2014; *Cohen et al.*, 2015]. The PBL scheme determines the lapse rate, vertical turbulence fluxes and radiation admittance of the vertical layer. Hence, it can potentially affect the heat exchanges fluxes between the surface layer and the boundary layer to determine the urban-induced heating. Notwithstanding the inconsistent and site-specific performance of each boundary layer scheme, the PBL schemes are widely tested in the mid-latitude region, but little information is available for applicability in tropical regions. This has therefore rendered the site-specific investigation necessary to adopt more appropriate scheme for detailed UBL study within the region.

1.6 Research questions

The temperature increment within the urban dome is perceived as one of the detrimental factor that affects the environmental health and living quality of urban dwellers. As a consequence of urban heating, the stronger surface forcing has caused the growth of the UBL from which influence the flux dynamics of the surrounding atmosphere [*Sertel et al.,* 2009; *Zhang et al.,* 2011; *Giovannini et al.,* 2013; *Li and Bou-Zeid*, 2014]. Greater sensible heat stored has evidently shown to relate with the enhancement the convective cells within urbanized region and initiation of downwind precipitation [*Changnon,* 1981; *Bornstein and Lin,* 2000; *Dixon and Mote*, 2003; *Carraca and Collier*, 2007]. To counter the heat stress, increased usage of indoor cooling duty also amplifies the production rate of pollutants such as NO_x, VOC, CO, etc. These O_3 precursors can potentially be carried away to the downwind region and converts into fatal ground O_3 [*Pugliese et al.*, 2014; *Baklanov et al.*, 2016; *Huszar et al.*, 2016]. The neglect of these problems will further lead to urban heat, local circulation flow change, depreciated air quality, health problem and even global climate change [*Akbari et al.,* 2001; *Grimmond,* 2007; *Fiore et al.,* 2012].

The GKL urban agglomeration located near the coast and well within the central backbone of the Sumatra island and Malay Peninsula is experiencing coastal valley climate [*Oki and Musiake*, 1994; *Fujita et al.*, 2010; *Varikoden et al.*, 2010]. Under such circumstance, the presence of urban further complicates the topographically-induced circulation as seen in other coastal cities [*Freitas et al.,* 2006; *Chen et al.,* 2011a; *Ryu and Baik*, 2013]. Despite all the documented information, the urban studies in the most developed urban agglomeration in Malaysia is still lacking. Hence, this research attempts to study the effect of urbanization on the local climate and urban air quality for GKL, Malaysia. In this study, the contributing factor to the urbanization is narrowed down to modification of land use, i.e. introduction of urban land use.

This thesis uses the WRF numerical prediction software to study and reproduce the historical weather phenomenon in urban. Despite the growing WRF users in SEA region, the problem remains as to how accurate and robust is WRF, a modelling tool developed in the mid-latitude, to apply in the high resolution urban climate interest in tropics. As discussed in Section 1.5.1, the original WRF geological maps has failed to identify the urban area in the GKL region. Here lies one of the biggest challenge of the urban study is the inability of the modelling tool to capture the location of the urban land use. A thorough analysis of the land surface map therefore renders imperative before the WRF model is deemed suitable for high resolution application outside the USA.

On top of that, wide range of physics schemes is developed and is progressively improved to accommodate for distinctive applications considering area of interest, local climate condition, computational capability and etcetera. However, little information is available for the physics schemes selection to represent the heat, momentum and moisture fluxes of the urban surface, surface layer and up to the boundary layer in the case study region. This intrigues the model accuracy if the WRF is directly applied with default settings. Unsurprisingly, such consideration becomes more pressing when the case study is conducted with a non-locally developed model. The model evaluation for applicability is seen as a remedy to assure the reliability of the numerical tool.

1.7 Research scope and method

This thesis conducts an in-depth study of the urban-induced heating due to land use change using the state-of-art WRF numerical software in GKL, the most established urban conurbation Malaysia. Firstly, the project wants to identify the effect of urbanization on local climate and pollution at different scale, from the local near-surface canopy level to the regional circulation on the boundary level. Secondly, knowing that the application of WRF model in the region of Malaysia is at a rudimentary stage, the model is extensively tested with available measurement data to identify its strengths as well as weaknesses. In order to achieve these two aims, several objectives are outlined as below:

a) Evaluate the WRF model sensitivity to reproduce the urban climate on the surface layer and boundary layer extent.
b) Identify the urban heating phenomenon in GKL using the WRF software through the temperature profile of urban and non-urban case.
c) Investigate the effect of urban heating in GKL on the local climate and air quality.

In an attempt to effectively address all the research questions, the project conducted is split according to the scope with their respective research method elaborated as follow.

1.7.1 Scope 1: Evaluation of WRF performance on reproducing urban near-surface environment in GKL

In WRF, the land surface condition is characterized by the geographical surface map with supplementary surface thermal and physics information on each land use, vegetation and soil type. These surface data map supplied by WRF are invariant with time. The numerical methods in combination with the land use information from the remote sensing images are adopted to address spatio-temporal the heat accumulation scenario [*Freitas et al.*, 2006; *Miao et al.*, 2009; *Zhang et al.*, 2011; *Li et al.*, 2016]. Evidences above correspondingly show large discrimination between two WRF land use dataset provided. Given the rapid development of GKL, Geographical Information System (GIS) software is used to develop the updated land use map for the study period from the remote sensing images. WRF model coupled with Noah LSM is used to simulate several cases with different combination of land use maps and UCM settings. The sensitivity analysis of each combination is able to instigate the sensitivity studies of land use map in reproducing the boundary layer climate. It also sheds light on the ability of UCM and its calibrated urban variables to capture the momentum, heat and moisture fluxes produced on the near-surface environment. The meteorological data measured from ground weather station is used to verified the model performance on predictability of surface dynamics. However, development of local information such as land use map, surface parameters and urban parameters from scratch is an intricate process, especially when local information is scarce and inadequate. This scope attempts to examine the significance of updated land use map and calibrated urban parameters to improve the model performance in reproducing the urban heating phenomenon in GKL, from which the effect of urbanization is able to be identified.

1.7.2 Scope 2: Evaluation of WRF performance on reproducing urban boundary layer environment in GKL

Sensitivity study is performed on several physics which has extensive effect on localized climate case. This scope tests the performance of the physics scheme to ensure the appropriate representation of boundary layer before applying to the UBL study in GKL. The PBL schemes in WRF are sensitively tested against the measurement and sounding data to assess their respective strength and weakness. The distinct features of each parameterization schemes are first discussed. The accuracy of the boundary layer is evaluated for the near-surface environment. Ability of the schemes to predict the vertical profile and height of the boundary layer is also tested to ensure the scheme reproduces the vertical flux dynamics and later the distribution of precipitation.

1.7.3 Scope 3: Effect of urbanization on local climate and circulation in GKL

The urban region is able to induce local circulation and also modify the topographic flow as demonstrated in the past studies. The GKL agglomeration is a coastal city with the city center located less than 30 km from the less urbanized district, Klang on the west coast of Malay Peninsula (see Figure 1.2). On the east side, it is well sheltered by the

Titiwangsa mountain ranges. Hence, the urban thermal system is expected to interact with the local topographic flow, namely sea/land breeze and downhill/uphill breeze. Therefore, this scope aims to investigate the effect of urbanization on the local climate in GKL, with particular interest on its interaction with the evolution of land-sea and orographic flow. Studies are conducted during two inter-monsoon periods to evaluate the implication of synoptic influence on the aforementioned flow interaction. With the NWP tool, the thesis is able to compare existing case with control case without urban land use to isolate the external factors other than urbanization such as climatic forcing. Hence, for each simulation cases run, the corresponding non-urban cases are also simulated.

1.7.4 Scope 4: Effect of urbanization on atmospheric chemical constituent in GKL

Due to the complexity of the O_3 pollution issue, the local pollution condition has to be scrutinized. In this scope, the current O_3 pollution condition in GKL is studied to elucidate the existing nature of the O_3 pollution problem through the air quality monitoring record. The urban-induced changes of local weather and circulation pattern are subsequently studied to scrutinize the extent of featured urban environment contributes to the air quality issue. For this scope, WRF-Chem is be deployed to study the implication of urbanization on the regional air composition.

1.8 Significance of project

Recently, there is a growing interest of the usage of WRF numerical model in the SEA region. This study tests the applicability of the WRF software as an alternative approach to study the urban climate in GKL, one of the most rapid developing city in the SEA. With the extensive sensitivity study conducted, the study provides valuable information on the development of geological map. The knowledge of physics comparative study has great importance for the modelling community in the region on suitability of physics, namely the UCM and PBL physics.

The research project thus focuses on the identification of the UHI phenomenon in GKL and scrutinize the effect of urbanization on the near surface and local climate and atmospheric chemistry composition. Learning the genuine factors contributing to the warming phenomenon is able to foresee and tackle the problem of continuous development and growth of remaining cities in Malaysia, and also cities that share similar geographical properties, topographic structure and background weather. This is particularly important for the tropical countries that urban heating is often overlook due to the hot and humid weather. With the aid of numerical approach, the comprehension of the heating phenomenon in the country can be communicated with scientific evidence to garner more attention to the problem. From which, corresponding heat abatement strategy can be planned out to alleviate the ramification of urbanization. Therefore, this work is expected to provide a rigid scientific reference for the policy maker on the existing state of the environmental problem posed by the urban development. In order to thoroughly study the environmental impact of land use change in GKL, this thesis attempts to begin with the local urban heating on the surface layer before extending to the influence on the vertical boundary layers and its atmospheric composition.

1.9 Thesis organization

This chapter (Chapter 1) covers the introduction of the overall research project and overview of the thesis structure. Several imperative backbones for the induction of this research project are discussed, including the research aim and objectives. In-depth review on the main scopes, focusing on UHI, numerical weather forecasting, land use map quality, WRF physical options are compiled and discussed in this chapter. Documentations of literature have enable the author to arrive at several imperative research gaps that require serious attention and further investigation. Methodology and research direction are then formulated to strategically tackle these questions. Chapter 2 compiles similar methodologies adopted in this thesis. These include descriptions of WRF input and model evaluation. Several techniques and indicators to analyze output data from WRF are also elucidated in the chapter.

The research content starts in Chapter 3 (Scope 1) to evaluate the performance of WRF in simulating the urban surface layer. The first scope of the project requires preparation of updated land use map for the Selangor region. A brief introduction and problem statement is given to highlight the work scope. Methodology is included to cover the processing of images using ArcGIS software and conversion of format readable by WRF. Analysis subsequently focuses on the comparison of performance between the original and updated land use map in terms of meteorological difference. The updated land use maps developed will be further deployed to investigate the effect of urbanization in Selangor state. Chapter 4 covers the second scope (Scope 2) and extends the urban heating effect onto the boundary layer scale. The sensitivity test is first conducted for the major physical settings of WRF software, PBL physics. The type of parameterization schemes chosen for these physics can deviate the result of simulation. Hence, the best PBL option is returned to investigate change of land use on the local climate and circulation in Chapter 5 (Scope 3). The result of the sensitivity analysis is feed into WRF-Chem in Chapter 6 (Scope 4) to investigate the effect of urbanization on the air quality. The result of this case can finally be used to analyze the relationship of anthropogenic emission from urbanization with the heat phenomenon in Selangor state. The findings of each chapters and overall contributions are highlighted in Chapter 7. The problem statement and research questions posted in the first chapter are also answered in the chapter. Several suggestions are raised to improve the current project, without overlooking the potential outlook to continue the research work.

CHAPTER 2: METHODOLOGY

2.1 Introduction

The information collection in the previous chapter narrows down the scope of the urban study. It forms the basis of the model settings, including the case study domain and period. The background weather condition plays a crucial role in affecting the effect of urbanization, hence it is first analyzed during the case study period in Section 2.2. Section 2.3 hence presents the detailed execution flow of the WRF software, from the system configuration, general operation, preparation of input dataset to the selection of physics options. The experiment design varies on case-by-case basis so the detailed info for each scope is given in their respective chapter. The detailed evaluation methods and observation data for WRF model performance are also documented in Section 2.4. The model verification is particularly important to identify the most suitable physics options for the local application in the sensitivity analysis.

2.2 Background weather

The study domain is classified as tropical wet climate that is hot and receives rather consistent rainfall and precipitation throughout the year [*Roth*, 2007]. The climatic forcing from mainland Asia plays an immense role on the seasonal wind field and precipitation pattern in the Malay Peninsula [*Sani*, 1977]. The North-East Monsoon (NEM) during boreal winter (November to March) carries large amount of moisture to the east coast of Malaysia while the South-West Monsoon (SWM) during boreal summer (May to September) first passes Sumatra island and is rather dry when it arrives at Malay Peninsula. To focus on the study of local weather phenomenon, periods with less seasonal synoptic atmospheric forcing and rainfall anomalies are preferred [*Jauregui et al.*, 1992; *Santamouris*, 2015]. The inter-monsoonal period has minimal seasonal implication on local urban heating of west coast of Malaysia in October [*Sani*, 1977]. The two calm inter-monsoon months, April and October are chosen to represent the boreal spring and boreal fall respectively during 2003, the year of weak El-Niño [*McPhaden*, 2004]. According to the measurement from weather stations in GKL, the region receives rather weak winds in both months with average wind speed of 1.7 ms^{-1} and 2.1 ms^{-1} in April and October respectively as shown in Table 2.1. April experiences higher average daytime temperature of 30.6 °C and higher amount of precipitation, compared to October (29.6 °C). Convective raining usually occurs during the late afternoon in the April and night time in October. Such diurnal rainfall signal is common in the MC due to the presence of mountain near the coastline in the region [*Sow et al.*, 2011; *Teo et al.*, 2011; *Bhatt et al.*, 2016].

The meso-scale profile in Figure 2.1 shows strong synoptic wind blowing towards the southeast direction in October while weaker winds from northeast prevails in April. Despite the lesser rainfall amount measured in GKL, frequent precipitation activities are recorded in October than April. A contrasting precipitation profile is observed at the Straits of Malacca off the coast of GKL rest of MC in Figure 2.1a,b. Extracted from the Tropical Rainfall Measuring Mission (TRMM)[2] dataset [*Goddard Earth Sciences Data and Information Services Center,* 2016], the zonal statistical precipitation in Figure 2.2 has also shown that Selangor, Melaka and Johor have reversed rainfall precipitation trend during the two months compared to the whole Malaysia. Dissimilar to Perlis, Kedah, Pulau Pinang and Perak that are also located on the west coast region, these regions are

---

[2] TRMM dataset used the daily accumulated precipitation product at Level 3 (3B42) generated from the 3-hourly research-quality derived with the Version 7 TRMM Multi-Satellite Precipitation Analysis (TMPA) algorithm. The product is available at 0.25° x 0.25° resolution. The daily product is averaged during the period of study (refer to Section 2.3.3.1) and show in Figure 2.1.

well shaded by the elevated Titiwangsa mountain range, central backbone of the peninsula and the Sumatra island. Such an out-of-phase climatic behavior is especially outstanding amongst the other Maritime continent region, owing to the orientation of coast that is perpendicularly facing towards the prevailing monsoonal wind.

Following the withdrawal of the winter monsoon in April, the weakening of prevailing anti-cyclone, if any, over the Bay of Bengal significantly reduces the strength of north-easterlies over each coast of Malay Peninsula [*Ding and Chan*, 2005]. The sea-breezes from the Straits of Malacca and leeward wind originating from the dissipating monsoon enhances the convergence over the GKL in April [*Joseph et al.*, 2008]. On the other hand, the asymmetrical march of monsoon trough from the boreal summer to winter forms a low pressure belt off the coast of Borneo in October [*Chang et al.*, 2005]. The westerlies from equatorial Indian Ocean is induced and flows past the Malay Peninsula towards the convergence zone as shown in Figure 2.1c,d. It carries a large amount of moisture over the MC region well before the onset of the winter monsoon in 2003 [*Moten et al.*, 2014]. The sheltering effect of Sumatra island has subsequently obstructed the moisture bearing flow and creates a wet and cloudy environment for the entire MC but relatively dry in GKL in October.

Table 2.1: Weather information extracted from the measuring stations marked in Figure 2.6, except for the rain data which are extracted from Sepang (ST6) only. Data are compiled during the 18 day-simulation period listed in Table 2.3. MYT stands for Malaysian Time.

Weather parameters		**October**	**April**
Temperature (°C)	Daily	27.1	27.5
	Daytime (0830-1730)	29.6	30.6
Humidity (%)	Daily	77.1	81.1
	Daytime (0830-1730)	66.9	69.1
Wind speed (ms^{-1})	Daily	1.5	1.2
	Daytime (0830-1730)	2.1	1.7
Rain amount (mm) at ST6		42.8	324.6
Raining percentage at ST6*	Mostly cloudy	90.4%	84.3%
	Rain	9.6%	15.7%
	Frequent occurrence (rain)	2100 - 0800 MYT (49%)	2100 - 0800 MYT (15%)
	Thunderstorm	4.1%	11.8%
	Frequent occurrence (thunderstorm)	1400 - 2000 MYT (21%)	1400 - 2000 MYT (55%)

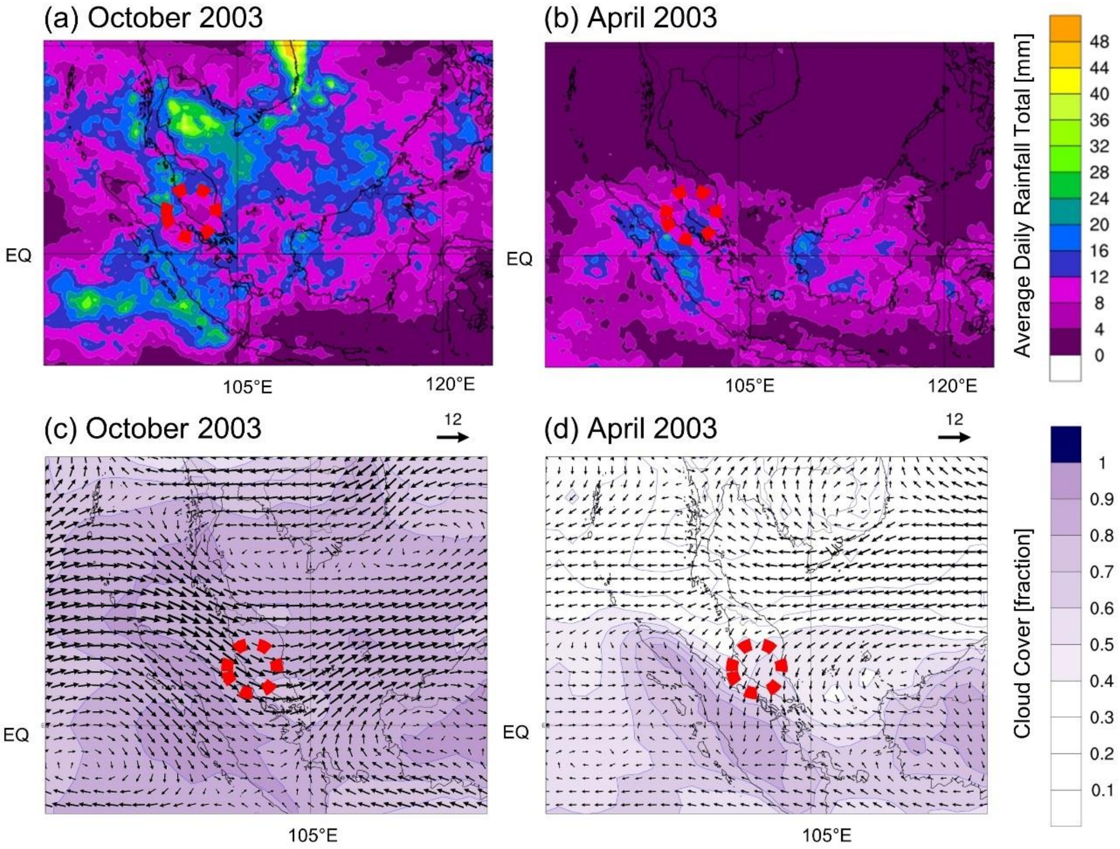

Figure 2.1: Precipitation profile extracted in year 2003 from TRMM for (a) October and (b) April. Cloud cover profile and wind field at 850 hPa from the ERA-interim reanalysis data (see Section 2.3.3.2) (c) October and (d) April. Location of GKL is marked with red dotted circle.

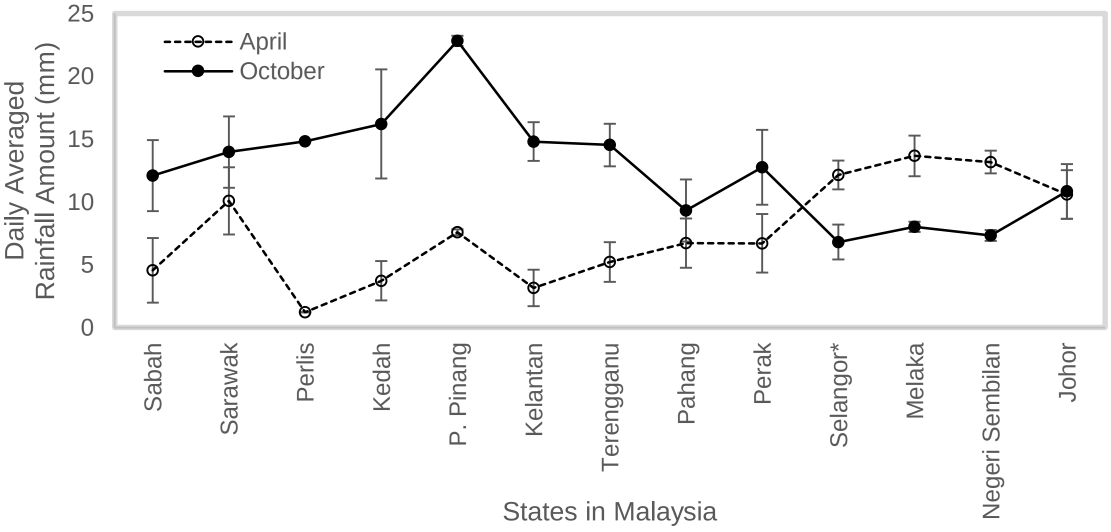

Figure 2.2: Daily-averaged rainfall amount and standard deviation for each state in Malaysia extracted from TRMM dataset.

2.3 WRF software

The handling of WRF software is the major part of the methodology. WRF is a Linux based software written in Fortran code. The WRF solver based on fully compressible non-hydrostatic Eulerian equation, with a terrain-following pressure coordinate in

Equation 2-1: Vertical coordinate

$$\eta = \frac{p_h - p_{ht}}{p_{hs} - p_{ht}} = \frac{p_h - p_{ht}}{\mu}$$

where p_{hs} and p_{ht} is the pressure of the dry atmosphere at the surface and top atmospheric layer respectively. μ represents the mass of dry air per unit area within the column in the model domain (x,y). The governing equations discussed below are in the flux form, as

	Cartesian coordinate	**WRF vertical coordinate system**
Equation 2-2: Momentum (u)	$\frac{\partial U}{\partial t} + \left(\nabla \cdot \vec{V} u\right) + \frac{\partial}{\partial x} P(p, \phi) = F_U$	$\frac{\partial U}{\partial t} + \left(\nabla \cdot \vec{V} u\right) + \frac{\partial p \phi_\eta}{\partial x} + \frac{\partial p \phi_x}{\partial \eta} = F_U$
Equation 2-3: Momentum (v)	$\frac{\partial V}{\partial t} + \left(\nabla \cdot \vec{V} v\right) + \frac{\partial}{\partial y} P(p, \phi) = F_V$	$\frac{\partial V}{\partial t} + \left(\nabla \cdot \vec{V} v\right) + \frac{\partial p \phi_\eta}{\partial y} + \frac{\partial p \phi_y}{\partial \eta} = F_V$
Equation 2-4: Momentum (w)	$\frac{\partial W}{\partial t} + \left(\nabla \cdot \vec{V} w\right) + \frac{\partial}{\partial \eta} P(p, \mu) = F_W$	$\frac{\partial W}{\partial t} + \left(\nabla \cdot \vec{V} w\right) + g(\frac{\partial p}{\partial \eta} - \mu) = F_W$
Equation 2-5: Mass Continuity	$\frac{\partial \Theta}{\partial t} + \left(\nabla \cdot \vec{V} \theta\right) = F_\Theta$	$\frac{\partial}{\partial \eta} \frac{\partial \Theta}{\partial t} + \frac{\partial}{\partial \eta} \left(\nabla \cdot \vec{V} \theta\right) = F_\Theta$
Equation 2-6: Thermodynamics	$\frac{\partial \phi}{\partial t} + \mu^{-1}\left[\left(\vec{V} \cdot \nabla \phi\right) - gW\right] = 0$	
Equation 2-7: Moist Thermodynamics	$\frac{\partial}{\partial t} Q_m + \left(\nabla \cdot \vec{V} Q_m\right) = F_{Q_m}$	$\frac{\partial}{\partial t} Q_m + \frac{\partial}{\partial \eta} \left(\vec{V} \cdot \nabla q_m\right) = F_{Q_m}$
Equation 2-8a: State	$p = p_0 \left(\frac{R_d \theta}{\alpha_d p_0}\right)^\gamma$	

The flux form variables are $\mathrm{U} = \mu\vec{u}/m, \mathrm{V} = \mu\vec{v}/m, \mathrm{W} = \mu\vec{w}/m$ with the map factor ($\mathrm{m} = (\Delta x, \Delta y)/(\text{distance on earth})$) that allows mapping of equation to sphere. Θ is the potential temperature under dry air condition and Q_m ($=\mu q_m$) is the mass mixing ratio of moisture form such as water vapor, cloud water, cloud ice, rain water, etc. The geopotential is given in $\phi = gz$ while p is pressure. The specific volume of air (α) is given in the form of specific volume of dry air (α_d) including the composition of other moisture species in $\alpha = \alpha_d(1 + q_v + q_c + q_i + \cdots)^{-1}$. The system is closed by using the diagnostic relation for specific volume with hydrostatic relation for dry air, $\phi_\eta = -\alpha_d\mu$ and the moist equation of state. Hence the equation of state (Equation 2-8) is updated to the moist potential temperature

Equation 2-8b:

$$p = p_0\left(\frac{R_d\theta_m}{\alpha_d p_0}\right)^{\gamma}$$

Where the moisture potential temperature, $\theta_m = \theta[1 + \left(\frac{R_v}{R_d}\right) q_v]$. The $\gamma = C_p/C_v = 1.4$, p_0 is the reference pressure (10^5 Pa). R_d and R_v is the gas constant of dry air and moist air respectively.

WRF modelling system consists of two key data processing stages which are WRF Pre-Processing System (WPS) and ARW core. When the calculation is done, the output result is sent to post processing system for extraction, analysis and visualization (see Figure 2.3). For real data simulation, WPS program specifies the location of interest and interpolates both time-invariant terrestrial data (such as albedo, land use index and terrain height) and time-varying meteorological data (such as surface temperature, sea pressure and humidity) together before feeding into the main core for iterative calculation. Several tools developed by different institutions are suitable for the extraction of the output data in Network Common Data Form (NETCDF) format. This study mainly uses NCAR

Command Language (NCL) as post processing purpose due to its ability to customize plots with inclusive features [*The NCAR Command Language*, 2016].

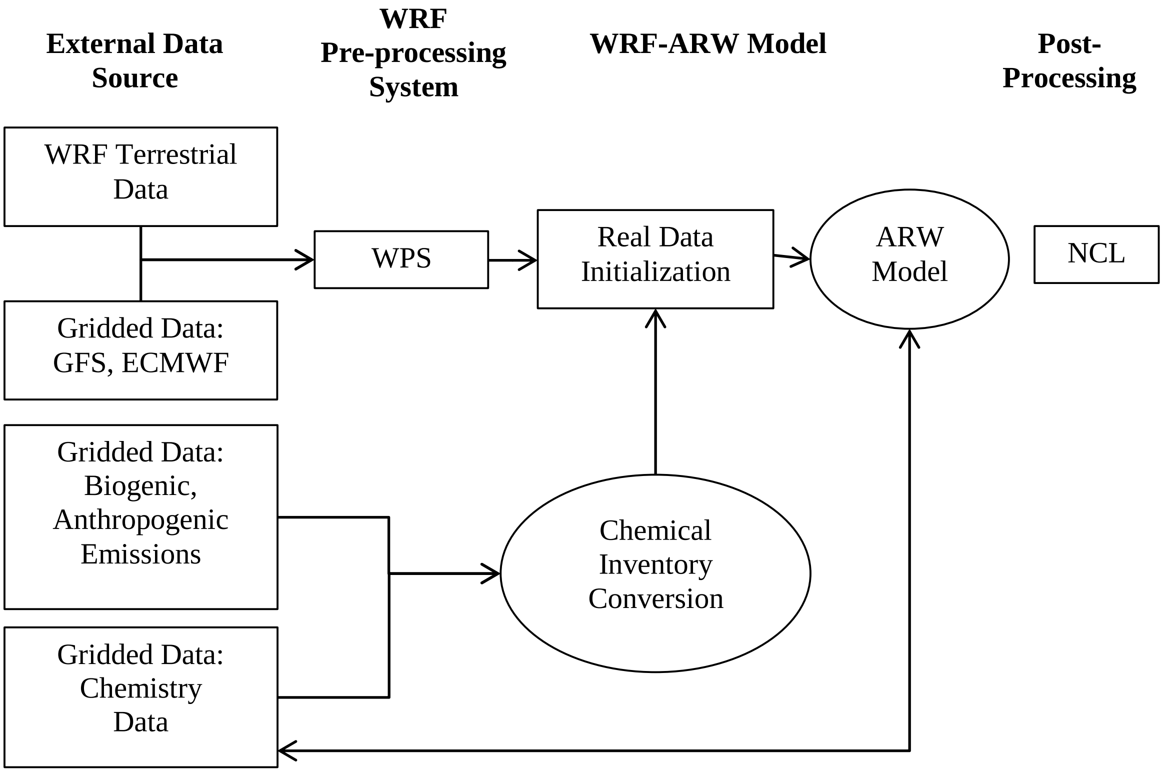

Figure 2.3: *WRF-ARW with online chemical module modelling flow **chart**, from Peckham et al.* [2014a]

2.3.1 Software compilation

Operation and compilation of software require knowledge of LINUX operating system to prepare of workstation with necessary libraries for the complete functionality of the software. As every computer supplier provides different CPU system, substantial time is undertaken for the installation and debugging of errors and warning messages. The compilation procedures of the software used such as WRF, WPS and post-processing tools are given in the Appendix A.1.

2.3.2 General steps to execute WRF

The simulation study runs with WRF version 3.6.1 compiled in the University of Nottingham High Performance Computing Facility (Minerva). The WPS system comprises of three main execution commands, namely GEOGRID, UNGRIB and METGRID. GEOGRID is a tool to define simulation domain and interpolate terrestrial data to simulation domains. The static terrestrial data is nested and interpolated onto the horizontal grid in GEOGRID function. The land use data is prepared and updated for the case study. Section 3.2 gives detailed development of updated land use map. The reanalysis meteorological data in General Regularly-distributed Information in Binary form (GRIB) form is used as lateral boundary condition in the model. GRIB file is selected upon the data resolution, time intervals and necessary variables which suit the case study settings. UNGRIB decodes the time-series data acquired from NCAR’s Research Data Achieve (RDA) database and converts into simplified intermediate file. The METGRID function subsequently interpolates the decoded GRIB data into the domain nests produced by GEOGRID. In the pre-processing steps, these WPS executables read domain information and input data from the *namelist.wps* given in Section 2.3.3.

During the initialization, the REAL function interpolates a series of intended variables such as temperature, pressure, layer thickness into the defined vertical arrays to produce the initial and boundary condition. The solver then computes the governing equation and selects the physics and dynamics forcing information specified in the *namelist.input* file [*Skamarock et al.*, 2008]. The WRF simulation output is verified against the ground weather station, sounding data and extracted satellite data to evaluate its accuracy and reliability for each study scope in Section 2.4. The assessed result is then analyzed according to respective scope there onwards using post-processing and illustration tool. Table 2.2 tabulates the general steps for the WRF execution.

Table 2.2: Execution step for WRF

Step no.	**Step description**	**Remarks**
Preparation of input data		
Step 1	Static geological data	Default WRF dataset. Preparation of LU map is shown in Section 3.2
Step 2	Temporal weather data	Download from rda.ucar.edu
WPS execution		
Step 3	Prepare namelist.wps	Time and spatial domain settings discussed in Section 2.3.3.
Step 4	Run GEOGRID	Make sure specification in GEOGRID.TBL reads the static data (Step 1) and interpolate it correctly
Step 5	Run UNGRIB	Make sure appropriate Vtable is used to convert the GRIB data (Step 2)
Step 6	Run METGRID	Make sure specification in METGRID.TBL read output data from Step 3 and Step 4 and interpolate it correctly
WRF execution		
Step 7	Prepare namelist.input	Domain information from namelist.wps in Step 3, physics and dynamics settings shown in Section 2.3.3.
Step 8	Run real.exe	Make sure eta-level in namelist.input in Step 7 is set correctly.
Step 9	Run wrf.exe	
Post-processing		
Step 10	Verification	Ground weather parameters collected from ground stations, sounding data, satellite data. Detail of model verification is shown in Section 2.4.
Step 11	Analysis of result	Plot spatial/ vertical profile with post-processing and visualization software in Appendix A.1.11.

2.3.3 WRF model settings and physics

2.3.3.1 Time and domain settings

All simulations are initiated from the 0800 Malaysia Time (MYT) starting on 1st day to 0800 MYT of 20th day for both month (April and October) respectively. The results analyze exclude the first 24 hours which is the spin-up period. The remaining 18 days are then analyzed and discussed in this thesis. The model domain is centered at GKL as shown in Figure 2.4. The parent domain covering the entire Malaysia (including Borneo) is dynamically downscaled from 27 km (110 x 100) to 9 km (100 x 103). It is further downscaled to cover the west coast of Peninsula Malaysia at 3 km (100 x 100) and to 1 km (139 x 148) for Selangor state where GKL is located in the 4th domain (d04). Information in parenthesis is the number of grids in zonal and meridional direction respectively. The spatial domain is projected onto the Mercator coordinate and cuts the equator (0 °) as the true latitude.

2.3.3.2 Input dataset

The default static geological dataset provided by WRF is used. Amongst the two original land use map, the MODIS map is used to represent the LU. It is further updated for the 4th domain with detailed step explained in Section 3.2. All cases incorporate 1 km high resolution MODIS green fractional map. The simulation model uses the 6-hourly ERA-Interim Reanalysis[3] data supplied by European Centre for Medium-Range Weather Forecasts (ECMWF) initial and lateral boundary conditions [*Dee et al.*, 2011]. Improved from the previous version ERA-40, ERA-Interim dataset is available in higher horizontal resolution of 0.703° longitude and 0.702° latitude at 60 model levels within the case study period. Collective assessment effort has also affirmed the reliability of the reanalysis dataset to reproduce the air temperature and precipitation profile [*Dee et al.*, 2011; *Decker et al.*, 2012]. The sea surface temperature is nudged at every six hours to allow the integration of the regional influence of ocean wind flow for the coastal city [*Tangang and Juneng*, 2004].

---

[3] Official download link for ERA-interim data: http://apps.ecmwf.int/datasets/data/interim-full-daily/levtype=sfc/

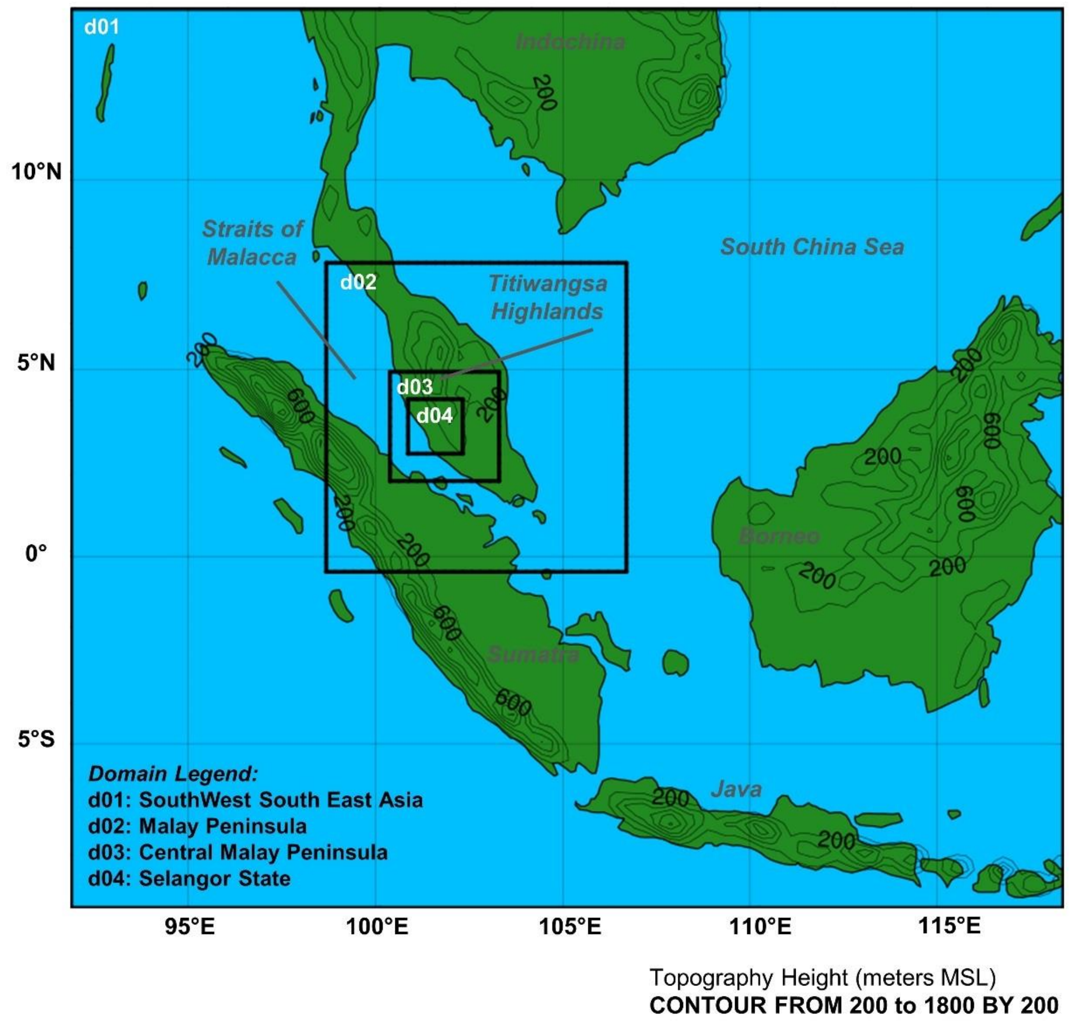

Figure 2.4: Location map with terrain height information and domain settings of GKL for WRF simulation; d is denoted as domain with the following numbering indicates the number of domain.

2.3.3.3 Physics Options

There are 37 full sigma vertical levels from surface up to model top at 50 hPa. 15 levels are allocated below the lowest 1 km as tabulated in Table 2.3. The increment of the vertical resolution closer to the surface is required to resolve the rapid near-surface atmospheric variability. Vertical velocity is stronger near the higher terrain but vertical atmospheric layers is more compressed in the WRF terrain-following pressure vertical coordinate. Hence, they are carefully designed to prevent the potential violation of stability criterion (Courant–Friedrichs–Lewy (CFL) condition < 1) for the study site that is surrounded by mountain ranges [*Jacobson*, 2005; *Wang et al.*, 2015]. The ERA-interim data with 60 model levels supplies sufficient lateral boundary data for quality vertical interpolation to the specified model level as illustrated in the full vertical level diagram in Figure 2.5.

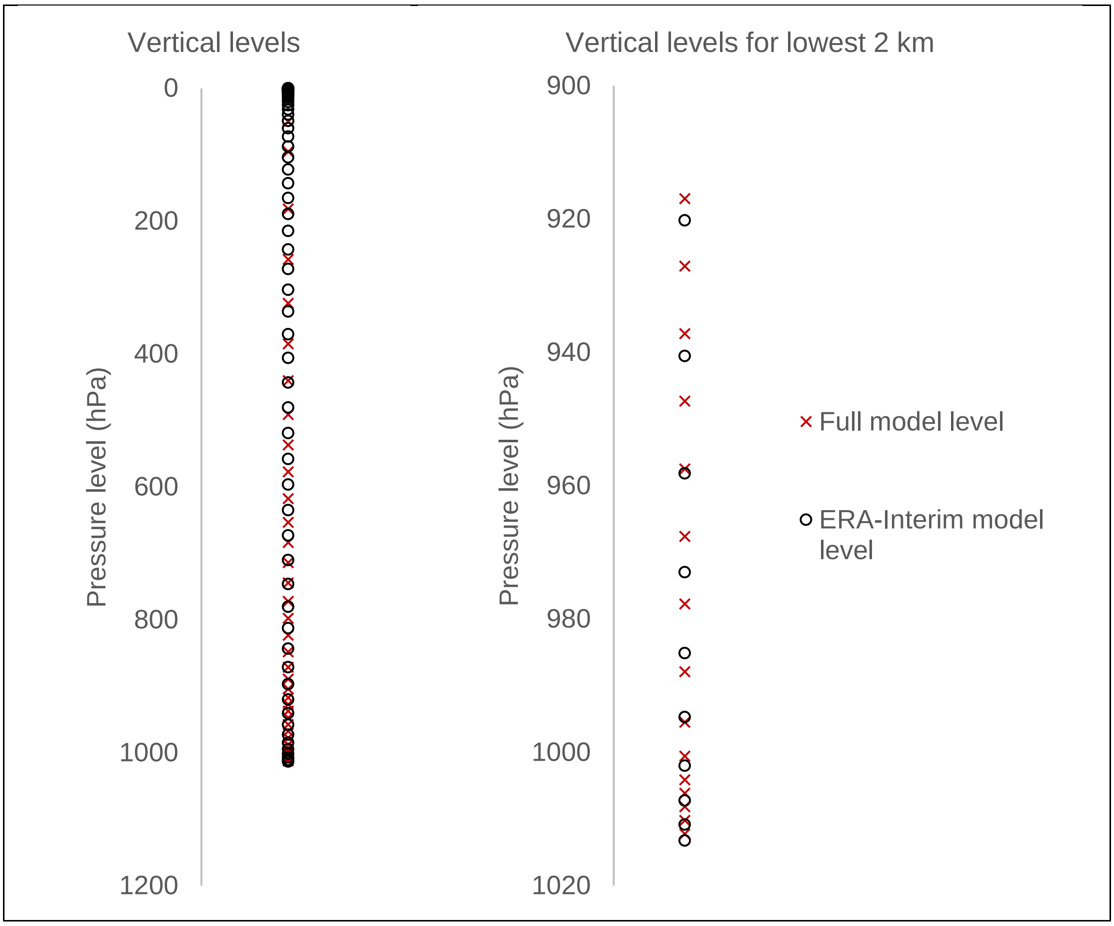

Figure 2.5: Vertical coordinate of model and ERA-interim data

Table 2.3: Model settings and physics options

Parameters	**Value/ Option**	**Detail**
Simulation period	19 days	1st April/October 2003 0800 MYT – 20th April/October 2003 0800 MYT;
Analyzed period (One-day spin up)	18 days	2nd April/October 2003 0800 MYT – 20th April/October 2003 0800 MYT;
Domain setting	1st (d01): 27 km (110 x 100)	The entire Malaysia including Borneo
	2nd (d02): 9 km (100x 103)	Malay Peninsula
	3rd (d03): 3 km (100 x 100)	West coast of Peninsula
	4th (d04): 1 km (139 x 148)	Selangor state
Vertical levels (in eta levels)	37 vertical eta levels	1.0, 0.9958, 0.9916, 0.9874, 0.9832, 0.9789, 0.9705, 0.9621, 0.9537, 0.9453, 0.9368, 0.9284, 0.9179, 0.9074, 0.8968, 0.8863, 0.8705, 0.8547, 0.8389, 0.8158, 0.7895, 0.7632, 0.7368, 0.7053, 0.6737, 0.6421, 0.6105, 0.5684, 0.5263, 0.4842, 0.4316, 0.3789, 0.3158, 0.2526, 0.1789, 0.0947, 0.0
Land surface model (LSM)	Noah LSM	Discussed in Section 1.5.2
Urban canopy model (UCM)	No UCM/ bUCM/ SLUCM/ calSLUCM	Only enabled for d03 and d04. Further discussed in Chapter 3
Planetary boundary layer (PBL) scheme	MYJ/ YSU/ ACM2	Further discussed in Chapter 4
Surface layer scheme	Eta/ MM5	Depending on PBL scheme used
Microphysics scheme	Purdue Lin single moment	
Cumulus scheme	Betts-Miller-Janjić	Only enabled for d01 and d02.
Radiation scheme (long wave and short wave)	RRTMG	
Lateral boundary data	ERA-interim 6-hourly reanalysis data	
Static geological data	Default WRF dataset	Land use data is updated and preparation step is given in Section 3.2

WRF has a complete physics options for the land surface, boundary layer, radiation, microphysics and cumulus parameterization [*Skamarock et al.*, 2008]. They supply necessary variables for physics calculation and modify the tendencies according to its presumed condition. The selection of parameterization schemes for surface (LSM, UCM) and boundary layer (PBL), as discussed in Chapter 1, will be selected after in-depth assessment in following Chapter 3 and 4. For the rest of the cases, Rapid Radiative Transfer Model (RRTM) scheme is adopted to handle radiative problem including ground heating budget from incident solar shortwave radiation as well as heating and flux divergence through longwave radiation emissions [*Mlawer et al.*, 1997]. Betts-Miller-Janjić (BMJ) cumulus scheme is incorporated for the two outer domains that convective process is unable to explicitly resolve the convective process at grid scale larger than 5 km [*Janjić*, 1994]. The scheme reproduces the convective rainfall pattern and intensity well [*Salimun et al.*, 2010] in the Malay Peninsula where the afternoon precipitation mainly occurs due to instability of rising air movement over mountain [*Sow et al.*, 2011; *Teo et al.*, 2011]. Microphysics physics is a series of explicit derivation of water vapor cycle in different phase to maintain their saturation condition [*Skamarock et al.*, 2008]. It is parameterized with Purdue Lin single moment microphysics scheme to determine the mixing ratios of water substance in six forms including water vapor, cloud water, rain, ice, snow and graupel [*Lin et al.*, 1983]. These physics options are mainly selected because they are able to produce reliable model accuracy with the limited computational time and resources.

2.4 Model evaluation

While using WRF software to work on the simulation modelling, model output is compared to historical meteorological data to confirm and ensure the accuracy and reliability result. The term “verification” is used in place of “validation” in the remaining context to measure the ability of algorithms and codes to reproduce real life phenomenon [*Kukkonen et al.*, 2012].

2.4.1 Error Indicators

The model is tested with the four statistical error indices to reflect the conformity of modelled data [*Willmott and Matsuura*, 2005; *Yu et al.*, 2006; *Morris et al.*, 2016]. Mean Absolute Error (MAE) shows the average departure of simulated value from actual result while Root Mean Square Error (RMSE) is able to emphasize the impact of larger error that run away from the observation,

Equation 2-9: MAE

$$\boldsymbol{MAE = \frac{1}{Nt}\sum |M_{ni} - O_{ni}|}$$

Equation 2-10: RMSE

$$\boldsymbol{RMSE = \left(\frac{1}{Nt}\sum (M_{ni} - O_{ni})^2\right)^{1/2}}$$

where n is the station number, i is the simulation time in hour, N is the total number of stations and t represents the total simulation hours. M and O represents the modelled and observed variables respectively. Both of the indicators give positive value and the larger value implies larger error departure from measured data. The asymmetrical of result is accounted with Fractional Averaged Error (FAE) by referencing it to the average of both datasets,

Equation 2-11: FAE

$$\boldsymbol{FAE = \frac{1}{Nt}\sum \frac{|M_{ni} - O_{ni}|}{(M_{ni} + O_{ni})/2}}$$

Seeing that the value range (in fractions) of the latter might be confused with conventional representation, Normalized Mean Absolute Error (NMAE) is therefore introduced to represent the absolute error factor of the mean observation value, particularly for the accuracy evaluation of model simulated air pollutant concentration.

Equation 2-12: NMAE

$$\boldsymbol{NMAE = \frac{\sum |M_{ni} - O_{ni}|}{\sum O_{ni}}}$$

The mean bias of modelled result and observed data is not derived because the model performance is likely to vary diurnally. Hence, the hourly accuracy of the modelled parameters is compared with the observation to compare the model variation diurnally. Hourly RMSE is calculated to show the hourly variation of the error indices,

Equation 2-13: Hourly RMSE

$$\boldsymbol{RMSE_j = \left(\frac{1}{NT_j}\sum\left(M_{nj} - O_{nj}\right)^2\right)^{1/2}}$$

where j is the hour in a day (0000 – 2300 MYT) while T_j is the total number of daily hour within the simulation period. For example, if the analysis starts from 2nd Oct 2003 at 0800 MYT to 20th Oct 2003 at 0800 MYT, T_j is 19 for 0800 MYT while for T_j is 18 for the remaining hours other than 0800 MYT.

2.4.2 Near-surface parameters

Eight ground weather stations operated by Malaysian Meteorological Department (MMD) and Department of Environment Malaysia (DOE) supply 2-meter temperature, 2-meter relative humidity and 10-m wind profile for model verification. The stations (ST) are plotted in Figure 2.6 with details information listed in Table 2.4. The accuracies of modelled near-surface variables are evaluated with the aforementioned four error indices compiled at each hour for each stations. The post-processing tool (NCL) is scripted to extract the point-wise time-series data for the verification. The near-surface data is evaluated according to the statistical benchmark proposed by *Emery et al.* [2001]. The benchmark has allowed less than 20th percentile error for the basic near-surface parameters after detailed assessment based on the performance of past MM5 (previous version of WRF) studies [*Emery et al.*, 2001; *Mcnally and Wilkinson*, 2010]. The adopted benchmark is compiled in Table 2.5.

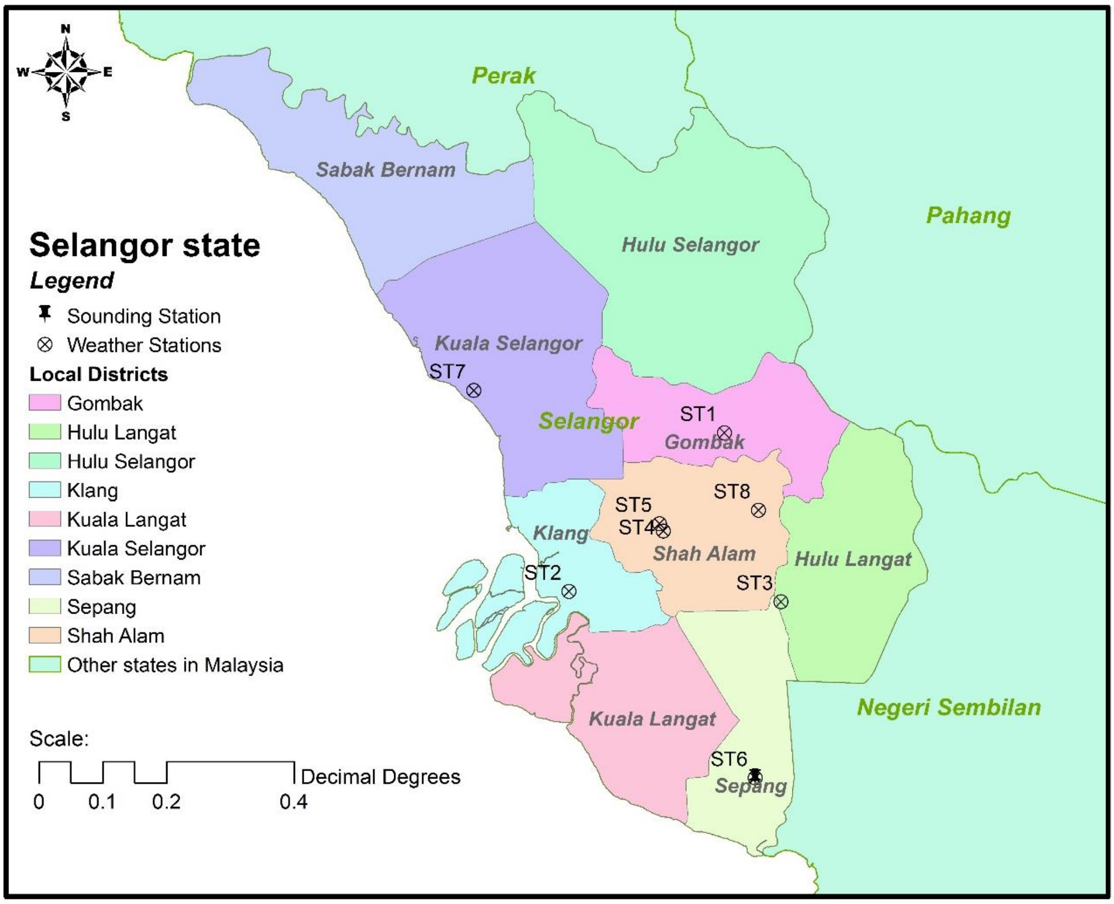

Figure 2.6: Location of administrative center of Selangor state and distribution of weather and air quality stations that supply data for verification. Refer to Table 2.4 for description of each weather station.

Table 2.4: Information on weather station for meteorological verification and air quality with latitude (Lat) and longitude (Long) location. Original LU (Figure 3.1a) and updated land use (Figure 3.1c) for each ground observation station in Figure 2.6. The urban land use has three urbanization levels (Refer to Table 3.2): low density residential (LDR), high density residential (HDR) and commercial/ industrial region (COM). † The station is located in urban land use that is surrounded by grasslands and shrubs.

Station code	Station name	Lat	Long	Operator	Original WRF LU (LO)	Updated LU (LN3)
ST1	Gombak	3.262	101.652	JAS	Urban	Urban (COM)
ST2	Klang	3.010	101.408	JAS	Open shrubs	Urban (LDR)
ST3	Kajang	2.994	101.740	JAS	Urban†	Urban (HDR)†
ST4	Shah Alam	3.105	101.556	JAS	Urban	Urban (COM)
ST5	Subang	3.117	101.550	MMD	Croplands	Urban (COM) †
ST6	Sepang	2.717	101.700	MMD	Croplands	Croplands adjacent to Urban (COM)
ST7	Kuala Selangor	3.327	101.259	JAS	Croplands	Grasslands and shrubs
ST8	KL	3.138	101.705	JAS	Open shrubs	Urban (HDR)

Table 2.5: Statistical benchmark of error index for near-surface parameters

Near-surface parameters	Error index	Adopted benchmark
Temperature	RMSE	≤ 2 °C
	Bias	≤ ±0.5 °C
Humidity	RMSE	≤ 2 g/kg
	Bias	≤ ±1 g/kg
Wind Speed	RMSE	≤ 2 ms^{-1}
	Bias	≤ ±0.5 ms^{-1}
Wind Direction	RMSE	≤ 30°
	Bias	≤ ±10°

2.4.2.1 2-meter temperature (T2) and relative humidity (RH2)

T2 is a diagnostic model output produced from the skin surface temperature (TSK). In WRF, the 2-meter mixing ratio (Q2) is diagnostically derived from the T2 and also the surface water vapor mixing ratio. To verified against the relative humidity data from measurement, Q2 is converted into RH2. Detail calculation steps are provided in Appendix A.2.1.

2.4.2.2 10-meter horizontal wind speed (uv10) and direction (wdir10)

Similar to T2, the uv10 is derived diagnostically based on the Monin-Obukhov similarity theory. It is tested against the data collected from the weather stations. In order to derive the average direction of the wind vector, horizontal wind vector is split into x- and y- component using sine and cosine portion. From which the difference in each wind component is identified and compiles to give the error indices. Detail calculation steps are provided in Appendix A.2.2.

2.4.3 Ground air pollutant level

The same eight ground weather stations co-operated by MMD and DOE also supply air quality monitoring data for ground pollutant verification (see Figure 2.6, Table 2.4). The same error indices are evaluated for the air pollutants including O_3, NO and NO_2. It is later shown in Chapter 6 that the model has only reliably generated the O_3 concentration. In order to utilize the available data, the chronological measurement data are studied at consistent four-year interval at 1999, 2003, 2007 and 2011, with the last entry chosen in year 2014. 2015 is not selected because that year recorded one of the most severe haze episode from the SEA forest fire which has caused the worst pollution around the SEA region in that year [*GFED*, 2017]. The relocation, break down and on-going maintenance of the air quality logging stations causes discontinuity of data collected. The number of operating stations is tabulated in Table 2.6.

Table 2.6: List of operating air quality monitoring stations during period of study

Year	**Month**	**Air pollutants**					
		Hourly/ 8-hourly O_3	**NO_2**	**NO**	**CO**	**NMHC**	**THC**
1999	April	7	7	7	7	5	5
2003		8	8	8	7	7	7
2007		8	8	8	8	6	6
2011		6	6	6	6	0	0
2014		6	6	6	6	0	0
1999	October	7	8	8	7	5	5
2003		8	8	8	8	7	7
2007		8	8	8	8	6	6
2011		6	6	6	6	0	0
2014		6	6	6	6	0	0

2.4.4 Surface skin temperature (TSK)

Surface skin temperature (TSK) represents the temperature at the top surface including the thin top soil layer and plant canopy. Its value is derived from the surface energy balance equation in LSM from the surface and model-level [*Skamarock et al.*, 2008]. The prognostic TSK is then forced back into the coupled boundary layer and radiation routine. It responses instantaneously towards external forcing such as incoming radiation since it does not have heat capacity [*Xie et al.*, 2012; *ECMWF*, 2013]. As a result, TSK changes more spontaneous compared to T2 with the change of land use map [*Jin and Dickinson*, 2010; *Li and Bou-Zeid*, 2014]. Hence, this variable is chosen to evaluate the model spatial performance of the land use map, which is shown in Chapter 3.

2.4.4.1 MODIS LST image

Land-use performance of WRF in predicting TSK is compared with land surface temperature (LST) data extracted from satellite image. Clear images with less than 30% of cloud coverage are selected. However, there is hardly any image captured within the time frame that contained complete spatial information of LST in Selangor. Three images captured by MODIS/TERRA satellite (MYD11A1)[4] with more than half of spatial coverage (~55.9%) are extracted for the validation purposes. Detail information of the satellite imageries is tabulated in Table 2.7. This surface irradiance data is pre-processed, collated and resampled to collocate with WRF grids for verification for respective days. The compilation of satellite images, with total of 7194 pixel cells, represents approximately 25% of the WRF domain for three days. The derivation of error statistics is performed in ArcMAP python script using the Raster Calculator function.

Table 2.7: Information of images deployed for TSK validation

Terra (MOD11A1)		**Image captured (Day/Night)**	**Passing Time (UTC)**	**Passing time (GMT)**
Date	***Julian Date (in 2003)***			
10th Oct 2003	283	Day	03:55-04:00	12:00pm
14th Oct 2003	287	Day	03:30-03:35	11:30pm
19th Oct 2003	292	Day	03:50-03:55	12:00pm

---

[4] Available freely at http://glovis.usgs.gov/

2.4.5 Vertical parameters

The vertical atmospheric profile is verified with sounding data logged at the Kuala Lumpur International Airport (KLIA) in Sepang (ST6) marked in Figure 2.6. This data is compiled and is made available by Department of Atmospheric Science, University of Wyoming [*University of Wyoming*, updated daily]. It is measured twice a day at local time 0800 and 2000 MYT, representing the morning and evening transitional periods synchronous to sun activities. From which, the modelled potential temperature (θ), vertical mixing ratio (Q_v) and horizontal wind speed (uv_h) data are verified against the recorded sounding data. The performance is shown through the aforementioned error indices. NMAE is excluded for the vertical profile assessment because it involves the averaged data that might be meaningless due to the great variability of daily vertical profile that subjected to the prevailing weather conditions. The verification of vertical data only applies in the Chapter 4 and 6 where the vertical atmospheric advection and transportation within the boundary layer are assessed.

2.4.6 Boundary layer height (PBLH)

The diurnal evolution of planetary boundary layer height (PBLH) is one of the indication of the convective movement within the boundary layer. The height shows the vertical extent of mixing of the boundary layer, well within free troposphere [*Seidel et al.*, 2010]. This parameter is widely determined in the parameterization scheme as separation margin between boundary layer and free atmosphere aloft. Seeing that there is no actual division between the atmospheric layers, various definitions are suggested to quantify the PBLH. Proposed methods are: (1) the conventional parcel theory with the height where the virtual potential temperature (θ_v) equates with the near-surface temperature [*Holzworth*, 1967], (2) height attains when the vertical gradient of virtual potential temperature, potential temperature, humidity or refractivity attains a prescribed minimum condition (maximum for temperature) [*Seidel et al.*, 2010], (3) height where turbulent kinetic energy (TKE) drops to a minimal value [*Stull*, 1988; *Janjic*, 2001] and (4) determination from the Richardson number which serves as the ratio of suppression to production of TKE [*Le Mone et al.*, 2013]. Measured quantities from sounding data facilitate derivation of planetary boundary layer height using methods (1), (2) and (4) [*Cooper and Eichinger*, 1994]; the last two methods are commonly adopted in modelling when high resolution data are available at the same vertical level.

In this context, the conventional approach is adopted to determine the mixing height from the sounding data. This method defines PBLH as the height where the near-surface θ_v matches with the θ_v of its environment, i.e. the air parcel lifted reaches equilibrium with its surrounding environment. Taking the surface environment as the reference value, the parcel theory approach is hence more sensitive to the changes of surface condition and shows an edge to produce the large and consistent diurnal variation of PBLH compared to the other methods [*Seidel et al.*, 2010]. The lack of near-surface measurement data near the radiosonde station has prompted the usage of the first level sounding data as the near-surface reference value. However, it can also potentially underestimate the daytime PBLH under the convective boundary layer (CBL) condition where underlying surface is hotter than the air aloft. The modelled PBLH is compared to the PBLH derived from the sounding data. Since the PBLH is defined differently for each PBL physics schemes, the normalization of PBLH and model evaluation are discussed in details in Chapter 4.

The sounding data measurement is collected during the morning and evening transitional periods (0800 and 2000 MYT) where the residual layer of atmospheric is largely stochastic and generically difficult to model [*Skamarock et al.*, 2008]. The residual layer might be mixed with the daytime CBL and nighttime stable boundary layer (SBL) condition. Under such circumstances, large variation of PBLH value is expected. The large uncertainty of modelled result then prompts the adoption of hit rate as the model performance indicator [*Schlünzen and Katzfey*, 2003]. The hit rate of PBLH is counted when the MAE (see Equation 2-9) generated by modelled result comparing to observed is lower than 100 meter.

2.4.7 Urbanization indicator

The Urban Heat Island intensity (UHII) is the universal indicator of the temperature difference between developed urban and non-urban regions [*Oke and Maxwell*, 1975]. The measured UHII is usually defined as the temperature difference between an urban and non-urban site, from which the coolest non-urban background point is usually picked which subsequently gives a stronger urban-induced heating effect [*Bhati and Mohan*, 2015; *Santamouris*, 2015]. This method has generic difficulty to ensure the heating effect is free from influence of site-specific weather. In this context, the numerical model is able to deduce the effect of sole urbanization by removing the background influence of no urbanization activities in the region. Hence, an additional modelling case (noURB) is set up to simulate the background weather condition when there is no urbanization; this replaces urban land with non-urban land. The effect of urbanization on the near-surface meteorological condition and the local circulation could be evaluated by eliminating the site-specific background weather condition and filtering of possible synoptic influences unrelated to urbanization. Grassland and shrub land category (CAT10, shown in Table 3.2) introduced in the updated land use is chosen to represent the non-urban land use in this context for its dissimilar night thermal response with the urban region [*Li et al.*, 2013b]. Hence, the UHII is taken as the difference of the hourly averaged T2 between urban land use of urbanized cases and the collocated non-urban grid points in noURB. The mean UHII and UHII for individual urban classes are extracted for separate analysis.

CHAPTER 3: EVALUATION OF WRF PERFORMANCE ON URBAN NEAR-SURFACE LEVEL: A SENSITIVITY ANALYSIS OF LAND USE MAP AND URBAN CANOPY MODEL

3.1 Introduction

The numerical modelling software, WRF-ARW is used to investigate the effect of urban land use change. In consideration of the model accuracy, the ability of the model to simulate the local heating phenomenon is thoroughly evaluated. In modelling context, urban land feature is represented by the LU map and its morphological parameters. The urban-scale energy budget and dynamics are then resolved through the UCM. The surface forcings from the land use and urban morphological change directly reflect on the near-surface canopy layer. Hence, this chapter focuses on the assessment of model performance on this layer in response to the urban land use characterization in the GKL urban agglomeration of Malaysia. In an attempt to improve the model representation, the geological LU map is updated and urban parameters are locally calibrated for the UCM. The model performance is site-specific and greatly varies with the background weather condition and domain settings as discussed in Section 1.5. Here, the sensitivity study provides an important reference information for the reliability of the default WRF setting.

The objectives of the chapter include:

1. Develop an updated WRF LU map for the case study region and period
2. Investigation of the performance of updated land use map to model the urban near-surface environment
3. Investigation of the performance of calibrated UCM to model the urban near-surface environment

The first part of the chapter includes the preparation and description of different LU map and UCM options available. Section 3.2 demonstrates the procedure to update the WRF LU data map for the case study period. It is followed by Section 3.3 with the explanation of the how respective UCMs assign the urban surface and morphology features, from which they parameterize the thermodynamics and moisture fluxes of the urban canopy. Section 3.4 gives detailed information for the case settings for effective comparison. The models performance of each LU maps and UCM options is sensitively evaluated in Section 3.5 and Section 3.6.

3.2 Preparation of customized WRF LU map

A local LU map for Selangor state where GKL situated is updated with the Landsat satellite images from existing WRF dataset. The land use map is developed using Landsat satellite images in year 2003 when the case study is conducted. It is also noted that the WRF MODIS-20 terrestrial map (here onwards known as original WRF LU map) is developed in the overlapping time frame [*Bai*, 2010]. From which, the quality assessment of both LU datasets becomes more credible and meaningful. Table 3.1 gives an overview of the procedure undertaken for the update of the WRF LU map. The detail of the preparation steps (Step 1-7, 9) are given in Appendix A.3. In this chapter, the discussion focuses on the updated land use map and its validation.

Table 3.1: Procedure to update LU from existing WRF land use

Step	Step description	Tools
1	Download and pre-process satellite images	ERDAS Imagine 2011
2	Manual classification of satellite images	ESRI ArcMAP 10.2.2: Supervised classification
3	Normalization of land use classes	ESRI ArcMAP 10.2.2: Raster calculator
4	Resample images to desired WRF resolution	ESRI ArcMAP 10.2.2: Resample
5	Conversion of original WRF LU binary file into ASCII output (.ASC)	dmbrown source code
6	Replace updated LU map (Step 4) for Selangor in original WRF LU raster file	ESRI ArcMAP 10.2.2: Raster calculator
7	Conversion from updated WRF LU map to raster text file (.TXT)	ESRI ArcMAP 10.2.2: Conversion tool
8	Validation of updated LU map with JPBD data	ESRI ArcMAP 10.2.2: ArcMAP python script (ArcPy)
9	Conversion of updated WRF LU map text file (.TXT) back to binary file	dmbrown source code

3.2.1 New land use map

Using the updated 2003 map, two land use maps are produced to accommodate the assumption of urban feature in different urban canopy treatment models – one urban class (CAT13) and 3 urban classes (CAT31, CAT32, CAT33) that correspond to low-density residential (LDR), high-density residential (HDR) and commercial/industry (COM). Summing up, there are three land use maps produced in the model as shown in Figure 3.1. LO is the original MODIS-20 land use supplied by WRF, LN is the updated land use map with one urban category (CAT13) and LN3 is the updated land use map with three urban land classes. The change of LN3 and LO is marked in Figure 3.1d to show the spatial changes in land use cover. The total amount of broadleaf trees (CAT1 and CAT2) remains in the new land use map. It is notable that the urban cover grows from the original 4.8% to 18% in the new map. The areal coverage of croplands does not grow much but it is greatly displaced hence it is separated into original croplands, old croplands and new croplands categories in Figure 3.1d.

Table 3.2: Updated list of category for Selangor state Land Use Map in WRF.

Code in LN	Code in LN3	New Category	Description
CAT1		Oil palm plantation	Palm plantation as a separated category of evergreen perennial woody.
CAT2		Evergreen broadleaf forest	More than 60% coverage are trees shrubs with at least 2m tall and remains green all year.
CAT10		Grasslands and Shrubs	Herbaceous cover and woody vegetation with height less than 2 meter.
CAT12		Croplands	Land with temporary crops which undergo process of harvesting and bare soil period.
CAT16		Sparsely vegetated	Land with no more than 10% vegetated cover or cleared forest land that has left undeveloped.
CAT17		Water	Water body
CAT13	CAT31	Urban – LDR	Urban region with combination of built-up and vegetation cover, composition varies with UCM. This area commonly includes single-family housing units with lower population densities.
	CAT32	Urban – HDR	Urban region with combination of built-up and vegetation cover, composition varies with UCM. This residential area accommodates more people than low density residential with buildings like apartment complexes and row houses.
	CAT33	Urban – COM	Urban region that serves as infrastructure, transportation network and all highly developed areas not classified as HDR.

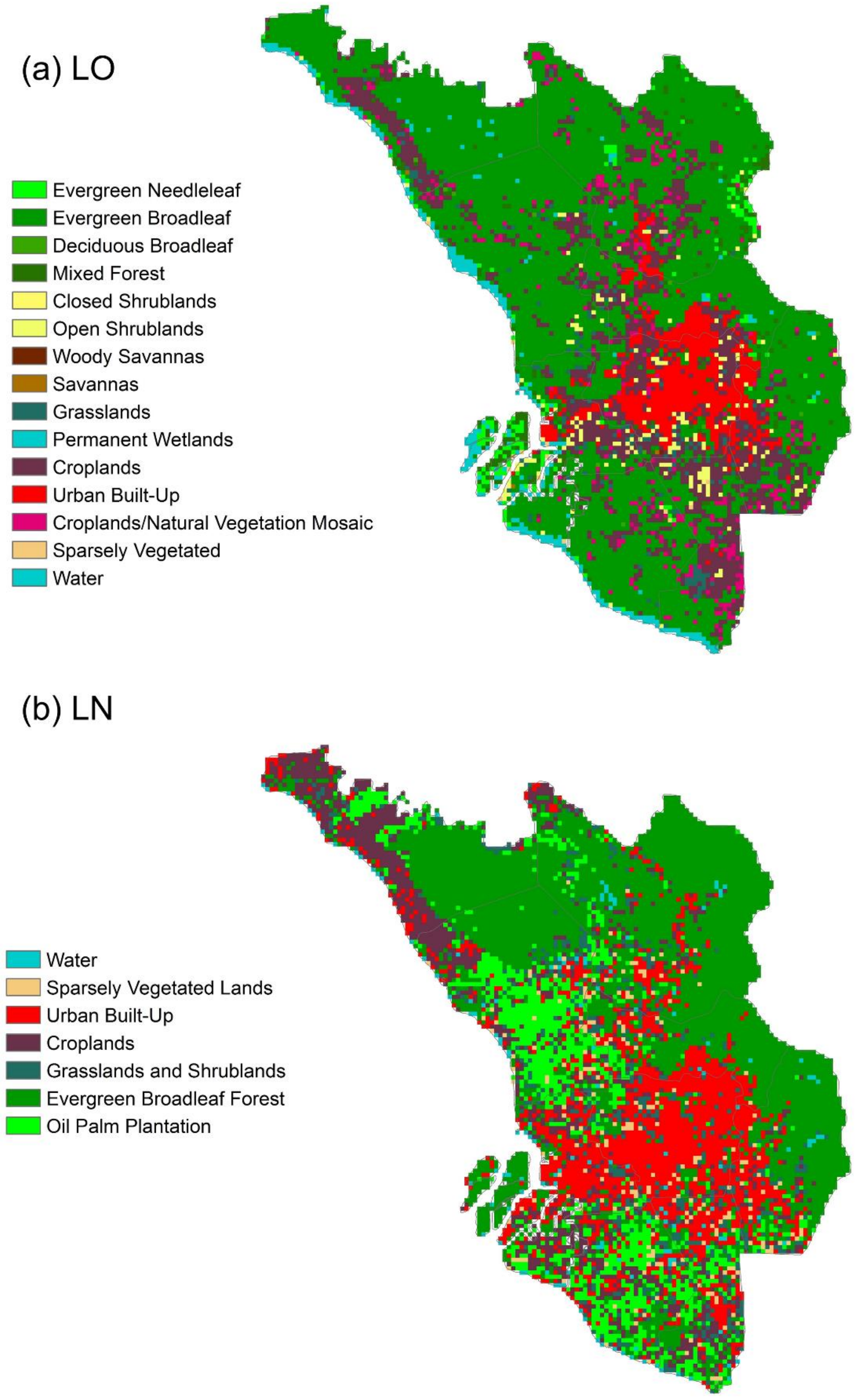

Figure 3.1: The land use map for Selangor state. (a) LO: WRF original MODIS land use map, (b) LN: Updated land use map with one urban category

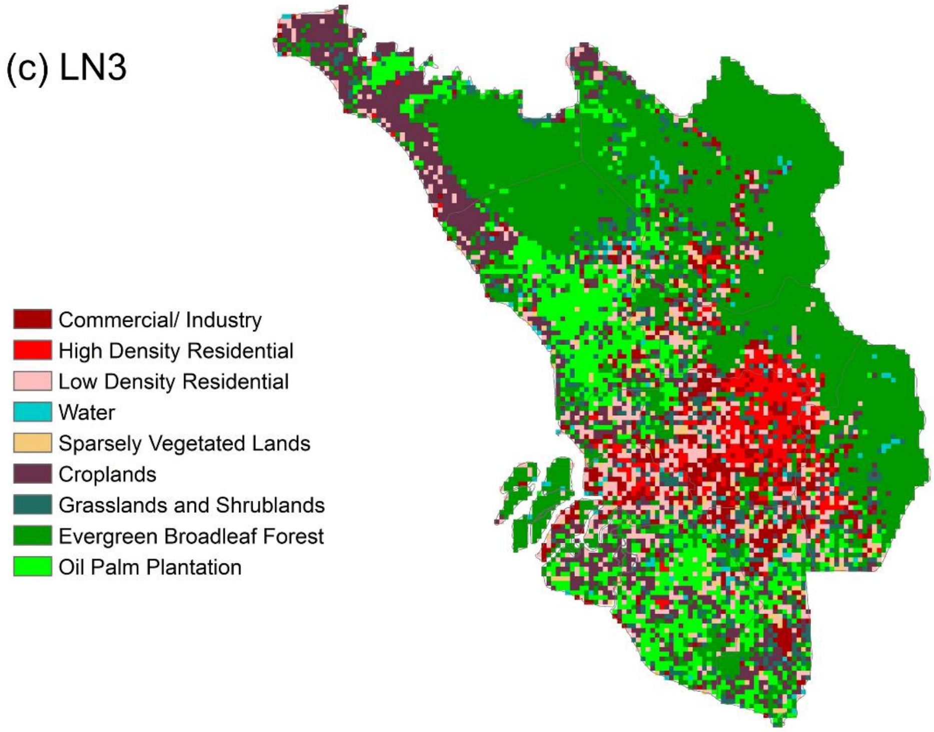

(c) LN3

(d) Land use change

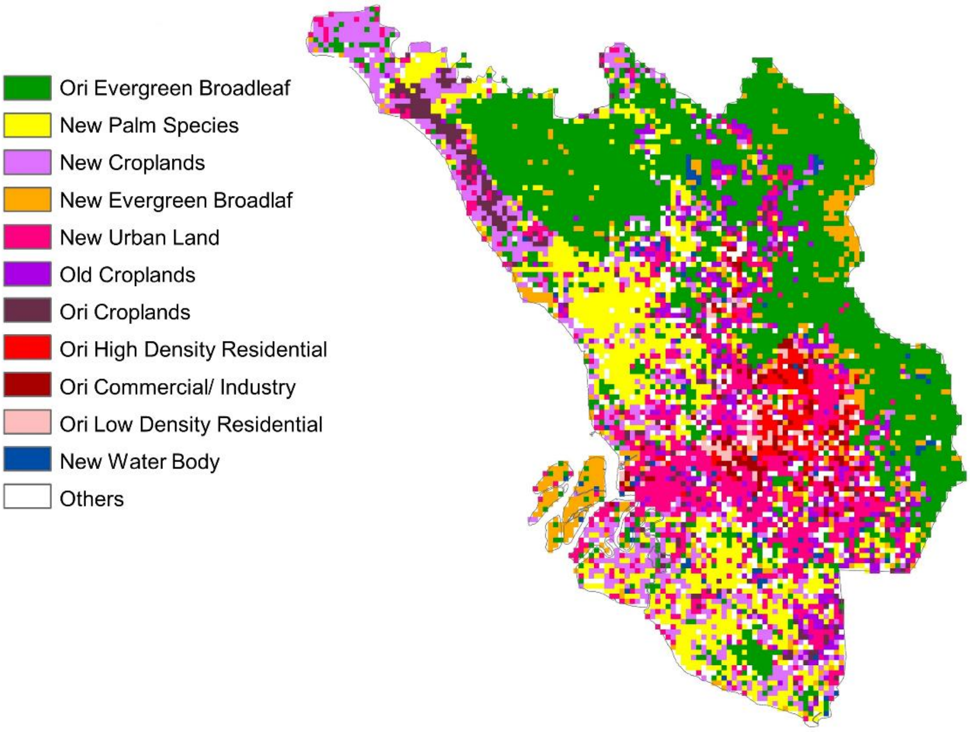

Figure 3.1 (cont.): The land use map for Selangor state. (c) LN3: Updated land use map with 3 urban categories, (d) Land use change: Land use difference between LN3 and LO. Legend for (d) that starts with "Ori" means the land use is original and unchanged, "New" means land use changes by giving the name of the new land use, while "Old" means land use changes but giving the name of the original land use class.

3.2.2 Validation of updated LU map

Figure 3.1d depicts the spatial distribution difference of the original and new land use maps. The reclassified land use maps are statistically verified with the official town plan map supplied by Selangor Town and Country Planning Department (JPBD; Jabatan Perancangan Bandar dan Desa). The accuracy of updated land use map (LN) is determined through correctly identified pixels in comparison to the processed JPBD town plan map. The town plan map is projected onto the grid position of original and updated land use map. From which ArcMAP returns the land use code for overlaid grids with the same adjusted land use type (Appendix A.3.7). LN is verified in place of LN3 due to the limitation information on the level of urbanization provided by the JPBD dataset (Appendix A.3.6). The land use distribution percentage and accuracy information are summarized in Table 3.3. Broadleaf Forest, Oil Palm Plantation, Urban and Croplands are the more populous land cover within the state making up 90.8% of the land. Both LO and LU3 maps have achieved the best compliance of more than 85% for Evergreen Broadleaf Forest (CAT2) as shown. Oil palm plantation (CAT1) that follows CAT2 in terms of distribution is now distinguishable in the updated map. Although the identification of oil palm and paddy clusters on the southwest and northwest of GKL reduce the broadleaf forest coverage by more than 16 %, it does not affect the classification accuracy of the latter (Ngah et al. 2013). The correct identification of the major crops, namely paddy fields and rubber estates, improves the accuracy of cropland (CAT12) identification by 13.4%.

Improvement of urban (CAT13) is most remarkable among all land uses by attaining a 74.2% accuracy, nearly doubled that of the original LU map. The peripheral residential regions surrounding Kuala Lumpur city, which encompass the whole of Petaling Jaya, part of Gombak, Klang and Hulu Langat (refer to Figure 2.6) are successfully detected with the inclusion of urban subdivision system (LDR, HDR and COM). The new land use map has also identified the new administration center, Putrajaya, the first phase of which completed in 2003 [*Ho*, 2006]. More than 10 % of the Selangor land use map is now covered with cities, which is doubled accuracy of the original LU map. The reclassification has successfully extended the coverage for residential areas of different configurations as well as transportation network, industrial cluster and the likes. The assessment result tabulated in Table 3.3 has shown that updated land use map has attained an overall spatial accuracy of 60.6%, which is 18.3% better than the original land use map. The updated map now provides an improved representation of the key land use types in the study region.

Table 3.3: Accuracy of land use classification after merging of classes for comparison

Land use type	**Adjusted land use code (Original WRF land use code)**	**Area Coverage of Town Plan Map**	**Accuracy of original map (LO)**	**Accuracy of updated LU map (LN)**
Oil Palm Plantation	CAT1 (1)	21.3%	-	49.6%
Evergreen Broadleaf Forest	CAT2 (2,4,5)	42.2%	84.9%	86.6%
Grassland and Shrubland	CAT10 (6,7,9,10)	4.6%	8.1%	10.9%
Croplands	CAT12 (12,14)	11.9%	29.8%	43.2%
Urban and Built-up Land	CAT13 (13,31,32,33)	15.4%	32.8%	74.2%
Sparsely Vegetated Land	CAT16 (16)	2.4%	0.5%	8.6%
Water Body	CAT17 (11,17)	2.1%	13.6%	16.8%
Overall Classification Accuracy Improvement			18.3%	

3.3 Urban Canopy Model (UCM) in WRF

LSM derives the forcing conditions of land surface from geological data that governs the flux dynamics of atmospheric layer aloft. WRF model has several options of urban treatment approach. The original Noah LSM, noUCM uses the Noah LSM vegetation evaporation algorithm to treat the urban surfaces and assumes it as 100% impervious surface [*Chen and Dudhia*, 2001]. The Noah LSM coupled with bulk UCM (bUCM) parameterizes the sub-grid scale interaction of localized urban surface texture and near-surface atmospheric condition. It assigns a general set of empirical value for the urban canopy [*Kusaka et al.*, 2001]. Impervious urban fraction parameter is introduced to represent the composition of urban and vegetation within a grid cell (90%) [*Chen et al.*, 2004b; *Liu et al.*, 2006]. Despite its simplicity, the bulk representation of surface feature has found to reproduce the urban canopy environment better that more sophisticated scheme [*Grimmond et al.*, 2010; *Liao et al.*, 2014].

The single-layer UCM has the similar concept with bUCM but it includes the two-dimensional urban morphology with building height, roof and road width. It redefines these canopy information according to urbanization levels including LDR, HDR and COM. The single-layer UCM therefore is able to parameterize the solar radiation trapping, reflection, and shadowing effects, defined by the street canyon dimensions and orientation as well as the solar azimuth angle [*Kusaka and Kimura*, 2004; *Chen et al.*, 2011b]. This UCM specifies the amount of the impervious fraction of urban grid (F_{urb}) for the determination of the total grid sensible heat fluxes from surface (Q_H), as

Equation 3-1:

$$Q_H = F_{veg}Q_{Hveg} + F_{urb}Q_{Hurb}$$

where the F_{urb} is specified in the UCM input parameters as shown in Table 3.4 and F_{veg} = 1-F_{urb}. The sensible heat fluxes for vegetated surface (Q_{Hveg}) is derived in Noah LSM by accounting the total evaporation algorithm. In UCM, the sensible heat fluxes for urban surface (Q_{Hurb}) is computed in the single-layer UCM with consideration of heat fluxes exchange between urban architecture (H_a) and the canopy environment and thereafter heat exchange of canopy environment with the atmosphere above the canopy top (H_{can}),

Equation 3-2: Sensible heat fluxes of urban canopy

$$H_{urb} = H_{can} + [H_a] = l_t H_r + [l_w 2H_w + l_r H_g]$$

where H_r, H_w, H_g is the sensible heat fluxes from the building top, wall and ground surfaces respectively. The normalized length of the roof (l_t), canopy width (l_r) and wall height (l_w) are computed from the roof width, road width and building height info from Table 3.4. It has also incorporated the diurnal effect of anthropogenic heat into the sensible heat fluxes. The coupling of single-layer UCM model into Noah LSM therefore realistically resolves the dynamics of surface heat, momentum and moisture fluxes of regional urbanized plot [*Chen et al.*, 2014] as well as predicting the development of boundary layer [*Lin et al.*, 2008; *Zhang et al.*, 2011].

In this chapter, four UCM settings are used to examine the influence of the urban surface treatment. They are (1) original Noah LSM without UCM coupling (noUCM), (2) bulk UCM (bUCM), (3) single-layer UCM with original parameters (SLUCM) and (4) single-layer UCM with locally calibrated parameters (calSLUCM) [*Morris*, 2016a]. The latter has estimated the urban parameters of the three urbanization level of GKL. Urban fraction of each urban classes is quantified through GIS data using unity minus vegetation fraction. The composition of impervious surface of LDR, HDR and COM is updated to 29%, 50%, 80% respectively. The canopy geometry, roughness length and thermal characteristics are collectively estimated through the standard building configuration and materials determined by the Public Works Department Malaysia (JKR) for GKL. Detailed information is compiled in Table 3.4.

Table 3.4: Constant parameters for UCM urban treatment approaches

UCM type		**noUCM**			**bUCM**		
Reference		[*Chen and Dudhia*, 2001]			[*Liu et al.*, 2006]		
Roughness length (m)		0.5			0.8		
Surface albedo		0.15			0.15		
Volumetric heat capacity (Jm^{-3}K^{-1})		-			3		
Soil thermal conductivity (W/m/K)		-			3.24		
Urban fraction of grid (F$_{urb}$)		1			0.9		
UCM type		**SLUCM**			**calSLUCM**		
Reference		[*Kusaka and Kimura*, 2004]			[*Morris*, 2016a]		
Urban LU class		CAT31	CAT32	CAT33	CAT31	CAT32	CAT33
Urban fraction of grid (F$_{urb}$)		0.50	0.90	0.95	0.68	0.75	0.89
Building/roof height (m)		5	7.5	10	8	12.5	14
Standard deviation of building height (m)		1	3	4	1	4	5
Roof width (m)		8.3	9.4	10	9	11	11
Road width (m)		8.3	9.4	10	5	14	18
Anthropogenic heat (Wm^{-2})		20	50	90	17	23	123
Heat capacity (1 x 10^{6}) (J m^{-3}K^{-1})	roof	1.0	1.0	1.0	1.2	1.2	1.2
	building wall	1.0	1.0	1.0	1.4	1.4	1.4
	road	1.0	1.0	1.0	1.6	1.6	1.6
Thermal conductivity (J m^{-1}s^{-1}K^{-1})	roof	0.67	0.67	0.67	0.67	0.67	0.67
	building wall	0.67	0.67	0.67	0.8	0.8	0.8
	road	0.40	0.40	0.40	1	1	1
Surface albedo	roof	0.2	0.2	0.2	0.2	0.2	0.2
	building wall	0.2	0.2	0.2	0.2	0.2	0.2
	road	0.2	0.2	0.2	0.2	0.2	0.2
Surface emissivity	roof	0.9	0.9	0.9	0.9	0.9	0.9
	building wall	0.9	0.9	0.9	0.9	0.9	0.9
	road	0.95	0.95	0.95	0.95	0.95	0.95
Roughness length for momentum (m)	roof	0.01	0.01	0.01	0.01	0.01	0.01
	building wall	0.0001	0.0001	0.0001	0.0001	0.0001	0.0001
	road	0.01	0.01	0.01	0.01	0.01	0.01

3.4 Experiment Design

This work uses UCM coupled with Noah LSM in WRF to model the urban heating phenomenon of the GKL region. Six cases are set up to verify the effect of land use and urban parameters as shown in Table 3.5. noUCM and bUCM can only identify one urban class and therefore they are used with LN instead of LN3. Four cases are set up for comparative studies of effect of land use change, namely (i) LO_noUCM, (ii) LN_noUCM, (iii) LO_bUCM and (iv) LN_bUCM. The default and calibrated SLUCM use new land use with 3 urban classes (LN3), forming SLUCM and calSLUCM cases. These two cases along with the default setting, LO_noUCM and LN_bUCM case are analyzed for the sensitivity of the urban treatment scheme for urban grids. The performances of updated LU map and compatibility of different urban surface parameterization methods are evaluated against ground weather parameters (see Section 2.4.2) and heating profile from satellite images (see Section 2.4.4) using statistical error indices. An extra simulation without urban land use (noURB) is run as a base case to evaluate the performance of different UCM in simulating effect of urbanization. Detailed information of noURB is given in Section 2.4.7. The cases are spun up for a day and last for 18 days from 2nd Oct 2003 0800 MYT to 20th Oct 2003 0800 MYT. All the remaining model settings are similar as stated in Section 2.3.3. In this chapter, all cases use the Mellor-Yamada-Janjić (MYJ) scheme as the PBL scheme. The selection of PBL schemes is later assessed in Chapter 4.

Table 3.5: Experiment design

Land Use Map **UCM Settings**		**Original (LO)**	**New (1 urban) (LN)**	**New (3 urbans) (LN3)**	**New (without urban)**
No UCM		LO_noUCM	LN_noUCM		noURB
With UCM	**Bulk UCM**	LO_bUCM	LN_bUCM		
	Default SLUCM			SLUCM	
	Calibrated SLUCM			calSLUCM	

3.5 Model evaluation for land use map

We first examine the sensitivity of modelled near-surface parameters for the original WRF LU map (LO) and our newly developed LU map (LN) for Selangor. With the updated LU map, we then explore the effect of urban canopy treatment approach (UCM) on the near-surface condition and their respective influence on the urban heating phenomenon in Section 3.6.

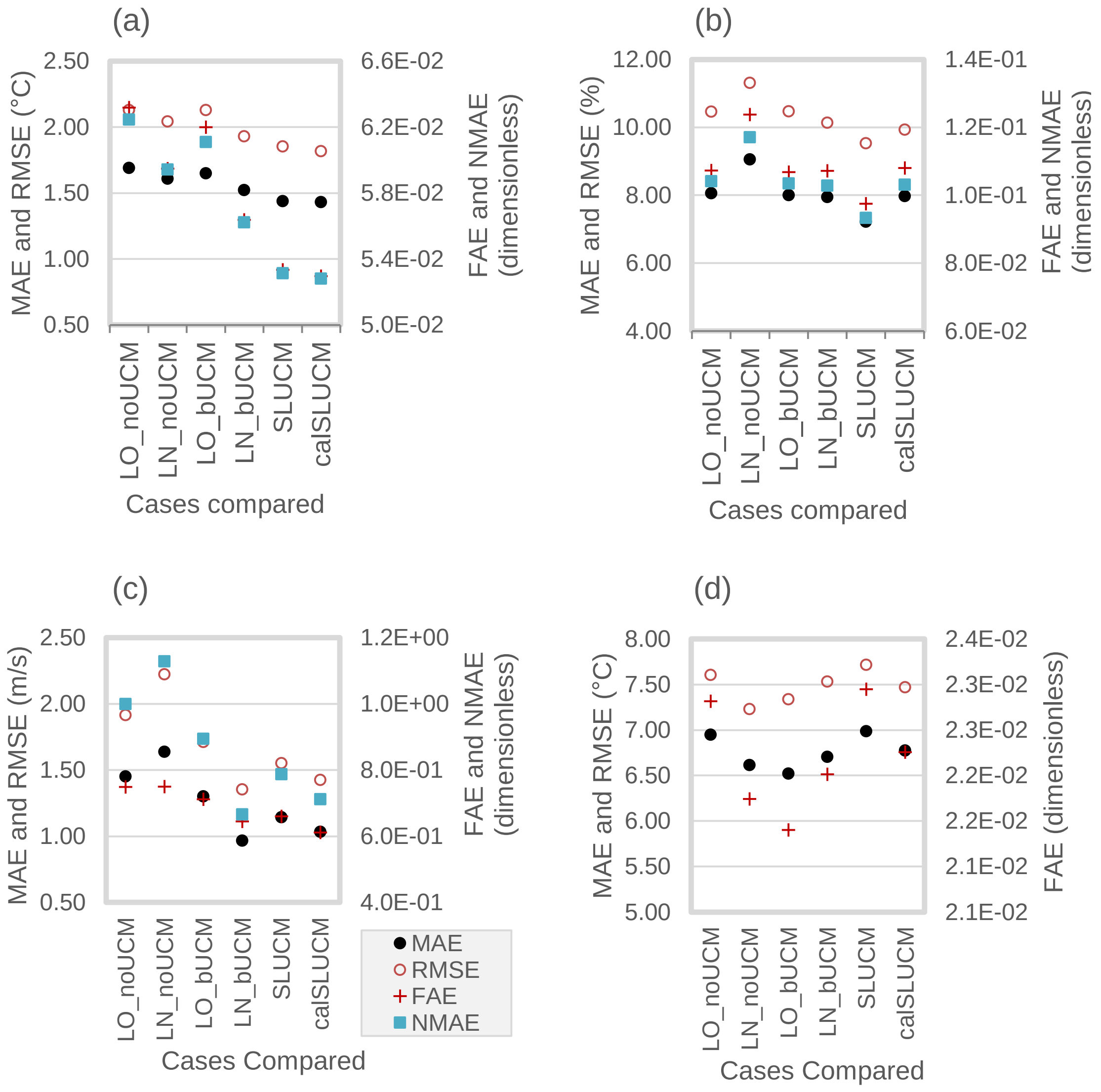

Figure 3.2: Error indices deviation (MAE, RMSE, FAE and NMAE) of different cases for variables: (a) T2, (b) RH2, (c) uv10 and (d) TSK are computed for performance of all cases.

The sensitivity of model result to input land use map is analyzed through comparing LO_noUCM and LO_bUCM with LN_noUCM and LN_bUCM respectively. The similarity between the two sets of same UCM highlights the role of land use map. Figure 3.2 shows that LN_bUCM performs the best amongst the 4 cases in improving the RMSE of T2, Q2, uv10 and skin surface temperature by 0.2 °C, 0.32 %, 0.56 ms^{-1}, 0.07 °C respectively compared to the original setting (LO_noUCM). The performance of updated land use map (LN_noUCM, LN_bUCM) clearly improves the T2 profile regardless the choice of UCM. The calibration of LU map together with noUCM does not show significant improvement for modelling Q2 and 10-m wind speed and hence highlights the role of UCM. It is notable that LN_bUCM is the only case that meets the RMSE statistical benchmark (see Table 2.5) of T2 less than 2 °C and 10-m wind speed less than 2 ms^{-1}.

The hourly-averaged near-surface weather condition throughout the simulation period is compiled in the left panel of Figure 3.3. While using the original land use (LO), cold biases and excessive wetness are observed all day long and especially severe during the hot period from 1200 to 1600 MYT. The cases with updated land use (LN_noUCM and LN_bUCM) reduce the bias with the identification of urban grids in the measurement sites. The increasing urban surface rises the temperature due to limited amount of moisture and hence impedes the latent heat dissipation. Higher T2 is also recorded for these two models compared to their LO counterparts from 2000 to 0700 MYT. LN_bUCM improves the model prediction while LN_noUCM greatly overestimates the night T2 and underestimates 2-meter humidity. In noUCM, the urban grid is assumed to be completely impervious to prevent excessive evaporation in the vegetation evaporation algorithm [*Lee et al.*, 2011; *Li and Bou-Zeid*, 2014]. Such assumption overly inhibits the evaporative ability when the amount of urban grids increases which then creates a hotter and dryer night weather condition. This indicates the performance of the new land use (LN) fluctuates with the choice of UCM scheme at night. It is true that under the stable night atmosphere, the ground heat absorbed before nighttime is the sole heat source. Hence, the exchange of heat fluxes is essentially governed by accurate amount and fraction of urban land use to estimate the stored ground heat. All cases modelled stronger wind during the day as shown in Figure 3.3(c). From which, the LN_bUCM reduces the wind strength predicted in LN_noUCM and gives the best agreement. The model performance of wind speed is dependent on both update of LU map and UCM. In Figure 3.4, the urban sprawling effect of LN reduces the latent heat fluxes released and increases ground heat fluxes absorbed during the day, the diminishing amount of total heat reduces the turbulence of the atmosphere and hence of the wind speed. On top of that, it is also attributed to the increased roughness level in bUCM (0.8 m) compared to noUCM (0.5 m) which generates stronger aerodynamic resistance on the canopy level and decelerates the flow.

Model evaluation for LU maps **Model evaluation for UCMs**

(a) 2-meter temperature

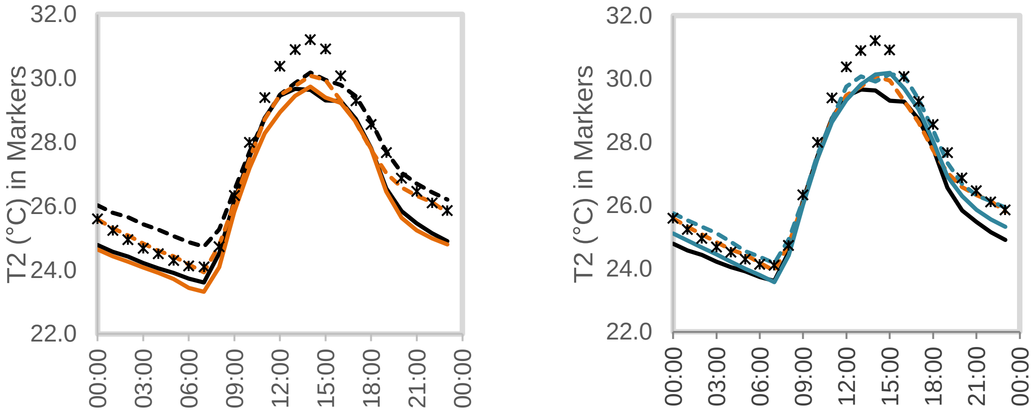

(b) 2-meter relative humidity

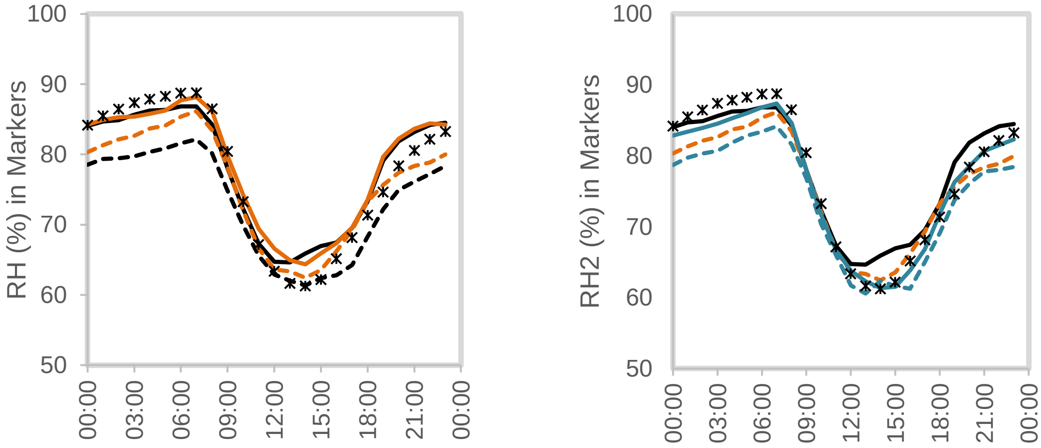

(c) 10-meter wind speed

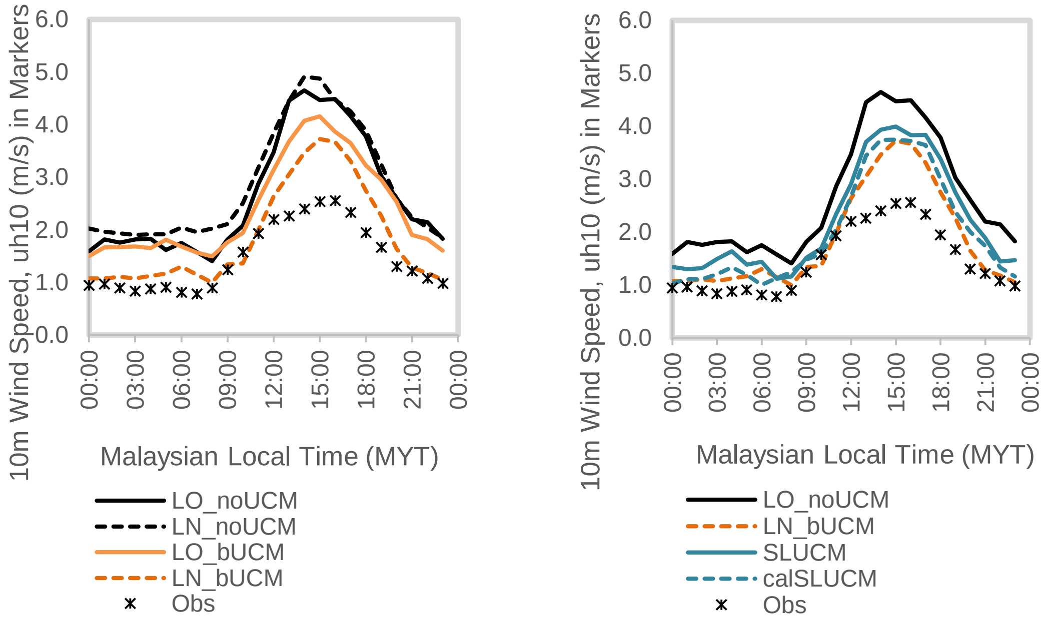

Figure 3.3: Hourly averaged of (a) T2, (b) RH2 and (c) uv10 for grid points that collocate with 8 ground observation stations (Obs). Left panel illustrates the cases for LU map evaluation (LO_noUCM, LO_bUCM, LN_noUCM, LN_bUCM) while right panel illustrates the cases for UCM evaluation (LO_noUCM, LN_bUCM, SLUCM, calSLUCM).

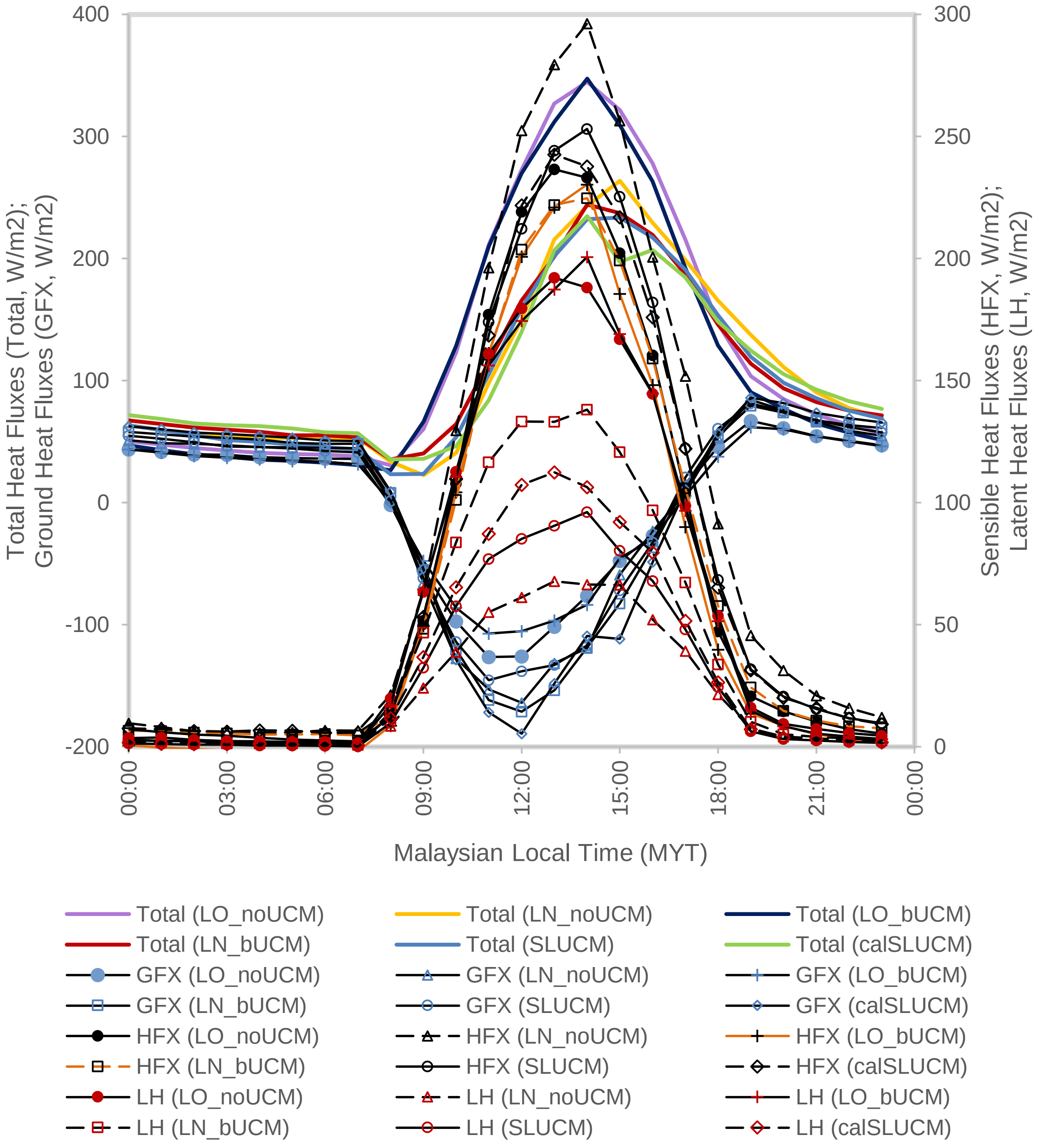

Figure 3.4: Hourly averaged heat fluxes, for grid points that collocate with 8 ground observation stations for 4 LU map model: LO_noUCM, LN_noUCM, LO_bUCM, LN_bUCM and 4 urban treatment models: LO_noUCM, LN_bUCM, SLUCM, calSLUCM.

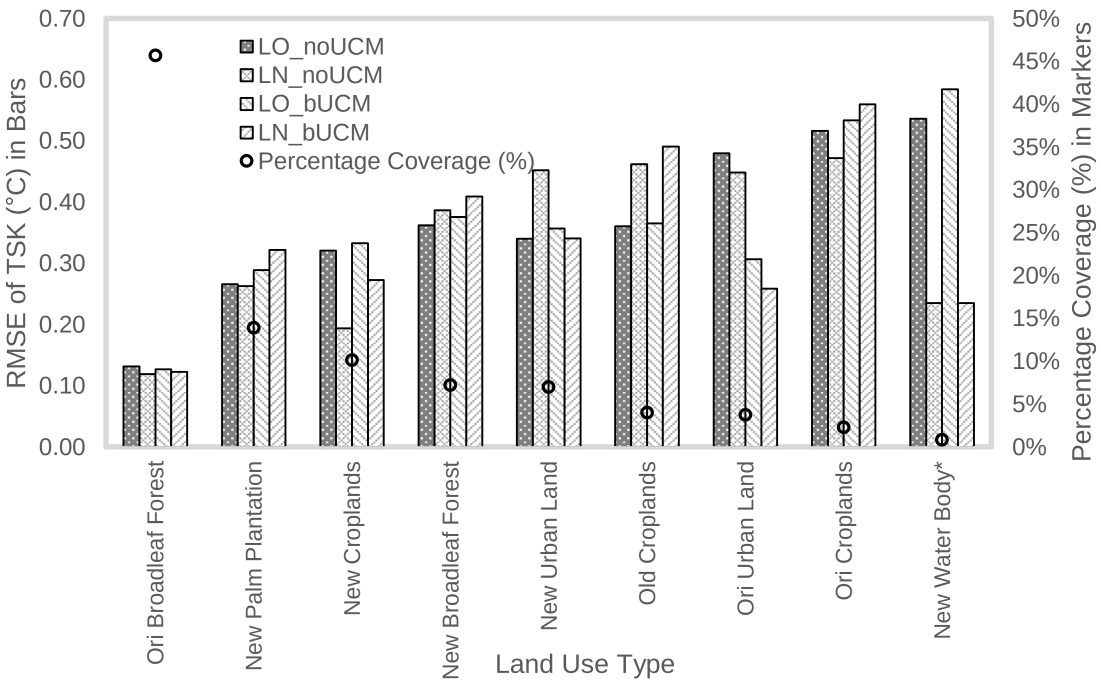

Figure 3.5: RMSE of surface skin temperature (TSK) obtained for LO_noUCM, LN_noUCM, LO_bUCM, LN_bUCM according to the changes of land use between LO and LN3 map (Figure 3.1d). The land use classes are arranged from the largest to smallest composition from left to right. *RMSE value for water body is halved to fit into the graph.

The model sensitivity on LU map is subsequently evaluated on the spatial extent with remote sensing data to complement the limitation of point-wise verification of near-surface weather condition. The grid-by-grid comparison of modelled TSK and LST for the mentioned less-cloud days gives the RMSE index. Figure 3.5 shows that correction to original MODIS land use (see Figure 3.1d) improves TSK accuracy significantly, especially for the land use type with low accuracy tolerance to misclassification, especially urban, water, croplands and evergreen forest [*Gao and Jia*, 2013]. Water body and croplands achieve reduction up to 0.6 °C and 0.1 °C RMSE respectively. The identification of new urban land use improves modelled TSK for LN_bUCM by 0.17 °C but not for LN_noUCM. This again highlights the role of UCM in deviating the modelled result despite feeding in locally calibrated LU map. Nevertheless, the same figure shows that the modelled TSK for newly classified vegetation fabric does not improve as well as the urban surface. *Kumar et al.* [2014] compares several vegetated surface parameters and found that the specification for green vegetation fraction and leaf area index have affected the appropriate partitioning of heat fluxes on vegetated surface. On top of that, the application of default coarse time-invariant initialization data for soil moisture and temperature has generic limitation to represent the heterogeneity of the soil condition and hence the initial value for near-surface weather condition [*Chen et al.*, 2007; *Sharma et al.*, 2016b]. Although the main focus of this study is on the urban surface, the modification of vegetated surface parameters is imperative to affirm the model reliability for the future study, especially on a finer scale.

3.6 Model evaluation for UCM

The influence of UCM on the sensitivity of the model performance is studied through LO_noUCM, LN_bUCM, SLUCM and calSLUCM cases. Figure 3.2 shows that the conjoint updates on land use and urban physics parameters (calSLUCM) performs the best and efficiently reduces the total RMSE of T2, Q2, 10-m wind speed and skin surface temperature by 0.31 °C, 0.52 %, 0.49 ms^{-1} and 0.14 °C, respectively compared to the default setting (LO_noUCM). Except LO_noUCM, all cases fulfill the statistical benchmark test for the RMSE of 2-m temperature and 10-m wind speed. The implementation of detailed characterization of urban surfaces in original SLUCM does not outperform the basic bUCM especially in 10-m wind speed and TSK. bUCM performs adequately well despite the bulk representation of the urban surface. The result agrees that the reliability of UCM relies on the accuracy of urban input variables more than its complexity [*Grimmond et al.,* 2011; *Liao et al.*, 2014]. It is also found that updating land use map (LN_bUCM) is imperative in reducing the modelled error before the coupling of UCM can simulate closer value to the measured near-surface parameters. This is discussed in Grimmond et al. (2011) that the impervious urban fraction has the greatest impact on the performance of UCM compared to the detailed urban morphology and urban material characteristics. The role of impervious urban fraction is also highlighted in Li et al. (2013) when the SLUCM in WRF has found to predict the near-surface meteorological condition reasonably well compared to noUCM and bulk UCM.

The right panel of Figure 3.3 shows the performance of near-surface weather parameters in an attempt to evaluate the UCMs. All UCMs reproduce the 2-m temperature well. In terms of 2-meter humidity, calSLUCM and bUCM slightly underestimates the moisture content while SLUCM predicts better for the night and generates similar profile with the bUCM. The larger moisture content predicted in LO_noUCM generates the largest latent heat fluxes, nearly double of SLUCM and lower ground heat fluxes as shown in Figure 3.4. This is pertinent to the original land use that has underspecified the urban area. Although the heat fluxes shown in the diagram is extracted from the grids collocated with the eight weather stations which mainly consist of urban, the larger amount of moisture emitted from the plant evapotranspiration around the surrounding region in Figure 3.3a is readily mixed under the dynamic daytime atmosphere. Similarly, the increased urban surfaces in LN_bUCM reduces the latent heat fluxes. Coupling of UCM models reduces the near-surface moisture amount and thus the latent heat fluxes through incorporation of algorithm to impede soil moisture retention ability in the mosaicked urban grid. However, the scarcity of surface heat fluxes measurement during the study period hinders the verification possibility. Figure 3.3c shows that all models generally produce stronger wind throughout the day compared to the observation data but coupling of UCM manages to reduce the bias by more than 0.5 ms^{-1} during the day. The underestimation of urban sprawling minimizes the effect of boundary drag which reduces the uv10. Similar result of uv10 is again observed for bUCM and calSLUCM.

Local modification of the surface parameters proves its robustness in characterizing the local features and reproducing the urban canopy environment. The result suggests that the local calibration of both land use map and urban parameters complements each other to affirm the robustness of the model. Discrepancies up to 1.5 °C 2-m temperature and 1.3 ms^{-1} uv10 from 1200 to 1500 MYT are retained in calSLUCM despite the improvement to the urban-specified parameters. The performance during the hottest hours is likely to be affected by the vertical air movement (interaction) of surface atmospheric boundary layer, which is not tested in this chapter. The inappropriate prediction of vertical motion is also likely to affect the vertical transportation of air masses in the mixing layer and microphysics performance in generating the right amount of precipitation [*Hu et al.*, 2010; *Shin and Hong*, 2011; *Li et al.*, 2013a].

3.6.1 Urban Heat Island Intensity (UHII)

The UHII value from these grid points are averaged hourly and illustrated in Figure 3.6. In calSLUCM, effect of urbanization on temperature is more apparent at night (2000-0500 MYT) with higher UHII of 1.44 ºC than the day (UHII: 0.9 ºC) due to the slower cooling rate of urban surface compared to the non-urban surfaces. Effect of urbanization on temperature is more apparent at night due to the thermal properties of urban and non-urban surface. The nocturnal UHII level in calSLUCM corresponds well to the level of urbanization with higher UHII recorded at most urbanized CAT33 (1.75 ºC) and lowest UHII recorded in CAT31 (1.11 ºC). The model agrees well with similar UHII diurnal profile and range modelled in the neighboring tropical city, Singapore [*Li et al.*, 2013b]. The modelled night UHI is lower compared to the measured data in KL (5.5 ºC in 2004) is likely due to the underestimation of the T2 during the daytime. However, such discrimination is expected due to the designation of the coolest reference point as rural for in-situ measurement [*Santamouris*, 2015].

At night, noUCM produces a spatially smaller and weaker UHI (0.56 ºC) compared to the calSLUCM as shown in Figure 3.7a. The underestimation of heating region is attributed to the missing urban grids of the conurbation in LO map. This agrees well with the influential role of urban land use coverage on land-atmospheric heat exchanges as discussed in Section 1.5.1. The inverted effect of UHI, urban “cool pool” is observed in the noUCM from 1200 to 1600 MYT, which is different from the common urban “cool pool” that occurred after the sunrise [*Jauregui*, 1997; *Chow and Roth*, 2003]. Without shadowing effect implemented in noUCM, the negative UHII is formed due to the misclassification of the urban land use as non-urban land which leads to rapid cooling. This emphasizes the importance of land use map accuracy in modelling both urban heating and cooling pattern. In Figure 3.6a, bUCM treats all urban land use with same set of empirical condition predicts a reasonably resembling diurnal general profile of UHII with calSLUCM. However, Figure 3.6b shows the heterogeneity of the urban canopy is not well reflected through the bulk model [*Kusaka et al.*, 2001]. The correct representation of urban level is especially vital given the increasing demand for the in-depth study of high resolution down-scaling model [*Chen et al.*, 2004b]. In SLUCM, the introduction of class-specified designation of the urban canyon geometry and thermal properties produces clearly defined heat intensity profile of each urban subdivision in Figure 3.6b. SLUCM, nevertheless, produces a much lower UHII for less-packed residential (CAT31). Figure 3.7c also similarly shows that urban heating effect of SLUCM is rather constrained within the urban core and shows no evidence of heating near the urban peripherals, which covers with CAT31. Such discrimination of result points out the limitation of original urban morphological and surface material parameters in sophisticated model to generically apply to localized UHI study.

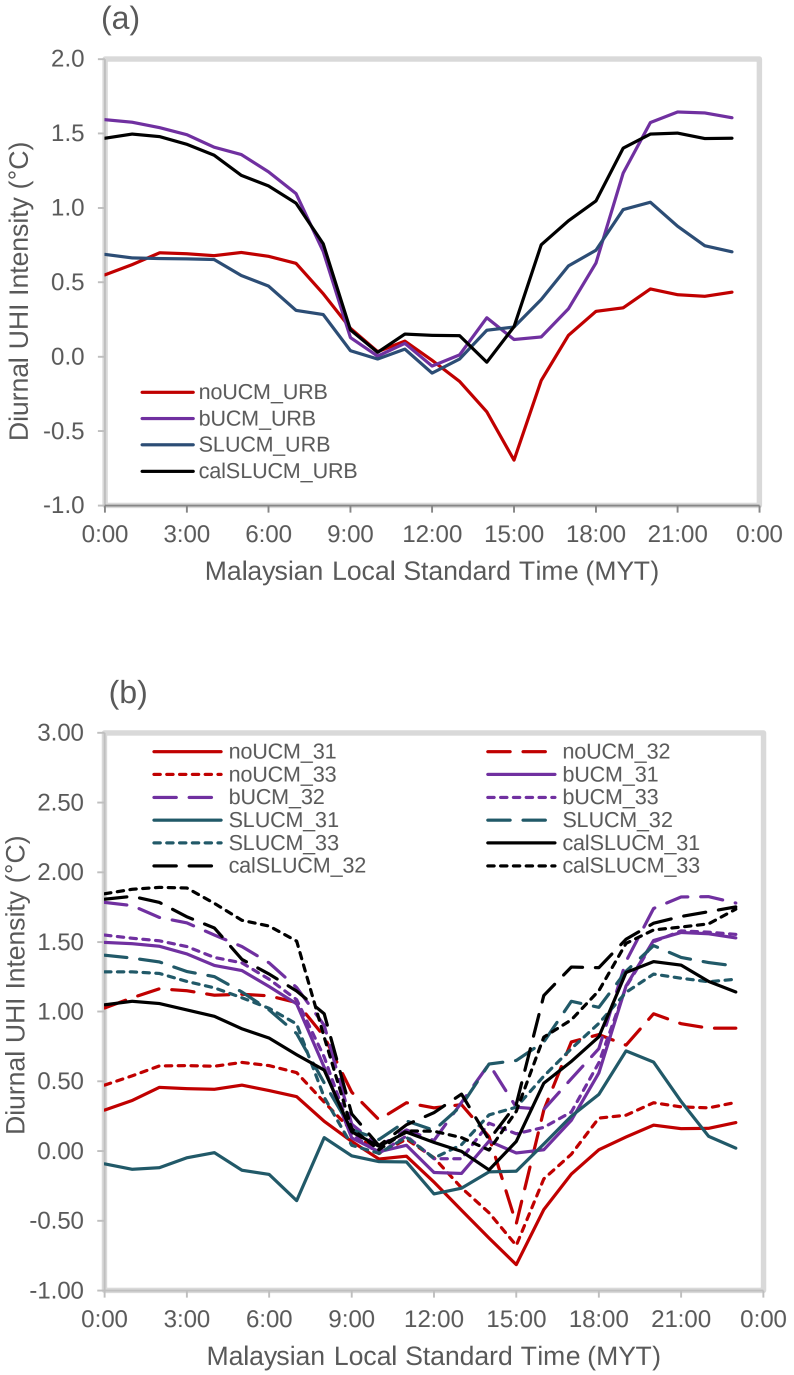

Figure 3.6: Hourly averaged UHI intensity of (a) all, (b) individual urban surfaces obtained through the difference between simulation and noURB case. The final two digits represent the urban land use types, 31: LDR, 32: HDR, 33: COM.

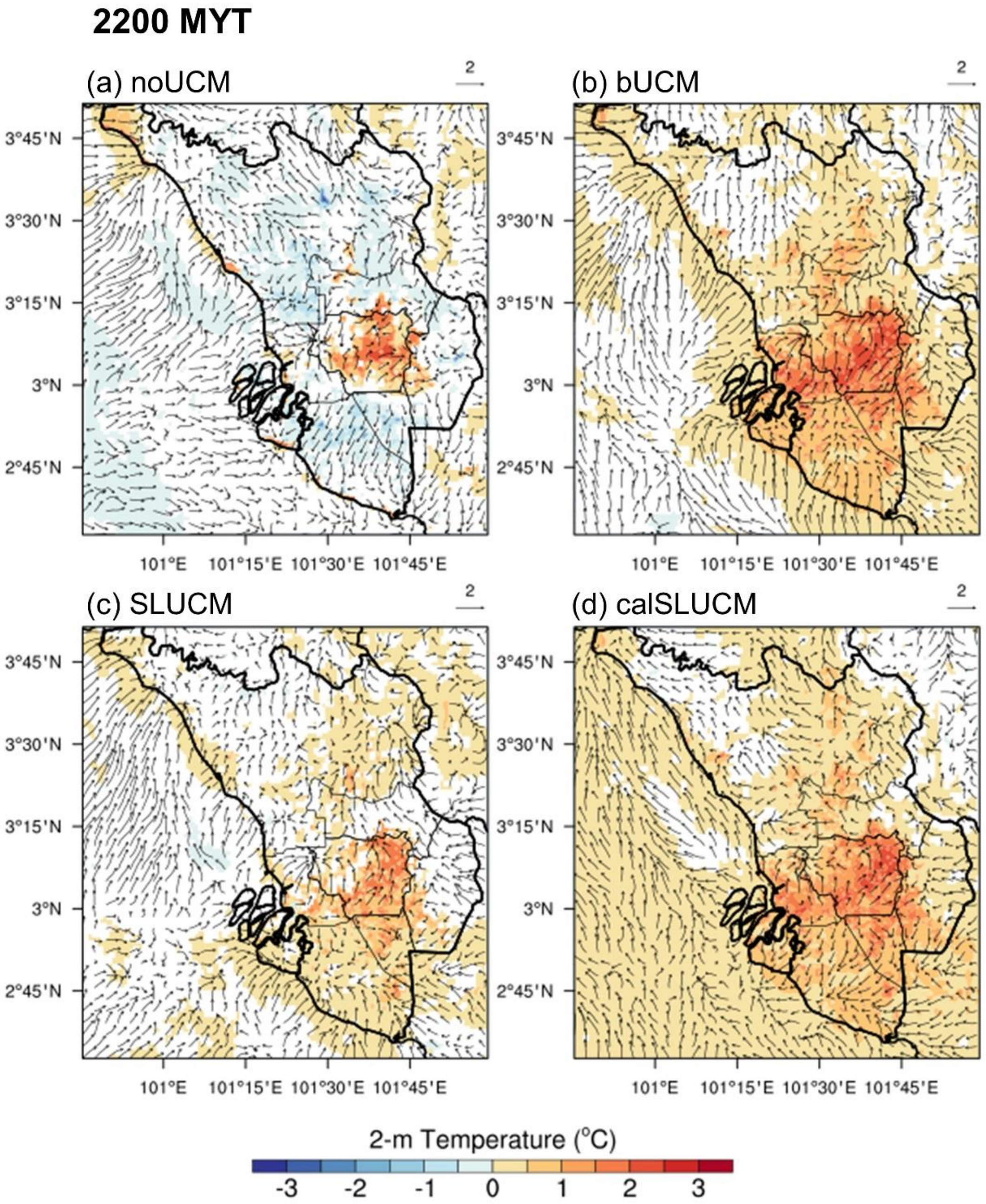

Figure 3.7: T2 (°C) [Filled contour, masked for values greater than 0.05 ºC or less than -0.2 ºC] and spatial 10m-wind (ms^{-1}) [Vectors] profile of the differences between model case (a) noUCM (LO_noUCM), (b) bUCM (LN_bUCM), (c) SLUCM, (d) calSLUCM with noURB case at 2200 MYT.

3.7 Findings

The case without UCM overestimates the total heat fluxes of urban and therefore forms cool pool during midday. The false specification of urban parameters in default SLUCM fails to generate the appropriate heating intensity for the surrounding suburb region. Comparable profile is simulated by bUCM and calSLUCM with an extensive influence of urbanization in terms of strength and coverage. The downwind effect of urban heat, double of the size of the city, is captured by the two performing models. Therefore, bUCM would be a good indicator for the general urban heating phenomenon if urban geometry and material information is lacking for individual urban classes. Calibration of the urban morphology and physical properties with calSLUCM manages to produce a relatively heterogeneous and wider areal influence of heating effect. Most importantly, the modification through LN3 greatly improves the prediction accuracy (RMSE) of the default settings and the combination usage with calSLUCM further improves the model to comply with the benchmark test.

The calSLUCM is thereafter taken as the reference setting for appropriate urban climate simulation for its ability to generate relatively accurate temporal and spatial thermal profile. With the improved model prediction, the updated LU map and the calibrated single layer UCM are used in the remaining urban climate study to represent the land use surface and parameterize the urban surface in LSM. After the verification of the performance of the land use map and urban canopy model, the ability of WRF to reproduce the vertical transportation and mixing within the boundary layer is examined. The vertical gradient of the turbulent fluxes is parameterized by the PBL scheme in WRF. Hence, the PBL schemes is analyzed to improve model integrity in simulating the vertical layers in Chapter 4.

CHAPTER 4: EVALUATION OF WRF PERFORMANCE ON URBAN BOUNDARY LEVEL: A SENSITIVITY ANALYSIS OF BOUNDARY LAYER PHYSICS

4.1 Introduction

The urban boundary layer (UBL) is the internal advection layer of atmosphere above urban region. The processes within the UBL determine the exchanges of momentum, water and other atmospheric constituents between the land surface and the free troposphere. Unlike the near-surface layer that highlights the surface heterogeneity, the urbanization effect on the local climate is better distinguished at the boundary scale. This chapter hence extends the ability assessment of WRF in simulating the boundary layer of GKL. Sensitivity test is conducted for the PBL parameterization schemes to ensure the applicability and weakness of the schemes to reproduce the transportation and dynamics within the vertical layers. The sensitivity analyses also determine the best suit scheme with lowest statistical error for subsequent study on effect of urbanization in the region. From which the better performing scheme is subsequently deployed to investigate the influence of urbanization on the local climatic condition in GKL in Chapter 5.

The objective of the chapter is to conduct sensitivity analysis of PBL schemes to predict the near-surface and vertical boundary layer structure for the GKL.

Similar to Chapter 3, several cases are run with selected PBL parameterization schemes and their performance is evaluated. Section 4.2 first discusses the parameterization method and features of the selected PBL schemes. Adopting the improved LU map and UCM settings in Chapter 3, the simulation cases are set up in Section 4.3. Each PBL physics is consecutively evaluated with the vertical sounding profile (Section 4.4.1), boundary layer height, (Section 4.4.1.1) near-surface condition

(Section 4.4.2), and rainfall amount (Section 4.4.3) before settling on the better performing scheme to reproduce the turbulent transportation and mixing within the UBL.

4.2 WRF PBL schemes description

The boundary layer physics is evaluated to characterize the model ability to reproduce boundary condition induced by urbanization as discussed in Section 1.5.3. Three widely applied PBL schemes, namely the local scheme, Mellor-Yamada-Janjić (MYJ) and two non-local schemes, Yonsei University scheme (YSU) and Asymmetric Convective Model (ACM2) are chosen for comparison. The strategy of each PBL schemes to address the generic subgrid-scale issues such as non-local transport, entrainment near PBL top, trainsitions between stable and convective boundary is addressed in the following.

Firstly, MYJ is an implementation of Mellor-Yamada boundary layer parameterization [*Mellor and Yamada*, 1982] into numerical weather prediction field [*Janjić*, 1990, 1994]. It is a level 2.5 model with 1.5 order local closure scheme with additional prognostic equation to predict the generation, transportation and dissipation of turbulent kinetic energy (TKE) and represents the entrainment near PBL top [*Skamarock et al.*, 2008],

Equation 4-1:

$$\frac{\partial e}{\partial t} = -\frac{1}{\rho}\frac{\partial}{\partial z}\rho\overline{w'e'} - \overline{w'u'}\frac{\partial U}{\partial z} - \overline{w'v'}\frac{\partial V}{\partial z} + \beta\overline{w'\theta'} - \varepsilon$$

where e is TKE. The first term on the right is the vertical divergence of vertical transport of TKE by w', second and third term make up the shear production of momentum, the fourth term is the buoyancy production due to heat and the ε is the dissipation term. Amongst them, the $\overline{w'e'}$, $\overline{w'u'}$, $\overline{w'v'}$, $\overline{w'\theta'}$ are flux variance (generalized as $\overline{w'C'}$) closed by gradient transport theory (same in Equation 1-2) and the eddy diffusivity coefficient (K_c) is defined as a function of mixing length (l) and proportionate coefficient which varies amongst the PBL schemes,

Equation 4-2:

$$\overline{w'C'} = -K_c \frac{\partial C}{\partial z}$$

Equation 4-3:

$$K_c = lS_c\sqrt{e}$$

There is no separation between the boundary layer and the entrainment layer in MYJ hence prognostic TKE is used to represent the entrainment near PBL top. Therefore, this scheme is suitable for stable and slightly unstable flows when turbulences are small which ensures the conservation of rapidly changing features within the boundary layer [*Nolan et al.*, 2009; *Hu et al.*, 2010]

The YSU scheme [*Hong and Pan*, 1996] on the other hand, is an improved version of the Middle Range Forecast model (MRF) where the concept of non-local parameterization is introduced [*Troen and Mahrt*, 1986]. The 1st order scheme is simple and stable since specified profile for diffusivity (Equation 4-2) and counter-gradient term (γ_c) are prescribed in the same equation,

Equation 4-4:

$$\frac{\partial C}{\partial t} = \frac{\partial}{\partial z}[K_c\left(\frac{\partial C}{\partial z} - \gamma_c\right) - \overline{(w'C')}_h\left(\frac{z}{h}\right)^3]$$

To be highlighted is the explicit treatment of entrainment process at the top of PBL (last term on the right hand side) caused by thermal and shear-driven turbulence at the PBL top. The boundary layer height is defined with critical bulk Richardson number and hence the buoyancy profile [*Skamarock et al.*, 2008]. It is suitable in predicting unstable flows by addressing the non-local fluxes when rigorous eddies circulation approaches the depth of the boundary layer. [*Hu et al.*, 2010; *Shin and Hong*, 2011].

The ACM2 scheme [*Pleim*, 2007a, 2007b] is a hybrid scheme combining both local upward eddy diffusion (rightmost term in Equation 4-5) and non-local transport scheme from ACM1 [*Pleim and Chang*, 1992]. Transilient matrix is used to explicitly treat non-local fluxes during convective condition (CBL) with upward mixing fluxes (M_u) from the top of the first model layer (C_l) that compensates with downward fluxes transport to a layer below (M_{d_i})and from the layer above ($M_{d_{i+1}}$),

Equation 4-5

$$\frac{\partial C_i}{\partial t} = f_{conv} M_u C_l - f_{conv} M_{d_i} C_i + f_{conv} M_{d_{i+1}} C_{i+1} \frac{\Delta z_{i+1}}{\Delta z_i} + \frac{\partial}{\partial z} [K_c (1 - f_{conv}) \frac{\partial C}{\partial z}]$$

The ratio of non-local fluxes to total fluxes near-surface, known as partitioning factor (f_{conv}), is introduced as a stability indicator for the smooth transition between stable and convective conditions [*Skamarock et al.*, 2008; *Xie et al.*, 2012]. In short, under SBL, partitioning ratio is small and ACM2 uses local closure scheme to solve the diffusivity equations.

In WRF, the associated MM5 similarity surface layer scheme is introduced to complement the derivation of PBL schemes and therefore, each PBL scheme is bonded to associated surface layer scheme. YSU and ACM2 PBL schemes are tied to MM5 Monin-Obukhov surface parameterization scheme. The MM5 scheme parameterizes thermal roughness length to a ratio of momentum roughness length [*Carlson and Frederick,* 1978],

Equation 4-6:

$$z_{0t} = \frac{1}{\left(\frac{\kappa u_*}{K_a} + \frac{1}{z_l}\right)}$$

where K_a is the molecular thermal diffusivity of air at 0°C (2.4 x 10^{-5} m^2 s^{-1}), u_* is the friction velocity. $z_l$is taken as 0.01m to represent the lowest height where turbulent heat transfer mechanism becomes important. MYJ scheme is coupled to Janjić Eta Monin-Obukhov surface layer parameterization (Eta). The thermal roughness length is expressed as a function of roughness Reynolds number in

Equation 4-7:

$$z_{0t} = z_{0m} e^{-\kappa C_{zil}\sqrt{Re}}$$

$$C_{zil} = 10^{-0.4 h_c}$$

where Re is the roughness Reynolds number ($u_* z_{0,m} / \upsilon_a$), υ_a is the kinematic viscosity of air (1.6 x 10^{-5} m^2 s^{-1}), The Zilitinkevich empirical constant (C_{zil}) is based on the canopy height (h_c) of each vegetation cover to predict their respective thermal roughness length [*Chen and Zhang*, 2009].

4.3 Experiment Design

The background weather condition (see Section 2.2) shows that strong synoptic flow prevails in October while April is rather calm and invariant. Due to the variability of atmospheric boundary layer to the background weather condition, this chapter tests the PBL scheme performance for two stated months, April and October of 2003 (see Table 4.1). The inter-monsoonal period with weaker synoptic forcing is studied to emphasize on the local climate, especially urban heating and its influence on topographic flow. The cases adopt the domain and physics settings in Chapter 2. The land use map is updated to the LN3 in Section 3.2.1 (Figure 4.1) while local calibrated urban parameters [*Morris*, 2016a] are integrated into the single layer UCM for surface characterization as mentioned in Chapter 3. Simulation cases adopting MYJ, YSU and ACM2 planetary boundary layer schemes are respectively run for the two aforementioned inter-monsoonal periods as shown in Table 4.1.

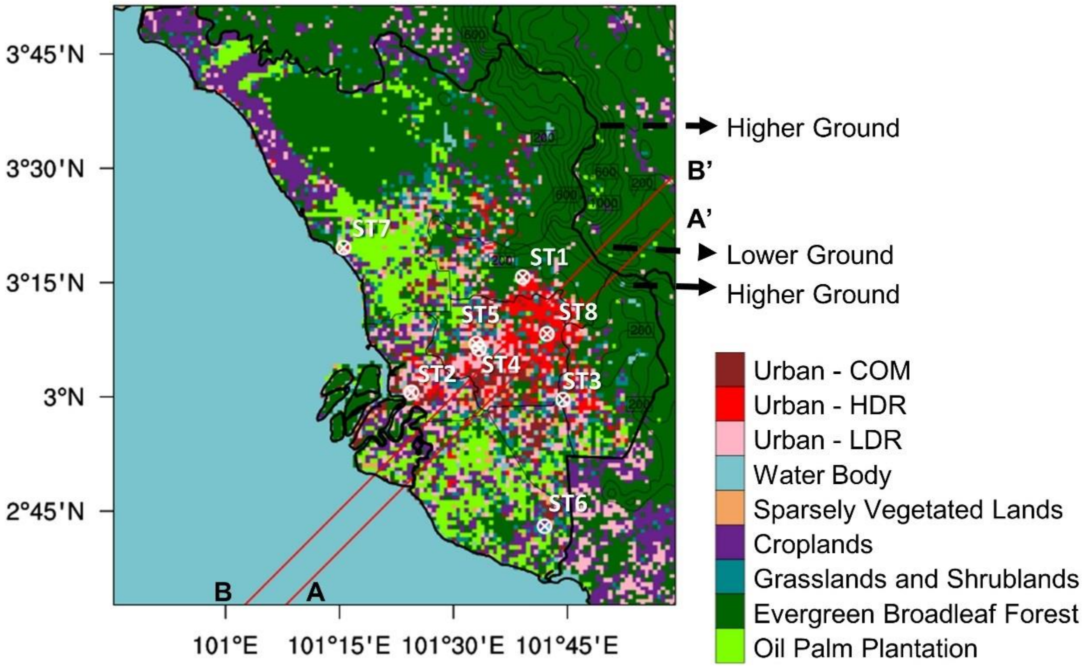

Figure 4.1: Updated LU map (LN3) with terrain height. Two lines indicate the vertical cross sectional profile extracted in later analysis. AA' has crossed plane (70,28) while BB' crosses plane (60,28), both with angle of 45°. White marker shows the ground weather stations similar to Figure 2.6 and Table 2.4.

Table 4.1: Experiment design

Case ID	PBL scheme	Surface layer scheme	LU map	Analysis period
MYJ_Apr	MYJ	Eta	Updated map (LN3)	08:00 2nd Apr - 08:00 20th Apr 2003
YSU_Apr	YSU	MM5		
ACM2_Apr	ACM2	MM5		
MYJ_Oct	MYJ	Eta		08:00 2nd Oct - 08:00 20th Oct 2003
YSU_Oct	YSU	MM5		
ACM2_Oct	ACM2	MM5		

4.4 Model evaluation

4.4.1 Vertical profile

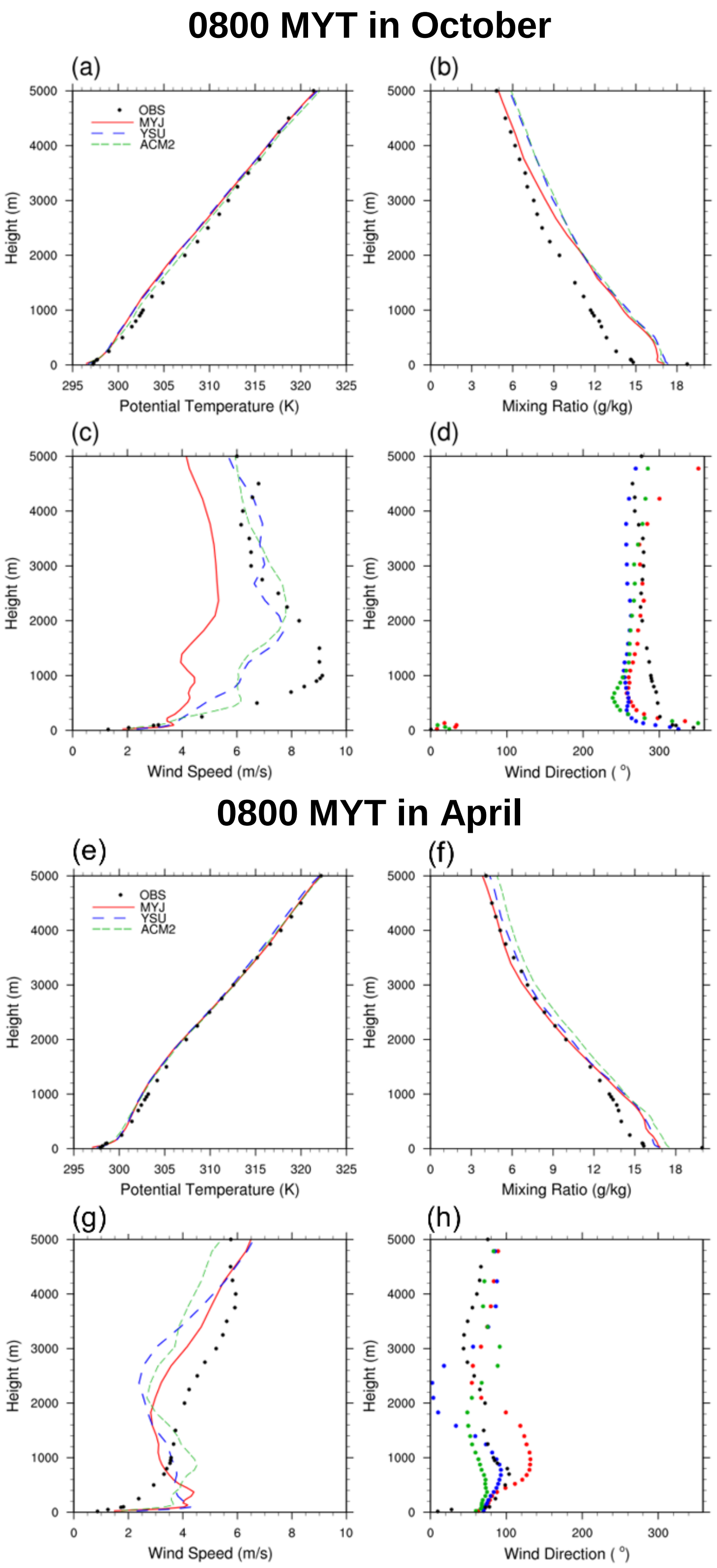

Figure 4.2: Evaluation of MYJ (in red line), YSU (in blue dashed line) and ACM2 PBL (in green dotted line) schemes performance to sounding data (in markers) for vertical profile of (a)(e) potential temperature, (b)(f) mixing ratio, (c)(g) horizontal wind speed and (d)(h) horizontal wind direction against sounding data at 0800 MYT in October and April 2003 respectively.

2000 MYT in October

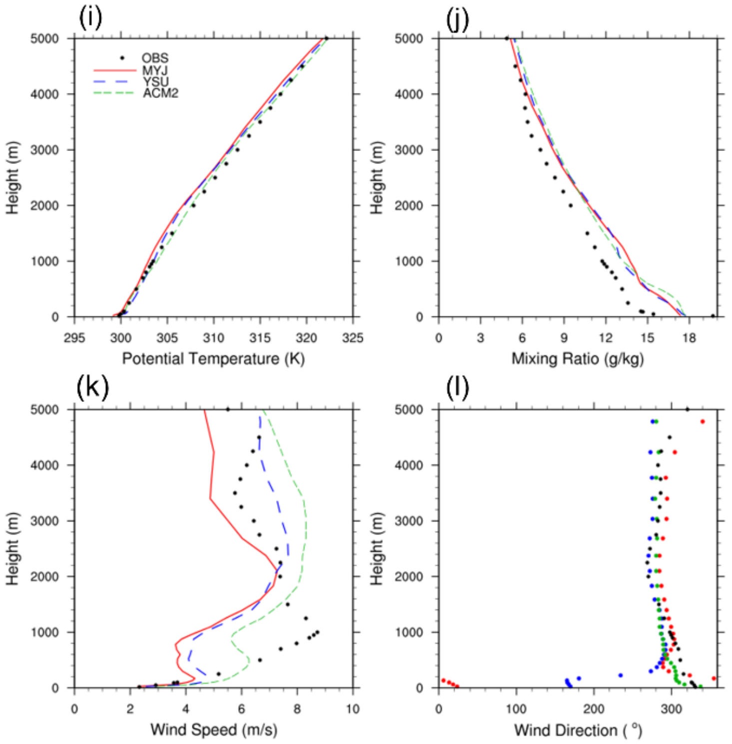

2000 MYT in April

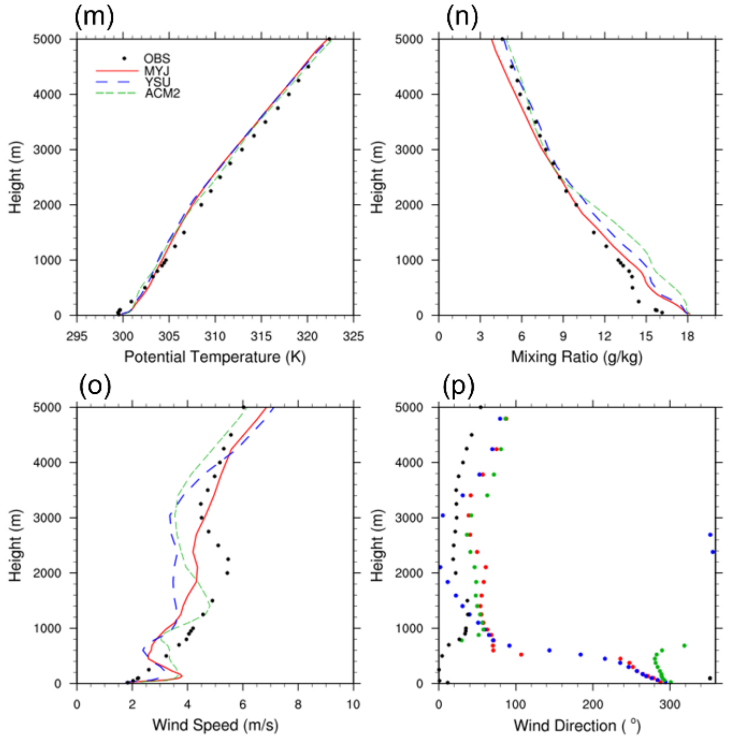

Figure 4.2(cont.): Evaluation of MYJ (in red line), YSU (in blue dashed line) and ACM2 PBL (in green dotted line) schemes performance to sounding data (in markers) for vertical profile of (i)(m) potential temperature, (j)(n) mixing ratio, (k)(o) wind speed and (l)(p) wind direction against sounding data at 2000 MYT in October and April 2003 respectively.

The performances of each PBL schemes in October and April are evaluated with available sounding data during the morning and evening transitional hours at 0800 MYT and 2000 MYT in Figure 4.2. The potential temperature and mixing ratio show slight variation for both months, hence is analyzed together. At 0800 MYT, the low potential temperature near the surface suggests the stably stratified boundary layer is still sustained at the morning hour in Figure 4.2a,e. The sounding data recorded mixing ratio around -0.125 kg/kg per meter on the first two vertical level of boundary layer (17 m to 50 m). However, the simulated mixing ratio profile shows a clearer mixed surface layer with much smaller inversion (around -0.005 kg/kg per meter) in Figure 4.2b,f. The mixing ratio is over-predicted for the bottom 1 km of the boundary layer but the error narrows down as it extends upwards. At 2000 MYT, an inversion layer below 100 m is also formed when the dissipating heat near-surface is unable to support the mixing layer along with disappearance of solar radiation (Figure 4.2i,m). A thick stably stratified layer is observed along with the formation of residue layer, indicated by steep mixing ratio gradient in Figure 4.2j,n. A good agreement is achieved by all schemes with less than 1 °C and 2 kg/kg of bias in potential temperature and vertical mixing ratio respectively. The bias value of vertical variables has a larger statistical tolerance compared to the near-surface variables due to the larger variability and uncertainty within the vertical layers. The temperature and humidity profiles are similar for all schemes with less than ±0.4 K and ±0.6 g/kg bias respectively among each cases with the largest deviation observed between 1000 m to 1500 m. This is the typical mixing layer height of the UBL [*Li et al.*, 2013b; *Morris et al.*, 2016].

The lower modelled wind speed for the entire vertical level suggests that the suppressed vertical mixing within the boundary layer in Figure 4.2c,g,k,o. The insufficient mixing from the hotter and wetter surface layer hence explains the negative bias of the modelled temperature and mixing ratio around the mixing height. The major difference of the horizontal wind profile between the schemes is shown near the same levels. It is expected that the non-local schemes produce a higher mixing height in the day by considering the mixing of surface layer to the entire CBL [*Xie et al.*, 2012; *Balzarini et al.*, 2014]. However, the positive bias between the non-local and local schemes at 0800 MYT is significantly higher in October (1.2±0.8 ms^{-1}) than in April (0.6±0.3 ms^{-1}). The major difference between the two inter-monsoon periods is shown in the strong northwest wind dominates the upper layer atmosphere in October in Figure 4.2c,d,k,l while April experiences weak influence of north-easterlies as shown in Figure 4.2g,h,o,p. The former agrees well with the reanalysis data at 850 hPa level portrayed in Figure 2.1. In October, the lower jet flow driven by the convergence belt near Borneo [*Chang et al.*, 2005] is flowing northwest with wind speed exceeding 9 ms^{-1} in the range of 1000 meter to 1400 meter height throughout the day (Figure 4.2c,k). The jet flow is within 850 hPa pressure level, where the convective heating in the Asian monsoon region is most indicative [*Wang et al.*, 2001]. The strongest shearing within this range therefore implies that intensive convective heating and moisture convergence are occurring over the boundary layer in October. On contrary, the vertical wind profile shows a smoothly increasing curve with a slight inflection near the SBL in April (see Figure 4.2g,h,o,p). The low boundary layer during this period is relatively calm and invariant compared to the October period. It is therefore arrived that the performance between the non-local and local schemes deviates greatly under influence of strong synoptic flow. Among all schemes, MYJ simulates a closer prediction except for morning wind profile in October that is better determined by ACM2.

Table 4.2: Error indices deviation of MYJ, YSU and ACM2 PBL schemes for vertical variables (potential temperature, mixing ratio and wind speed) and near-surface variables: T2, Q2 and uv10. FAE and NMAE are dimensionless (†). In order to effectively present the data within limited spaces, some data is adjusted through multiplication (the data include multiplication of 100 (*), multiplication of 10 (#))

Month	**October**						**April**					
Schemes	**MYJ**		**YSU**		**ACM2**		**MYJ**		**YSU**		**ACM2**	
Time	8am	8pm	8am	8pm	8am	8pm	8am	8pm	8am	8pm	8am	8pm
Error indices	***Vertical parameters***											
	Vertical potential temperature (K)											
MAE	0.64	0.66	0.63	0.45	0.42	0.29	0.35	0.69	0.43	0.75	0.31	0.65
RMSE	0.74	0.73	0.73	0.54	0.46	0.34	0.43	0.77	0.48	0.83	0.37	0.71
FAE*†	0.21	0.21	0.21	0.15	0.14	0.09	0.12	0.22	0.14	0.24	0.10	0.21
	Vertical mixing ratio (kg/kg)											
MAE	1.58	1.41	2.05	1.40	2.02	1.54	0.73	0.85	0.81	1.07	1.22	1.39
RMSE	1.83	1.61	2.18	1.56	2.13	1.73	1.03	1.12	1.07	1.37	1.34	1.77
FAE†	0.13	0.12	0.18	0.12	0.18	0.14	0.06	0.07	0.07	0.08	0.11	0.10
	Vertical wind speed (ms^{-1})											
MAE	2.39	1.66	1.16	1.47	1.00	1.45	0.89	0.73	1.16	0.90	1.14	0.79
RMSE	2.81	2.22	1.49	1.99	1.45	1.65	1.06	0.83	1.42	1.01	1.23	0.91
FAE†	0.41	0.29	0.20	0.24	0.15	0.23	0.26	0.20	0.35	0.23	0.33	0.21
	Original PBLH (m)											
Hit Rate	70.6%		52.8%		58.8%		70.6%		57.1%		68.6%	
MAE	20.21		14.96		26.07		20.90		22.18		31.77	
	Adjusted PBLH (m)											
Hit Rate	66.7%		73.0%		72.2%		72.2%		72.2%		77.8%	
MAE	15.50		16.97		21.95		11.36		12.34		18.06	
	Near-surface parameters											
	2-meter temperature (°C)											
Average	27.09						27.49					
MAE	1.43		1.72		1.67		1.76		1.77		1.83	
RMSE	1.82		2.19		2.13		2.24		2.20		2.33	
FAE*†	5.30		6.37		6.16		6.36		6.42		6.61	
NMAE*	5.28		6.34		6.17		6.41		6.46		6.67	
	2-meter relative humidity (%)											
Average	77.08						81.12					
MAE	7.35		8.18		8.45		10.73		10.22		10.36	
RMSE	9.27		10.50		10.65		13.19		12.46		13.20	
FAE*†	9.93		10.99		11.57		14.35		13.57		14.19	
NMAE*	9.54		10.61		10.96		13.22		12.60		12.77	
	10-meter wind speed (ms^{-1})											
Average	1.47						1.22					
MAE	1.05		1.39		1.77		1.02		1.16		1.26	
RMSE	1.45		1.86		2.25		1.38		1.55		1.64	
FAE$^{\#\dagger}$	6.56		7.41		8.23		7.12		7.56		7.99	
NMAE$^{\#}$	7.16		9.48		12.02		8.41		9.53		10.35	

The physics performance is evaluated with statistical error indices (see Section 2.4.4) in Table 4.2. On the vertical scale, October is better estimated with the non-local schemes while the weak wind condition during April is better estimated with MYJ. This clearly reveals the respective strength of PBL schemes. The non-local schemes able to account for the vertical diffusion within the highly convective boundary layer, especially during October month. ACM2 with the physical representation of local and non-local eddy diffusion movement return the best compliance among the non-local schemes under convective synoptic condition [*Pleim*, 2007a]. The local parameterization scheme (MYJ) is known to estimate vertical quantities through prognostic eddy diffusivity of adjacent grids and hence simulate cases under stable and slightly unstable condition better compared to convective condition [*Mellor and Yamada*, 1982]. Therefore, MYJ induces insufficient mixing under such large scale boundary condition in October. This is similarly demonstrated in the sensitivity analysis during summer in Texas, USA [*Hu et al.*, 2010]. Nonetheless, it shows an edge in solving cases of stable and localized boundary conditions well in the calm month, April.

4.4.1.1 Boundary layer height

The vertical tendency of these variables is principally dependent on the boundary layer height (PBLH) derived in the PBL schemes. This is especially imperative for the non-local schemes that pre-determine the PBLH as the depth of the well-mixed layer before the vertical gradient for each layers is computed [*Hong and Noh*, 2006; *Pleim*, 2007a]. The PBLH extracted from the sounding data (Section 2.4.6) is overlaid with the modelled data in Figure 4.3a,c. The PBLH hits its peak during daytime with the formation of well-mixed CBL while PBLH gradually reduces when SBL forms near the surface at night, with the presence of receding residue layer. However, Figure 4.3 shows that the modelled PBLH peaks are much lower than the measured PBLH value during the evening transitional period. It is also noticeable that the modelled PBLH is less than 1000 m and well below the level derived for the SEA region (PBLH = 1250 ± 670 m; *Von Engeln and Teixeira* [2013].

It is found that all PBL schemes have respective definition for the PBLH variable [*Shin and Hong*, 2011]. The MYJ scheme mainly derives the vertical fluxes of quantities from the turbulent kinetic energy calculated. The scheme attains PBLH when the calculated value of TKE reduces to 0.005 m^2s^{-2} in the setting of WRF [*Janjić,* 2001; *Shin and Hong*, 2011]. The non-local schemes determine PBLH by matching the prescribed value of critical Richardson number, $R_{crit.}$ From which, YSU obtains the PBLH from first neutral level above unstable layer when R_{crit} reduces to zero for CBL and increases to 0.25 for SBL condition. On top of the neutral layer derived in YSU, ACM2 includes the height of the entrainment layer. The definition of PBLH is not consistent for each scheme and hence not directly comparable. Hence, the modelled PBLH algorithm is standardized to compare with the measured PBLH. The lapse rate method ($\Delta\theta/\Delta z \leq 0.002\ Km^{-1}$) is adopted to determine consistent PBLH regardless of the type of PBL schemes and model resolution [*Hu et al.*, 2010; *LeMone et al.*, 2013].

(a) Oct – Original PBLH

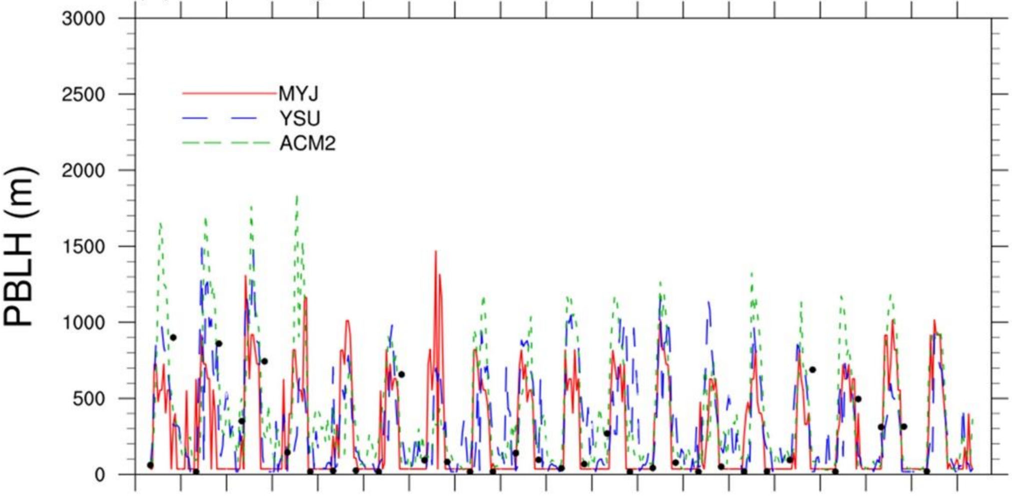

(b) Oct – Adjusted PBLH

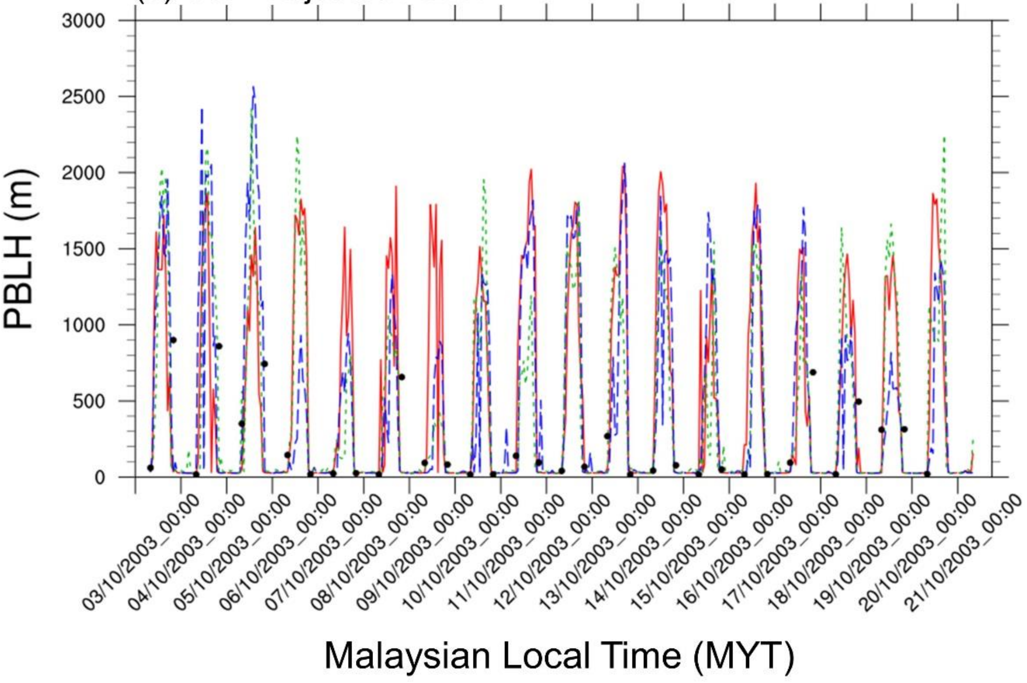

Figure 4.3: PBLH extracted from WRF output as (a) original value in October, (b) after adjustment in October, (c) original value in April and (d) after adjustment in April are compared with the measured sounding data marked as filled black dot at 0800 and 2000 MYT.

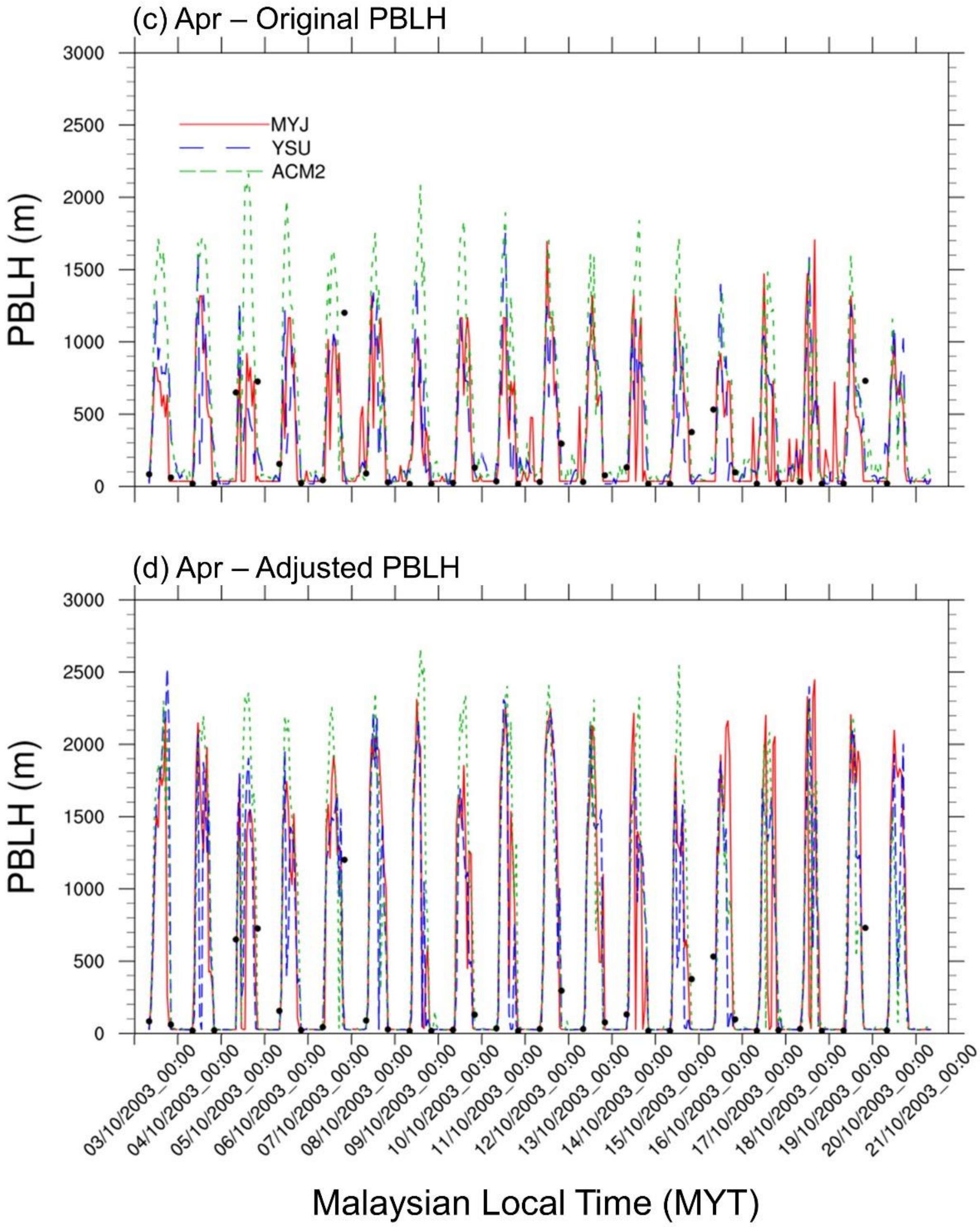

Figure 4.3 (cont.): PBLH extracted from WRF output as (c) original value in April and (d) after adjustment in April are compared with the measured sounding data marked as filled black dot at 0800 and 2000 MYT.

The boundary layer height of each scheme is evaluated against the measured PBLH extracted from sounding with hit rate and MAE (Refer to Section 2.4.6). The MAE among values that within hit rate threshold is also tabulated in the same table and a lower value is desirable. Relative to non-local schemes, the collective statistical evaluation of PBLH shows that MYJ model complies better with the measured ones during the period of investigation with 72.2% hit rate (11.36 m MAE) recorded in April and 66.7% hit rate

(15.50 m MAE) attained in October shown in Table 4.2. The standardized method increases the modelled PBLH depth as shown in Figure 4.3b,d. The adjusted PBLH profile has shown that the mixing layer predicted by MYJ rises immensely during the day and produces similar profile with the non-local schemes. Although MYJ is often shown to underestimate the PBLH [*Xie et al.*, 2012; *LeMone et al.*, 2013], the adjusted PBLH demonstrates that it is able to capture the entrainment of the free atmosphere into the boundary layer like the non-local scheme. The non-local schemes, in turn, decrease during the calm night. Among which, the ACM2 produces a more turbulent boundary layer with the highest modelled PBLH peak during the day. It is also noticeable that the hotter month (April) produces a generally higher mixing layer height during the day due to enhance convective activities nearing summer [*Von Engeln and Teixeira*, 2013; *Kusaka et al.*, 2014]. The higher PBLH produced by ACM2 implies better mixed UBL which associates well with the higher value of vertical profile of temperature and lower mixing ratio.

With the limited sounding data, all the schemes predict the PBLH reasonably well during the transition period, especially after the normalization of PBLH retrieval method. Each scheme gives less than ±100 m difference for the daytime PBLH (0900 – 1900 MYT) between the schemes. The unified derivation approach associates well among the schemes. The boundary layer prediction in numerical model is generically difficult to predict the transitions between different stability conditions and transportation of fluxes under unstable layers. In this context, the model is able to determine the performing PBL scheme under the entraining and detraining process between the stable and unstable atmospheric condition at the transitional hours. Currently the hourly profile is not available for vertical parameters, hence it could not be tested on hourly basis, including the well-mixed layer and night stable boundary layer.

4.4.2 Near-surface environment

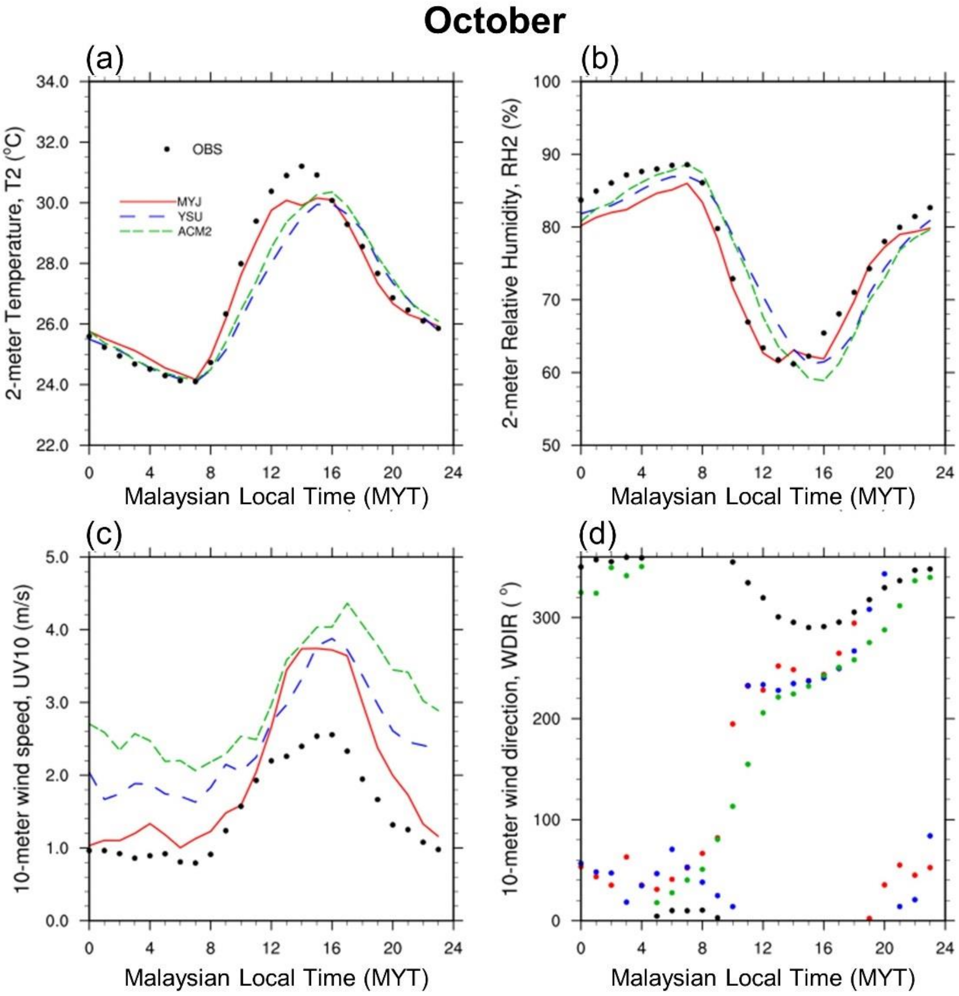

Figure 4.4: Hourly averaged of (a) T2, (b) RH2, (c) uv10 and (d) wdir10 extracted from simulated PBL schemes for grid points that collocate with 8 ground observation stations in October 2003.

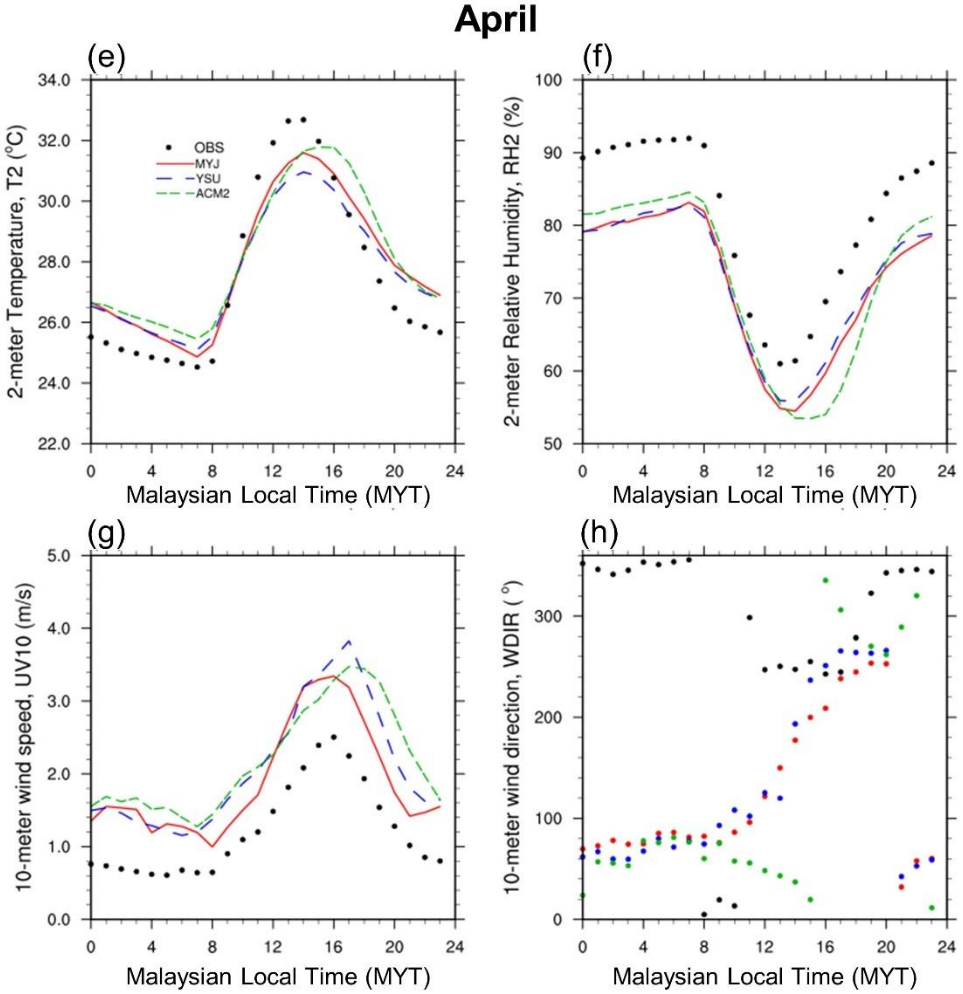

Figure 4.4(cont.): Hourly averaged of (e) T2, (f) RH2, (g) uv10 and (h) wdir10 in April 2003.

Diurnal data from ground weather network is analyzed for each surface layer scheme. In Figure 4.4a,e, the model reproduces the hourly T2 trend reasonably well but it hardly captures the occurrence of peak temperature at 1400 MYT in October. A generally lower amplitude variation is observed, i.e. modelled result is colder during the day and hotter at night. Figure 4.4b,f show that all schemes typically underestimate the Q2 during April. YSU and ACM2 cases delay the response up of peak temperature and relative humidity up to two hours. MYJ case, nevertheless produces closer agreement especially in October for the diurnal profile. The uv10 profile shows stronger air flow during the day, doubled of the night, in response to the perturbative movement induced by the heated land surface. All schemes overestimate the wind strength in the day as shown in Figure 4.4c,g. MYJ case produces comparably reasonable agreement to the near-surface wind speed. The wind direction is reproduced during the night but none of the schemes capture it in the day. The difficulty in estimating it lies in the chaotic profile of turbulence induced during the day, especially when the wind direction profile is averaged over several stations scattered within the domain. The near-surface layer condition predicted by each scheme has smaller bias between each other compared to the vertical profile. The bias level records 0.4±0.2 °C T2, 2.1±1.2% RH2 and 0.5±0.2 ms^{-1} uv10. A large bias for T2 and RH2 equally observed around 1700 – 2000 MYT during both inter-monsoon seasons. It is potentially related to the precipitation events that occur during the concurrent period. This is further discussed in 4.4.3.

Table 4.2 compiles the error statistics for the different PBL physics schemes and MYJ records overall the lowest statistical error. The ability to reproduce the near-surface condition is found to depend on the accompanying surface layer scheme of each PBL scheme [*Shin and Hong*, 2011; *Xie et al.*, 2012]. The closer prediction of MYJ scheme implies that Eta similarity theory of MYJ scheme determines T2 and Q2 well. The good performance of the local scheme can be attributed to the determination of heat transfer coefficient according to the roughness length of the surfaces [*Chen and Zhang*, 2009]. In general, larger discrepancy is predicted for the near-surface condition in October, especially the non-local scheme. This reveals that the performance of the vertical layer profile is greatly determined by the surface exchange coefficient derived from the surface layer scheme. Hence, the large discrimination of T2 during the peak hour (discussed in Section 3.6.1) can be attributed to the application of MYJ in this context. However, due to the incompetency of the non-local scheme to produce the temporal profile, the MYJ remains as the optimum choice to model the near-surface temperature.

4.4.3 Rainfall amount

(a) October

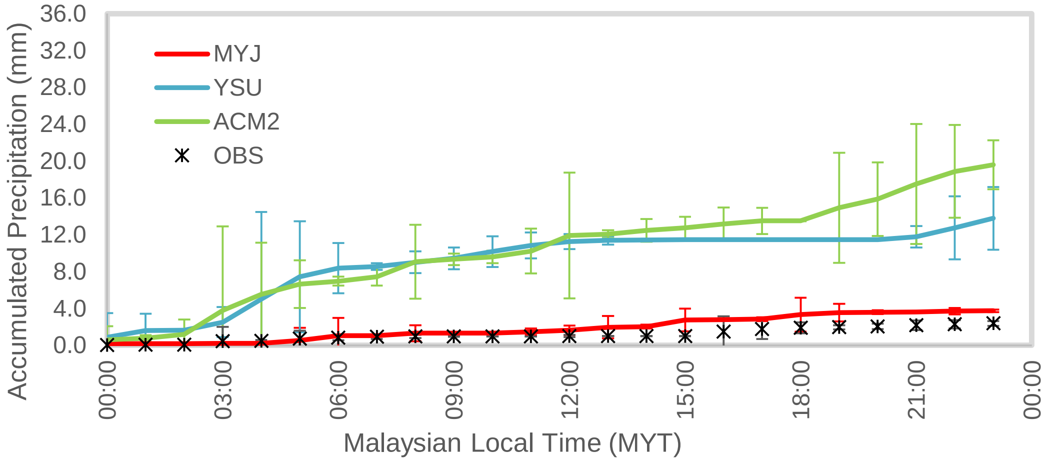

(b) April

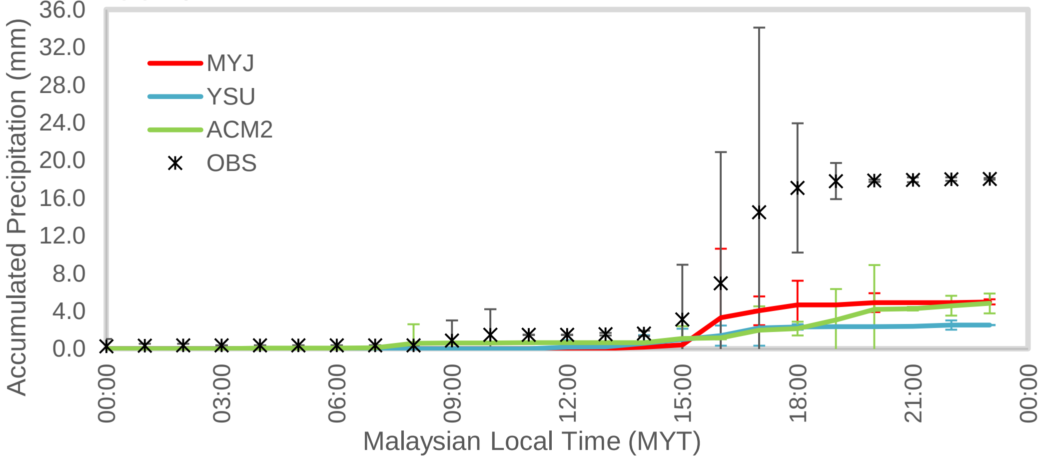

Figure 4.5: Accumulated hourly averaged of precipitation extracted from simulated PBL schemes at ST6 in (a) October 2003 and (b) April 2003.

The precipitation output produced simulated by full grid microphysics (RAINNC) and sub-grid cumulus (RAINC) drivers are summed for total precipitation to evaluate against the rain gauge data. Figure 4.5 shows that the precipitation in April usually occurs in the later afternoon from 1500 – 1900 MYT due to the occurrence of thunderstorm described in Section 2.2. Beside the late afternoon thunderstorm, October also record the precipitation throughout the night but it receives an overall lower precipitation amount than April. All schemes, notably MYJ successfully captures the initiation time of the convective activities at 1500 - 1600 MYT in both months and 0500 MYT in October. However, mean bias of 0.6±0.4 mm recorded in October and 0.2±0.2 mm recorded in April respectively, with largest the bias produced during the aforementioned precipitation period.

During the month with strong synoptic influence, the non-local fluxes predict a severely wet condition in the midnight and late afternoon. A good agreement of rainfall amount is produced by MYJ model which is generally less responsive to the large scale turbulent convection. It can therefore be attributed that despite the influence of synoptic condition, the heterogeneous land sea mask in MC shelters the GKL region from large scale turbulence movement and creates a relatively calm weather condition compared to the rest of the Malay Peninsula [*Chang et al.*, 2005]. The actively convective atmosphere generated by non-local scheme is considered less suitable for the application unless Ri_c threshold that determines the algorithm for stable or convective boundary layer is re-iterated for further adaptation. In such a context, the local scheme (MYJ) remains a more suitable candidate of PBL scheme for the current study under relative stable weather condition, resonating with the findings from *Shin and Hong* [2011].

4.5 Findings

From the investigation, it is observed that the performance of PBL schemes is greatly influenced by the synoptic condition. In general, all schemes in prediction of vertical profile, near-surface profile and precipitation amount are more uncertain in the October which experiences a stronger synoptic forcing. The PBL schemes give larger variation for the vertical profile and rainfall amount during the convective period. This is attributed to the relatively significant influence of the synoptic condition on these PBL processes.

It is also notable that the non-local scheme, namely ACM2 gives a closer agreement to the vertical profile in October. However, the remaining model evaluations of vertical and precipitation profile clearly inclines towards the local scheme, MYJ which performs relatively well. Similarly, the local closure scheme simulates more shallow PBLH but closer agreement with measured data after normalization. The allocation of thermal roughness length to respective land use also improves the ability of the Eta similarity theory surface layer scheme (coupled with MYJ scheme) to estimate the heat transfer coefficient and hence better determines the near-surface condition than the other schemes. Therefore, the strong coupling of the MYJ PBL scheme and Eta similarity surface scheme prompt the subsequent analysis on the effect of urbanization to be conducted with the combination.

CHAPTER 5: RELATIONSHIP BETWEEN LAND USE AND LOCAL FLOW CIRCULATION

5.1 Introduction

The turbulent movements and vertical structure of the UBL are substantially different compared to the pre-urban form due to the surface forcing induced by the presence of urban fabric at the surface. In this chapter, the WRF-ARW mesoscale model is used to study the effect of urban heating on the local near-surface climate of the GKL. The selected PBL scheme in Chapter 4 is used in this chapter. The urban heating and topographic circulation have a mutual influence as discussed in Section 1.2. On top of that, they are equally subjected to the directional impact of the climatic forcing. Therefore, this chapter studies the interaction of urbanization with the local topographic flow circulation during two inter-monsoon seasons which characterized by strength of synoptic flow forcing and sea breeze orientation.

The objectives of the chapter include:

a) Investigate the effect of UHI on the regional climate in the GKL during the inter-monsoon periods
b) Investigate the interaction of urbanization and the local circulation
c) Investigate climate implication on the interaction of UHI and local circulation

The simulation experiment in this chapter adopts the optimum settings obtained in the past two chapter (Chapter 3 and 4). They are briefly explained in Section 5.2. The spatio-temporal effect of urbanization in terms of temperature change, i.e. urban heating on the near-surface environment and local circulation, is analyzed and discussed in Section 5.3.1 and Section 5.3.2 respectively. From which, Section 5.3.3 shows the variation of local circulation in response to the urban heating profile and vice versa. This section also identifies the role of the synoptic forcing of the background weather on the interaction of the urban thermal and topographic flow systems. Last but not the last, the influence of urban-induced change on the precipitation profile is analyzed in Section 5.3.4.

5.2 Experiment design

The same domain settings are adopted as shown in Chapter 4. Simulation cases adopts MYJ PBL scheme with Eta surface layer scheme for the two inter-monsoonal periods to evaluate their corresponding performance with simulation cases set up as shown in Table 5.1. Similar to the previous chapter, the noURB is set up for each month to identify the influence of urban land development on the boundary climate. It retains the same domain and physics setups but with a pre-urbanized land use map.

Table 5.1: Experiment design

Case ID	**PBL scheme**	**Land use map**	**Month**
Apr	MYJ	Updated LU map (LN3)	April
Oct			October
Apr_noURB		No urban map (noURB)	April
Oct_noURB			October

5.3 Effect of urbanization on local climate

5.3.1 Diurnal analysis of near-surface UHI intensity

The thermal response of canopy level to urbanization is indicated through the difference of diurnal T2 between the simulation case with and without urban development (noURB). The discrepancy is known as the UHI intensity (see Section 2.4.7). Figure 5.1a records daily-averaged UHI intensity of 0.98 °C and 0.78 °C for October and April respectively. The intensity profile is observed to vary between three time segments marked by the thick boxes: night (1900 to 0700 MYT), morning to midday (0900 to 1300

MYT) and late afternoon (1500 to 1800 MYT). The highest intensity of 1.38 °C is observed for both months after sunset from 1900 to 0700 MYT. The highest UHI intensity recorded (1.9 °C at 0000 MYT) at the commercial land uses and is comparable with the nocturnal maximum intensity from studies conducted in GKL (around 2.5 °C) [*Ahmed et al.*, 2014; *Morris et al.*, 2017] and Singapore (2.2 °C) [*Li et al.*, 2016]. The vegetated surface cools down at a higher rate than the urban surface and subsequently increases the nocturnal UHI intensity as shown in Figure 5.1b. The lower surface heat emissivity and width to height aspect ratio of urban canopy are responsible for the slower cooling at night [*Oke and Maxwell*, 1975; *Grossman-Clarke et al.*, 2008; *Loughner et al.*, 2012]. The surface cooling rate decreases from LDR (CAT31) to HDR (CAT32) and COM (CAT33) characterized with reducing aspect ratio (see Table 3.4).

During the early morning heating period (0900 to 1300 MYT), April yields a strong negative intensity up to -0.6 °C. Such “cool pool” phenomenon is commonly observed in tropical UHI study [*Jauregui*, 1997; *Chow and Roth*, 2003; *Zhao et al.*, 2014]. Similar to the decelerated cooling at night, urban surfaces with lower thermal admittance have a much lower heating rate, not to mention the shadowing effect of tall building that also hinders the absorption of radiative heat [*Oke*, 1987; *Santamouris*, 2015]. In Figure 5.1b, the heating rate profile highlights the dependency of UHI intensity on the vegetation heating rate. Compared to the impervious urban, the heating rate of vegetation is mainly determined by the amount of moisture content. Clearly, greater heating rate of vegetation in the morning of April highlights the immediate thermal response of the dry surface to the radiative cycle. As such, the humid vegetation cover caused by late night precipitation in October is heated up slower and therefore explains the near zero UHI intensity (0.14 °C). The prolonged effect of regular heavy showers and thunderstorm on the UHI intensity of the subsequent days is also pointed out by *Kim & Baik* (2002). This agrees well with the other low latitude cities where the thermal response is predominantly governed by the wet/dry condition than the hot/cold variation of the mid-latitude cities [*Jauregui*, 1997; *Arnfield*, 2003].

Subsequently, April yields UHI intensity of 0.64 °C, 0.42 °C lower than October from 1500 to 1800 MYT. This implies that the urban heating intensity is closely associated with the precipitation activities (see Section 4.4.3). The close connection of moisture content with UHI intensity during day time implies the potential association with the moisture-bearing sea breeze flow which prevailed during the day near the coast. The UHI intensity is only consistent in both months when the cooling rate returns to its steady state at night as shown in Figure 5.1b. The varied response of daytime UHI intensity highlights the potential tendency of daytime UHI to respond differently to the synoptic condition during the two inter-monsoonal season. The interaction of UHI and local topographic flow is further elaborated in the subsequent section.

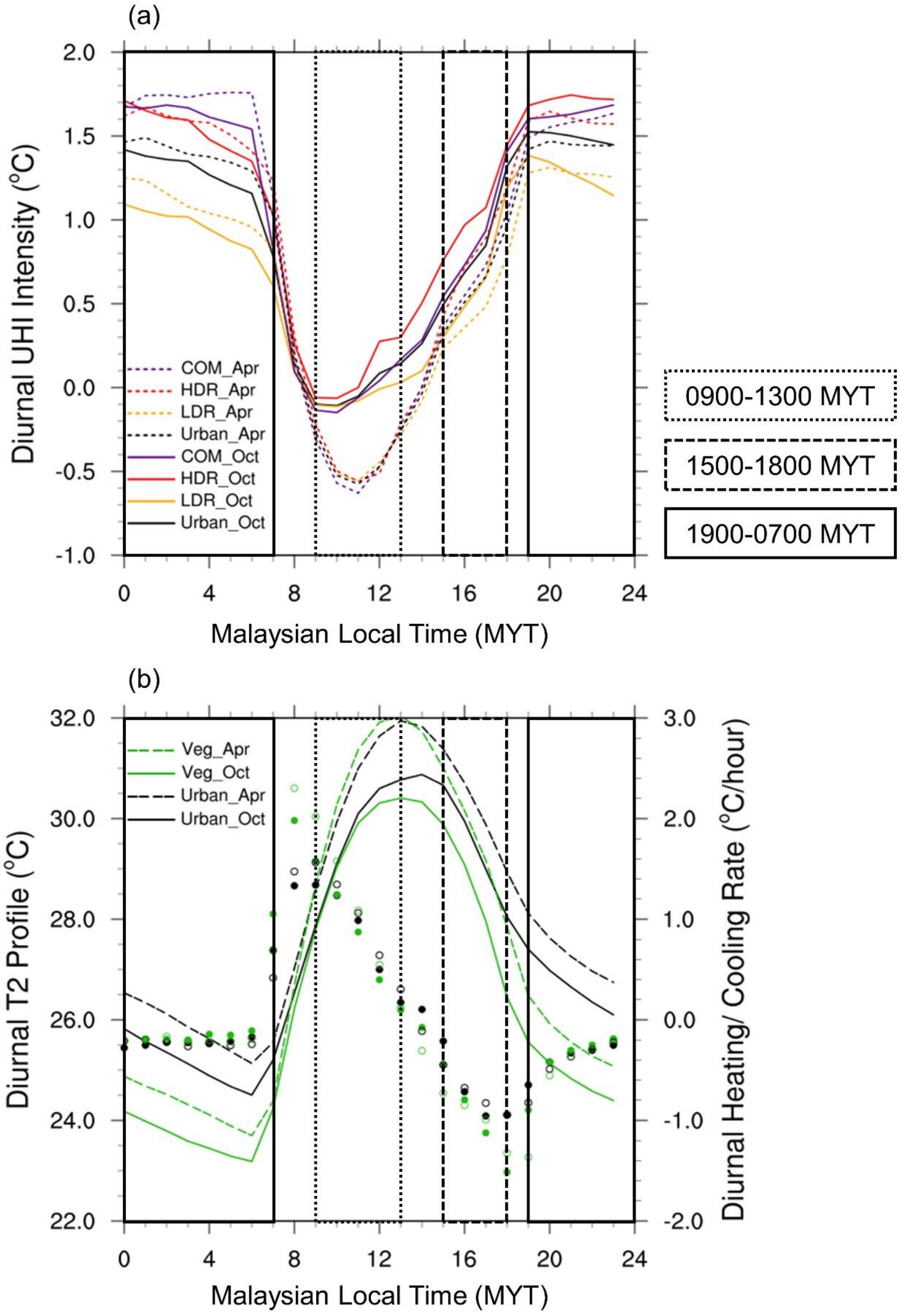

Figure 5.1: (a) Hourly averaged UHI intensity of urban surfaces obtained through the difference between simulation (urban and its 3 urbanization level: LDR, HDR and COM) and noURB case.; (b) Diurnal T2 profile (line: October; dotted line: April) and heating/cooling rate (filled dot: October, hollow dot: April) in both April and October months for urban surface (Urban) and after being replaced by vegetation (Veg; CAT10).

5.3.2 Effect of urbanization on local climate

An overview of local circulation between urbanization case with its corresponding noURB case during the October and April are depicted in Figure 5.2. The effect of urbanization on near-surface level is scrutinized through the profile of T2 and uv10 vector by comparing with the noURB case. The hourly variations spatial profile is analyzed at 1200 MYT, 1500 MYT and 2200 MYT in Figure 5.3 to represent the various response of UHI intensity as discussed in Section 5.3.1.

October

In Figure 5.2, higher coastal T2 is observed at 1200 MYT due to the inland movement of sea breeze. The inflow of moisture-bearing sea breezes carries water vapor to the coast which top up to the latent heat when land surface is heated. However, the heated coast is not perceived as an urbanization effect as depicted in UHII profile (Figure 5.3). In turn, the urban-induced hotter regions spread across a vast region of land surface. The heat accumulated over the land mask can be attributed to the widespread coverage of cloud in October as seen in Figure 5.4. The cloud cover is known to inhibit the vertical transportation of near-surface air [*Morris et al.*, 2001]. It decelerates the dissipation rate of heat generated at the urban and explains the heat accumulation. Around 1500 MYT, the sea breeze sweeps past GKL towards the mountain gap located on the right of the GKL (marked as lower ground in Figure 4.1). The presence of urban land along the wind path reduces the strength of the sea breeze especially on the upwind side of the urban. A “cool pool” is observed near the region as shown in Figure 5.3c. The region coincides with the urban-induced wet region as shown in Figure 5.5a. This indicates that the strong inland urban heating draws immense moisture from the sea to the coastal region during the initiation hour of afternoon convective precipitation. The increment of precipitation tendency due to urbanization is highlighted in several cities [*Zhong and Yang*, 2015;

Daniels et al., 2016] and this implication of urbanization is further discussed in detail in the Section 5.3.4. The urban cool pool recedes gradually and gives way to the growing urban heating patch in the evening. A prominent UHI is formed at 2200 MYT as shown in Figure 5.3. The presence of the rough urban surface as well as the heated urban convergence zone impede the mountain flow and thus the outflow of the urban air mass [*Li et al.*, 2013b; *Miao et al.*, 2015]. Such phenomenon is unfavorable for the dispersion of the heat and pollutant generated especially under the stably stratified night [*Wang et al.*, 2007; *Li et al.*, 2014].

April

A different scenario is observed in April. The clear sky in April (see Figure 5.4) facilitates the radiative heating transfer of the surface heat which the entire land surface heats up uniformly, as illustrated in Figure 5.3. Under weak synoptic forcing, the local surface heating greatly determines the thermal interaction between the topographic flow with the urban energy system during the day. The coastal region thus experiences a stronger sea breeze than in October at 1200 MYT (discussed in 5.3.3). While the sea breeze gradually propagates towards the mountainous region, it stalls over the urban core in case of urbanization at 1500 MYT. The urban confluence region drives in gap winds from the lower ground near the mountain (marked in Figure 4.1) and also the down-slope breeze from the inland mountain range. Unlike October, the GKL generates a clear profile of “urban dry island” with lower moisture content in Figure 5.5b. The lower strength of UHII in April month is attributed to the reduction of sea breeze strength and hence the moisture inflow. This is elaborated in the subsequent Section 5.3.3. The nocturnal thermal condition and circulation (2200 MYT) in April are similar to October in Figure 5.2. Despite being the hotter month, UHI intensity observed in April remains comparable with October due to the reference rural region that is also equally hot at night. This further affirms the nocturnal UHI effect is less governed by the temperature variation under months of different synoptic forcing.

The synoptic effect imposes larger urban-induced thermal response during the day than the night of both transitional months in the tropical region. Clear sky is responsible for the formation of urban cool pool in April from the morning to midday (0900 MYT – 1200 MYT). While the enhanced sea breeze flow due to urban confluence zone at 1500 – 1900 MYT has effectively subdued the urban heating influence on the upwind of urban. The passages of sea/land breezes and mountain/valley breezes vary according to the synoptic condition by comparing the two months. The presence of urban surface therefore alters the circulation of these flows depending on the synoptic frontal condition.

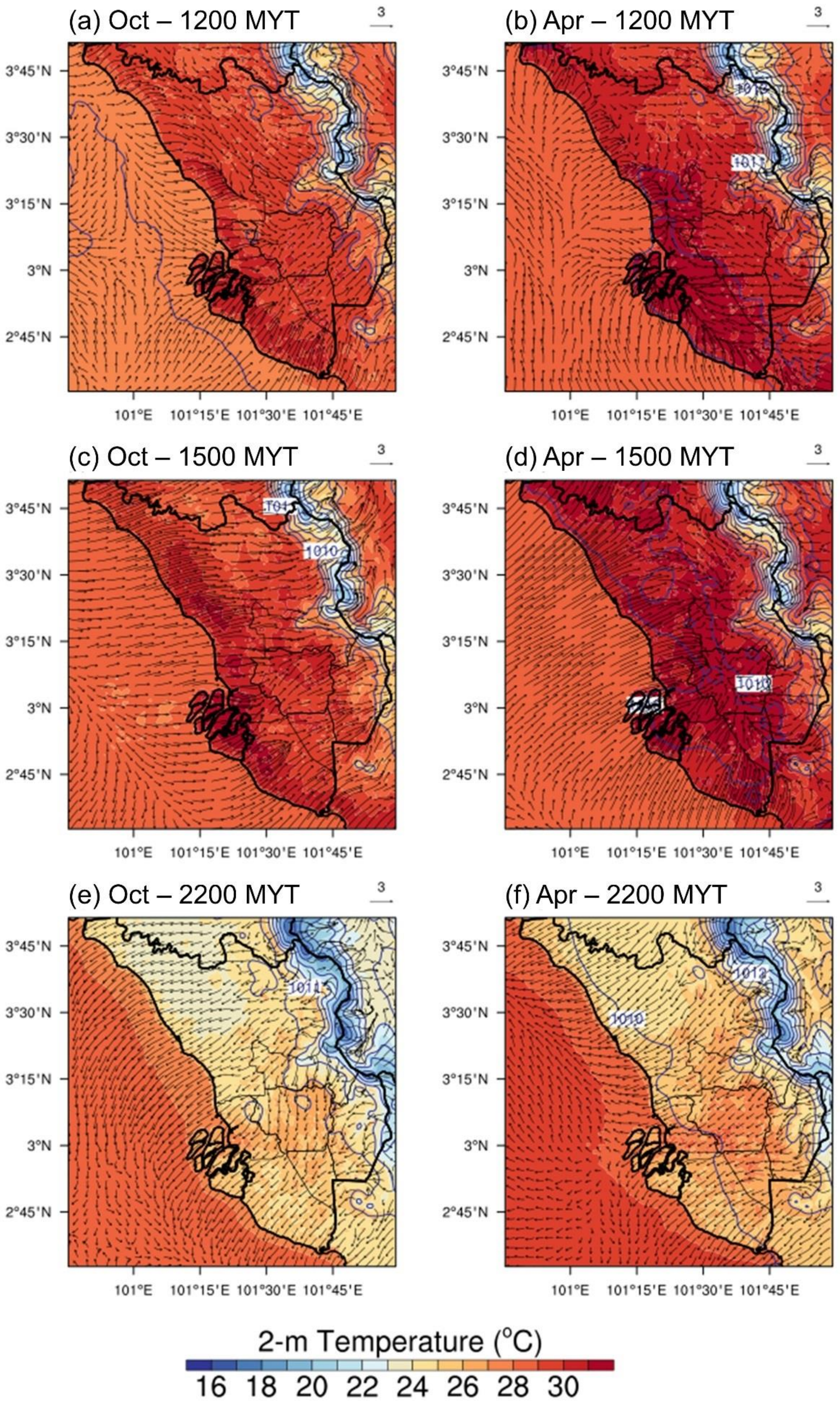

Figure 5.2: Spatial uv10 (ms^{-1}), T2 (°C) and sea level pressure (SLP) (hPa) profile at (a)(b) 1200 MYT, (c)(d) 1500 MYT, (e)(f) 2200 MYT for October (left panels) and April (right panels).

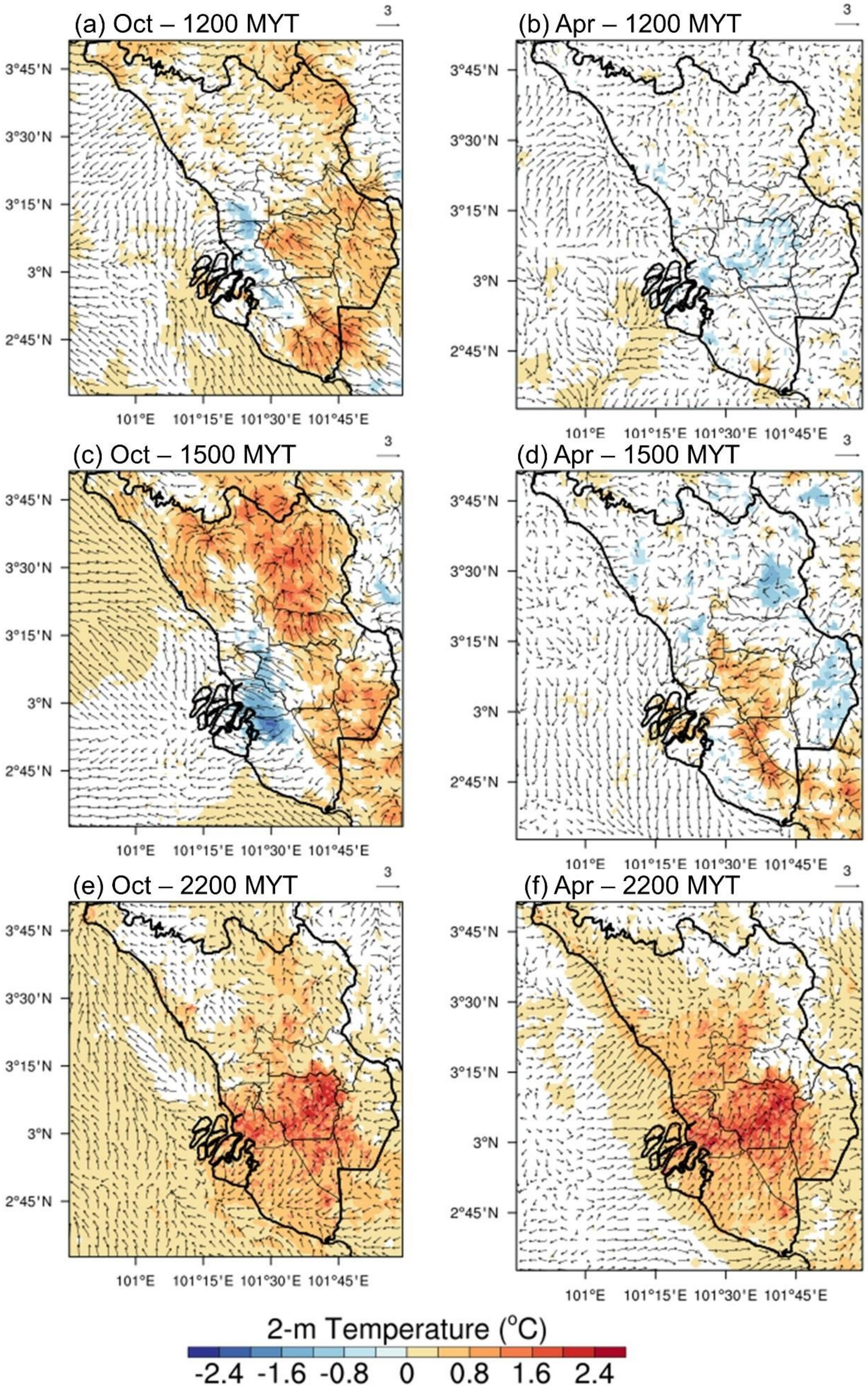

Figure 5.3: Spatial difference of T2 (°C) and uv10 vector (ms^{-1}) with noURB case at (a)(b) 1200 MYT, (c)(d) 1500 MYT, (e)(f) 2200 MYT for October (left panels) and April (right panels). Diagram masks out less significant thermal response between -0.5 °C and 0.05 °C.

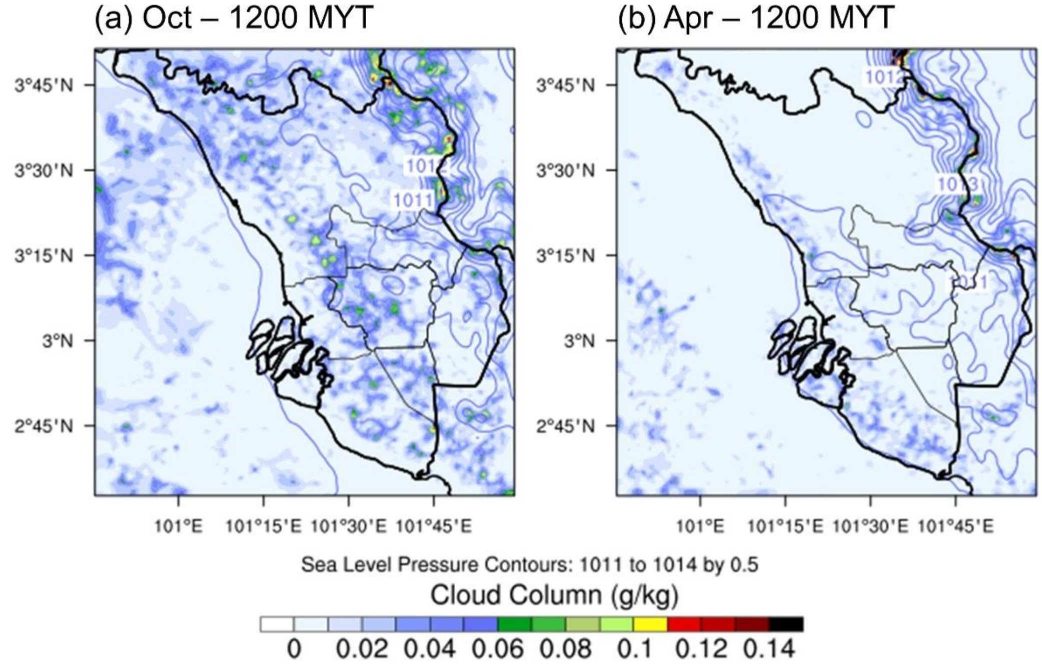

Figure 5.4: Hourly Averaged Total Cloud Column (g/kg) and SLP (hPa) for noURB case at 1200 MYT for (a) October and (b) April.

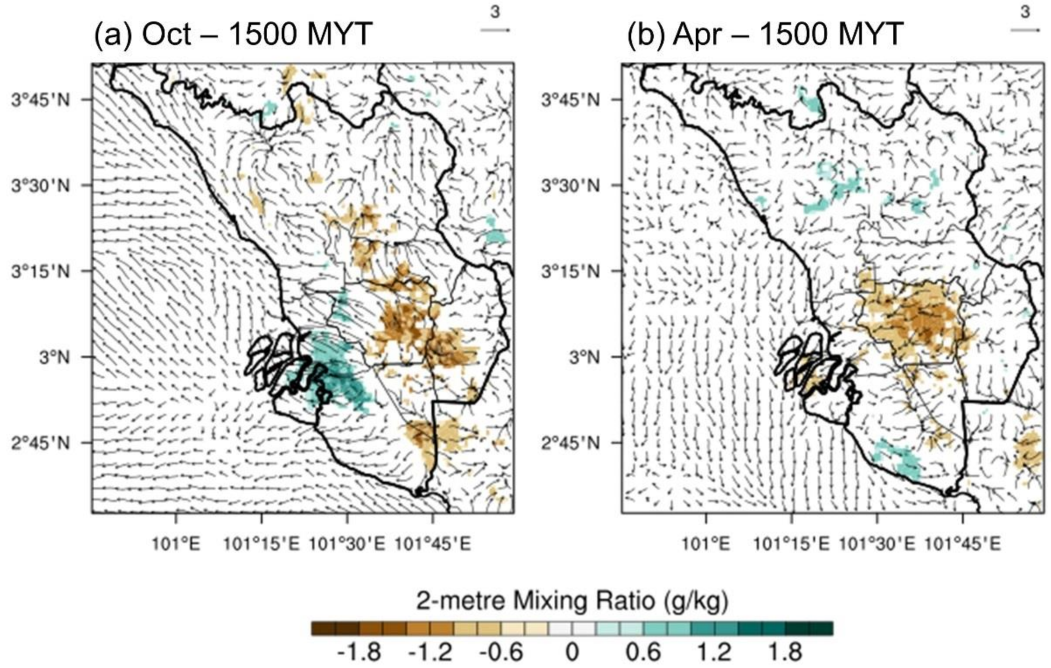

Figure 5.5: Spatial difference of 2-meter mixing ratio (g/kg) and uv10 vector (ms^{-1}) with noURB case for (a) October at 1500 MYT, (b) April at 1500 MYT. Diagram masks out less significant mixing ratio response between -0.5 g/kg and 0.5 g/kg.

5.3.3 Sea-land breeze and orographic breeze circulation

The vertical dynamics of local climatic circulation is investigated through the cross-sectional profile (AA') that cut perpendicularly across the sea surface, urban and the inland elevated ground as illustrated in Figure 4.1. In this context, the influence of synoptic forcing on the local circulation is only accounted for the portion which is orientated to the coastal breeze. Therefore, despite the strong synoptic forcing in October, the GKL region experiences weak synoptic flow which orientates with the sea breeze (SBOS) as seen in Figure 2.1a. Such condition is conducive for the formation of weak sea breeze front (SBF). The cold and dense sea breeze that pushes below the warm air over the land is lifted the latter and creates a convergence zone at the SBF. It is usually the frontal boundary where the cloud is formed. Conversely, the weak synoptic condition (Figure 2.1b) in April is flowing on the direct opposite of the sea breeze flow on the 850 hPa level, but not sufficiently strong to prevent the formation of sea breeze as discussed below. This thereby forms a strong SBF condition.

October

At 1300 MYT, the sea breeze is strengthened from 3.08 ms^{-1} (noURB) to 3.97 ms^{-1} by the confluence region created near the heated urban surface as shown in Figure 5.6. The stagnation of sea breeze at 1400 MYT is equally observed in noURB hence it could not be accounted as the effect of urbanization as in the previous studies [*Freitas et al.*, 2006; *Chen et al.*, 2011a]. During the day, the orographic factor is ruled out for the stagnation because the up-slope breeze which flows in the same direction with the sea breeze usually enhances the latter [*Ohashi and Kida*, 2002]. Therefore, the role of SBOS which counters the inland passage of sea breeze and comes into the picture. It is further elaborated in the following text. At 1500MYT, a large amount of moisture is carried into the upwind side of the urban in Figure 5.7, explaining the extra wetness near the coast as seen in Figure

5.5. The sea breeze has sustained inland for an hour longer until 1800 MYT for urbanization case. Subsequently at 1900 MYT, weaker cold air mass from the mountain top moves downhill over the urban region, parallel with the land breezes that flow towards the Straits of Malacca. The down-slope breezes are weakened by urban surface drag and also the weaker night inversion formed as a result of urban heating. This is a typical nocturnal phenomenon observed due to urbanization [*Giovannini et al.*, 2013; *Li et al.*, 2013b; *Kang et al.*, 2014]. The weakening of land breeze as a result of urbanization is prone to the inland progression of air mass from the sea.

During the day (from 0800 MYT to 1800 MYT), it is noticed that urbanization enhances the large-scale horizontal advection of air mass on the upper layer from the sea towards the inland mountainous region well before the initiation of sea breeze at 0800 MYT. The weak SBOS is equally observed in the upper boundary layer (1.5 km to 5 km) with less than 2 ms^{-1} from the mountain region as shown in Figure 5.6. The SBF is lifted as high as 850 hPa, almost one time more than the noURB case. At 1300 MYT as shown in Figure 5.7, the intensive vertical turbulence generated by the city reduces the tendency of weak opposing SBOS on the hillside of urban. This is more favorable for sea breeze passage inland. The ability of urban-induced circulation to weaken the mountain breeze flowing in the opposite direction of the sea breeze is similarly observed in Beijing agglomeration [*Miao et al.*, 2015]. This agrees well with *Ji et al.* [2013] that found that days with weak SBOS is conducive to develop deeper SBF. Without the presence of urban region, the meeting of the sea breeze and opposing downhill wind systems leads to the intensification of vertical updraft of the sea breeze to stagnate on the upwind of urban. This is also clearly shown in Figure 5.7 at 1500 MYT. The all-day depression on the mountain east explains the higher tendency of urban-side flow to be drawn towards the east after the SBOS is weakened as shown in Figure 5.8. Thus, the connection of both wind systems are the collective contribution the mountain gap and urbanization under

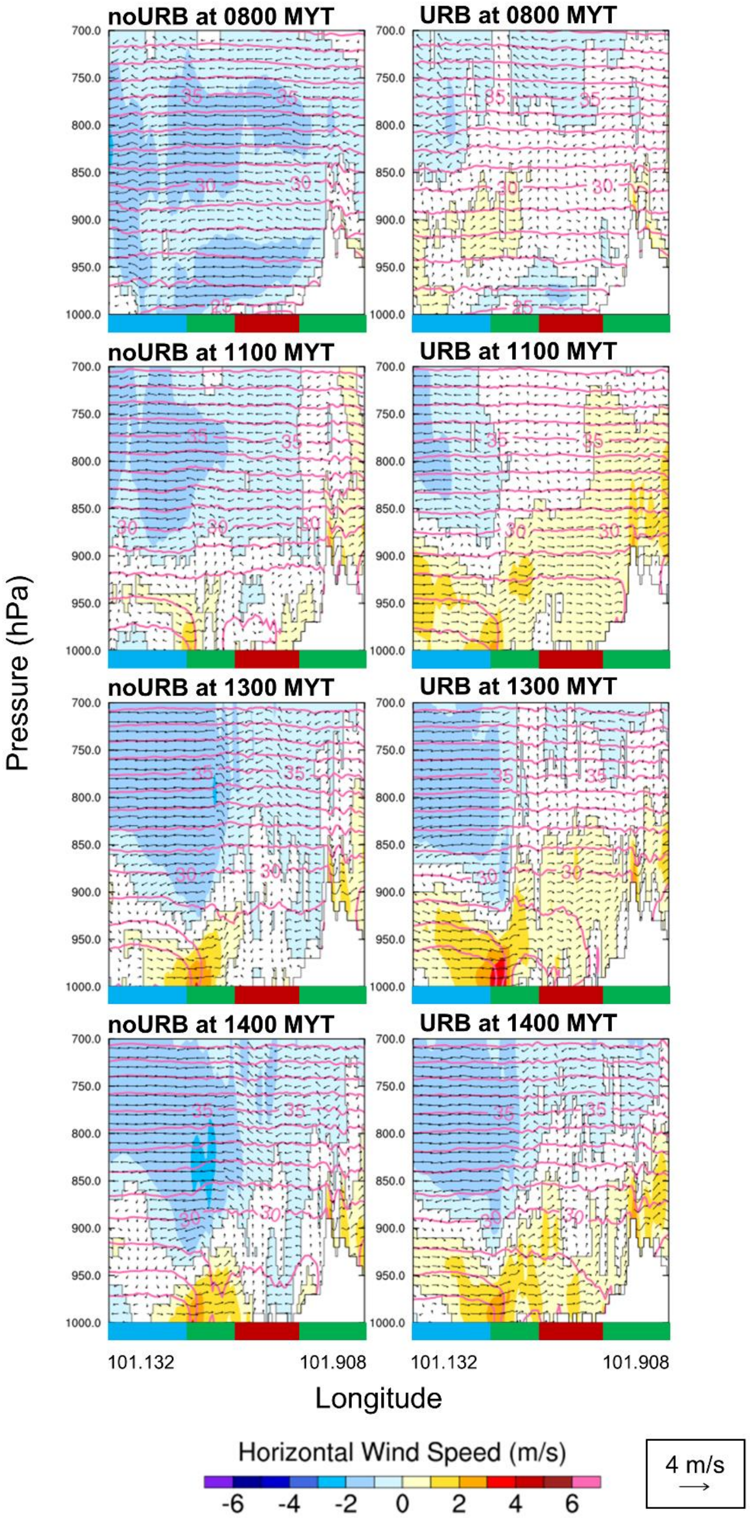

Figure 5.6: Vertical cross-sectional profile AA '(cross-sectional profile across the urban, shown in Figure 4.1) in October for horizontal wind (uv_h) at 1000 MYT, 1100 MYT, 1300 MYT, 1400 MYT, 1700 MYT, 1800 MYT, 1900 MYT, 2200 MYT. Horizontal wind displayed masks out less significant response between -0.25 ms^{-1} and 0.25 ms^{-1}. Wind vector represents the horizontal wind speed (uv_h) with annotation labelled in squared box. The pink contour represents the cross-sectional potential temperature profile. Corresponding left panels are noURB cases and right panels are URB cases. Color bar at the bottom indicates the land use type of the urbanization case along the longitude. Blue for water body, green for non-urban and red for urban.

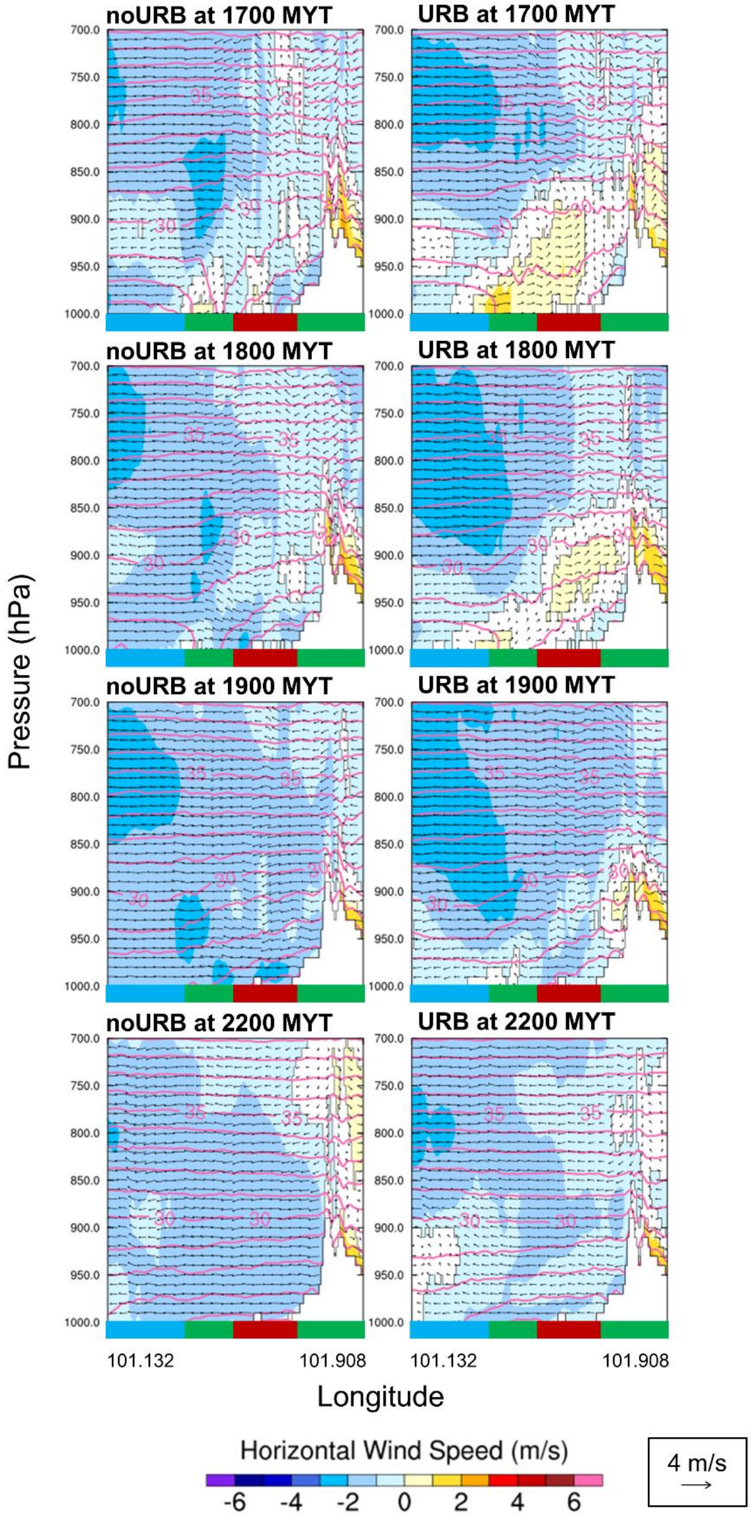

Figure 5.6 (cont.): October horizontal wind at 1700 MYT, 1800 MYT, 1900 MYT, 2200 MYT.

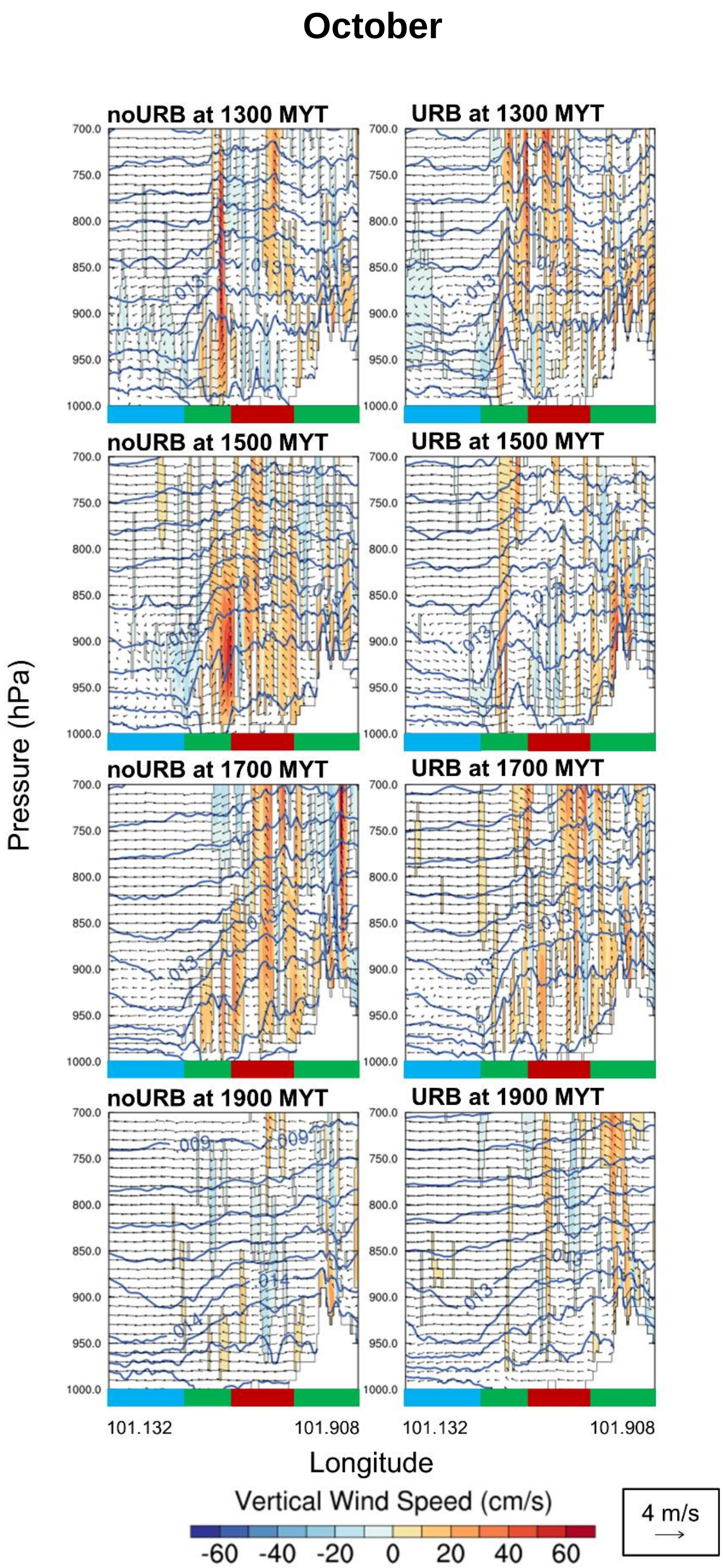

Figure 5.7: Vertical cross-sectional profile AA' for vertical wind speed (w) at 1300 MYT, 1500 MYT, 1700 MYT, 1900 MYT in October. w displayed masks out less significant response between -5.0 cms^{-1} and 5.0 cms^{-1}. The thick line blue contour indicates the water vapor mixing ratio. Refer to Figure 5.6 for detailed information.

April

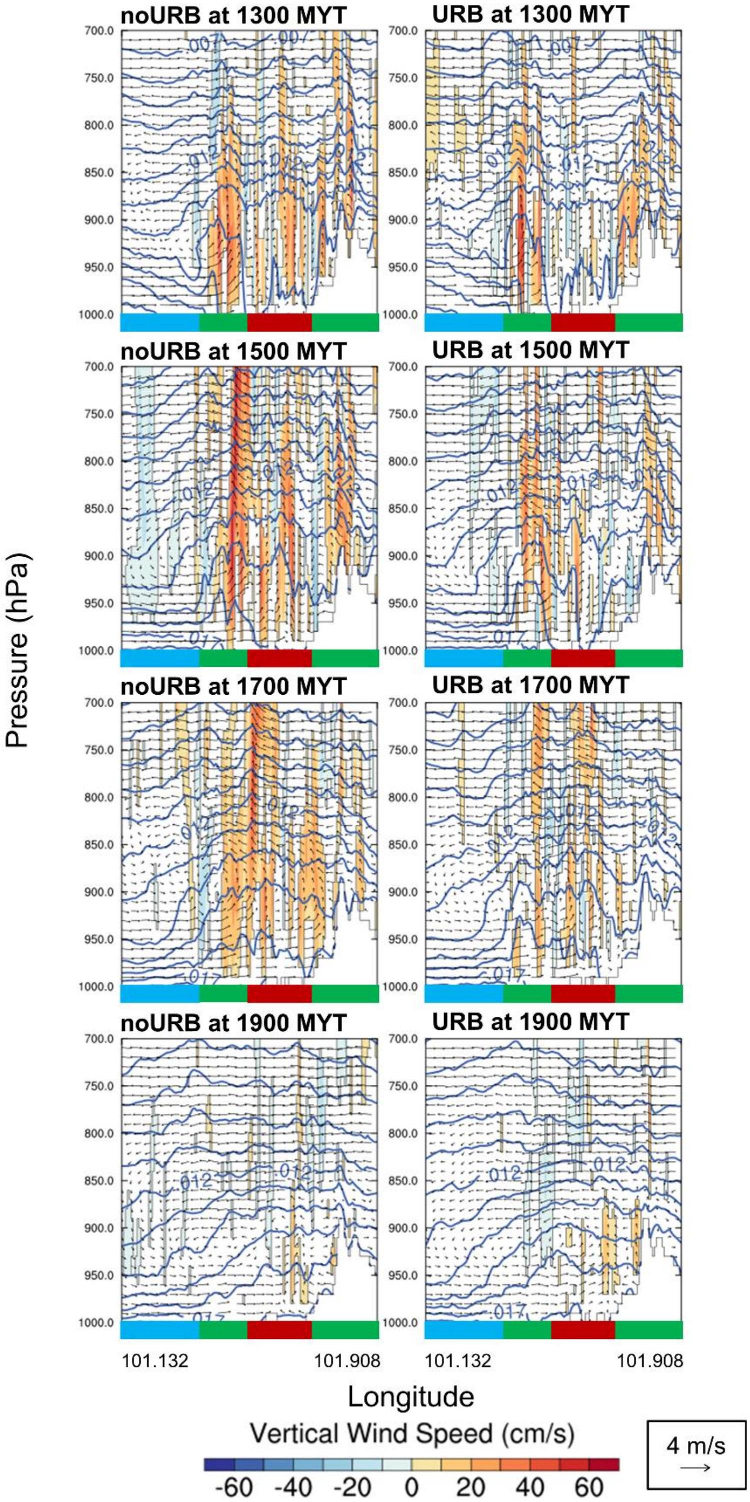

Figure 5.7 (cont.): Vertical cross-sectional profile AA' for April.

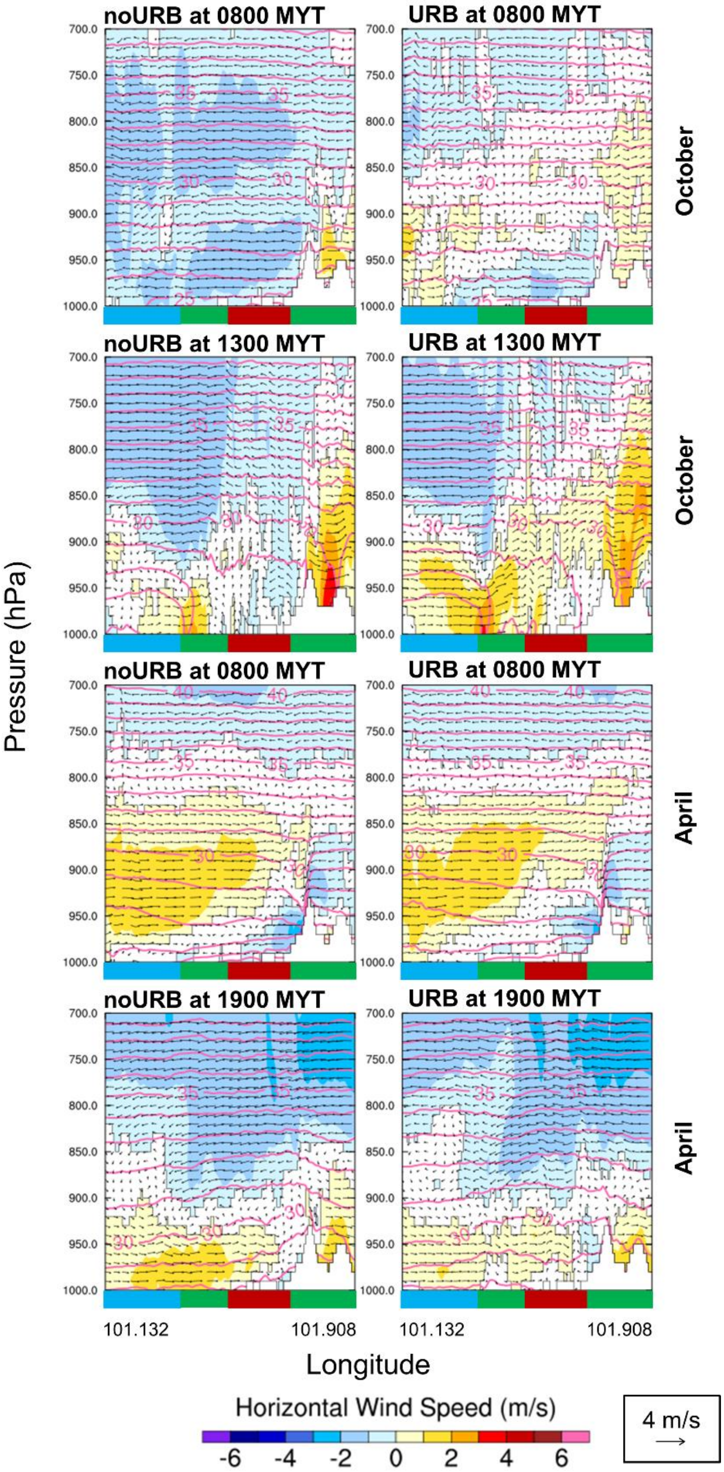

Figure 5.8: Vertical cross-sectional profile BB' (cross-sectional profile across the gap, shown in Figure 4.1) for uv_h of noURB at 0800 MYT, 1300 MYT in October and uv_h case at 0800 MYT, 1900 MYT in April. Refer to Figure 5.6 for detailed information.

weak SBOS condition. At this point, urban land weakens the hill-side SBOS and plays a critical role in bridging the two large scale wind movements from the east and west coast.

April

In April, the land breeze dissipates slightly later around 1000 MYT before sea breeze moves onshore at 1100 MYT, alongside with the up-slope mountain breezes shown in Figure 5.9. The sea breeze passage enters the urban cluster at 1500 MYT after accumulating sufficient strength (5.89 ms^{-1}). Without the drag imposed by the urban surface (noURB), the sea breezes grow stronger up to 6.65 ms^{-1} with a further 10.2 km penetration inland. This resonates well with the urban cool pool formed during the period which weakens the sea breeze strength. The down-slope breeze continues to flow towards the urban confluence zone while the core of the sea breeze remains around the upwind coastal region. It is well noted that similar to October, the nocturnal down-slope breeze and gap winds reduce in strength due to urbanization.

The vertical lifting of sea breeze is greatly suppressed under 850 hPa as shown in Figure 5.9. The unstable Kelvin-Helmholtz billow is also more likely to developed at the top of the sea breeze front under such circumstances [*Thompson et al.*, 2007; *Chemel and Sokhi*, 2012]. At night, a night clockwise circulation flow between the surface land breeze and upper layer inflow from the sea is induced where subsidence occurs near the Titiwangsa mountain region. This agrees well with the convergence of surface night flow along the Straits of Malacca during the calm inter-monsoon period [*Fujita et al.*, 2010]. Under the strong SBOS condition, April has shown a clear diurnal circulation of sea-land breeze in MC [*Hara et al.*, 2009].

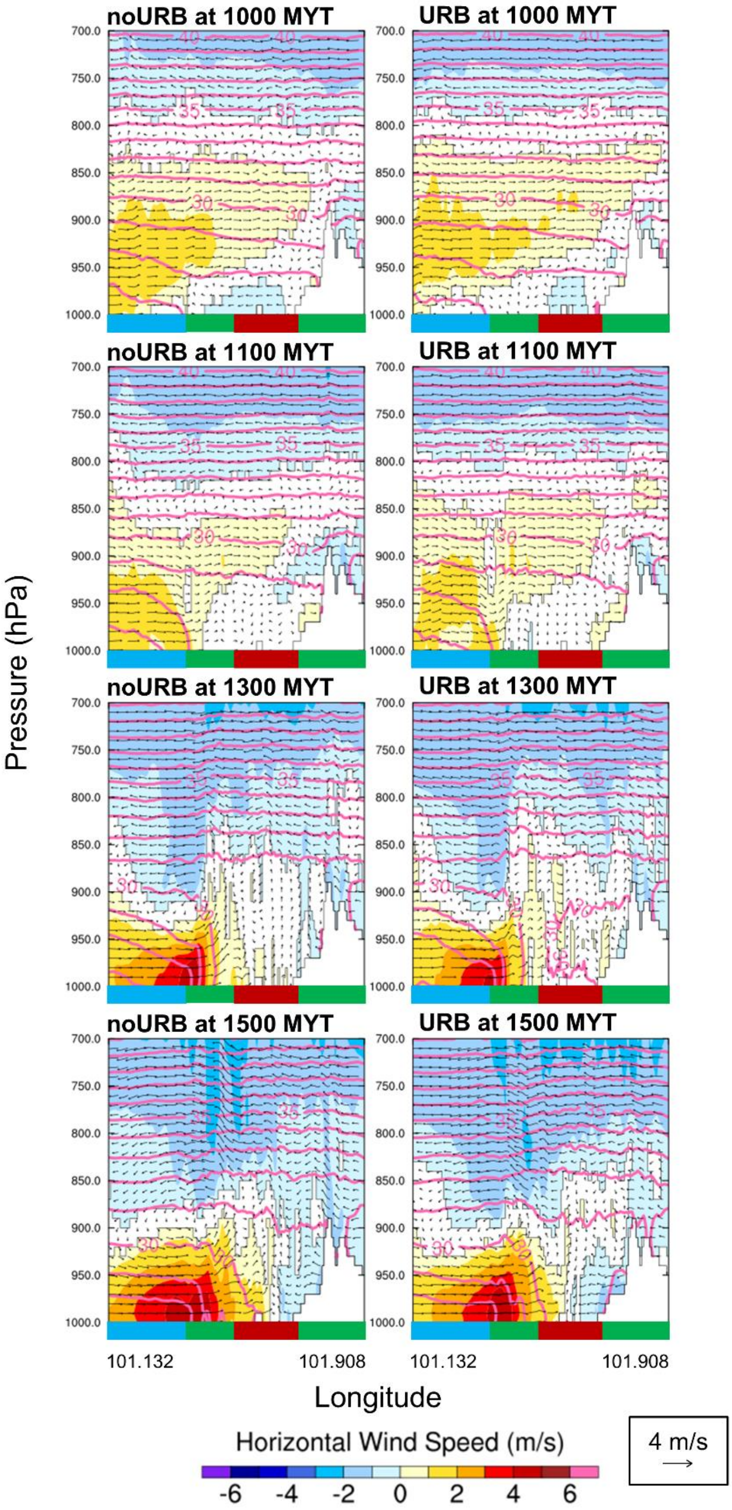

Figure 5.9: Same as Figure 5.6 but in April at 1000 MYT, 1100 MYT, 1300 MYT, 1500 MYT, 1700 MYT, 1800 MYT, 1900 MYT, 2200 MYT.

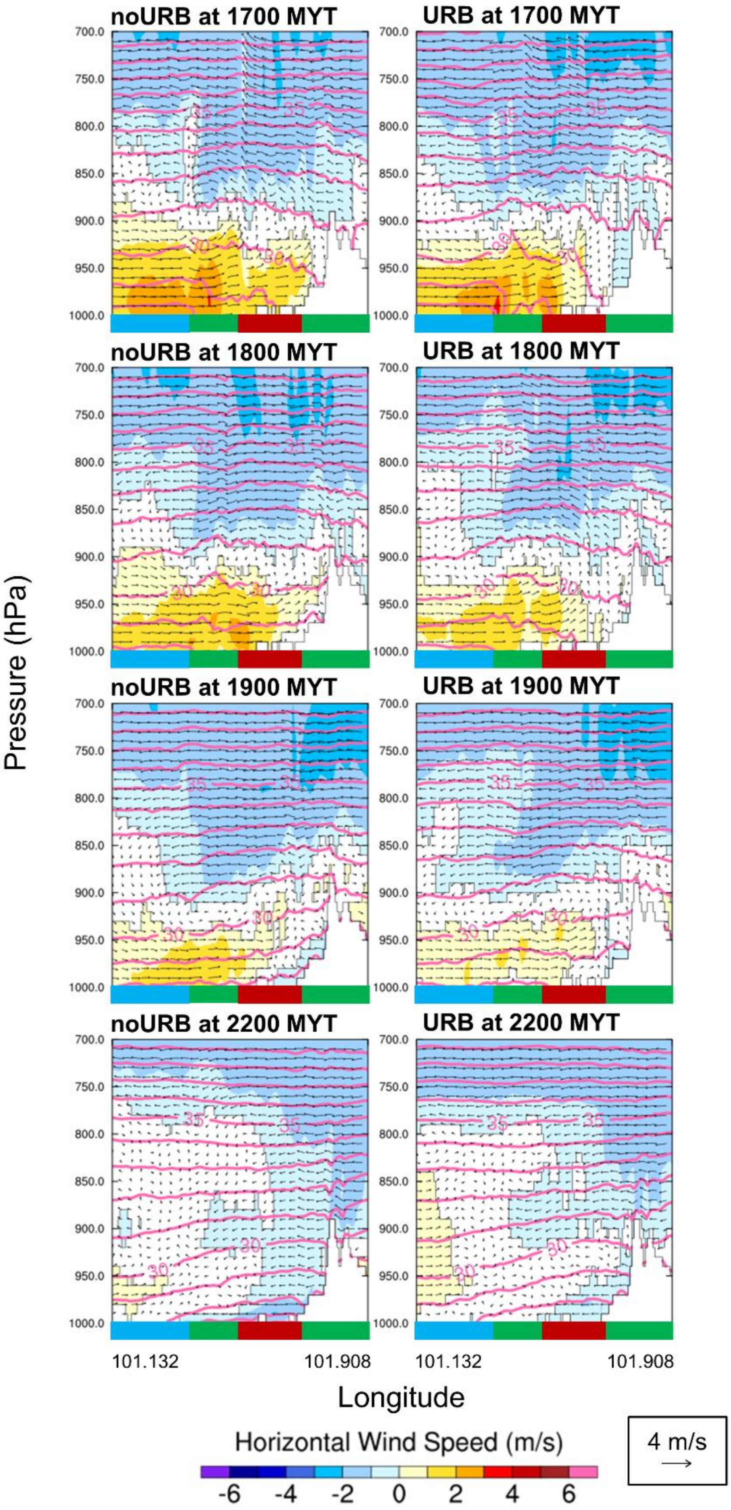

Figure 5.9 (cont.): April at 1700 MYT, 1800 MYT, 1900 MYT, 2200 MYT.

Under the calm and weak synoptic condition, the clear sky and scarce cloud coverage in April enhances the heating of the land surface and the subsequent growth of the sea breeze. The sea breeze flows at a greater magnitude with a prolonged duration (10 hours) compared to the October even without urbanization. It is because the lower pressure system is formed near the central of the GKL in April. Despite that, the UHI intensity becomes negative as a result of higher dissipation rate under clear sky in April. The urban cool pool in April has resisted the inflow of sea breeze. Conversely, the positively-induced UHI intensity increases the strength of the sea breeze flow in October. Taking account of the influence of SBOS, both months have similarly experience opposing flow but it is weaker in October than April. Under such circumstances, the strong UHI intensity becomes critical to weaken the opposing SBOS from the hillside in October. Subsequently, sea breeze gains sufficient momentum to push inland and enhances the horizontal advection of sea breeze passage and mountain breeze on a higher elevation height. On the other hand, the strong opposing SBOS in April enhances the gap winds and down-valley flows into the GKL region throughout the day as shown in Figure 5.8. The mountain breeze accelerates after 1500 MYT when the UHI starts to form in place of the cool pool. Therefore, the influence of urbanization on local flow circulation is subjected to both the cloud coverage and the strength and direction of SBOS.

5.3.4 Precipitation analysis

As discussed earlier, the existence of urban cluster enhances the interaction of sea breeze on the upper boundary layer connecting the sea and the mountain top in October. The moisture influx into the higher boundary layer on the windward side of the mountain suggests potential modification on the precipitation profile. The resulting inflow of moist air from the sea with the forced convection at the steep mountain slope is favorable for the formation of tropical convective raining [*Mori et al.*, 2004; *Sato and Kimura*, 2005] and also in the neighboring West Sumatra [*Sasaki et al.*, 2004]. Figure 5.10 hence shows a tendency to precipitate on the hilly side of the urban during the peak precipitation hours from 1700 MYT to 2000 MYT. Urbanization produces comparable total accumulated rainfall with noURB but the precipitation arrives two hours later as shown in Figure 5.10. This is in-sync with the delayed retreat of sea breeze and the subsequent initiation of the mountain breeze. The effect of urbanization on precipitation is found to be largely dependent on the urban influence on the evolution of moisture-rich sea breeze. Such delay is equally observed due to the prolonged effect of sea breeze in Greater Beijing Metropolitan Area [*Zhong and Yang*, 2015].

In April, the hourly total rainfall amount in Figure 5.10 notes that the rainfall is more concentrated on the upwind of urban. This is highly associated with confrontation of the sea breeze system and the mountain flow from the east during the strong sea breeze front month as shown in Figure 5.9. The gap between mountain range enhances the interaction of propagating wind systems from each side of the peninsula which initiates the thunderstorm in GKL during the calm synoptic condition [*Joseph et al.*, 2008; *Sow et al.*, 2011; *Teo et al.*, 2011]. The precipitation concentrates on the upwind region of urban due to the buoyancy lifting induced by the UHI at the late afternoon as shown in Figure 5.7. However, the weaker SBF during the day limits the amount of moisture influx into the plain, whereby diminishing the amount of rainfall produced as shown in Figure 5.10. Reduction of downdraft intensity might be also contributed by several other factors including the anthropogenic heat, type of urban surfaces, as well as the amount of cloud condensation nuclei especially in the polluted urban [*Kaufmann et al.*, 2007; *Han et al.*, 2014; *Sharma et al.*, 2016a]. However, this finding shows that urbanization does not necessarily induce precipitation as observed in many previous studies [*Thielen et al.*, 2000; *Dixon and Mote*, 2003; *Pathirana et al.*, 2014].

The result emphasizes the evolution of sea breeze movement on the precipitation profile [*Sakurai et al.*, 2005]. The presence of urban greatly modifies the sea breeze passage which has later reflected on the late afternoon precipitation pattern. However, it should be aware that the ability of simulation model to predict the short time-span convective precipitation is still limited and under continual assessment and improvement [*Bhatt et al.*, 2016].

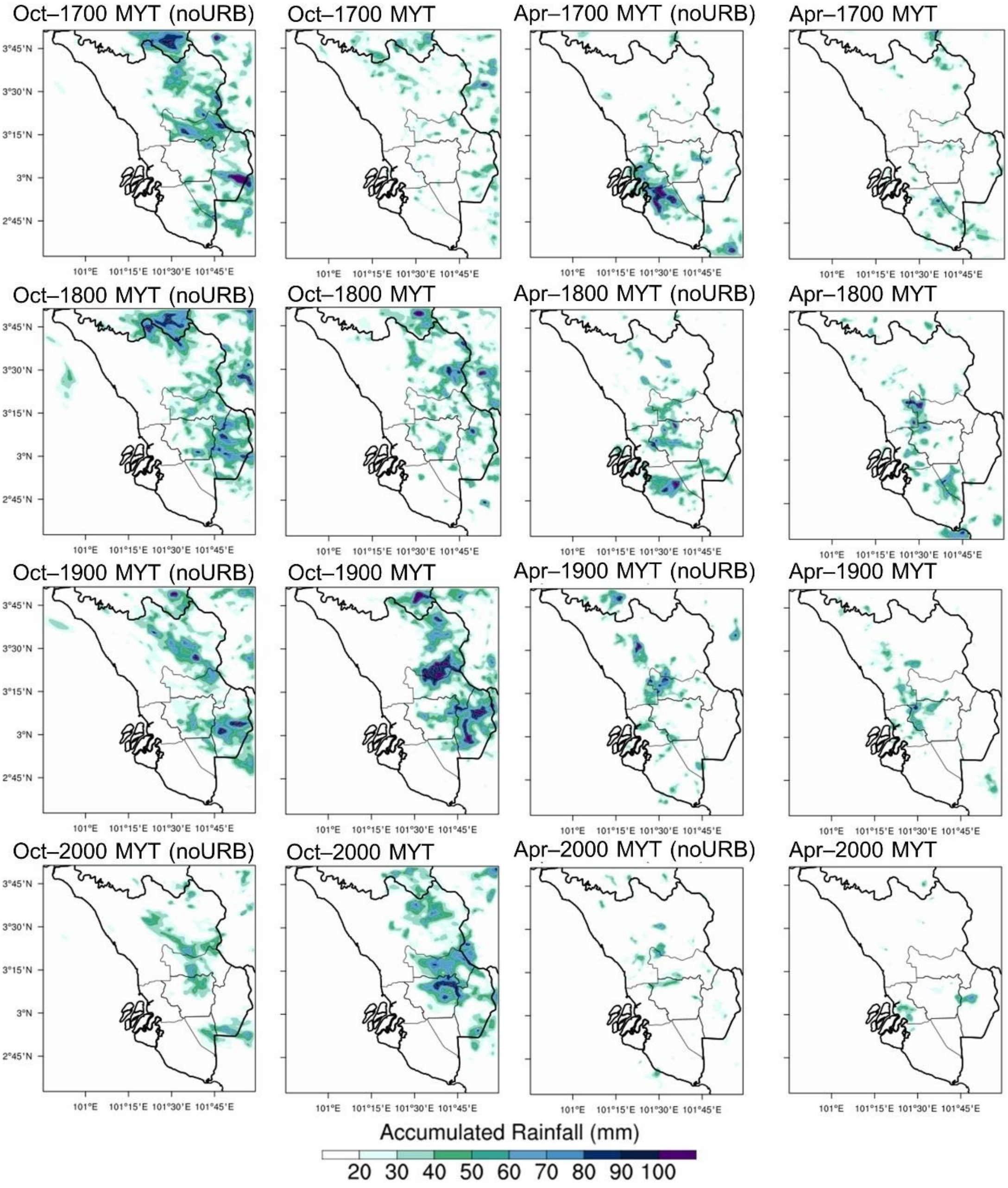

Figure 5.10: Rain water amount at 1700 MYT, 1800 MYT, 1900 MYT, 2000 MYT in October and April for noURB and urbanization cases.

5.4 Findings

The diurnal heating of urban surface is stronger at night than the day, recording around 1.4 °C in both months. Unlike the nocturnal UHI intensity that is rather consistent between the months, the daytime UHI intensity varies between October and April. Hot bias is observed in October while April month produces a colder surface in midday (0900 MYT-1400 MYT) compared to the noURB case. The negative UHI intensity in April during this period is mainly attributed to the higher heating rate of the vegetation cover influenced by the previous day precipitation. The differential heating rate is further enhanced in the clear sky condition of April. Later in 1500 MYT to 1900 MYT, larger positive UHI intensity developed in October carries more moisture to the upwind region of urban. This occurs concurrent to the initiation hours of late afternoon convective raining and therefore confirmed the association of urbanization with precipitation.

The local influence of urbanization generally depends on the strength of the urban heating and also SBOS. GKL experiences opposing synoptic flow which subsequently forms the SBF in both months. During the day, urban thermals tends to reduce the strength of the weak opposing SBOS in October. This enhances the magnitude of the sea breeze flow. The large inflow of moisture-bearing sea breeze towards the higher ground therefore generates larger amount of precipitation on the downwind of the urban region. On the other hand, the urban cool pool formed under the clear sky decelerates the sea breeze in April. The strong opposing SBOS in April further suppresses inland propagation of the sea breeze. Its accelerated core stalls over the upwind region before the urban where the convective precipitation occurs. The effect of urbanization on precipitation is hence found to be largely dependent on its influence on the evolution of moisture-rich sea breeze.

In April, the potential formation of Kelvin-Helmholtz billow under strong SBF condition. The SBF takes in the urban air at the front and is more likely to accumulate secondary pollutants such as ozone at the tail of the SBF [*Thompson et al.*, 2007; *Ji et al.*, 2013]. However, during the night, strong gap winds induced by the southwest flow continuously enters the urban region in April. This reveals that the region located near the saddle receives additional gap winds from the east on top of mountain breeze and therefore is better ventilated than October. The exit land breeze flow which responsible of the nocturnal air quality is enhanced in April while is impeded in October. Despite the conducive circulation flow, the formation of ozone is never a straightforward reaction. It involves the composition of air pollutant constituent to which determine its formation potential. Hence, this postulation of the effect of urbanization on the formation and transportation the local urban pollutant is elaborated in Chapter 6 by incorporating the online chemical driver (WRF-Chem).

CHAPTER 6: EFFECT OF URBANIZATION ON OZONE PRODUCTION AND TRANSPORTATION

6.1 Introduction

Ground ozone pollution is one of the major air quality problem in the case study site region [*Latif et al.*, 2012; *Banan et al.*, 2013]. The tropical region has a readily high amount of the biogenic VOC emitted from the vast evergreen forest, while rapid urbanization is boosting the amount of anthropogenic NO_X emitted from the urban. These ozone precursors are essential components that excite oxygen atom to form ozone. As discussed in Chapter 5, the UBL in GKL has become more stagnant near the urban core but rigorous near the urban fringe. Under such atmospheric environment ozone can be transported into or away from the populated urban, for either case, there is a high possibility for pollutant accumulation near the urban. This thereby modifies the atmospheric composition of the region.

In this chapter, the emission profile of local ozone and pollutants measured from the air quality monitoring stations is interpreted to comprehend the historical pollution condition in GKL. With the available data, the model performance to simulate the atmospheric chemical composition is verified. From which, the urban-induced changes of local weather and circulation pattern are subsequently studied to scrutinize the extent of featured urban environment contributes to the air quality issue. The objectives of the chapter include:

1. Analyses of the chronological pollutant level in GKL
2. Evaluation of the ability of WRF-Chem model to reproduce the atmospheric chemical composition
3. Investigation of the implication of urban-induced modification on local weather and circulation pattern on the ozone air quality in GKL

Basic ground ozone formation photochemical reaction is discussed in Section 6.2. The background pollutant level study during the period of study is analyzed to comprehend yearly and hourly change of the ground ozone level as well as its ozone precursors in Section 6.3. Section 6.4 compiles the details of simulation cases run including the set up and chemical emission inventories. Section 6.5 examines the application ability of WRF-Chem for the basic near-surface and vertical meteorological parameters as well as the air pollutants. With the comparison with noURB case, the effect of urbanization is scrutinized in Section 6.6 before settling upon the research findings of the chapter.

6.2 Ground ozone formation

Ozone formation is an intricate photochemistry chain reaction [*Sillman*, 1999; *Crutzen*, 2004; *Jacobson*, 2005]. The high temperature combustion of automobile and industrial heating turns nitrogen gas (N_2) into NO, which the conversion between NO and its oxidized product NO_2 provides the main reactant for ozone formation. Under the presence of sunlight, NO_2 is photolyzed into NO and oxygen atom (O). The oxygen atom quickly reacts with the oxygen molecule (O_2) to form the ozone where M is the gas particles, usually N_2 or O_2 that carries away energy released by the reaction,

Equation 6-1: Photolysis of NO$_2$ $\boldsymbol{NO_2 + h\nu \rightarrow NO + O}$

Equation 6-2: Generation of O$_3$ $\boldsymbol{O + O_2 + M \rightarrow O_3 + M}$

The reaction of NO and strong oxidizing agent, O_3 produced in the above two equations has completed the null cycle of ozone and its reactants without concentration change,

Equation 6-3: NO oxidation $\boldsymbol{NO + O_3 \rightarrow NO_2 + O_2}$

With the absence of dissociation energy for photolysis, the ozone is continually depleted during the night due to the lack of oxygen atom. The other scenario for the removal of O_3 is the excessive presence of NO, especially during winter or in the heavily industrialized area, this is known as NO_x titration [*Sillman*, 1999]. When other oxidizing reagents and agents, known as ozone precursors are involved in the oxidation of NO, in place of ozone, it supplies an alternative reaction to enhance ozone production. These precursors are commonly reactive peroxy radicals produced from long chain hydrocarbon (RH) or CO. The alkyl radical that is first formed as intermediate product after reaction with the hydroxyl radical then quickly reacts with O_2 to produce the peroxy radicals,

Equation 6-4: Production of organic peroxy radical $\boldsymbol{RH + OH \rightarrow \overset{O_2}{\rightarrow} RO_2 + H_2O}$

Equation 6-5: Production of hydroperoxy radical $\boldsymbol{CO + OH \rightarrow \overset{O_2}{\rightarrow} HO_2 + CO_2}$

These peroxy radicals then participate in the oxidation process of NO to NO_2, as

Equation 6-6: Oxidation of NO (2) $\boldsymbol{RO_2 + NO \rightarrow \overset{O_2}{\rightarrow} R'CHO + HO_2 + NO_2}$

Equation 6-7: Oxidation of NO (3) $\boldsymbol{HO_2 + NO \rightarrow \overset{O_2}{\rightarrow} OH + NO_2}$

From which the increased amount of NO_2 further drives Equation 6-1. Hence, the number of NO_2 available subsequently determines the amount of excited oxygen atom (O) available for ozone production after undergoing photolysis. Due to the complication of the mechanism, several factors are used to evaluate the ozone productivity. Amongst which, the VOC and NO_x ratio is the most popular seeing that it represents the interaction of the natural and the anthropogenic factors respectively. There is an optimum range of VOC/NO_x for the production of ozone which subjected to the reactivity of oxidation species such as OH, HO_2 and RO_2 [*Bowman and Seinfeld*, 1994]. Urbanized region riches with anthropogenic emissions (NO_x) in general has a lower VOC/NO_x ratio that terminates the photo-dissociation reaction [Equation 6-1] with RO_2 as a limiting factor [Equation 6-6]. Inversely, the VOC/NO_x in rural area is usually larger than 15 and absence of anthropogenic emission inhibits the photo-dissociation process [*Calfapietra et al.*, 2013]. Due to the relatively large amount of BVOC present in the troposphere naturally, most of the region is NO_x-sensitive (O_3 amount decreases with decreasing NO_x) or eventually turned into NO_x-sensitive after allowing certain period of photochemical aging [*Sillman*, 1999]. Therefore, the interaction of natural and man-made air pollutants fosters the interest to observe the ozone formation in the tropical urban region that are surrounded with high BVOC emitting forest. The interaction of both essential aerosol components for O_3 formation is the key to the study the O_3 concentration [*Bao et al.*, 2009; *Geng et al.*, 2011; *Kim et al.*, 2013]. In consideration of ozone chemistry, CH_4 which has a lower O_3 reactivity is not accounted in the RH groups [*Chameides et al.*, 1992]. From this point onwards it is known as the non-methane hydrocarbon (NMHC) or VOC.

6.3 Background study of measured air quality data

The hourly diurnal pollutant profile during the two months are similar as shown in Figure 6.1. April has an overall higher pollution level compared to October, for instance hourly ozone level in April is 42.9±15.4 ppbv while October records 38.0±9.8 ppbv. The seasonally variation of pollutant level is closely associated to the daily maximum temperature and wind profile [*Camalier et al.*, 2007; *Ooka et al.*, 2011; *Pugliese et al.*, 2014]. As pointed out in background weather (see Section 2.2), the atmospheric condition in GKL region is hotter but mainly dominated by weak wind with less defined direction. This renders the month more conducive to the accumulation of pollutant; this agrees with similar studies which observed higher O_3 concentration during the spring period in GKL [*Latif et al.*, 2012]. The concentration of photochemical pollutant, O_3 is at its maximum level during the day (hourly ozone: 1400-1500 MYT; 8-hourly ozone: 1100-1200 MYT) and quickly depletes in the evening.

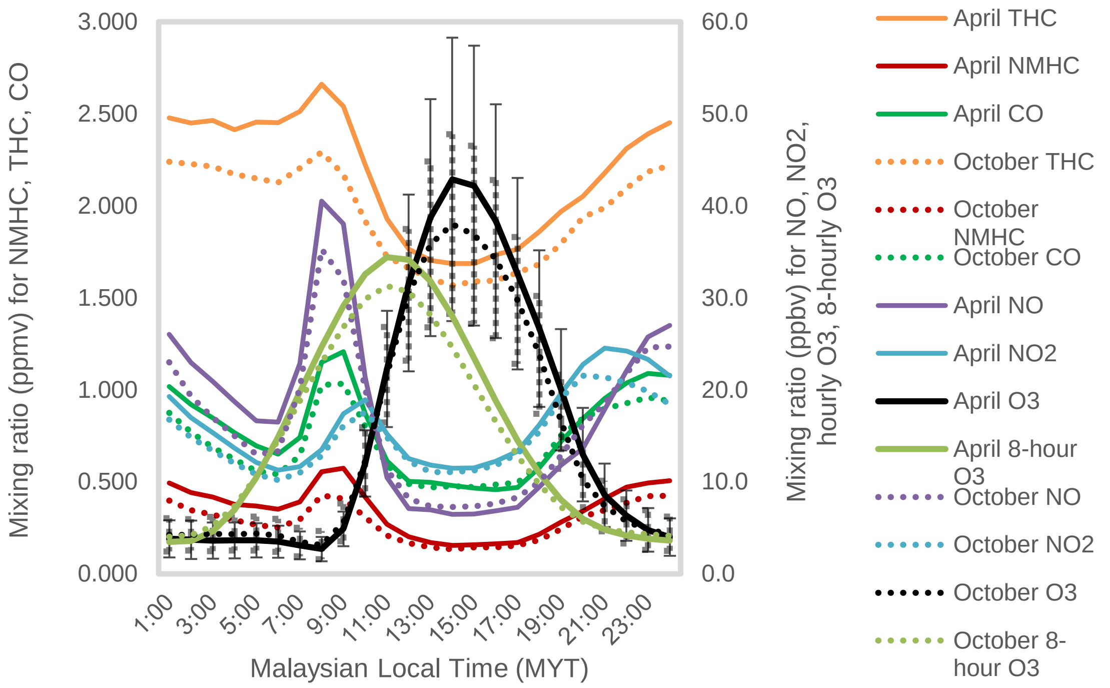

Figure 6.1: Diurnal variation of air pollutant for April and October months averaged for year 1999, 2003, 2007, 2011 and 2014.

Dissimilar with the ozone concentration which peaks during the day, the ozone precursors including NO, CO, THC, NMHC all record a sharp morning peak (0800-0900 MYT) and an evening peak after 2200 MYT. The double peaks are ubiquitously observed in other cities [*Pudasainee et al.*, 2006; *Han et al.*, 2011; *Ryu et al.*, 2013b]. The peaks of CO, THC and NMHC shows the emissions from incomplete combustion cycle of engines during working rush hours of the city. The oxidized products of the latter, HO_2 and RO_2 are not readily recorded through the measurement, but they contribute immensely as a strong driving agent for the NO to NO_2 oxidizing process. At this point, the multi-generation photochemical reaction of O_3 produces a delayed surge of NO_2 which later supplies the activated oxygen atom as raw material for O_3 formation. The NO_2 pollutant levels greatly plunge at the noon time owing to the reactive photochemical reaction and also the noontime heat convection enhances the pollution dilution [*Ooka et al.*, 2011; *Ryu et al.*, 2013b]. The evening peak of NO_2 directly reflects the absence of solar radiation inhibits the photolysis of the gas species. The concentrated amount of NO_2 then induces the reduction reaction which convert NO_2 back to the initial NO form, which culminates at 0000 MYT.

The pollution level for month April is studied to identify the chronological change for more than a decade in Figure 6.2. The stronger wind flow in 1999 (see Figure 6.2b) correlates well to the lower pollutant concentration recorded, namely O_3, NO_2 and NMHC. Conversely, year 2003 with relatively low wind speed corresponds to the higher pollutant concentration of NO, NO_2 and NMHC. Despite the surge of these ozone precursors, the level of O_3 is not exceptionally higher in 2003 compared to the remaining years. It is therefore understood that wind speed has a direct influence on the concentration of the primary pollutants. O_3 concentration, as a secondary pollutant is more variant and dependent on the atmospheric composition of ozone precursors. The 2-meter temperature is consistent throughout the years without showing clear rising trend nor correlation between the parameters, hence its contribution will later be inspected in the simulated study.

The morning rush-hour spike of NO is observed every year but most apparent in 2003 with notable rise in nocturnal concentration. The NO level shows clear reduction around 30 ppbv in 2007 and resumes by another 10 ppbv in 2011 before it rebounds in 2014. However, it is observed that the reduction of the anthropogenic pollutant does not significantly reduce the O_3 level, but it increases greatly in year 2011. The NO_2/NO ratio depicted in Figure 6.2e is used to indicate the photolysis potential of NO_x to produce oxygen atom to fuel O_3 generation. It is an simple indicator of oxidant amount available for ozone production process [*Clappa and Jenkin*, 2001; *Han et al.*, 2011]. The NO_2/NO level is lower than unity in the morning due to the morning surge of NO. The ratio increases during the day when the conversion rate to NO_2 is highest and then maintains until the evening around 1800 to 2000 MYT, varies between the years.

(a) Hourly O3

(b) Wind speed

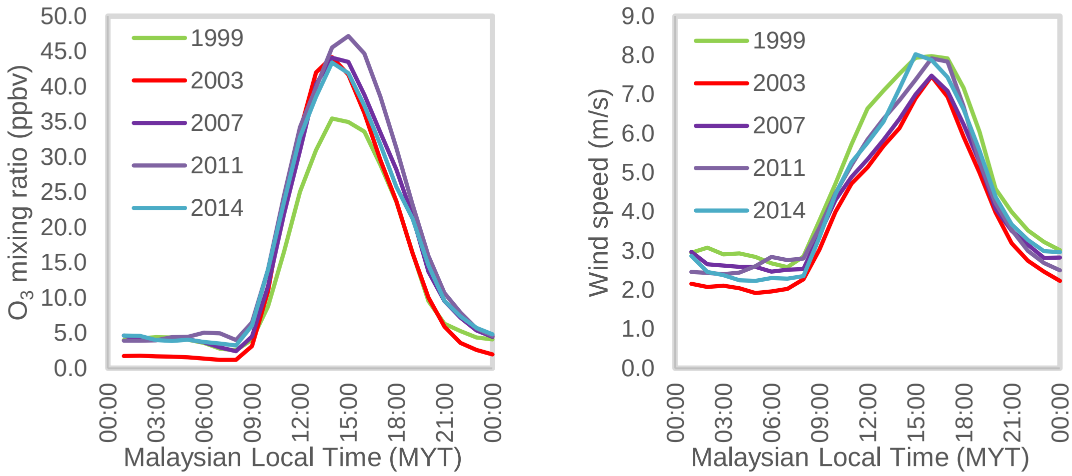

(c) NO

(d) NO2

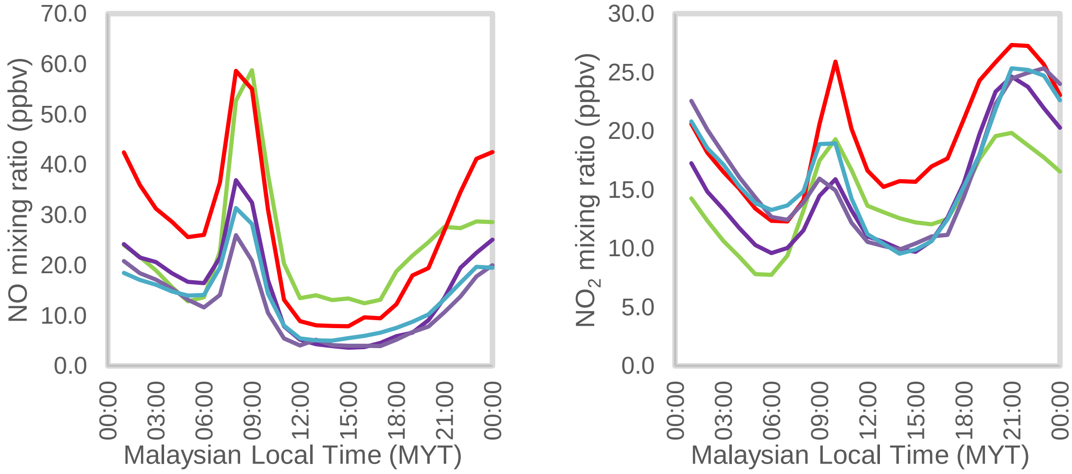

(e) NO2/NO

(f) NMHC

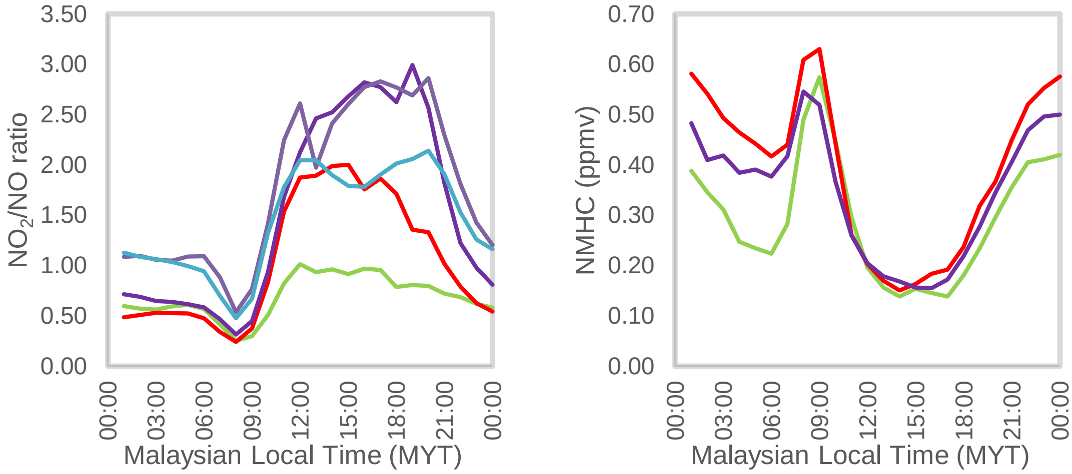

Figure 6.2: Diurnal hourly averaged (a) O_3, (b) uv10, (c) NO, (d) NO_2, (e) NO_2/NO, (f) NMHC for 1999, 2003, 2007, 2011, 2014 in April month

This correlates well with the higher ozone level recorded during the day. The higher value of NO_2/NO observed in 2007 and 2011 during the day generates greater level of oxidant and hence the growth of O_3 level. Inversely, it is applied to the lowest daytime O_3 level in 1999. Therefore, despite the highest value of individual NO and NO_2 species recorded in 2003, the ozone level is not exceptionally higher due to the moderate NO_2/NO ratio.

The ratio of NO_x to NMHC is investigated to identify the sensitivity regime of the formation of O_3. O_3 concentration increases linearly with NO_x and NMHC when they present at low concentration respectively. However, the ozone production reduces with the increase of the individual species. Hence, the local maxima of ozone occur when the atmospheric composition of NO_x and NMHC balances out. From which, the region above the margin belongs to the NMHC-sensitive and the region below falls under the NO_x-sensitive region. Best-fitted line for the NO_x against NMHC shows the general distribution of the atmospheric composition the O_3, from which the slope is compared with the typical maxima margin (NO_x/NHMC) in United Stated (0.105, [*Milford et al.*, 1994]). Due to the discontinued operation of NMHC measuring device after 2007, the analysis is only conducted for year 1999, 2003 and 2007 (Table 2.6). The comparison is performed during highest O_3 formation rate and NO_2/NO ratio from 1100-1900 MYT. It is found that the NO_x/NHMC ratio of the measured data decreases from 0.146 (year 1999), 0.119 (year 2003) to 0.076 (year 2007) in Figure 6.3. It also shows that the higher O_3 concentration (>50 ppb) gradually shifts to the NO_x-sensitive regime from 1999 to 2007. It resonates with above finding on the positive influence of NO_2/NO ratio during the high ozone years. Such circumstance suggests that the O_3 formation turns sensitive to the increment of NO_x due to the expansion and maturity of palm plantation that contributes to larger atmospheric composition of ISOP [*Silva et al.*, 2016]. Such circumstance is no longer limited to the forest in Borneo [*Hewitt et al.*, 2009] but also in the urban. Therefore, the GKL region is prone to the O_3 level surge if the anthropogenic pollutant level, especially NO_x levels increases in the coming years. Simulation is subsequently run to verify the potential possibility of these parameters to be enhanced by the surface forcing of the urbanization effect, and hence the formation of ground O_3.

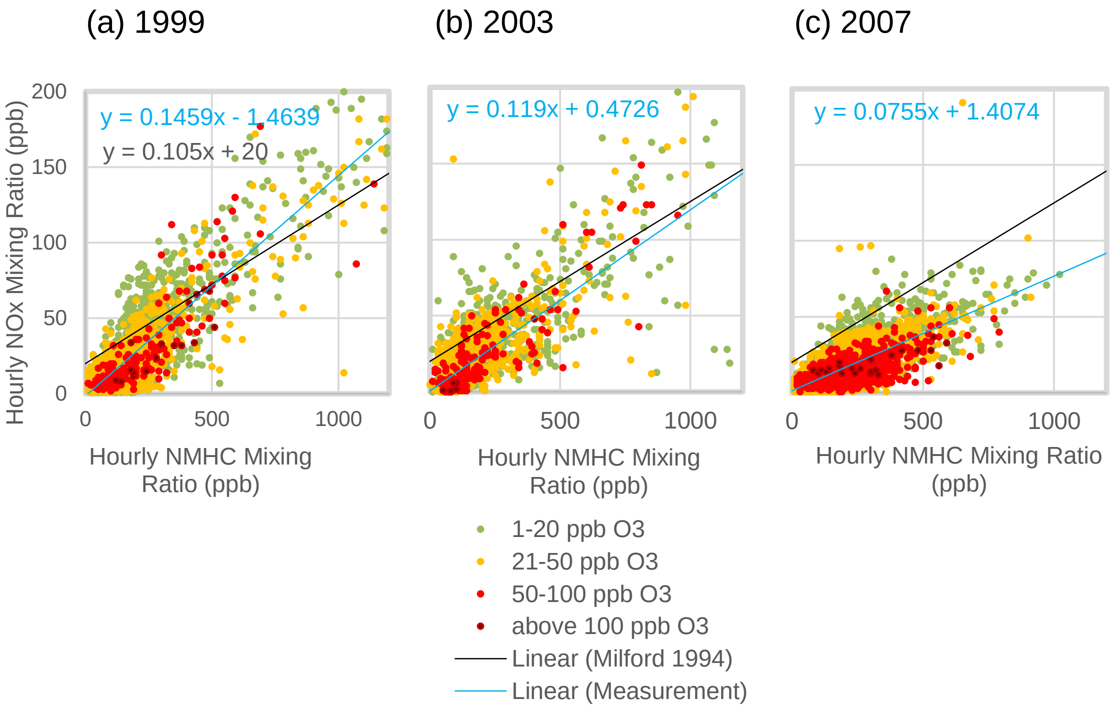

Figure 6.3: Concentration distribution of O_3 in the NMHC and NO_x xy-plot from 1100 to 1900 MYT in April and October of (a) 1999, (b) 2003, (c) 2007.

6.4 Model physics and experiment design

WRF-ARW in combination with the online chemistry model, typically known as WRF-Chem, is deployed to study the implication of urbanization on the regional air composition. Incorporation of chemical driver requires higher computation power, hence the simulation period of WRF-Chem is reduced compared to the two previous simulation. This simulation still starts at 1^{st} day for April and October 2003 but only last for 10 days. The first day result serves as the spin-up period for steady throughout. The domain setting similar to Figure 2.4 is adopted but owing to the limitation of the fine resolution chemical boundary data, the simulation is only nested down to the third domain (d03) with 3km resolution. Basic physics settings in Section 2.3.3 is used for the meteorological driver. The updated land use (LN3) tested in Chapter 3 is used as the input land use map while the MYJ PBL scheme with modified MZT roughness length evaluated in Chapter 4 is used as the PBL scheme.

Two anthropogenic inventories are used REanalysis of TROpospheric (RETRO)[5], a global emission dataset that provide monthly chemical composition from 1960 to 2000. 24 species of emissions are categorized into groups of anthropogenic and biomass emissions and are available at 0.5° x 0.5° [*Schultz et al.*, 2007]. Emission Database for Global Atmospheric Research (EDGAR) version 4.2[6] contains global inventory of 8 pollutants which are divided into anthropogenic and biomass burning groups. MOZART-4[7] is used as the chemical boundary condition with anthropogenic and fire emissions [*Emmons et al.*, 2010]. It is available at 1.9° x 2.5° horizontal resolution at 56 vertical levels up to 2 hPa. The 6-hourly data used is generated from the GEOS-5 lateral weather of 2007. Although it is available in 0.1° x 0.1° with data from 1970 to 2008, the data is only supplied annually. RADM2 is used as gas chemistry packages [*Stockwell et al.*, 1990], MADE/SORGAM as aerosol size distribution and chemistry packages to include the anthropogenic emissions. MADE is chosen for usage due to its reasonable particle size sorting scheme and flexibility in including additional schemes. SORGAM is able to predicts the POA (Primary Organic Aerosols) at comparably low computational cost [*Ahmadov et al.*, 2012; *Athanasopoulou et al.*, 2013]. Model for Emissions of Gases and Aerosols from Nature (MEGAN) biogenic emission option is selected to execute the biogenic driver with online feedback. The global biogenic emissions database is obtained

---

[5] RETRO data available in http://accent.aero.jussieu.fr/RETRO_metadata.php

[6] EDGAR V4 data available in http://edgar.jrc.ec.europa.eu/overview.php?v=431

[7] MOZART-4 and MEGAN data available in https://www.acom.ucar.edu/wrf-chem/download.shtml

from MEGAN Community Data Portal (CDP)[7]. The 30 sec x 30 sec inventory contains the information of emission factors (EF), leaf area index (LAI), plant functional types (PFT) based on year 2000 and MEGAN calculation algorithm [*Guenther et al.*, 2006]. noURB case is set up with 2003 to investigate the potential changes caused by urbanization. The experiment is set up as shown in Table 6.1.

6.5 Model Evaluation

The near-surface meteorological data is verified on hourly basis against the measured data from 8 weather stations. The verification through statistical errors in Table 6.2 records two-month average of error magnitude for T2 around 1.8 °C MAE and 2.7 °C RMSE while RH2 around 8.7 % MAE and 11.6 % RMSE. Compared to the model without inclusion of chemical driver (Table 4.2), inaccuracies increase for T2 by 1 °C RMSE and uv10 by 2.7 ms^{-1} RMSE. Compare to Chapter 4, the integration of chemical module creates higher uncertainty to the near-surface model result. It has unable to meet the proposed error benchmark. The radiosonde sounding station (ST6) supplies verification data for the vertical boundary weather profile. The vertical parameters similarly predict better during the month of October than April. This is largely due to the smaller influence of synoptic flow, from which April is calmer than the months of October, as elaborated in Chapter 4. The model generally predicts a good agreement of the potential temperature, mixing ratio and wind speed on the vertical scale.

Table 6.1: Experiment design for WRF-Chem

Case ID	**Land use map**	**Year**	**Month**
Apr_chem	Existing map (URB)	2003	April
Oct_chem			October
Apr_chem_noURB	No urban map (noURB)		April
Oct_chem _noURB			October
Parameters	**Value/ Option**	**Parameters**	**Value/ Option**
Analyzed period (One-day spin up)	9 days (2nd April/Oct 2003 0800 MYT – 10th April/Oct 2003 0800 MYT)	Vertical levels	37 vertical eta levels. 15 level for bottom 12 km
Domain setting	1st (d01): 27 km (110 x 100) Entire Malaysia	Chemical boundary data	MOZART
	2nd (d02): 9 km (100x 103) Malay Peninsula	Anthropogenic emission inventories	RETRO, EDGAR
	3rd (d03): 3 km (100 x 100) West Malay Peninsula	Biogenic emission inventory	MEGAN CDP
Lateral boundary data	ERA-interim 6-hourly reanalysis data	Boundary layer schemes	MYJ PBL scheme and Eta MM5 surface layer
Land surface model	Noah LSM coupled	Urban canopy model	Single-layer UCM with locally calibrated urban parameters
Cumulus scheme	Betts-Miller-Janjić (enabled for d01 and d02)	Microphysics scheme	Purdue Lin single moment
Radiation scheme	RRTMG long wave and short wave schemes	Gas chemistry mechanism	RADM2
Aerosol size distribution and chemistry mechanism	MADE/SORGAM	Biogenic gas chemistry	Online MEGAN

Table 6.2: The model performance of WRF-Chem evaluated through error indices. † FAE and NMAE are dimensionless

Months	**October**	**April**	**October**	**April**	**October**	**April**
Near-surface parameters	2-meter temperature (°C)		2-meter relative humidity (%)		10-meter wind speed (ms^{-1})	
Average OBS	25.94	26.12	77.1	68.0	5.24	3.91
MAE	1.79	2.02	8.72	8.50	3.58	2.49
RMSE	2.65	3.27	11.60	11.24	4.92	3.39
FAE†	0.070	0.075	0.119	0.116	0.913	0.811
NMAE†	0.069	0.077	0.113	0.125	0.684	0.638
Vertical parameters	Potential temperature (K)		Mixing ratio (kg/kg)		Wind speed (ms^{-1})	
MAE	0.53	0.58	1.76	0.70	2.62	0.70
RMSE	0.60	0.67	1.92	1.01	3.07	0.84
FAE†	0.002	0.002	0.155	0.054	0.496	0.179
Air pollutant concentration	O_3 (ppbv)		NO (ppbv)		NO_2 (ppbv)	
Average OBS	8.7	12.8	19.0	20.9	10.7	16.0
MAE	16.9	14.5	19.3	22.0	22.3	19.4
RMSE	21.0	18.1	36.2	37.9	36.6	28.3
FAE†	1.17	1.06	1.73	1.75	0.98	0.94
NMAE†	1.96	1.13	1.02	1.05	2.09	1.21

The further verification of O_3, NO and NO_2 is compiled in Table 6.2. The hourly diurnal ground O_3 profile obtains an overall RMSE of 21 ppbv and 18 ppbv for October and April respectively. As illustrated in Figure 6.4a, the O_3 concentration in April is much higher compared to the October case. The stagnant atmosphere during April month shown in Chapter 2.2 is more favorable for retention of air pollutant within the region. The model predicts a large variation of the atmospheric composition of NO_x. The hourly NO concentration is generally underestimated by ~19 ppbv throughout the day as shown in Figure 6.4b,c. Modelled NO_2 is underestimated during the day while a great out-of-phase exceedance is produced at night. Underestimation of these local surface sources closely dependent on the resolution of the emission inventory [*Tie et al.*, 2010; *Fallmann et al.*, 2016]. The emission inventory used for the anthropogenic emission is up to the resolution of 0.5° (~55 km) [*Zhang et al.*, 2009] and is relatively homogeneous and coarse for the model resolution up to 3 km. Moreover, it has surpassed the ability of down-scaling to accurately represent emission amount for the fine model grid. The resolution of the emission inventory is more crucial to accurately predict the NO_x level that is directly emitted from the surface source. The O_3 photochemical process and meteorological variables are generally resolved through the WRF model resolution hence its performance is less affected by the coarse emission inventory resolution [*Tie et al.*, 2010]. However, the involvement of NO_x in the O_3 reaction cycle still causes the O_3 to vary with inventory resolution. The model result, at this point, is only valid to serve as a control case study by comparing the effect of urbanization but not the quantitative investigation on the amount of pollutant produced.

6.6 Effect of urbanization on local pollutant

Isoprene (ISOP), the most abundance chemical compound of BVOC is used as surrogate to represent the NMHC in WRF [*Guenther et al.*, 2006]. In Figure 6.5a, it is interesting to note that urbanization increases the pollutant level during the night, except for the ground O_3. The O_3 level reduces as much as 22.8 ppbv in April and 12.9 ppbv in October. The depletion of O_3 is most severe during two time intervals: night period from 1900 to 0000 MYT and morning period from 0900 to 1300 MYT. The contributions of meteorological and pollutant variations are investigated in Figure 6.5a,b respectively.

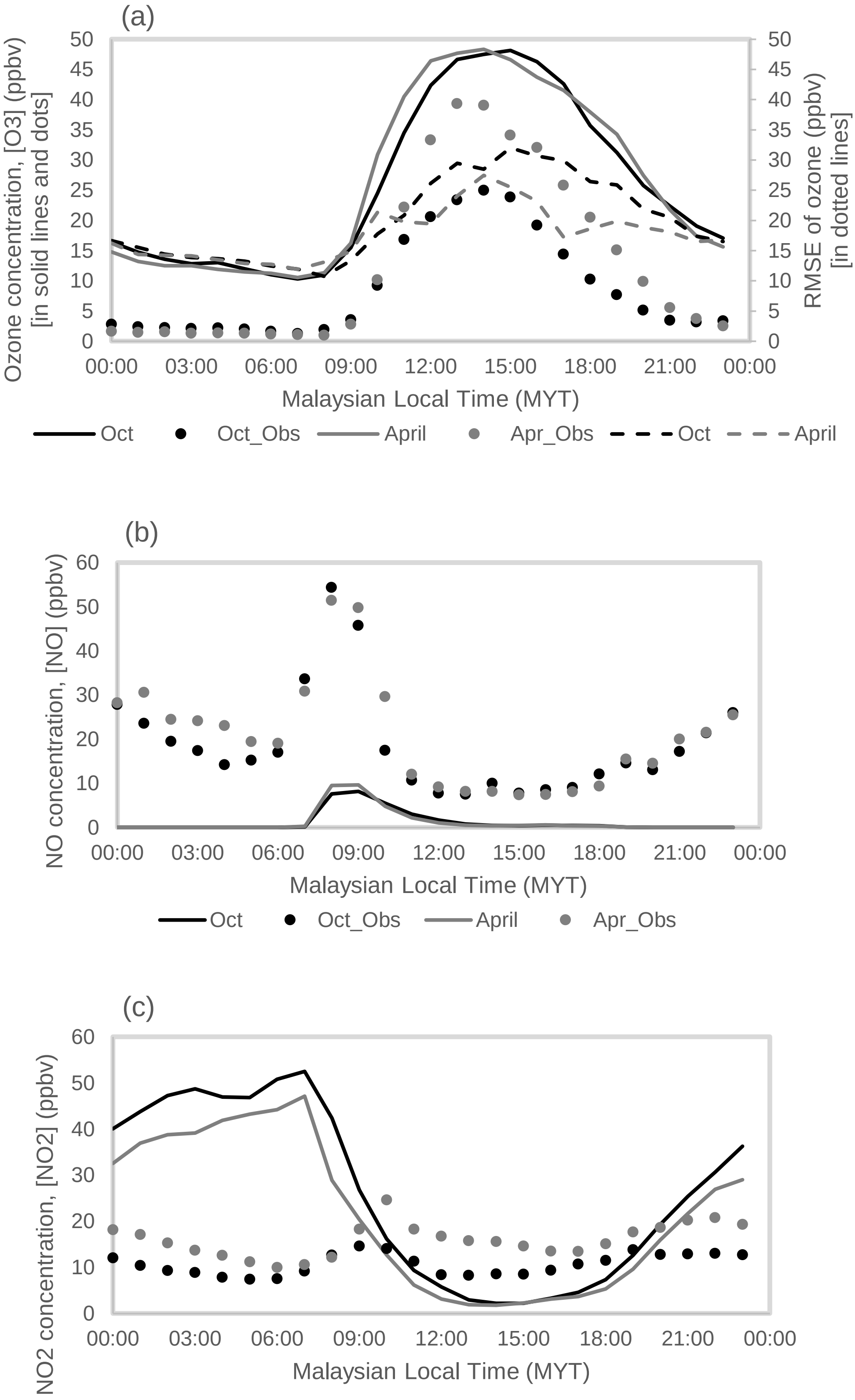

Figure 6.4: Comparison of hourly-averaged (a) O_3, (b) NO, (c) NO_2 concentration profile of modelled data to measured data for October and April.

During the morning period, the reduction of ozone indicates the reduction of ozone production rate. The role of pollutants is ruled out during the day since the ozone precursors (NO, NO_2 and ISOP) do not vary much. On the other hand, the urbanization exerts urban cool island (UCI; -0.5 °C) during both months. The reduction of temperature creates a high pressure region which suppress the vertical mixing in the region, evidently shown through a lowered boundary layer height. However, 0900 to 1300 MYT is the period when the sea breeze prevails in the urban region. The greater near-surface horizontal wind advection shown during the period (see Figure 6.5b and Figure 6.6) therefore depletes the ozone at a higher rate than it replenishes. The overall greater decrease in ozone level observed in April month with -21.4 ppbv compared to -9.9 ppbv in October concurs with the postulation in the Chapter 5. The local circulation in April month, though under weak synoptic forcing environment, is more capable to disperse the pollutant accumulated throughout the day under influence of urbanization. Although urbanization has alleviated for the ground ozone level dispersion, the continuous increment of the primary pollutants, especially the anthropogenic or natural precursors would still cause harm to the human health.

O_3 species is not produced with the absence of sunlight, hence the reduction of O_3 at night corresponds to the increased O_3 losing rate. The increased NO_2 at night contributes to the removal of O_3 ($NO_2 + O_3 \rightarrow NO_3 + O_2$) and followed up to the formation of dinitrogen pentoxide (N_2O_5) as the ozone sink ($NO_3 + NO_2 + M \rightarrow N_2O_5 + M$). From Figure 6.5b, it is also observed that the urban is experiencing great nocturnal UHI intensity (Oct: 1.66 °C, Apr: 1.48 °C). The larger heat stored in the urban enhances the vertical mixing and increases the boundary layer around 60 m into the night. Such condition is more favorable for pollutant dispersion, and hence leading to further reduction of O_3 level.

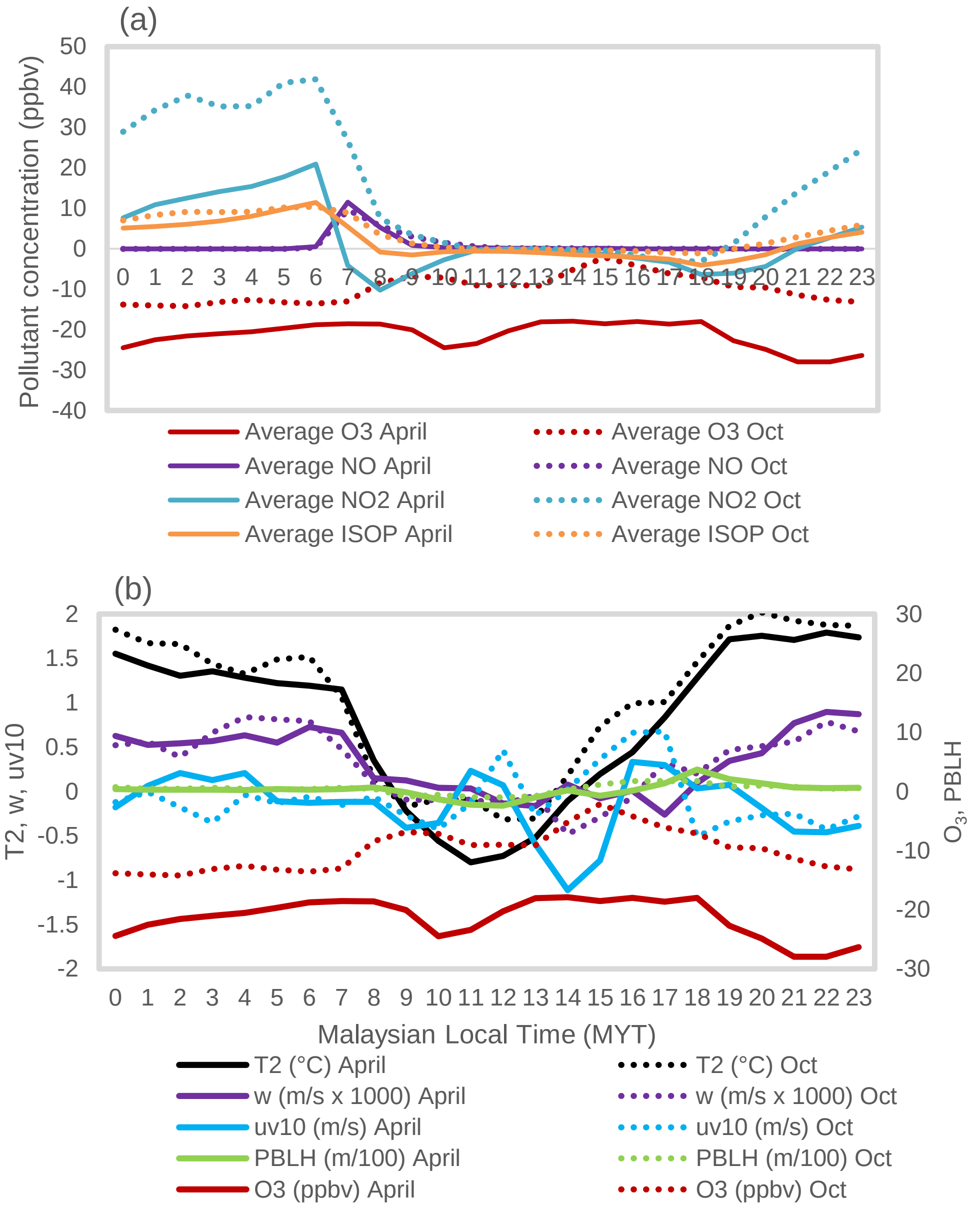

Figure 6.5: Difference of (a) pollutant concentration, (b) hourly averaged profile of meteorological condition on near-surface profile (T2, uv10) and first level profile (w), PBLH, O_3 mixing ratio extracted from simulation cases minus noURB case.

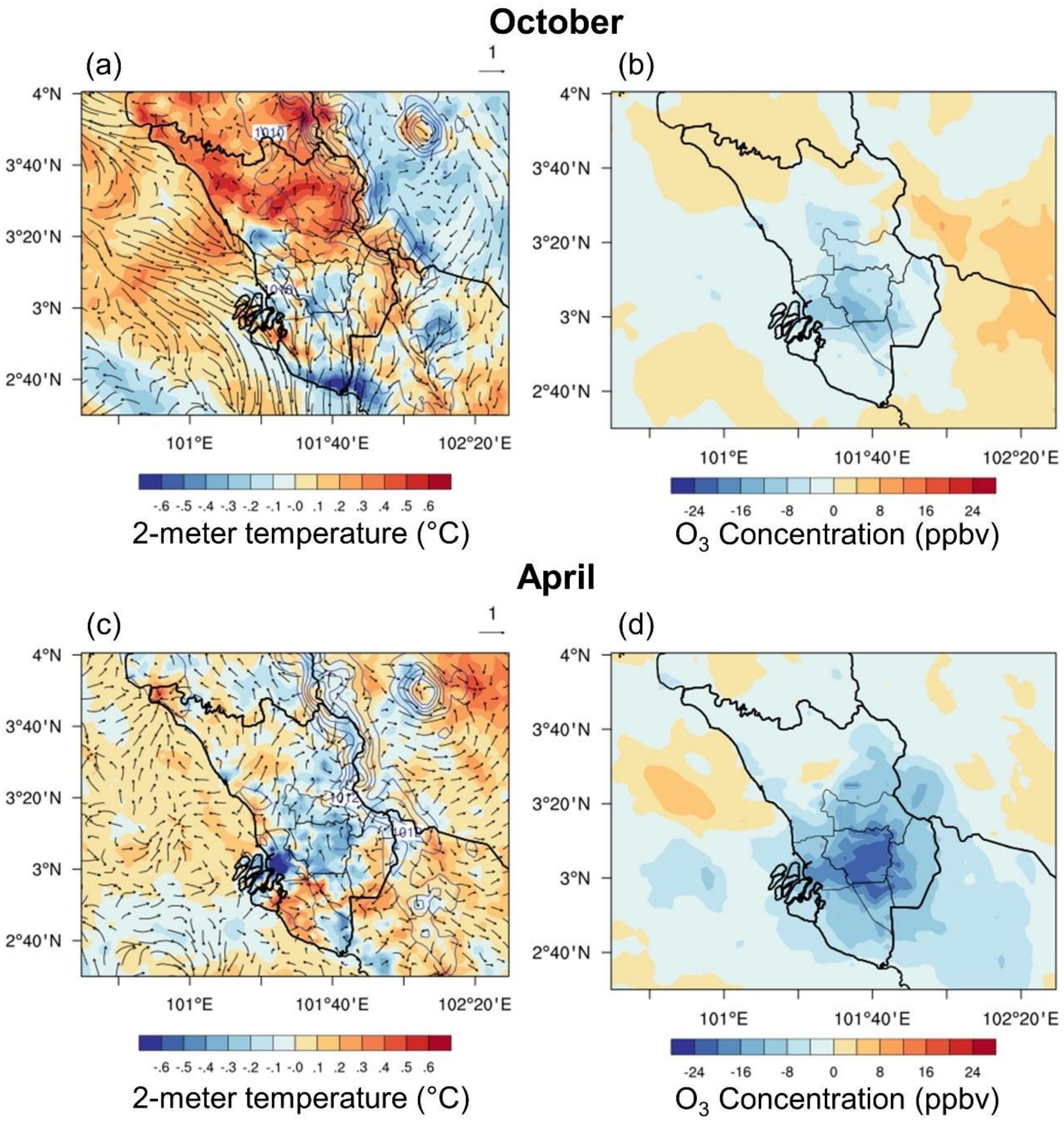

Figure 6.6: Difference of T2 and O_3 mixing ratio extracted from simulation cases minus noURB case for October and April 2003 from 0900-1300 MYT.

6.7 Findings

The daytime ozone pollutant level is higher in April compared to October. This affirms the hypothesis made in Chapter 4 on the accumulation of pollutant under the strong SBOS condition in April. The measured air quality data has pointed out the GKL region is shifting towards NO_x-sensitive regime from year 1999 to 2007. This highlights the essential role of the vegetation emission on the ground ozone formation in the tropical urban compared to the effect of urbanization in terms of urban-induced climatic change. Apart from the local dispersion effect from urban-induced circulation, the measurement data has also projected an increasing trend of O_3 level due to chemical forcings. Despite the essential role in ozone formation, the ground measurement of NMHC and THC is discontinued in all weather stations in Malaysia and prevent further research possibilities.

Although WRF-Chem is able to predict the ozone in the region well, it is unable to reproduce the ozone precursor, such as NO and NO_2. The study is therefore unable to investigate the contribution of urbanization on the air pollutants. In turn, the work is focused on the surface forcing and local circulation of urbanization on the ozone level. It is discovered that the ozone is experiencing a declining trend under urbanization condition. It is mainly due to the enhanced/suppressed mixing as a result of urban-induced heating/cooling. Care is to be taken with the findings where the emission change from the modification of land use is not accounted in this context. Many factors can cause the reliability issue of WRF-Chem. It includes the prediction of the meteorological field, the emission inventory, chemical reaction and aerosol mechanisms, spin up time, etc. It can be seen from the meteorological field that prediction becomes more inaccurate after implementation of the chemical module. To tackle the modelling quality, several approaches are proposed to build a reasonable emission inventory with the limited local emission data [*Streets et al.*, 2003; *Zhang et al.*, 2009; *Wang et al.*, 2010]. With the referenced top-down methodology, a basic inventory could be developed to overcome the incompetency resolution of global emission inventory for the intended case study region. The locally calibrated inventory database is able to improve the accuracies of anthropogenic emission and estimation of the meteorological field.

At this point, such limitation is mainly caused by the cost of the expensive model. With the limited resource, it is advisable to run it with the offline module (which is also supported by the WRF-Chem). It allows the understanding of the physics options and their interactions with the chemical models. Besides that, it can also identify the more suitable emission inventory or develop one to accommodate for the high resolution simulation case.

CHAPTER 7: CONCLUSION

Changes in land use/cover over years result in detrimental effect on the local climate, one of which is the urban-induced warming observed ubiquitously in the cities. This study uses WRF numerical modelling software as an approach to study the urban climate in GKL, one of the most urbanized city in the SEA.

7.1 Evaluation of WRF model

The original land use maps provided by WRF is neither updated nor accurately represents the surface land use. An updated terrestrial local land use map with diversified urban classes is developed for Selangor state. The new land use map reproduces the nocturnal near-surface temperature by accurately parameterizing the ground heat as the sole heat source at night. With the updated land use map, the model is able to reduce the statistical error (RMSE) by 0.2 °C T2, 0.32 % RH2, 0.56 ms^{-1} uv10 and 0.07 °C TSK. Greater improvement in modelled diurnal near-surface condition and spatial skin temperature is achieved by the calSLUCM with locally calibrated urban parameters, including detailed urban morphology and additional anthropogenic heat budget. It is also able to identify the spatial distribution of UHI and its scale of heating by accounting the heterogeneity of the urban surface (LDR, HDR and COM). This setting achieves a substantial reduction of RMSE by 0.31 °C T2, 0.52 % RH2, 0.49 ms^{-1} uv10 and 0.14 °C TSK and at this point, the WRF model is deemed reliable by meeting the allowable margin of statistical error. Fine adjustment to each urban types, complemented with updated land use map hence proven imperative for the WRF/Noah LSM model to reproduce the near-surface weather condition and the UHI effect.

The urban heat in the UBL essentially affects the vertical thermal profile and turbulent fluxes evolvement in the boundary layer processes. The vertical tendencies are forced by the PBL scheme coupled with corresponding surface layer scheme in the WRF. The evaluation of their respective performance showed that all schemes have generally overestimated the mixing condition in the bottom boundary layer. All PBL schemes produce a larger uncertainty during the synoptically convective month. The PBL schemes do not show great variation between each other in prediction of near-surface condition and vertical variables. Nevertheless, the local MYJ scheme, which predicts vertical quantities transportation through TKE gradient, is more consistent and invariant with the background synoptic forcing. The non-local schemes, in turn, require calibration on the instability indicator before application for the tropical atmospheric environment. The complex land-sea mask in the MC poses great challenge on the models to predict the precipitation profile. The discrepancies in wind speed on vertical layers near the PBLH, near-surface peak temperature and relative humidity suggest that uncertainties in PBL schemes persist due to the limitation of the measured data. This is the generic problem encountered during the verification process of numerical model, hence the verification procedure needs to be a continuous effort to effectively monitor the WRF performance.

7.2 Effect of urban land use change on local climate

The tested WRF model setting is employed to investigate the effect of urban heating phenomenon on local climate in GKL. The land use change is used as the contributing factor to the urban-induced warming that causes the modification of the local climate and air quality. The diurnal urban heating pattern is attributed to three predominant factors: (i) weak under calm and clear sky condition (morning heating), (ii) weak under larger atmospheric moisture content (late afternoon convection), (iii) largest (1.4 °C) due to differential cooling rate of urban and rural surface at night. The interaction of urban thermals and upper level SBOS affects the effect of urbanization on local circulation during the day. The urban thermals reduce the weak opposing SBOS (< 2 ms^{-1}) and enhances the inflow of moisture-rich sea breeze passage. This intensifies the downwind convective precipitation during late afternoon. On contrary, the strong opposing SBOS (> 2 ms^{-1}) suppresses the vertical lifting of urban thermals and decelerates the sea breeze front. It is discovered that the interaction of urban heating and topographic-induced flow is inter-dependent while the synoptic flow plays a critical role in modifying both factors respectively.

7.3 Effect of urban-induced local climate change on local air quality

The modelling result of WRF-Chem is used to study the effect of the urban-induced heat condition on the local air quality. It is found that the CTM model reproduces ozone well but not its precursors such as NO and NO_2. Therefore, the urbanization effect can only be compared qualitatively. The simulation result shows urbanization causes reduction of ozone level throughout the day, especially at night. The reduced ozone level is strongly correlated to the stronger horizontal SBF advection in the morning and urban-enhanced vertical mixing during the night which disperse either the ozone precursors or the ground ozone. The historical air quality monitoring data is related to the lower near-surface wind speed during the inter-monsoonal period, especially in the calm April month. The GKL is identified as an NO_x-sensitive region which ozone of high concentration is more likely to form when the amount of NO_x increases. This suggested a potentially increasing O_3 along with the urban expansion in the region.

7.4 General conclusion

The thesis has verified the applicability of numerical model WRF model to identify the UHI phenomenon in GKL and scrutinize its effect of urbanization. The introduction of urban land use on to the coastal valley urban agglomeration has caused major alteration in surface meteorological fields and overall energy budget of the boundary layer. The induced heat hence modifies alter the topographic circulation of GKL which lies in the flat valley between the coast and hills significantly. The primary air pollutant levels are greatly increased during the night and the continuous growth of urban is also projected to increase the concentration of detrimental ground ozone.

7.5 Limitations and Recommendations

This is a preliminary study of the urban heating phenomenon over the region of GKL using a numerical model. It is noteworthy that this study conducted is a first step to identify the influence of urbanization on the urban boundary climate in terms of thermal, wind circulation and precipitation condition in the particular year of weak precipitation anomaly. It should not be generalized to represent the typical response of the urbanization. In terms of the model robustness, we would like to point out that the model is still lacking in reproducing the precipitation amount. Future effort to investigate the performance of cumulus and microphysics physics routine are therefore imperative to appropriately simulate the convective rainfall mechanism in the region which involves frequent thunderstorms. An ensemble study with the combination of the PBL, microphysics and cumulus schemes can also greatly reduce the physics representation error introduced by different schemes

Now that the GKL region falls under NO_x-sensitive regime which the continual increment of urbanization rate in the region is conducive for the ground ozone formation, it would be interesting to look into the chemical forcing between the pollutants and the local climate using the CTM (WRF-Chem). The accuracy of WRF-Chem to predict the gas species, especially those primary pollutants such as NO and NO_2 that are directly extracted from, needs to be improved, so as the secondary pollutants such as O_3. The discrimination of the model result has suggested that the urban study requires corresponding high resolution chemical boundary condition before the output result of chemical constituents is deemed sensible. Hence, at this stage it is suggested to take a step back and venture into the selection of suitable emission inventory, if not, the building of inventory for the region. Such a research effort is absolutely beneficial to stimulate and attract more research interest in the SEA region.

Last but not the least, the comparison performed thus far has focused on the pure effect of urbanization but not the actual progress of urbanization. It is suggested that more recent case can be studied to identify the realistic effect of the urbanization case throughout the years. From which, the potential future effect of urbanization can be projected through the proposed future urban master plan. Urbanization factor studied only limits to the urban-induced local climate change on the air quality. It is suggested to incorporate the potential emission change that corresponds to the land use change. Notwithstanding its limitations, this study has offered some insight into the effect of urbanization in the SEA tropical region that is experiencing a rapid growth of population and urbanization rate.

REFERENCES

Ahamad, F., M. T. Latif, R. Tang, L. Juneng, D. Dominick, and H. Juahir (2014), Variation of surface ozone exceedance around Klang Valley, Malaysia, Atmos. Res., 139, 116–127, doi:10.1016/j.atmosres.2014.01.003.

Ahmad, S., N. Hashim, and Y. M. Jani (2009), Fenomena pulau haba bandar dan isu alam sekitar di Bandaraya Kuala Lumpur, Malaysian J. Soc. Sp., 5(3), 57–67.

Ahmadov, R. et al. (2012), A volatility basis set model for summertime secondary organic aerosols over the eastern United States in 2006, J. Geophys. Res., 117(D06301), 1–19, doi:10.1029/2011JD016831.

Ahmed, A. Q., D. R. Ossen, E. Jamei, N. A. Manaf, I. Said, and M. H. Ahmad (2014), Urban surface temperature behaviour and heat island effect in a tropical planned city, Theor. Appl. Climatol., (2015), 1–22, doi:10.1007/s00704-014-1122-2.

Akbari, H., S. Davis, S. Dorsano, J. Huang, and S. Winnett (1992), Cooling our communities: A guidebook on tree planting and light colored surfacing, U.S. Environmental Protection Agency, Office of Policy Analysis, Climate Change Division, Berkeley.

Akbari, H., M. Pomerantz, and H. Taha (2001), Cool surfaces and shade trees to reduce energy use and improve air quality in urban areas, Sol. Energy, 70(3), 295–310, doi:10.1016/S0038-092X(00)00089-X.

Akbari, H. et al. (2008), Reducing Urban Heat Islands : Compendium of strategies urban heat island basics, in reducing urban heat islands: Compendium of strategies2, edited by K. Hogan, J. Rosenberg, and A. Denny, pp. 1–22, United States Environmental Protection Agency, U.S.

Arnfield, A. J. (2003), Two decades of urban climate research: A review of turbulence, exchanges of energy and water, and the urban heat island, Int. J. Climatol., 23, 1–26, doi:10.1002/joc.859.

Athanasopoulou, E., H. Vogel, B. Vogel, a. P. Tsimpidi, S. N. Pandis, C. Knote, and C. Fountoukis (2013), Modeling the meteorological and chemical effects of secondary organic aerosols during an EUCAARI campaign, Atmos. Chem. Phys., 13, 625–645, doi:10.5194/acp-13-625-2013.

Bai, L. (2010), Comparison and validation of five land cover products over the African continent, Lund University.

Baklanov, A., L. T. Molina, and M. Gauss (2016), Megacities, air quality and climate, Atmos. Environ., 126(2016), 235–249, doi:10.1016/j.atmosenv.2015.11.059.

Balzarini, A. et al. (2014), Sensitivity analysis of PBL schemes by comparing WRF model and experimental data, Geosci. Model Dev. Discuss., 7, 6133–6171, doi:10.5194/gmdd-7-6133-2014.

Banan, N., M. T. Latif, L. Juneng, and F. Ahamad (2013), Characteristics of surface ozone concentrations at stations with different backgrounds in Malaysia Peninsula, Aerosol Air Qual. Res., 13, 1090–1106, doi:10.4209/aaqr.2012.09.0259.

Bao, H., K. L. Shrestha, A. Kondo, A. Kaga, and Y. Inoue (2009), Modeling the influence of biogenic volatile organic compound emissions on ozone concentration during summer season in the Kinki region of Japan, Atmos. Environ., 44(3), 421–431, doi:10.1016/j.atmosenv.2009.10.021.

Bell, M. L., A. Mcdermott, S. L. Zeger, J. M. Samet, and F. Dominici (2004), Ozone and Short-term Mortality in 95 US Urban Communities, 1987-2000, JAMA, 292(19), 2372–2378, doi:10.1001/jama.292.19.2372.

Bhati, S., and M. Mohan (2015), WRF model evaluation for the urban heat island assessment under varying land use/land cover and reference site conditions, Theor. Appl. Climatol., 1–16, doi:10.1007/s00704-015-1589-5.

Bhatt, B. C., S. Sobolowski, and A. Higuchi (2016), Simulation of diurnal rainfall variability over the Maritime Continent with a high-resolution regional climate model, J. Meteorol. Soc. Japan, 94A, 89–103, doi:10.2151/jmsj.2015-052.

Bornstein, R. (1968), Observation of UHI in NY.pdf, J. Appl. Meteorol., 7, 575–582.

Bornstein, R., and Q. Lin (2000), Urban heat islands and summertime convective thunderstorms in Atlanta: Three case studies, Atmos. Environ., 34, 507–516, doi:10.1016/S1352-2310(99)00374-X.

Bossioli, E., M. Tombrou, A. Dandou, E. Athanasopoulou, and K. V. Varotsos (2009), The role of planetary boundary-layer parameterizations in the air quality of an urban area with complex topography, Boundary-Layer Meteorol., 131(1), 53–72, doi:10.1007/s10546-009-9349-7.

Bowman, F. M., and J. H. Seinfeld (1994), Fundamental basis of incremental reactivities of organics in ozone formation in VOC/NOx mixtures, Atmos. Environ., 28(20), 3359–3368.

Calfapietra, C., S. Fares, F. Manes, a Morani, G. Sgrigna, and F. Loreto (2013), Role of Biogenic Volatile Organic Compounds (BVOC) emitted by urban trees on ozone concentration in cities: A review., Environ. Pollut., doi:10.1016/j.envpol.2013.03.012.

Camalier, L., W. Cox, and P. Dolwick (2007), The effects of meteorology on ozone in urban areas and their use in assessing ozone trends, Atmos. Environ., 41(33), 7127–7137, doi:10.1016/j.atmosenv.2007.04.061.

Carlson, T. N., and B. E. Frederick (1978), Analysis of urban-rural canopy using a surface heat flux/temperature model, J. Appl. Meteorol., 17, 998–1013.

Carraca, M. G. D., and C. G. Collier (2007), Modelling the impact of high-rise buildings in urban areas on precipitation initiation, Meteorol. Appl., 14, 149–161, doi:10.1002/met.

Chameides, W. L., R. W. Lindsay, J. Richardson, and C. S. Kiang (1988), The role of biogenic hydrocarbons in urban photochemical smog: Atlanta as a case study, Science, 241(4872), 1473–5.

Chameides, W. L. et al. (1992), Ozone precursor relationships in the ambient atmosphere, J. Geophys. Res., 97(D5), 6037–6055, doi:10.1029/91JD03014.

Chang, C. P., Z. Wang, J. McBride, and C. H. Liu (2005), Annual cycle of Southeast Asia - Maritime continent rainfall and the asymmetric monsoon transition, J. Clim., 18(2), 287–301, doi:10.1175/JCLI-3257.1.

Changnon, S. A. (1981), Metromex: A review and summary, Meteorol. Monogr., 18(40), 181.

Chemel, C., and R. S. Sokhi (2012), Response of London's urban heat island to a marine air intrusion in an easterly wind regime, Boundary-Layer Meteorol., 144(1), 65–81, doi:10.1007/s10546-012-9705-x.

Chen, F., and J. Dudhia (2001), Coupling an advanced Land Surface–Hydrology Model with the Penn State–NCAR MM5 modeling system. Part I: Model Implementation and Sensitivity, Mon. Weather Rev., 129(4), 569–585.

Chen, F., and Y. Zhang (2009), On the coupling strength between the land surface and the atmosphere: From viewpoint of surface exchange coefficients, Geophys. Res. Lett., 36(April), 1–5, doi:10.1029/2009GL037980.

Chen, F., Y. Liu, H. Kusaka, M. Tewari, J. Bao, C. F. Lo, and K. H. Lau (2004a), Challenge of forecasting urban weather with NWP models, in 5th MM5 and WRF Users Workshop, pp. 1–9, NCAR, Boulder, Colorado, USA.

Chen, F., K. W. Manning, D. Yates, M. A. Lemone, S. B. Trier, R. H. Cuenca, and D. Niyogi, 2004: Development of high-resolution land data assimilation system and its application to WRF [presentation]. 20th Conference on Weather Analysis and Forecasting/16th Conference on Numerical Weather Prediction, American Meteorological Society, Seattle, WA, US

Chen, F. et al. (2007), Description and evaluation of the characteristics of the NCAR high-resolution land data assimilation system, J. Appl. Meteorol. Climatol., 46(6), 694–713, doi:10.1175/JAM2463.1.

Chen, F., S. Miao, M. Tewari, J. W. Bao, and H. Kusaka (2011a), A numerical study of interactions between surface forcing and sea breeze circulations and their effects on stagnation in the greater Houston area, J. Geophys. Res. Atmos., 116(12), 1–19, doi:10.1029/2010JD015533.

Chen, F. et al. (2011b), The integrated WRF/urban modelling system: development, evaluation, and applications to urban environmental problems, Int. J. Climatol., 31, 273–288, doi:10.1002/joc.2158.

Chen, F., X. Yang, and W. Zhu (2014), WRF simulations of urban heat island under hot-weather synoptic conditions: The case study of Hangzhou City, China, Atmos. Res., 138, 364–377, doi:10.1016/j.atmosres.2013.12.005.

Cheng, F.-Y., Y.-C. Hsu, P.-L. Lin, and T.-H. Lin (2012), Investigation of the effects of different land use and land cover patterns on mesoscale meteorological simulations in the Taiwan area, J. Appl. Meteorol. Climatol., 52, 570–587, doi:10.1175/JAMC-D-12-0109.1.

Ching, J. et al. (2009), National urban database and access portal tool, NUDAPT, Bull. Am. Meteorol. Soc., 90(8), 1157–1168, doi:10.1175/2009BAMS2675.1.

Chow, W. T. L., and M. Roth (2003), Temporal dynamics of the urban heat island of Singapore, Int. J. Climatol., 26, 2243–2260, doi:10.1002/joc.1364.

Civerolo, K. et al. (2007), Estimating the effects of increased urbanization on surface meteorology and ozone concentrations in the New York City metropolitan region, Atmos. Environ., 41, 1803–1818, doi:10.1016/j.atmosenv.2006.10.076.

Civerolo, K. L., G. Sistla, S. T. Rao, and D. J. Nowak (2000), The effects of land use in meteorological modeling : implications for assessment of future air quality scenarios, Atmos. Environ., 34, 1615–1621.

Clappa, L. J., and M. E. Jenkin (2001), Analysis of the relationship between ambient levels of O3, NO2 and NO as a function of NOx in the UK, Atmos. Environ., 35, 6391–6405.

Cohen, A. E. et al. (2015), A review of planetary boundary layer parameterization schemes and their sensitivity in simulating a Southeast U.S. cold season severe weather environment, Weather Forecast., 117(12), 150224120634008, doi:10.1175/WAF-D-14-00105.1.

Cooper, D. I., and W. E. Eichinger (1994), Structure of atmosphere in an urban planetary boundary layer from lidar and radiosonde observations, J. Geophys. Res., 99(Dll), 22937–22948.

Crutzen, P. J. (2004), New Directions: The growing urban heat and pollution "island" effect - impact on chemistry and climate, Atmos. Environ., 3539–3540, doi:10.1016/j.atmosenv.2004.03.032.

Dandou, A., M. Tombrou, and S. Nikolaos (2009), The influence of the city of Athens on the evolution of the sea-breeze front, Boundary-Layer Meteorol., 131, 35–51, doi:10.1007/s10546-008-9306-x.

Daniels, E., G. Lenderink, R. Hutjes, and A. Holtslag (2016), Relative impacts of land use and climate change on summer precipitation in the Netherlands, Hydrol. Earth Syst. Sci., 20(10), 4129–4142, doi:10.5194/hess-20-4129-2016.

Decker, M., M. a. Brunke, Z. Wang, K. Sakaguchi, X. Zeng, and M. G. Bosilovich (2012), Evaluation of the reanalysis products from GSFC, NCEP, and ECMWF using flux tower observations, J. Clim., 25, 1916–1944, doi:10.1175/JCLI-D-11-00004.1.

Dee, D. P. et al. (2011), The ERA-Interim reanalysis: Configuration and performance of the data assimilation system, Q. J. R. Meteorol. Soc., 137(April), 553–597, doi:10.1002/qj.828.

Denman, K. L. et al. (2007), couplings between changes in the climate system and biogeochemistry, in climate change 2007: The physical science basis, edited by M. T. and H. L. M. (eds. . Solomon, S., D. Qin, M. Manning, Z. Chen, M. Marquis, K.B. Averyt, Cambridge University Press, Cambridge, United Kingdom and New York, NY, USA.

Department of Environment (1997), A guide to air pollutant index in Malaysia (API), Malaysia.

Department of Environment (2013), New Malaysia ambient air quality standard, Petaling Jaya.

Department of Statistics (2011a), Population distribution by local authority areas and mukims, 2010: Technical notes, Putrajaya.

Department of Statistics (2011b), Population distribution by local authority areas and mukims, 2010: Tables of local authority areas in Selangor, Putrajaya.

Department of Statistics (2011c), Population distribution by local authority areas and mukims, 2010: Mukims in Selangor, Putrajaya.

Dimoudi, A., and M. Nikolopoulou (2003), Vegetation in the urban environment: Microclimatic analysis and benefits, Energy Build., 35, 69–76.

Ding, Y., and J. C. L. Chan (2005), The East Asian summer monsoon: An overview, Meteorol. Atmos. Phys., 89(1–4), 117–142, doi:10.1007/s00703-005-0125-z.

Dixon, P. G., and T. L. Mote (2003), Patterns and causes of atlanta's urban heat island–initiated precipitation, J. Appl. Meteorol., 42(9), 1273–1284.

Duenas, C., M. C. Fernández, S. Canete, J. Carretero, and E. Liger (2002), Assessment of ozone variations and meteorological effects in an urban area in the Mediterranean Coast, Sci. Total Environ., 299(1–3), 97–113, doi:10.1016/S0048-9697(02)00251-6.

ECMWF (2013), Part IV: Physical processes, Reading, England.

Elsayed, I. S. M. (2012), Type of gardens that reduce the intensity of an urban heat island, Eur. J. Soc. Sci., 35(3), 343–356.

Emery, C., E. Tai, and G. Yarwood (2001), Enhanced meteorological modeling and performance evaluation for two Texas ozone episodes, California, US.

Emmons, L. K. et al. (2010), Description and evaluation of the Model for Ozone and Related chemical Tracers, version 4 (MOZART-4), Geosci. Model Dev., 3, 43–67, doi:10.5194/gmd-3-43-2010.

Von Engeln, A., and J. Teixeira (2013), A planetary boundary layer height climatology derived from ECMWF reanalysis data, J. Clim., 26(17), 6575–6590, doi:10.1175/JCLI-D-12-00385.1.

Environment Protection Agency (1997), 1997 National Ambient Air Quality Standards (NAAQS) for Ozone (revoked).

Fallmann, J., R. Forkel, and S. Emeis (2016), Secondary effects of urban heat island mitigation measures on air quality, Atmos. Environ., 125, 199–211, doi:10.1016/j.atmosenv.2015.10.094.

Fiore, A. M. et al. (2012), Global air quality and climate, Chem. Soc. Rev., 41, 6663–6683, doi:10.1039/c2cs35095e.

Foley, J. A. et al. (2005), Global consequences of land use, Science (80-.)., 309, 570–574.

Food and Agriculture Organization (2000), Forest cover mapping and monitoring with NOAA-AVHRR and other coarse spatial resolution sensors, Rome.

Freitas, E. D., C. M. Rozoff, W. R. Cotton, and P. L. S. Dias (2006), Interactions of an urban heat island and sea-breeze circulations during winter over the metropolitan area of São Paulo, Brazil, Boundary-Layer Meteorol., 122(1), 43–65, doi:10.1007/s10546-006-9091-3.

Fujita, M., F. Kimura, and M. Yoshizaki (2010), Morning precipitation peak over the Strait of Malacca under a calm condition, Mon. Weather Rev., 138, 1474–1486, doi:10.1175/2009MWR3068.1.

Gao, H., and G. Jia (2013), Assessing disagreement and tolerance of misclassification of satellite-derived land cover products used in WRF Model applications, Adv. Atmos. Sci., 30(1), 125–141, doi:10.1007/s00376-012-2037-4.

Gedzelman, S. D., S. Austin, R. Cermak, N. Stefano, S. Partridge, S. Quesenberry, and D. A. Robinson (2003), Mesoscale aspects of the urban heat island around New York City, Theor. Appl. Climatol., 75, 29–42, doi:10.1007/s00704-002-0724-2.

Geng, F., X. Tie, a. Guenther, G. Li, J. Cao, and P. Harley (2011), Effect of isoprene emissions from major forests on ozone formation in the city of Shanghai, China, Atmos. Chem. Phys., 11(20), 10449–10459, doi:10.5194/acp-11-10449-2011.

Giovannini, L., D. Zardi, M. de Franceschi, and F. Chen (2013), Numerical simulations of boundary-layer processes and urban-induced alterations in an Alpine valley, Int. J. Climatol., 34, 1111–1131, doi:10.1002/joc.3750.

Goddard Earth Sciences Data and Information Services Center (2016), TRMM (TMPA) Precipitation L3 1 day 0.25 degree x 0.25 degree V7, Goddard Earth Sciences Data and Information Services Center (GES DISC), Accessed [9 June 2016] https://disc.gsfc.nasa.gov/datacollection/TRMM_3B42_Daily_7.html

GFED (2017), Global Fire Emissions Database Updates: 2015 Fire Season (Indonesian fire season progression), Accessed on [21 Jan 2017] http://www.globalfiredata.org/updates.html

Von Glasow, R. et al. (2013), Megacities and large urban agglomerations in the coastal zone: Interactions between atmosphere, land, and marine ecosystems, Ambio, 42(1), 13–28, doi:10.1007/s13280-012-0343-9.

Grell, G. a., S. E. Peckham, R. Schmitz, S. a. McKeen, G. Frost, W. C. Skamarock, and B. Eder (2005), Fully coupled “online” chemistry within the WRF model, Atmos. Environ., 39(37), 6957–6975, doi:10.1016/j.atmosenv.2005.04.027.

Grimmond, C. S. B. et al. (2010), The international urban energy balance models comparison project: First results from Phase 1, J. Appl. Meteorol. Climatol., 49, 1268–1292, doi:10.1175/2010JAMC2354.1.

Grimmond, C. S. B. et al. (2011), Initial results from Phase 2 of the international urban energy balance model comparison, Int. J. Climatol., 31(October 2010), 244–272, doi:10.1002/joc.2227.

Grimmond, S. (2007), Urbanization and global environmental change: local effects of urban warming, Geogr. J., 173, 83–88, doi:10.1111/j.1475-4959.2007.232_3.x.

Grossman-Clarke, S., Y. Liu, J. a. Zehnder, and J. D. Fast (2008), Simulations of the urban planetary boundary layer in an arid metropolitan area, J. Appl. Meteorol. Climatol., 47(3), 752–768, doi:10.1175/2007JAMC1647.1.

Guenther, A., T. Karl, P. Harley, C. Wiedinmyer, P. I. Palmer, and C. Geron (2006), Estimates of global terrestrial isoprene emissions using MEGAN (Model of Emissions of Gases and Aerosols from Nature), Atmos. Chem. Phys. Discuss., 6(1), 107–173, doi:10.5194/acpd-6-107-2006.

Guenther, A. B., X. Jiang, C. L. Heald, T. Sakulyanontvittaya, T. Duhl, L. K. Emmons, and X. Wang (2012), The Model of Emissions of Gases and Aerosols from Nature version 2.1 (MEGAN2.1): An extended and updated framework for modeling biogenic emissions, Geosci. Model Dev., 5, 1471–1492, doi:10.5194/gmd-5-1471-2012.

Haagen-Smit, A. J. (1952), Smog research pays off, Eng. Sci., 15, 11–16.

Han, J.-Y., J.-J. Baik, and H. Lee (2014), Urban impacts on precipitation, Asia-Pacific J. Atmos. Sci., 50(1), 17–30, doi:10.1007/s13143-014-0016-7.

Han, S., H. Bian, Y. Feng, A. Liu, X. Li, F. Zeng, and X. Zhang (2011), Analysis of the relationship between O_3, NO and NO_2 in Tianjin, China, Aerosol Air Qual. Res., 11, 128–139, doi:10.4209/aaqr.2010.07.0055.

Hara, M., T. Yoshikane, H. G. Takahashi, F. Kimura, A. Noda, and T. Tokioka (2009), Assessment of the diurnal cycle of precipitation over the Maritime Continent simulated by a 20 km mesh GCM using TRMM PR data, J. Meteorol. Soc. Japan, 87A, 413–424, doi:10.2151/jmsj.87A.413.

Hewitt, C. N. et al. (2009), Nitrogen management is essential to prevent tropical oil palm plantations from causing ground-level ozone pollution., Proc. Natl. Acad. Sci. U. S. A., 106(44), 18447–18451, doi:10.1073/pnas.0907541106.

Hidalgo, J., G. Pigeon, and V. Masson (2008), Urban-breeze circulation during the CAPITOUL experiment: numerical simulations, Meteorol. Atmos. Phys., 102, 243–262, doi:10.1007/s00703-008-0345-0.

Ho, C. S. (2006), Putrajaya – Administrative centre of Malaysia -Planning concept and implementation-, in Sustainable urban development and governanace conference, pp. 1–20, SungKyunKwan University, Seoul.

Holzworth, G. C. (1967), Mixing Depths, Wind Speeds and Air Pollution Potential for Selected Locations in the United States, J. Appl. Meteorol., 6, 1039–1044, doi:10.1175/1520-0450(1967)006<1039:MDWSAA>2.0.CO;2.

Hong, S., V. Lakshmi, E. E. Small, F. Chen, M. Tewari, and K. W. Manning (2009), Effects of vegetation and soil moisture on the simulated land surface processes from the coupled WRF/Noah model, J. Geophys. Res. Atmos., 114(18), 1–13, doi:10.1029/2008JD011249.

Hong, S.-Y., and Y. Noh (2006), A new vertical diffusion package with an explicit treatment of entrainment processes, Mon. Weather Rev., 134, 2318–2341.

Hong, S.-Y., and H.-L. Pan (1996), Nonlocal boundary layer vertical diffusion in a medium range orecast model, Mon. Weather Rev., 124, 2322–2339.

Howard, L. (1833), The climate of London, 2nd Edition, Harvey and Darton, London.

Hu, X.-M., J. W. Nielsen-Gammon, and F. Zhang (2010), evaluation of three planetary boundary layer schemes in the WRF model, J. Appl. Meteorol. Climatol., 49(9), 1831–1844, doi:10.1175/2010JAMC2432.1.

Huong, H. T. L., and A. Pathirana (2013), Urbanization and climate change impacts on future urban flooding in Can Tho city, Vietnam, Hydrol. Earth Syst. Sci., 17(1), 379–394, doi:10.5194/hess-17-379-2013.

Huszar, P., M. Belda, and T. Halenka (2016), On the long-term impact of emissions from central European cities on regional air quality, Atmos. Chem. Phys, 16, 1331–1352, doi:10.5194/acp-16-1331-2016.

Ishak, A., Z. N. C. Hassan, N. H. Erdros, M. H. Zamberi, and M. N. Abd Rahman (2011), The effect of local climate on urban heat island trend; A case study in urban area of Ipoh and Kuantan. Malaysian Meteorological Department.

Jacobson, M. Z. (2005), Fundamentals of atmospheric modelling, 2nd ed., Cambridge University Press, New York.

Janjic, Z. I. (1990), The step-mountain coordinate: Physical Package, Mon. Weather Rev., 118, 1429–1443.

Janjic, Z. I. (1994), The step-mountain Eta coordinate model: Further developments of convection viscous sublayer, turbulence closure schemes, Mon. Weather Rev., 122, 927–945.

Janjic, Z. I. (2001), Nonsingular implementation of the Mellor-Yamada Level 2.5 scheme in the NCEP Meso model, NOAA/NWS/NCEP Off. Note 437, 61.

Jauregui, E. (1997), Heat island development in Mexico City, Atmos. Environ., 31(22), 3821–3831, doi:10.1016/S1352-2310(97)00136-2.

Jauregui, E., L. Godinez, and F. Cruz (1992), Aspects of heat-island development in Guadalajara, Mexico, Atmos. Environ., 26B(3), 391–396.

Ji, H. E., S. H. Lee, and H. W. Lee (2013), Characteristics of sea breeze front development with various synoptic conditions and its impact on lower troposphere ozone formation, Adv. Atmos. Sci., 30(5), 1461–1478, doi:10.1007/s00376-013-2256-3.

Jiang, X., C. Wiedinmyer, F. Chen, Z.-L. Yang, and J. C.-F. Lo (2008), Predicted impacts of climate and land use change on surface ozone in the Houston, Texas, area, J. Geophys. Res., 113(D20), 1–16, doi:10.1029/2008JD009820.

Jin, M., and R. E. Dickinson (2010), Land surface skin temperature climatology: benefitting from the strengths of satellite observations, Environ. Res. Lett., 5(44004), 1–13, doi:10.1088/1748-9326/5/4/044004.

Joseph, B., B. C. Bhatt, T. Y. Koh, and S. Chen (2008), Sea breeze simulation over the Malay Peninsula in an intermonsoon period, J. Geophys. Res. Atmos., 113(20), 1–8, doi:10.1029/2008JD010319.

Jusuf, S. K., N. H. Wong, E. Hagen, R. Anggoro, and Y. Hong (2007), The influence of land use on the urban heat island in Singapore, Habitat Int., 31(2), 232–242, doi:10.1016/j.habitatint.2007.02.006.

Kalnay, E., and M. Cai (2003), Impact of urbanization and land-use change on climate, Nature, 423, 528–531, doi:10.1038/nature01675.

Kang, H. Q., B. Zhu, T. Zhu, J. L. Sun, and J. J. Ou (2014), Impact of megacity Shanghai on the urban heat-island effects over the downstream city Kunshan, Boundary-Layer Meteorol., 152(3), 411–426, doi:10.1007/s10546-014-9927-1.

Kantzioura, A., P. Kosmopoulos, and S. Zoras (2012), Urban surface temperature and microclimate measurements in Thessaloniki, Energy Build., 44, 63–72, doi:10.1016/j.enbuild.2011.10.019.

Kataoka, K., F. Matsumoto, T. Ichinose, and M. Taniguchi (2009), Urban warming trends in several large Asian cities over the last 100 years, Sci. Total Environ., 407, 3112–3119, doi:10.1016/j.scitotenv.2008.09.015.

Kaufmann, R. K., K. C. Seto, A. Schneider, Z. Liu, L. Zhou, and W. Wang (2007), Climate response to rapid urban growth: Evidence of a human-induced precipitation deficit, J. Clim., 20(10), 2299–2306, doi:10.1175/JCLI4109.1.

Kikuchi, K., and B. Wang (2008), Diurnal precipitation regimes in the global tropics, J. Clim., 21(11), 2680–2696, doi:10.1175/2007JCLI2051.1.

Kim, S.-Y., X. Jiang, M. Lee, A. Turnipseed, A. Guenther, J.-C. Kim, S.-J. Lee, and S. Kim (2013), Impact of biogenic volatile organic compounds on ozone production at the Taehwa Research Forest near Seoul, South Korea, Atmos. Environ., 70, 447–453, doi:10.1016/j.atmosenv.2012.11.005.

Kim, Y.-H., and J.-J. Baik (2002), Maximum urban heat island intensity in Seoul, J. Appl. Meteorol., 41, 651–659.

Kubota, T., and D. R. Ossen (2009), Spatial characteristics of urban heat island in Johor Bharu city, Malaysia, in 3rd South East Asian Technical Universities Consortium (SEATUC), pp. 39–44, Johor Bharu.

Kukkonen, J. et al. (2012), A review of operational, regional-scale, chemical weather forecasting models in Europe, Atmos. Chem. Phys., 12, 1–87, doi:10.5194/acp-12-1-2012.

Kumar, A., F. Chen, M. Barlage, M. B. Ek, and D. Niyogi (2014), Assessing impacts of integrating MODIS vegetation data in the weather research and forecasting (WRF) model coupled to two different canopy-resistance approaches, J. Appl. Meteorol. Climatol., 53, 1362–1380, doi:10.1175/JAMC-D-13-0247.1.

Kusaka, H., and F. Kimura (2004), Coupling a Single-Layer Urban Canopy Model with a simple atmospheric model: Impact on urban heat island simulation for an idealized case, J. Meteorol. Soc. Japan, 82(1), 67–80, doi:10.2151/jmsj.82.67.

Kusaka, H., H. Kondo, Y. Kikegawa, and F. Kimura (2001), A simple single-layer urban canopy model for atmospheric models: Comparison with multi-layer and slab models, Boundary-Layer Meteorol., 101, 329–358.

Kusaka, H., K. Nawata, A. Suzuki-Parker, Y. Takane, and N. Furuhashi (2014), Mechanism of precipitation increase with urbanization in Tokyo as revealed by ensemble climate simulations, J. Appl. Meteorol. Climatol., 53(4), 824–839, doi:10.1175/JAMC-D-13-065.1.

Lacour, S. a, M. de Monte, P. Diot, J. Brocca, N. Veron, P. Colin, and V. Leblond (2006), Relationship between ozone and temperature during the 2003 heat wave in France: consequences for health data analysis, BMC Public Health, 6(261), doi:10.1186/1471-2458-6-261.

Lai, L.-W., and W.-L. Cheng (2009), Air quality influenced by urban heat island coupled with synoptic weather patterns, Sci. Total Environ., 407, 2724–2733, doi:10.1016/j.scitotenv.2008.12.002.

Latif, M. T., S. H. Lim, and J. Liew (2012), Variations of surface ozone concentration across the Klang Valley, Malaysia, Atmos. Environ., 61, 434–445, doi:10.1016/j.atmosenv.2012.07.062.

Lee, S.-H., S.-W. Kim, W. M. Angevine, L. Bianco, S. a. McKeen, C. J. Senff, M. Trainer, S. C. Tucker, and R. J. Zamora (2011), Evaluation of urban surface parameterizations in the WRF model using measurements during the Texas Air Quality Study 2006 field campaign, Atmos. Chem. Phys., 11, 2127–2143, doi:10.5194/acp-11-2127-2011.

LeMone, M. a., M. Tewari, F. Chen, and J. Dudhia (2013), Objectively-determined fair-weather CBL depths in the ARW-WRF model and their comparison to CASES-97 observations, Mon. Weather Rev., 141, 30–54, doi:10.1175/MWR-D-12-00106.1.

Lemonsu, A., and V. Masson (2002), Simulation of a summer urban breeze over Paris, Boundary-Layer Meteorol., 104, 463–490.

Leung, D. Y. C., P. Wong, B. K. H. Cheung, and a. Guenther (2010), Improved land cover and emission factors for modeling biogenic volatile organic compounds emissions from Hong Kong, Atmos. Environ., 44(11), 1456–1468, doi:10.1016/j.atmosenv.2010.01.012.

Li, D., and E. Bou-Zeid (2014), Quality and sensitivity of high-resolution numerical simulation of urban heat islands, Environ. Res. Lett., 9(5), 55001, doi:10.1088/1748-9326/9/5/055001.

Li, D., E. Bou-Zeid, M. L. Baeck, S. Jessup, and J. A. Smith (2013a), modeling land surface processes and heavy rainfall in urban environments: sensitivity to urban surface representations, J. Hydrometeorol., 14, 1098–1118, doi:10.1175/JHM-D-12-0154.1.

Li, J., M. Georgescu, P. Hyde, A. Mahalov, and M. Moustaoui (2014), Achieving accurate simulations of urban impacts on ozone at high resolution, Environ. Res. Lett., 9(114019), 1–11, doi:10.1088/1748-9326/9/11/114019.

Li, X.-X., T.-Y. Koh, J. Panda, and L. K. Norford (2016), Impact of urbanization patterns on the local climate of a tropical city Singapore: An ensemble study, J. Geophys. Res. Atmos., 121, 4386–4403, doi:10.1002/2015JD024452.

Li, X. X., T. Y. Koh, D. Entekhabi, M. Roth, J. Panda, and L. K. Norford (2013b), A multi-resolution ensemble study of a tropical urban environment and its interactions with the background regional atmosphere, J. Geophys. Res. Atmos., 118(17), 9804–9818, doi:10.1002/jgrd.50795.

Liao, J., T. Wang, X. Wang, M. Xie, Z. Jiang, X. Huang, and J. Zhu (2014), Impacts of different urban canopy schemes in WRF/Chem on regional climate and air quality in Yangtze River Delta, China, Atmos. Res., 145–146, 226–243, doi:10.1016/j.atmosres.2014.04.005.

Lin, C.-Y., F. Chen, J. C. Huang, W.-C. Chen, Y.-A. Liou, W.-N. Chen, and S.-C. Liu (2008), Urban heat island effect and its impact on boundary layer development and land–sea circulation over northern Taiwan, Atmos. Environ., 42, 5635–5649, doi:10.1016/j.atmosenv.2008.03.015.

Lin, Y.-L., R. D. . Farley, and H. D. . Orville (1983), Bulk parameterization of snow field in a cloud model, Am. Meteorol. Soc., 22, 1065–1092.

Ling, O. H. L., K. H. Ting, A. Shaharuddin, A. Kadaruddin, and M. J. Yaaskob (2010), Urban growth and air quality in Kuala Lumpur city, Malaysia, Environ. Asia, 3(2), 123–128.

Liu, Y., F. Chen, T. Warner, and J. Basara (2006), Verification of a mesoscale data-assimilation and forecasting system for the Oklahoma City area during the joint urban 2003 field project, J. Appl. Meteorol. Climatol., 45(7), 912–929, doi:10.1175/JAM2383.1.

Lo, C. P., and D. A. Quattrochi (2003), Land-use and land-cover change, urban heat island phenomenon , and health implications : A remote sensing approach, Photogramm. Eng. Remote Sens., 69(9), 1053–1063.

Lo, J. C. F., A. K. H. Lau, J. C. H. Fung, and F. Chen (2006), Investigation of enhanced cross-city transport and trapping of air pollutants by coastal and urban land-sea breeze circulations, J. Geophys. Res. Atmos., 111(14), 1–13, doi:10.1029/2005JD006837.

Loughner, C. P., D. J. Allen, D.-L. Zhang, K. E. Pickering, R. R. Dickerson, and L. Landry (2012), Roles of urban tree canopy and buildings in urban heat island effects: Parameterization and preliminary results, J. Appl. Meteorol. Climatol., 51(10), 1775–1793, doi:10.1175/JAMC-D-11-0228.1.

Mahmood, R., R. A. S. Pielka, K. G. Hubbard, D. Niyogi, G. Bonan, and More (2010), Impacts of land use/land cover change on climate and future research priorities, Bull. Am. Meteorol. Soc., 91(1), 37–46, doi:10.1175/2009BAMS2769.1.

Mcnally, D., and J. G. Wilkinson (2010), The MMIFstat statistical analysis package Version 1.0, Colorado, US.

McPhaden, M. J. (2004), Evolution of the 2002/03 El Niño, Bull. Am. Meteorol. Soc., 85, 677–695, doi:10.1175/BAMS-85-5-677.

Mellor, G. L., and T. Yamada (1982), Development of a Turbulence Closure Model for Geophysical Fluid Problems, Rev. Geophys. Sp. Phys., 20(4), 851–875.

Meng, W., Y. Zhang, J. Li, W. Lin, G. Dai, and H. Li (2011), Application of WRF/UCM in the simulation of a heat wave event and urban heat island Around Guangzhou, J. Trop. Meteorol., 17(3), 257–267, doi:10.3969/j.issn.1006-8775.2011.03.007.

Miao, S., F. Chen, M. A. LeMone, M. Tewari, Q. Li, and Y. Wang (2009), An observational and modeling study of characteristics of urban heat island and boundary layer structures in Beijing, J. Appl. Meteorol. Climatol., 48(3), 484–501, doi:10.1175/2008JAMC1909.1.

Miao, Y., S. Liu, Y. Zheng, S. Wang, and B. Chen (2015), Numerical study of the effects of topography and urbanization on the local atmospheric circulations over the Beijing-Tianjin-Hebei, China, Adv. Meteorol., 2015, doi:10.1155/2015/397070.

Miettinen, J., H.-J. Stibig, and F. Achard (2014), Remote sensing of forest degradation in Southeast Asia—Aiming for a regional view through 5–30 m satellite data, Glob. Ecol. Conserv., 2, 24–36, doi:10.1016/j.gecco.2014.07.007.

Milford, J. B., Dongfen Gao, S. Sillman, P. Blossey, and A. G. Russell (1994), Total reactive nitrogen (NOy) as an indicator of the sensitivity of ozone to reductions in hydrocarbon and NOx emissions, J. Geophys. Res., 99(D2), 3533–3542, doi:10.1029/93JD03224.

Mirzaei, P. A., and F. Haghighat (2010), Approaches to study urban heat island – Abilities and limitations, Build. Environ., 45, 2192–2201, doi:doi:10.1016/j.buildenv.2010.04.001.

Misztal, P. K. et al. (2011), Direct ecosystem fluxes of volatile organic compounds from oil palms in South-East Asia, Atmos. Chem. Phys., 11(17), 8995–9017, doi:10.5194/acp-11-8995-2011.

Mitchell, K. et al. (2005), Noah Land Surface Model (LSM) User's Guide, Boulder, Colorado, USA.

Mlawer, E. J., S. J. Taubman, P. D. Brown, M. J. Iacono, and S. a. Clough (1997), Radiative transfer for inhomogeneous atmospheres: RRTM, a validated correlated-k model for the longwave, J. Geophys. Res., 102(D14), 16663–16682, doi:10.1029/97JD00237.

Monin, A. S., and A. M. Obukhov (1954), Basic laws of turbulent mixing in the surface layer of the atmosphere, Contrib. Geophys. Inst. Acad. Sci. USSR, 24(151), 163–187.

Mori, S., H. Jun-Ichi, Y. I. Tauhid, M. D. Yamanaka, N. Okamoto, F. Murata, N. Sakurai, H. Hashiguchi, and T. Sribimawati (2004), diurnal land–sea rainfall peak migration over Sumatera Island, Indonesian Maritime Continent, Observed by TRMM satellite and intensive rawinsonde soundings, Mon. Weather Rev., 132(8), 2021–2039, doi:10.1175/1520-0493(2004)132<2021:DLRPMO>2.0.CO;2.

Morris, C. J. G., I. Simmonds, and N. Plummer (2001), Quantification of the influences of wind and cloud on the nocturnal urban heat island of a large City, J. Appl. Meteorol., 40, 169–182.

Morris, K. I. (2016a), Computational study of Klang Valley's urban climatology, and urbanisation of Putrajaya City, Malaysia, University of Nottingham.

Morris, K. I. (2016b), Effect of vegetation and waterbody on the garden city concept: An evaluation study using a newly developed city, Putrajaya, Malaysia, Comput. Environ. Urban Syst., 58, 39–51, doi:http://dx.doi.org/10.1016/j.compenvurbsys.2016.03.005.

Morris, K. I., S. A. Salleh, A. Chan, M. C. G. Ooi, Y. A. Abakr, M. Y. Oozeer, and M. Duda (2015), Computational study of urban heat island of Putrajaya, Malaysia, Sustain. Cities Soc., 19(2015), 359–372, doi:10.1016/j.scs.2015.04.010.

Morris, K. I., A. Chan, S. A. Salleh, M. C. Ooi, M. Y. Oozeer, and Y. A. Abakr (2016), Numerical study on the urbanization of Putrajaya and its interaction with the local climate, over a decade, Urban Clim., 16, 1–24, doi:10.1016/j.uclim.2016.02.00.

Morris, K. I., A. Chan, K. J. K. Morris, M. C. G. Ooi, M. Y. Oozeer, Y. A. Abakr, M. S. M. Nadzir, and I. Y. Mohammed (2017), Urbanisation and urban climate of a tropical conurbation, Klang Valley, Malaysia, Urban Clim., 19(December), 54–71, doi:10.1016/j.uclim.2016.12.002.

Moten, S., F. Yunus, M. Ariffin, N. Burham, D. Jeong Yik, M. K. Mat Adam, and Y. Weng Sang (2014), Statistics of northeast monsoon onset , withdrawal and cold surges in Malaysia, Petaling Jaya.

Ng, M. W., A. Camerlengo, and A. K. Abdul Wahab (2005), A study of global warming in Malaysia, J. Teknol., 42(F), 1–10.

Nolan, D. S., J. a. Zhang, and D. P. Stern (2009), evaluation of planetary boundary layer parameterizations in tropical cyclones by comparison of in situ observations and high-resolution simulations of Hurricane Isabel (2003). Part I: initialization, maximum winds, and the outer-core boundary layer, Mon. Weather Rev., 137(11), 3651–3674, doi:10.1175/2009MWR2785.1.

Ohashi, Y., and H. Kida (2002), Effects of mountains and urban areas on daytime local-circulations in the Osaka and Kyoto regions, J. Meteorol. Soc. Japan, 80(4), 539–560, doi:Doi 10.2151/Jmsj.80.539.

Oke, T. R. (1973), City size and the urban heat island, Atmos. Environ., 7, 769–779.

Oke, T. R. (1976), The distinction between canopy and boundary - layer urban heat islands, Atmosphere (Basel)., 14(4), 37–41, doi:10.1080/00046973.1976.9648422.

Oke, T. R. (1987), Boundary layer climates, 2nd ed., Routledge, London.

Oke, T. R. (1995), The heat island of the urban boundary layer: characteristics, causes and effects, in wind climate in cities, edited by J. E. Cermak, A. G. Davenport, E. J. Plate, and D. X. Viegas, pp. 81–107, Kluwer Academic Publishers, Netherlands.

Oke, T. R., and G. B. Maxwell (1975), Urban heat island dynamics in Montreal and Vancouver, Atmos. Environ., 9, 191–200.

Oki, T., and K. Musiake (1994), Seasonal change of the diurnal cycle of precipiration over Japan and Malaysia, J. Appl. Meteorol., 33, 1445–1463.

Ono, R., Y. Nakagawa, Y. Tokumitsu, H. Matsumoto, and T. Oda (2014), Effect of humidity on the production of ozone and other radicals by low-pressure mercury lamps, J. Photochem. Photobiol. A Chem., 274(2014), 13–19, doi:10.1016/j.jphotochem.2013.09.012.

Ooka, R., M. Khiem, H. Hayami, H. Yoshikado, H. Huang, and Y. Kawamoto (2011), Influence of meteorological conditions on summer ozone levels in the central Kanto area of Japan, Procedia Environ. Sci., 4, 138–150, doi:10.1016/j.proenv.2011.03.017.

Pathirana, A., H. B. Denekew, W. Veerbeek, C. Zevenbergen, and A. T. Banda (2014), Impact of urban growth-driven landuse change on microclimate and extreme precipitation - A sensitivity study, Atmos. Res., 138(2014), 59–72, doi:10.1016/j.atmosres.2013.10.005.

Peckham, S. E. et al. (2014a), 2014-WRF-Chem V3.6 User’s Guide.

Peckham, S. E. et al. (2014b), WRF-Chem emissions guide, Boulder, Colorado, USA.

Pielke, R. a. et al. (2011), Land use/land cover changes and climate: Modeling analysis and observational evidence, Wiley Interdiscip. Rev. Clim. Chang., 2(6), 828–850, doi:10.1002/wcc.144.

Pleim, J. E. (2007a), A combined local and nonlocal closure model for the atmospheric boundary layer. Part I: Model description and testing, J. Appl. Meteorol. Climatol., 46(9), 1383–1395, doi:10.1175/JAM2539.1.

Pleim, J. E. (2007b), A combined local and nonlocal closure model for the atmospheric boundary layer. Part II: Application and evaluation in a mesoscale meteorological model, J. Appl. Meteorol. Climatol., 46(9), 1396–1409, doi:10.1175/JAM2534.1.

Pleim, J. E., and J. S. Chang (1992), A non-local closure model for vertical mixing in the convective boundary, Atmos. Environ., 26A(6), 965–981.

Pudasainee, D., B. Sapkota, M. L. Shrestha, A. Kaga, A. Kondo, and Y. Inoue (2006), Ground level ozone concentrations and its association with NO x and meteorological parameters in Kathmandu valley, Nepal, Atmos. Environ., 40, 8081–8087, doi:10.1016/j.atmosenv.2006.07.011.

Pugliese, S. C., J. G. Murphy, J. A. Geddes, and J. M. Wang (2014), The impacts of precursor reduction and meteorology on ground-level ozone in the Greater Toronto Area, Atmos. Chem. Phys, 14, 8197–8207, doi:10.5194/acp-14-8197-2014.

Quan, J., Y. Gao, Q. Zhang, X. Tie, J. Cao, S. Han, J. Meng, P. Chen, and D. Zhao (2013), Evolution of planetary boundary layer under different weather conditions, and its impact on aerosol concentrations, Particuology, 11(1), 34–40, doi:10.1016/j.partic.2012.04.005.

Romero, H., M. Ihl, A. Rivera, P. Zalazar, and P. Azocar (1999), Rapid urban growth, land-use changes and air pollution in Santiago, Chile, Atmos. Environ., 33, 4039–4047.

Rosenfeld, D. (2000), Suppression of rain and snow by urban and industrial air pollution, Science, 287, 1793–1796, doi:10.1126/science.287.5459.1793.

Roth, M. (2007), Review of urban climate research in (sub)tropical regions, Int. J. Climatol., 27, 1859–1873, doi:10.1002/joc.

Ryu, Y.-H., J.-J. Baik, and S.-H. Lee (2013a), Effects of anthropogenic heat on ozone air quality in a megacity, Atmos. Environ., 80, 20–30, doi:10.1016/j.atmosenv.2013.07.053.

Ryu, Y.-H., J.-J. Baik, K.-H. Kwak, S. Kim, and N. Moon (2013b), Impacts of urban land-surface forcing on ozone air quality in the Seoul metropolitan area, Atmos. Chem. Phys, 13, 2177–2194, doi:10.5194/acp-13-2177-2013.

Ryu, Y. H., and J. J. Baik (2013), Daytime local circulations and their interactions in the Seoul metropolitan area, J. Appl. Meteorol. Climatol., 52(4), 784–801, doi:10.1175/JAMC-D-12-0157.1.

Sakurai, N., F. Murata, M. D. Yamanaka, S. Mori, J.-I. Hamada, H. Hashiguchi, Y. I. Tauhid, T. Sribimawati, and B. Suhardi (2005), diurnal cycle of cloud system migration over Sumatera island, J. Meteorol. Soc. Japan, 83(5), 835–850, doi:10.2151/jmsj.83.835.

Salamanca, F., A. Martilli, M. Tewari, and F. Chen (2011), A study of the urban boundary layer using different urban parameterizations and high-resolution urban canopy parameters with WRF, J. Appl. Meteorol. Climatol., 50(5), 1107–1128, doi:10.1175/2010JAMC2538.1.

Salimun, E., F. Tangang, and L. Juneng (2010), Simulation of heavy precipitation episode over eastern Peninsular Malaysia using MM5: sensitivity to cumulus parameterization schemes, Meteorol. Atmos. Phys., 107(1–2), 33–49, doi:10.1007/s00703-010-0067-y.

Salleh, S. A., Z. Abd.Latif, W. M. N. W. Mohd, and A. Chan (2013), Factors contributing to the formation of an urban heat island in Putrajaya, Malaysia, Procedia - Soc. Behav. Sci., 105, 840–850, doi:10.1016/j.sbspro.2013.11.086.

Sanderson, M. G. (2003), Effect of climate change on isoprene emissions and surface ozone levels, Geophys. Res. Lett., 30(18), 10–13, doi:10.1029/2003GL017642.

Sani, S. (1977), Aspects of air pollution climatology in the Kuala Lumpur-Petaling Jaya area, Malaysia, University of Canterbury.

Sani, S. (1984), Urban development and changing patterns of night time temperatures in the Kuala Lumpur- Petaling Jaya area Malaysia, J. Teknol., 5, doi:10.11113/jt.v5.937.

Sani, S. (1986), The effects of urbanization on cliamte in Kuala Lumpur and the Klang Valley, in Design for High Intensity Development, edited by M. B. Svenko, pp. 67–74, Cambridge, Massachusetts.

Santamouris, M. (2015), Analyzing the heat island magnitude and characteristics in one hundred Asian and Australian cities and regions, Sci. Total Environ., 512–513, 582–598, doi:10.1016/j.scitotenv.2015.01.060.

Sarrat, C., A. Lemonsu, V. Masson, and D. Guedalia (2006), Impact of urban heat island on regional atmospheric pollution, Atmos. Environ., 40(10), 1743–1758, doi:10.1016/j.atmosenv.2005.11.037.

Sasaki, T., P. Wu, S. Mori, J. I. Hamada, Y. I. Tauhid, M. D. Yamanaka, T. Sribimawati, T. Yoshikane, and F. Kimura (2004), Vertical moisture transport above the mixed layer around the mountains in western Sumatra, Geophys. Res. Lett., 31(8), 2–5, doi:10.1029/2004GL019730.

Sato, T., and F. Kimura (2005), Diurnal cycle of convective instability around the central mountains in Japan during the warm season, J. Atmos. S, 62, 1626–1636, doi:10.1175/JAS3423.1.

Schlünzen, K. H., and J. J. Katzfey (2003), Relevance of sub-grid-scale land-use effects for mesoscale models, Tellus, 55A, 232–246, doi:10.1034/j.1600-0870.2003.00017.x.

Schultz, M. et al. (2007), RETRO Deliverable D1-6, Report on Emissions, Hamburg.

Seasman, N. L., F. L. Ludwig, E. G. Donall, T. T. Warner, and C. M. Bhumralkar (1988), Numerical Studies of Urban Planetary Boundary-Layer Structure under Realistic Synoptic Conditions, J. Appl. Meteorol., 28, 760–781, doi:10.1175/1520-0450(1989)028.

Seidel, D. J., C. O. Ao, and K. Li (2010), Estimating climatological planetary boundary layer heights from radiosonde observations: Comparison of methods and uncertainty analysis, J. Geophys. Res. Atmos., 115(16), 1–15, doi:10.1029/2009JD013680.

Sertel, E., A. Robock, and C. Ormeci (2009), Impacts of land cover data quality on regional climate, Int. J. Climatol., 1–12, doi:10.1002/joc.

Sharma, A. et al. (2016a), Green and cool roofs to mitigate urban heat island effects in the Chicago metropolitan area: evaluation with a regional climate model, Environ. Res. Lett., 11(6), 64004, doi:10.1088/1748-9326/11/6/064004.

Sharma, A., H. J. S. Fernando, A. F. Hamlet, J. J. Hellmann, M. Barlage, and F. Chen (2016b), Urban meteorological modeling using WRF: a sensitivity study, Int. J. Climatol., doi:10.1002/joc.4819.

Shepherd, J. M. (2005), A review of current investigations of urban-induced rainfall and recommendations for the future, Earth Interact., 9(12), 1–27, doi:10.1175/EI156.1.

Shin, H. H., and S.-Y. Hong (2011), Inter-comparison of planetary boundary-layer parametrizations in the WRF Model for a single day from CASES-99, Boundary-Layer Meteorol., 139(2), 261–281, doi:10.1007/s10546-010-9583-z.

Sillman, S. (1999), The relation between ozone, NOx and hydrocarbons in urban and polluted rural environments, Atmos. Environ., 33, 1821–1845.

Silva, S. J., C. L. Heald, J. A. Geddes, K. G. Austin, P. S. Kasibhatla, and M. E. Marlier (2016), Impacts of current and projected oil palm plantation expansion on air quality over Southeast Asia, Atmos. Chem. Phys, 16, 10621–10635, doi:10.5194/acp-16-10621-2016.

Skamarock, W. C., J. B. Klemp, D. O. Gill, D. M. Barker, M. G. Duda, W. Wang, and J. G. Powers (2008), A description of the Advanced Research WRF Version 3, Boulder, Colorado, USA.

Sohrabinia, M., W. Rack, and P. Zawar-reza (2012), Analysis of MODIS LST compared with WRF model and in situ data over the Waimakariri River Basin, Canterbury, New Zealand, Remote Sens., 4, 3501–3527, doi:10.3390/rs4113501.

Sow, K. S., L. Juneng, F. T. Tangang, A. G. Hussin, and M. Mahmud (2011), Numerical simulation of a severe late afternoon thunderstorm over Peninsular Malaysia, Atmos. Res., 99(2), 248–262, doi:10.1016/j.atmosres.2010.10.014.

Steyn, D. G. (1996), Air pollution in coastal cities, in Air Pollution Modeling and Its Application XI, edited by G. and Schiermeier, pp. 505–518, Plenum Press, New York.

Stockwell, W. R., P. Middleton, J. S. Chang, and X. Yang (1990), The second generation Regional Acid Deposition Model Chemical Mechanism for Regional Air Quality Modeling, J. Geophys. Res., 95(D10), 16343–16367.

Strahler, A., D. Muchoney, J. Borak, M. Friedl, S. Gopal, E. Lambin, and A. Moody (1999), MODIS land cover product Algorithm Theoretical Basis Document (ATBD) Version 5.0, MODIS Land Cover and Land-Cover Change, Boston, US.

Streets, D. G. et al. (2003), An inventory of gaseous and primary aerosol emissions in Asia in the year 2000, J. Geophys. Res., 108(D21), 8809, doi:10.1029/2002JD003093.

Stull, R. B. (1988), An introduction to boundary layer meteorology, Book, 13, 666, doi:10.1007/978-94-009-3027-8.

Taha, H., S. Konopacki, and H. Akbari (1998), Impacts of lowered urban air temperatures on precursor emission and ozone air quality, J. Air Waste Manag. Assoc., 48(9), 860–865, doi:10.1080/10473289.1998.10463733.

Tan, K. C., H. S. Lim, and M. Z. Mat Jafri (2014), Multiple regression analysis in modeling of columnar ozone in Peninsular Malaysia, Environ. Sci. Pollut. Res. Int., 21, 7567–77, doi:10.1007/s11356-014-2697-y.

Tangang, F. T., and L. Juneng (2004), Mechanisms of Malaysian rainfall anomalies, J. Clim., 17(18), 3616–3622, doi:10.1175/1520-0442(2004)017<3616:MOMRA>2.0.CO;2.

Teo, C., T. Koh, J. LO Chun-fung, and B. Chandra Bhatt (2011), Principal component analysis of observed and modeled diurnal rainfall in the Maritime Continent, J. Clim., 24, 4662–4675, doi:10.1175/2011JCLI4047.1.

Thielen, J., W. Wobrock, A. Gadian, P. G. Mestayer, and J. D. Creutin (2000), The possible influence of urban surfaces on rainfall development: A sensitivity study in 2D in the meso-γ-scale, Atmos. Res., 54(1), 15–39, doi:10.1016/S0169-8095(00)00041-7.

The NCAR Command Language (Version 6.3.0) [Software]. (2016). Boulder, Colorado: UCAR/NCAR/CISL/TDD. Accessed http://dx.doi.org/10.5065/D6WD3XH5

The World Bank (2017) World Development Indicators: Population Growth Rate (1960-2015), available online at: http://databank.worldbank.org/data/ [accessed on 7 March 2017]

Thompson, W. T., T. Holt, and J. Pullen (2007), Investigation of a sea breeze front in an urban environment, Q. J. R. Meteorol. Soc., 133, 579–594, doi:10.1002/qj.52.

Tie, X., G. Brasseur, and Z. Ying (2010), Impact of model resolution on chemical ozone formation in Mexico City: application of the WRF-Chem model, Atmos. Chem. Phys. Atmos. Chem. Phys., 10, 8983–8995, doi:10.5194/acp-10-8983-2010.

Troen, I. B., and L. Mahrt (1986), A simple model of the atmospheric boundary layer; sensitivity to surface evaporation, Bound. Layer Meteorol., 37, 129–148.

Tso, C. P. (1996), A survey of urban heat island studies in two tropical cities, Atmos. Environ., 30(3), 507–519, doi:10.1016/1352-2310(95)00083-6.

United Nations (2014), World urbanization prospects: The 2014 Revision, Highlights, New York.

University of Wyoming (updated daily), Atmospheric soundings: Upper air soundings. Department of Atmospheric Science, University of Wyoming, Wyoming. Accessed [July 1, 2014] http://weather.uwyo.edu/upperair/sounding.html

Varikoden, H., A. A. Samah, and C. A. Babu (2010), Spatial and temporal characteristics of rain intensity in the peninsular Malaysia using TRMM rain rate, J. Hydrol., 387(3–4), 312–319, doi:10.1016/j.jhydrol.2010.04.023.

Valuntaite, V., V. Šerevičiene, R. Girgždiene, and D. Paliulis (2012), Relative humidity and temperature impact to ozone and nitrogen oxides removal rate in the experimental chamber, J. Environ. Eng. Landsc. Manag., 20(1), 35–41, doi:10.3846/16486897.2011.633335.

Von Glasow, R. et al. (2013), Megacities and large urban agglomerations in the coastal zone: Interactions between atmosphere, land, and marine ecosystems, Ambio, 42(1), 13–28, doi:10.1007/s13280-012-0343-9.

Wang, B., R. Wu, and K.-M. Lau (2001), Inter-annual variability of the Asian summer monsoon : Contrasts between the Indian and the Western North Pacific – East Asian Monsoons, J. Clim., 14, 4073–4090, doi:10.1175/1520-0442(2001)014<4073:IVOTAS>2.0.CO;2.

Wang, H., L. Fu, and J. Chen (2010), Developing a high-resolution vehicular emission inventory by integrating an emission model and a traffic Model: Part 2—A Case Study in Beijing, J. Air Waste Manage. Assoc., 60(12), 1471–1475, doi:10.3155/1047-3289.60.12.1471.

Wang, W. et al. (2015), WRF-ARW V3.6.1: User’s Guide, Boulder, Colorado, USA.

Wang, X. M., W. S. Lin, L. M. Yang, R. R. Deng, and H. Lin (2007), A numerical study of influences of urban land-use change on ozone distribution over the Pearl River Delta region, China, Tellus, 59B, 633–641, doi:10.1111/j.1600-0889.2007.00271.x.

Willmott, C. J., and K. Matsuura (2005), Advantages of the mean absolute error (MAE) over the root mean square error (RMSE) in assessing average model performance, Clim. Res., 30, 79–82.

World Health Organisation (2005), Air quality guidelines for particulate matter, ozone, nitrogen dioxide and sulfur dioxide, Switzerland.

Wu, S., L. J. Mickley, J. O. Kaplan, and D. J. Jacob (2012), Impacts of changes in land use and land cover on atmospheric chemistry and air quality over the 21st century, Atmos. Chem. Phys., 12, 1597–1609, doi:10.5194/acp-12-1597-2012.

Xie, B., J. C. H. Fung, A. Chan, and A. Lau (2012), Evaluation of nonlocal and local planetary boundary layer schemes in the WRF model, J. Geophys. Res. Atmos., 117(D12103), 1–26, doi:10.1029/2011JD017080.

Yu, M., G. R. Carmichael, T. Zhu, and Y. Cheng (2012), Sensitivity of predicted pollutant levels to urbanization in China, Atmos. Environ., 60, 544–554, doi:10.1016/j.atmosenv.2012.06.075.

Yu, S., B. Eder, R. Dennis, S.-H. Chu, and S. E. Schwartz (2006), New unbiased symmetric metrics for evaluation of air quality models, Atmos. Sci. Lett., 7(1), 26–34, doi:10.1002/asl.125.

Zhang, N., L. Zhu, and Y. Zhu (2011), Urban heat island and boundary layer structures under hot weather synoptic conditions: A case study of Suzhou City, China, Adv. Atmos. Sci., 28(4), 855–865, doi:10.1007/s00376-010-0040-1.

Zhang, Q., D. G. Streets, G. R. Carmichael, K. B. He, H. Huo, A. Kannari, Z. Klimont, I. S. Park, and S. Reddy (2009), Asian emissions in 2006 for the NASA INTEX-B mission, Atmos. Chem. Phys., 9, 5131–5153.

Zhao, L., X. Lee, R. B. Smith, and K. Oleson (2014), Strong contributions of local background climate to urban heat islands, Nature, 511(7508), 216–219, doi:10.1038/nature13462.

Zhong, S., and X. Q. Yang (2015), Ensemble simulations of the urban effect on a summer rainfall event in the Great Beijing Metropolitan Area, Atmos. Res., 153(2015), 318–334, doi:10.1016/j.atmosres.2014.09.005.

LIST OF PUBLICATIONS AND PAPERS PRESENTED

Published papers:

M.C.G. Ooi, A. Chan, M.J. Ashfold, K.I. Morris, M.Y. Oozeer, S. Aekbal Salleh (2017) Numerical Study on Effect of Urban Heating on Local Climate during Calm Inter-Monsoon Period in Greater Kuala Lumpur, Malaysia. Urban Climate, 20, pp. 228-250, 2017. ***(Thesis Chapter 3)***

Research manuscripts submitted (under review status):

M.C.G. Ooi, A. Chan, K., Subramaniam, K.I., Morris, M.Y. Oozeer. (-) Interaction of urban heating and topographic-induced circulation during the calm inter-monsoon seasons in the tropics. Journal of Geophysical Research: Atmosphere. (1st revision submitted on 9 July 2017) ***(Thesis Chapter 5)***

M.C.G. Ooi, A. Chan, M.A. Ashfold, M.Y. Oozeer, K.I., Morris. (-) The role of land use on the local climate and ground ozone level during calm inter-monsoon in a tropical city. Geoscience Frontiers. (Manuscript submitted on 10 Apr 2017) ***(Thesis Chapter 6)***

Conferences presentation:

M.C.G. Ooi, K.I. Morris, M.Y. Oozeer, A. Chan, S. Aekbal Salleh (2014) Urban heat island phenomenon and ozone formation in Putrajaya, Malaysia [presentation]. Urban Environmental Pollution 2014 (UEP2014) Conference, Toronto, Canada.

M.C.G. Ooi, A. Chan, Kumarenthiran Subramaniam, S. Aekbal Salleh, M.Y. Oozeer, K.I. Morris, Temperature Response of Boundary Layer Schemes on Urbanization Level in Klang Valley, Malaysia [presentation]. Asia Oceania Geoscience Society (AOGS), Singapore. ***(Thesis Chapter 4)***

APPENDIX

A.1 Software Installation and Operation

A.1.1 Shell Installation

bash, ksh, csh, bsh

A.1.2 Library installation

From software center:

a) gfortran (& gfortran-multilib, gfortran4.6-multilib)
b) C (gcc)
c) Java pure (gcj – gnu java compiler)
d) perl
e) Python
f) m4
g) libmpich2-dev
h) autotools (autoconfig, automake)

From respective software developer:

i) Grib 2 – libgrib2c-dev, libgrib2c0d
j) Zlib
k) png
l) jasper
    1. Install jasper version 1.701.0.
    2. File obtained from http://www.ece.uvic.ca/~frodo/jasper/
    3. configure into /usr/local, make, sudo make install

A.1.3 Netcdf installation (Version 4.1.3)

1) Download source file version 4.1.3 at http://www2.mmm.ucar.edu/wrf/OnLineTutorial/compile_tutorial/tar_files/netcdf-4.1.3.tar.gz

2) Setting environment variables (in .bashrc)

```
export NETCDF=/usr/local; export LD_LIBRARY_PATH=/usr/local/lib
export CPPFLAGS=-I/usr/local/include
export LDFLAGS=-L/usr/local/lib
```

If library is more than two (eg. Hdf5 folder is built in /usr/local, add another link into CPPFLAGS by using *export CPPFLAGS="-I/usr/local/include -I/usr/local/hdf5/include"*

if any problem regarding not a valid identifier, please retype the inverted commas "" within the terminal again

3) Installation steps (for building with classic library only)

- **Configure**:

```
./configure --prefix/usr/local --enable-shared --disable-netcdf-4 --disable-dap-remote-tests
make check
sudo make install
```

```
--if reinstall: make clean
```

- **Possible Errors**:

a) Can't find or link to the hdf5 library. Use --disable-netcdf-4, or see config.log for errors
   - Solution: install hdf5 library

b) configure: error: NetCDF-4 requires HDF5, but hdf5.h cannot be found.
   - Solution: install hdf5 prebuilt binaries

c) From config.log,
   - /usr/bin/ld: cannot find -lcurl
     - ✓ Resolved after including CPPFLAGS=-I/home/usr/local/include
   - /usr/bin/ld: cannot find -lzib1 (confirm?)
   - /usr/bin/ld: cannot find -lhdf5dll (confirm?)
   - /usr/bin/ld: cannot find -hdf5 (confirm?)

d) unsuccessful for hdf, temporarily give up for hdf: --disable-netcdf4
   - WRFV3.3.1 doesn't support netcdf4 year so need to disable.

e) make check no successful: --disable-dap-remote-tests
   - ERROR: "syntax error, unexpected SCAN_WORD, expecting SCAN_ATTR or SCAN_DATASET or SCAN_ERROR"
   - According to http://www.unidata.ucar.edu/support/help/MailArchives/netcdf/msg10778.html, it's a remote access testing of OpenDAP, it might be a problem of server down or occupation of server, so temporary solution is skipping the test

4) If successful, show a square with **"Congratulations! You have successfully installed netCDF"**

A.1.4 WRF-ARW installation

1) Setting environment variables:

```
export WRF_EM_CORE=1
export WRF_NMM_CORE=0
export WRF_DA_CORE=0
export OMP_NUM_THREADS=4
export MP_STACK_SIZE=2M
```

2) Installation steps:

```
./configure
./compile em_real
```

A.1.5 WRF-CHEM installation

1) Install chem package for WRF (enabling WRF_CHEM in environment variable)
2) Install general emission preprocessor - prep_chem_src (convert_emiss.exe)
3) Install megan input preprocessor (megan_bio_emiss.exe)
4) Install MOZART-4 boundary condition preprocessor (mozbc)

A.1.6 WPS Installation

```
./configure – current version: Linux i486 i586 i686, gfortran (dmpar) – with GRIB2
./compile >& compile.log
```

Status: installed successfully with no error

Execution and description file should be compiled in the installed directory as below:

No	**Util**	**Description**
1	*avg_tsfc.exe*	Computes daily mean surface temperature from intermediate files. *Recommended for using with the 5-layer soil model (sf_surface_physics = 1) in WRF*
2	*g1print.exe*	List the contents of a GRIB1 file
3	*g2print.exe*	List the contents of a GRIB2 file
4	*mod_levs.exe*	Remove superfluous levels from 3-d fields in intermediate files
5	*calc_ecmwf_p.exe*	Create a pressure field for use with ECMWF sigma-level data sets
6	*plotfmt.exe*	Plot intermediate files *(dependent on NCAR Graphics - if you don't have these libraries, plotfmt.exe will not compile correctly)*
7	*plotgrids.exe*	Generate domain graphics. An excellent tool to configure domains before running geogrid.exe *(dependent on NCAR Graphics - if you don't have these libraries, plotgrids.exe will not compile correctly)*
8	*rd_intermediate.exe*	Read intermediate files

A.1.7 Ncar Command Language (NCL)

1. Obtained prebuilt binary from :http://ngwww.ucar.edu/
2. NCL command language 6.0.0
3. Set environment variable
4. Extra packages to install:
    a) Install **libx11-dev** [installed version: 2:1.4.99.1-0]
    b) Install **xorg-dev**
    c) Install **libxrender-dev** [installed version: 1:0.9.6-2]
    d) Install **libxext**
        1. **x11proto-xext-dev** [installed version: 7.2.0-3]
        2. Install **xmlto** (XML-to-any converter: software center)- tick all the check box
        3. Install xorg-macros (util-macros-1.17: http://www.x.org/releases/X11R7.7/src/util/)
        a. ./configure=/usr/local, make, sudo make install
        4. Install **xsltproc** (installed)
        5. All x files can be get from http://www.x.org/releases/X11R7.7/src/
        6. Install **libxext-dev, libxext6-dbg, libxmu-dev** from software center
    e) Install **libbz2-dev** [installed version 1.0.6-1] from software center

5. Testing of ncar
    a. ng4ex gsun01n
    b. ncargex cpex08 -clean ; ctrans -d X11 cpex08.ncgm

6. NCAR Tutorial available: http://www.ncarg.ucar.edu/fund/fundhome.html

A.1.8 Working on WPS

1) Running geogrid.exe
    a) Update namelist.wps is being specified (see Section A.1.12)
    b) link executables into the folder
    c) copy geogrid.tbl file into the working directory
    d) Run geogrid.exe & obtain a .nc file

* MODIS land use data can only use for Noah LSM

```
ln -sf ~/WRF/WPS/*.exe .
cp ~/WRF/WPS/namelist.wps .
cp ~/WRF/WPS/geogrid/GEOGRID.TBL.NMM
~/WRF/WPS/geogrid/GEOGRID.TBL
./geogrid.exe
```

2) Running on ungrib.exe
    a) Obtain grib1 input data and create in another file
    b) Run all grib1 file with link_grib.csh, create links of GRIBFILE.AAA and file directory should not contain spacing
    c) Link -sf the correct Vtable in ungrib/Variable_Tables into working directory
    d) Run ungrib.exe >& ungrib.log
    e) Obtained FILE:yyyy-mm-dd_hh intermediate file. Check with util/rd-intermediate.exe or using util/plotfmt.exe
    f) Data obtained from: http://rda.ucar.edu/

```
ln -sf ~WRF/WPS/link_grib.csh
./link_grib.csh ../../../GRIBdata/NAM/20050123_f00_i0
ln -sf ~/WRF/WPS/ungrib/Variable_Tables/Vtable.NAM Vtable
./ungrib.exe >& ungrib.log
```

3) Running on metgrid.exe
    a) Copy metgrib.tbl & metgrib.tbl.nmm file into working direcory
    b) In namelist specify where is metgrid.tbl file.
    c) Run metgrid.exe and obtain all nc file. Contents can be viewed with ncdump –h

```
cp ~/WRF/WPS/metgrid/METGRID.TBL.NMM
~/WRF/metgrid/METGRID.TBL
./metgrid.exe
```

A.1.9 Working on WRF

1) Running real
    a) Copy running files into working directory

```
ln -sf ../../../WRFV3/run/*_DATA .
ln -sf ../../../WRFV3/run/*.TBL .
ln -sf ../../../WRFV3/run/tr* .
ln -sf ../../../WRFV3/run/*.txt .
ln -sf ../../../WRFV3/run/*.tbl .
ln -sf ../../../WRFV3/run/co2* .
ln -sf ../../../WRFV3/main/*.exe .
ln -sf ../../../WRFV3/run/ETAMPNEW_DATA.expanded_rain
copy namelist.input
link metgrid files
```

b) Update namelist.input file (see Section A.1.12)
c) Run real.exe
d) Error of NetCDF attribute not found can be ignored, it's due to the lack of some parameters from Vtable chose during ungrib.
e) Boundary conditions (wrfbdy_d01) and initial conditions (wrfinput_d01) will be created.

2) Running wrf
a) Run wrf.exe
b) Obtain wrf output file with wrfout_d01_date_time

3) Nesting
a) Buffer zone
    1. Minimum distance between parent domain and nested domain is at least 4 grid cell
    2. Since the parent and nested domain ratio is 3, therefore it is reasonable to have around 1/3 of buffer zone surrounding the nested domain.
b) If parent_grid_ratio is 3, then parent_time_step_ratio is also 3. Nest domains need 3 times as many time steps to keep pace with parent domain
    1. Grid_ratio: Normally odd number is chosen for real time data case
    2. Reduce time step can ensure the stability of coarse grid, but more expensive
    3. Reduce the time step ratio of nest domains, will be cheaper
c) Cost saving & time saving
    1. Double coarse grid points
d) If there is a stability problem, then it is most probably caused by the coarse grid

A.1.10 Working on WRF-Chem

1) Run WPS (A.1.8) and check output

2) Run real.exe with disabled chem function (adjust in namelist.input) and check wrfinput and wrfbdy output

3) Run convert_emiss.exe for chemical initial condition with prep_chem_src.inp for each domain

4) Run megan_bio_emiss.sh for biogenic emission initial condition with megan_bio_emiss.inp

5) Link and rename all the output files from 3 and 4 into working directory

6) Run real.exe with chem function (Refer to Appendix A.1.12)
7) Run mozbc for to edit the lateral chemical condition for wrfinput and wrfbdy
8) Run wrf.exe for chem (Refer to Appendix A.1.12) with updated wrfinput and wrfbdy

A.1.11 Post processing

A.1.11.1 Data extraction from wrf output file:

Method 1: NCO

The WRF output file for the finest domain is usually of the size above 30 GB. It is time-consuming to download from the cluster server and for further processing. NETCDF operators (NCO) is a regularly-updated freeware[8] intended to extracted file saved in NETCDF format. It comes with numerous in-line commands to subset, calculate and modify variables of the NETCDF file.

Method 2: ncdump

Ncdump is a simple software to check the content of the NETCDF file. The most used function is the display the header file information for the NETCDF.

Method 3: netcdf4excel

This is a Windows macro file as add-ins for Microsoft Excel. It is similar to ncdump but the output file will be delimited and organised in the xlsx format. For every use, you will need to open NetCDF4Excel_2007.xlsm file. Link for download is http://code.google.com/p/netcdf4excel/.

A.1.11.2 Running NCL (post processor)

NCL is one of the most commonly used visualization tool for the WRF output [*The NCAR Command Language,* 2016]. It dedicates a page solely for WRF users with guides and template script, hence it is easier to pick up compared to other tools. On top of that, the NCL does not have a graphical user interface (GUI) and can be more efficient in processing the diagram. This powerful tool is able to produce xy-plot, contour plot, vector plot, etc., hence most of the diagrams in this thesis are produced with NCL. Refer to http://www.ncl.ucar.edu/Applications/wrf.shtml for WRF script templates.

---

[8] Official download link: http://nco.sourceforge.net/

A.1.12 Namelist files

A.1.12.1 namelist.wps

```
&share
 wrf_core = 'ARW',
 max_dom = 4,
 start_date  =  '2003-10-01_00:00:00','2003-10-01_00:00:00','2003-10-01_00:00:00','2003-10-01_00:00:00','2003-10-01_00:00:00',
 end_date    =  '2003-10-20_00:00:00','2003-10-20_00:00:00','2003-10-20_00:00:00','2003-10-20_00:00:00','2003-10-20_00:00:00',
 interval_seconds = 21600,
 io_form_geogrid = 2,
/

&geogrid
 parent_id         =   0,   1,   2,   3, 4,
 parent_grid_ratio =   1,   3,   3,   3, 3,
 i_parent_start    =   1,   29,  20,  25, 18,
 j_parent_start    =   1,   38,  30,  28,25,
 e_we              =  110,   100,  100, 139,136,
 e_sn              =  100,   103,  100,  148,151,
 geog_data_res     =  'modis_30s+10m',  'modis_30s+5m',  'modis_30s+2m' ,'modis_30s+30s','modis_30s+30s'
 dx = 27000,
 dy = 27000,
 map_proj = 'mercator',
 ref_lat   =  2.5,
 ref_lon   = 105,
 truelat1  =  0.0,
 stand_lon = 102.0,
 geog_data_path = '/home/WRF_DATA/maggie/geog',
 opt_geogrid_tbl_path='/home/ezaog1/cases/case029'
/

&ungrib
 out_format = 'WPS',
 prefix = 'FILE',
/

&metgrid
 fg_name = 'FILE','PRES'
 io_form_metgrid = 2,
 OPT_METGRID_TBL_PATH='/home/ezaog1/cases/case029',
/
```

A.1.12.2 namelist.input

```
&time_control
 run_days                 = 0,
 run_hours                = 456,
 run_minutes              = 0,
 run_seconds              = 0,
 start_year               = 2003, 2003, 2003, 2003,
 start_month              = 10,   10,   10, 10,
 start_day                = 01,   01,   01, 01,
 start_hour               = 00,   00,   00, 00,
 start_minute             = 00,   00,   00, 00,
 start_second             = 00,   00,   00, 00,
 end_year                 = 2003, 2003, 2003,2003,
 end_month                = 10,   10,   10, 10,
 end_day                  = 20,   20,   20, 20,
 end_hour                 = 00,   00,   00,00,
 end_minute               = 00,   00,   00,00,
 end_second               = 00,   00,   00,00,
 interval_seconds         = 21600,
 input_from_file          = .true.,.true.,.true.,.true.,
 history_interval         = 480, 480, 480,60,
 frames_per_outfile       = 480, 480, 480,480,
 restart                  = .false.,
 restart_interval         = 1440,
 auxinput4_inname               = "wrflowinp_d<domain>",
 auxinput4_interval             = 360,
 io_form_auxinput4              = 2,
 io_form_history          = 2,
 io_form_restart          = 2,
 io_form_input            = 2,
 io_form_boundary         = 2,
 debug_level              = 1,
 /

 &domains
 time_step                = 150,
 time_step_fract_num      = 0,
 time_step_fract_den      = 1,
 max_dom                  = 4,
 e_we                     = 110,   100,   100,    139,
 e_sn                     = 100,   103,   100,    148,
 e_vert                   = 37,    37,    37,    37, ,
 num_metgrid_levels       = 61,
 num_metgrid_soil_levels  = 4,
 dx                       = 27000, 9000, 3000, 1000,
 dy                       = 27000, 9000,  3000, 1000,
 grid_id                  = 1,     2,     3,    4,
 parent_id                = 0,     1,     2,    3,
 i_parent_start           = 1,     29,    20,   25,
```

```
 j_parent_start                  = 1,     38,    30,   28,
 parent_grid_ratio                  = 1,     3,     3,    3,
 parent_time_step_ratio             = 1,     3,     3,    3,
 p_top_requested                   = 5000,
 eta_levels                             =
1.0,0.9958,0.9916,0.9874,0.9832,0.9789,0.9705,0.9621,0.9537,0.9453,0.9368,0.9284,0.9179,
0.9074,0.8968,0.8863,0.8705,0.8547,0.8389,0.8158,0.7895,0.7632,0.7368,0.7053,0.6737,0.6
421,0.6105,0.5684,0.5263,0.4842,0.4316,0.3789,0.3158,0.2526,0.1789,0.0947,0.0
 numtiles                               = 4,
 feedback                        = 1,
 smooth_option                      = 0,
 /
 sfcp_to_sfcp                     = .true.

 &physics
 mp_physics                        = 2,    2,     2,   2,
 ra_lw_physics                      = 4,     4,     4,   4,
 ra_sw_physics                      = 4,     4,     4,   4,
 radt                          = 30,    30,   30,  30,
 sf_sfclay_physics                  = 2,     2,     2,   2,
 sf_surface_physics                  = 2,     2,     2,   2,
 bl_pbl_physics                     = 2,     2,     2,   2,
 bldt                          = 0,     0,     0,   0,
 cu_physics                       = 2,     2,     0,   0,
 cudt                           = 0,     0,     0,   0,
 ishallow                         = 0,
 isfflx                         = 1,
 ifsnow                          = 1,
 icloud                          = 1,
 iz0tlnd                           = 1,
 surface_input_source               = 1,
 num_soil_layers                    = 4,
 sf_urban_physics                    = 0,     0,     1,    1,
 num_land_cat                           = 33,
 sst_update                             = 1,
 usemonalb                              = .true.
 /

 &fdda
 /

 &dynamics
 w_damping                          = 0,
 diff_opt                        = 1,
 km_opt                           = 4,
 diff_6th_opt                      = 0,      0,      0,   0,
 diff_6th_factor                    = 0.12,   0.12,   0.12,   0.12,
 base_temp                         = 290.,
 damp_opt                          = 0,
 zdamp                          = 5000.,  5000.,  5000., 5000.,
```

```
dampcoef                    = 0.2,    0.2,    0.2,   0.2, ,
khdif                    = 0,      0,      0,   0,
kvdif                    = 0,      0,      0,   0,
non_hydrostatic             = .true., .true., .true., .true.,
moist_adv_opt               = 1,      1,      1,   1,
scalar_adv_opt              = 1,      1,      1,   1,
/

&bdy_control
spec_bdy_width               = 5,
spec_zone                   = 1,
relax_zone                  = 4,
specified                 = .true., .false.,.false.,.false.,
nested                    = .false., .true., .true.,.true.,
/

&namelist_quilt
nio_tasks_per_group = 0,
nio_groups = 1,
/
```

A.1.12.3 namelist.input.chem

```
&time_control
 run_days                    = 0,
 run_hours                   = 216,
 run_minutes                  = 0,
 run_seconds                  = 0,
 start_year                  = 2003, 2003, 2003, 2003,2003,
 start_month                  = 10,   10,   10, 10,10,
 start_day                   = 01,   01,   01, 01,01,
 start_hour                  = 00,   00,   00, 00,00,
 start_minute                 = 00,   00,   00, 00,00,
 start_second                 = 00,   00,   00, 00,00,
 end_year                     = 2003, 2003, 2003, 2003,2003,
 end_month                     = 10,   10,   10, 10,10,
 end_day                     = 10,   10,   10, 10,10,
 end_hour                     = 00,   00,   00,00,00,
 end_minute                    = 00,   00,   00,00,00,
 end_second                    = 00,   00,   00,00,00,
interval_seconds               = 21600,
 input_from_file                = .true.,.true.,.true.,.true.,.true.,
 history_interval              = 480, 480, 60,60,60,
 frames_per_outfile               = 480, 480, 480,480,480,
 restart                   = .false.,
 restart_interval               = 12960,
```

```
auxinput4_interval                    = 360,
io_form_auxinput4                     = 2,
io_form_history                  = 2,
io_form_restart                  = 2,
io_form_input                    = 2,
io_form_boundary                   = 2,
auxinput5_inname                      = 'wrfchemi_d<domain>',
auxinput6_inname                   = 'wrfbiochemi_d<domain>',
auxinput7_inname                   = 'wrffirechemi_d<domain>',
auxinput8_inname                   = 'wrfchemi_gocart_bg_d<domain>',
auxinput12_inname                  = 'wrf_chem_input',
auxinput13_inname                  = 'wrfchemv_d<domain>',
auxinput5_interval_m               = 86400, 86400, 86400,86400,
auxinput7_interval_m               = 86400, 86400, 86400,86400,
auxinput8_interval_m               = 86400, 86400, 86400,86400,
auxinput13_interval_m               = 86400, 86400, 86400,86400,
io_form_auxinput2                  = 2,
io_form_auxinput5                  = 2,
io_form_auxinput6                  = 0,
io_form_auxinput7                  = 0,
io_form_auxinput8                  = 0,
io_form_auxinput12                  = 0,
io_form_auxinput13                  = 0,
debug_level                     = 100,
auxinput1_inname                   = "met_em.d<domain>.<date>",
/

&domains
time_step                      = 150,
time_step_fract_num                = 0,
time_step_fract_den                = 1,
max_dom                         = 3,
e_we                          = 110,   100,   100,    139,136,
e_sn                          = 100,   103,   100,    148, 151,
e_vert                        = 37,    37,    37,    37,37,
num_metgrid_levels                 = 61,
num_metgrid_soil_levels             = 4,
dx                            = 27000, 9000, 3000, 1000,
dy                            = 27000, 9000,  3000, 1000,
grid_id                        = 1,     2,     3,    4, 5,
parent_id                       = 0,     1,     2,    3,4,
i_parent_start                    = 1,     29,    20,   25,18,
j_parent_start                    = 1,     38,    30,   28,25,
parent_grid_ratio                   = 1,     3,     3,    3,3,
parent_time_step_ratio               = 1,     3,     3,    3,3,
p_top_requested                    = 5000,
eta_levels                              =
1.0,0.9958,0.9916,0.9874,0.9832,0.9789,0.9705,0.9621,0.9537,0.9453,0.9368,0.9284,0.9179,
```

```
0.9074,0.8968,0.8863,0.8705,0.8547,0.8389,0.8158,0.7895,0.7632,0.7368,0.7053,0.6737,0.6
421,0.6105,0.5684,0.5263,0.4842,0.4316,0.3789,0.3158,0.2526,0.1789,0.0947,0.0
 numtiles                          = 4,
 feedback                    = 1,
 smooth_option                 = 0,
 zap_close_levels              = 50,
 interp_type                 = 1,
 t_extrap_type                = 2,
 force_sfc_in_vinterp            = 0,
 use_levels_below_ground          = .true.,
 use_surface                  = .true.,
 lagrange_order                = 1,
 /
 sfcp_to_sfcp                 = .true.

 &physics
 mp_physics                   = 2,    2,     2,   2,2,
 progn                              = 1,    1,     1,   1,
 ra_lw_physics                 = 4,     4,     4,   4,4,
 ra_sw_physics                 = 4,     4,     4,   4,4,
 radt                      = 30,    30,   30,  30,30,
 sf_sfclay_physics              = 2,     2,     2,   2,2,
 sf_surface_physics              = 2,     2,     2,   2,2,
 bl_pbl_physics                = 2,     2,     2,   2,2,
 bldt                      = 0,     0,     0,   0,0,
 cu_physics                  = 2,     2,     0,   0,0,
 cu_diag                    = 0,     0,     0,   0,0,
 cudt                      = 0,     0,     0,   0,0,
 ishallow                   = 0,
 isfflx                    = 1,
 ifsnow                     = 1,
 icloud                    = 1,
 iz0tlnd                     = 1,
 surface_input_source             = 1,
 num_soil_layers               = 4,
 sf_urban_physics               = 0,     0,     1,    1, 0,
 num_land_cat                       = 33,
 sst_update                         = 1,
 usemonalb                          = .true.
 mp_zero_out                   = 2,
 mp_zero_out_thresh              = 1.e-12,
 cu_rad_feedback                = .false.,
 /

 &fdda
 /

 &dynamics
 rk_ord                     = 3,
 w_damping                     = 1,
```

```
diff_opt                 = 1,
km_opt                   = 4,
diff_6th_opt             = 0,      0,      0,   0,
diff_6th_factor          = 0.12,   0.12,   0.12,   0.12,
base_temp                = 290.,
damp_opt                 = 0,
zdamp                    = 5000.,  5000.,  5000., 5000.,
dampcoef                 = 0.2,    0.2,    0.2,   0.2,
khdif                    = 0,      0,      0,   0,
kvdif                    = 0,      0,      0,   0,
non_hydrostatic          = .true., .true., .true., .true.,
moist_adv_opt            = 2,      2,      2,   2,
scalar_adv_opt           = 2,      2,      2,   2,
chem_adv_opt             = 2,      2,      2,   2,
tke_adv_opt              = 2,      2,      2,   2,
time_step_sound          = 4,      4,      4,   4,
h_mom_adv_order          = 5,      5,      5,   5,
v_mom_adv_order          = 3,      3,      3,   3,
h_sca_adv_order          = 5,      5,      5,   5,
v_sca_adv_order          = 3,      3,      3,   3,
/

&bdy_control
spec_bdy_width           = 5,
spec_zone                = 1,
relax_zone               = 4,
specified                = .true., .false.,.false.,.false.,
nested                   = .false., .true., .true.,.true.,
/

&namelist_quilt
nio_tasks_per_group = 0,
nio_groups = 1,
/

&chem
kemit                    = 1,
chem_opt                 = 11,11,11,11,
bioemdt                  = 30,30,30,30,
photdt                   = 30,30,30,30,
chemdt                   = 0,0,0,0,
io_style_emissions       = 2,
emiss_opt                = 3,         3,3,3,
emiss_opt_vol            = 0,         0,          0,0,
emiss_ash_hgt            = 20000.,
chem_in_opt              = 0,         0,          0,0,
phot_opt                 = 2,         2,2,2,
gas_drydep_opt           = 1,         1,          1,1,
aer_drydep_opt           = 1,         1,          1,1,
bio_emiss_opt            = 3,         3,          3,3,
```

```
ne_area                          = 41,
dust_opt                    = 2,
dmsemis_opt                   = 1,
seas_opt                    = 2,
gaschem_onoff                  = 1,       1,1,1,
aerchem_onoff                  = 1,       1,1,1,
wetscav_onoff                 = 0,       0,0,0,
cldchem_onoff                  = 0,       0,0,0,
vertmix_onoff                 = 1,       1,1,1,
chem_conv_tr                  = 0,       0,0,0,
conv_tr_wetscav                  = 0,    0,0,0,
conv_tr_aqchem                          = 0,    0,0,0,
biomass_burn_opt                = 0,       0,0,0,
gas_bc_opt                   = 1,       1,1,1,
gas_ic_opt                   = 1,       1,1,1,
aer_bc_opt                   = 1,       1,1,1,
aer_ic_opt                   = 1,       1,1,1,
have_bcs_chem                  = .false., .false., .false.,.false.,
aer_ra_feedback                = 0,0,0,0,
aer_op_opt                   = 0,0,0,0,
diagnostic_chem                = 0,0,0,0,
/
```

A.2 Derivation of model output

A.2.1 Extraction of near-surface verification points with NCL script

```
;   Example script to produce plots for a WRF real-data run,
;   with the ARW coordinate dynamics option.

load "$NCARG_ROOT/lib/ncarg/nclscripts/csm/gsn_code.ncl"
load "$NCARG_ROOT/lib/ncarg/nclscripts/csm/gsn_csm.ncl"
load "$NCARG_ROOT/lib/ncarg/nclscripts/wrf/WRFUserARW.ncl"
load "$NCARG_ROOT/lib/ncarg/nclscripts/csm/contributed.ncl"
;load "./WRFUserARW.ncl"

begin
;
; The WRF ARW input file.
; This needs to have a ".nc" appended, so just do it.
  StatFile = addfile("/media/0c040666-40f0-4417-8c16-
a8b0442ef6a3/maggie/WRF/Cluster_data/case029/029_9/wrfout_d04_029_9.nc","r")

;  STATION_NAME = "Gombak"
 ; S_N = stringtointeger("80")  ; 81 from netcdf4excel
 ; W_E = stringtointeger("100") ; 101 from netcdf4excel

  STATION_NAME=(/"Gombak","Klang","PJ-JAS","Kajang","Shah
Alam","Subang","Sepang","Kuala Selangor","Kuala Lumpur"/)
; PJ_JAS station is not removed though it is not in use
; Because the excel file is prepared to include it
  S_N=(/80,52,63,50,62,64,19,87,66/)
  W_E=(/100,73,106,110,89,88,105,56,106/)
  WRFOUTBASEPATH = "/media/0c040666-40f0-4417-8c16-
a8b0442ef6a3/maggie/WRF/Cluster_data/case038"
  NESTNUM = "4"
  STARTTIME = "2003-10-01_00:00:00"
  NUMFORECASTHOURS = stringtointeger("456")
  FORECASTINTERVAL = stringtointeger("1")
  NCL_OUTPUT_FILENAME = "Multipoint_new_029-9.csv"

;**********************************************************
; Read in the data for these files
;**********************************************************

  StatArraySize = NUMFORECASTHOURS / FORECASTINTERVAL + 1
  StatTimestampArray = new((/StatArraySize/), string)

  dimStation=dimsizes(STATION_NAME)
;  StatStationArraySize=dimStation
  StatStationArraySize=StatArraySize
  StatStationArray=new((/StatStationArraySize/),string)
  StatS_N=new((/StatStationArraySize/),integer)
  StatW_E=new((/StatStationArraySize/),integer)
  StatNOx=0

  dataLine = StatStationArray

  do istat = 0, dimStation-1
  station_name=STATION_NAME
  StatStationArray(StatNOx)=station_name(istat)
```

```
  StatS_N(StatNOx)=S_N(istat)
  StatW_E(StatNOx)=W_E(istat)

  StatIdx = 0

    StatWindSpeed = new((/StatArraySize/), float)
    StatWindDir = new((/StatArraySize/), float)
    precip = new((/StatArraySize/), float)
    tsk = new((/StatArraySize/), float)
    t2 = new((/StatArraySize/), float)
    td2 = new((/StatArraySize/), float)
    q2 = new((/StatArraySize/), float)
    rh2 = new((/StatArraySize/), float)
    psfc = new((/StatArraySize/), float)
    hfx = new((/StatArraySize/), float)
    lh = new((/StatArraySize/), float)
    lu = new((/StatArraySize/), float)
    hgt = new((/StatArraySize/), float)
    pblh = new((/StatArraySize/), float)

    ; This section extracts from first set of wrfout forecast files
    do it = 0, NUMFORECASTHOURS, FORECASTINTERVAL

;;;;;;;;;;;;;;;;;;;;;;;;;;;;;;;;;;;;;;;;;;;;;;;;;;;;;;;;;;;;
; First get the variables we will need

   ; Wind speed and direction
   u10  = wrf_user_getvar(StatFile,"U10",it)      ; 3D U at mass points
   v10  = wrf_user_getvar(StatFile,"V10",it)      ; 3D V at mass points
   Windspd= sqrt(u10*u10+v10*v10)
   StatWindSpeed(StatIdx)=Windspd(StatS_N(StatNOx),StatW_E(StatNOx))

   ; Define a radians to degrees conversion factor for u,v wind dir computations
   R2DConvFactor = 45.0/atan(1.0)
   Winddir = atan2(u10,v10)*R2DConvFactor + 180.0
   StatWindDir(StatIdx)=Winddir(StatS_N(StatNOx),StatW_E(StatNOx))

   ; Precip
   RAINNC = StatFile->RAINNC(it,:,:)
   precip(StatIdx) = RAINNC(StatS_N(StatNOx),StatW_E(StatNOx))

   ; TSK
   TSK = wrf_user_getvar(StatFile, "TSK", it)                ;T2 in kelvin
   TSK = TSK-273.16
   tsk(StatIdx) = TSK(StatS_N(StatNOx),StatW_E(StatNOx))

   ; T2
   T2 = wrf_user_getvar(StatFile, "T2", it)                  ;T2 in kelvin
   T2 = T2-273.16
   t2(StatIdx) = T2(StatS_N(StatNOx),StatW_E(StatNOx))

   ; TD2
   TD2 = wrf_user_getvar(StatFile, "td2", it)                ;td2 in celcius
   td2(StatIdx) = TD2(StatS_N(StatNOx),StatW_E(StatNOx))

   ; Q2
   Q2 = StatFile->Q2(it,:,:)
```

```
    q2(StatIdx) = Q2(StatS_N(StatNOx),StatW_E(StatNOx))

    ; RH
    RH2 = wrf_user_getvar(StatFile, "rh2", it)                    ;td2 in celcius
    rh2(StatIdx) = RH2(StatS_N(StatNOx),StatW_E(StatNOx))

    ; PSFC
    PSFC = StatFile->PSFC(it,:,:)
    psfc(StatIdx) = PSFC(StatS_N(StatNOx),StatW_E(StatNOx))

    ; HFX
    HFX = StatFile->HFX(it,:,:)
    hfx(StatIdx) = HFX(StatS_N(StatNOx),StatW_E(StatNOx))

    ; LH
    LH = StatFile->LH(it,:,:)
    lh(StatIdx) = LH(StatS_N(StatNOx),StatW_E(StatNOx))

    ; Landuse
    LU = StatFile->LU_INDEX(it,:,:)
    lu(StatIdx) = LU(StatS_N(StatNOx),StatW_E(StatNOx))

    ; HGT
    HGT = StatFile->HGT(it,:,:)
    hgt(StatIdx) = HGT(StatS_N(StatNOx),StatW_E(StatNOx))

    ; PBLH
    PBLH = StatFile->PBLH(it,:,:)
    pblh(StatIdx) = PBLH(StatS_N(StatNOx),StatW_E(StatNOx))

      times  = chartostring(StatFile->Times)    ; convert to type string for plot
      StatTimestampArray(StatIdx) = times(it)
      StatIdx = StatIdx + 1
    end do       ; END OF TIME LOOP

  dataLine =       dataLine + "," + \
             StatStationArray(StatNOx) + "," + \
                 StatTimestampArray + "," + \
                     sprintf("%8.0f", StatS_N(StatNOx)) + "," + \
                     sprintf("%8.0f", StatW_E(StatNOx)) + "," + \
             sprintf("%8.2f", StatWindSpeed) + "," + \
             sprintf("%8.1f", StatWindDir) + "," + \
             sprintf("%8.3E", precip) + "," + \
             sprintf("%8.2f", rh2) + "," + \
             sprintf("%5.6f", t2) + "," + \
             sprintf("%8.6f", td2) + "," + \
             sprintf("%8.1f", psfc) + "," + \
             sprintf("%8.2f", hfx) + "," + \
             sprintf("%8.2f", lh) + "," + \
             sprintf("%8.0f", lu) + "," + \
             sprintf("%8.2f", pblh) + ","
; remove hgt (replace with pblh), remove tsk (replace with rh2)
    StatNOx = StatNOx + 1
  end do       ; END OF STATION LOOP
;;;;;;;;;;;;;;;;;;;;;;;;;;;;;;;;;;;;;;;;;;;;;;;;;;;;;;;;;;;;;;;;

; What we have now, folks, is a single column array, where each
```

```
; row is a full, formatted dataLine.  So, let's print this single
; column formatted array
   asciiwrite(NCL_OUTPUT_FILENAME, dataLine)

end
```

A.2.2 2-meter relative humidity (RH2)

The conversion method of Q2, T2 and PFSC into RH2 is extracted from ncl source code under WRF_RH in wrf_user.f:

$$T_k = T_2 \times (P_{SFC} \times 0.00001)^{C_c}$$

$$E_s = 10 \times C_{SVP1} \times \exp\left(\frac{C_{SVP2} \times T_k - C_{SVPT0}}{T_k - C_{SVP3}}\right)$$

$$Q_{vs} = \frac{C_{EP3} \times E_s}{0.01 \times P_{SFC} - (1 - C_{EP3}) \times E_s}$$

$$RH_2 = 100 \times \frac{Q_2}{Q_{vs}}$$

Where

Variables		
T2	:	2-meter temperature (in K)
PSFC	:	Surface pressure (in Pa)
Q_{vs}	:	Surface water vapor mixing ratio (kg/kg)
RH_2	:	2-meter relative humidity (in %)
Constant value		
C_c	:	0.285714
C_{SVP1}	:	0.6112
C_{SVP2}	:	17.67
C_{SVPT0}	:	273.15
C_{SVP3}	:	29.65
C_{EP_3}	:	0.622

A.2.3 10-meter wind direction (wdir10)

Hourly wind direction profile

1. Extract wind direction (wdir10) from wrf output file with ncl script. The range is 0 - 360°
2. Derive sin (wdir10) and cos (wdir10) for sim data (use Microsoft Excel from this point onwards)
3. For hourly value, take average of sin (wdir10) and cos (wdir10) at each daily hours
4. Convert the vector form into angular form in excel with arc tangent formula below. This formula gives degree range from -180 to 180
   ```
   DEGREES(ATAN2(cos(wdir10),sin(wdir10)))
   ```
5. To convert into conventional range of 0 to 360 , add 360 to value lesser than 0, you can use this formula below.
   ```
   IF(cell<0,cell+360,cell)
   ```
6. Repeat step 2,3,4,5 for observation data

Verify wind direction data using MAE

7. Repeat step 1,2 for simulation data
8. Repeat step 2 for observation data, produce sin (wdo) and cos (wdo).
9. Take difference of sin and cos for wd and wdo

   sin_diff = sin (wd) - sin (wdo)
   cos_diff = cos (wd) - cos (wdo)

10. For hourly value, take average of of sin_diff and cos_diff at each hour
11. Convert the vector form into angular form by repeating step 4,5.

A.3 Preparation of Land Use Map

A.3.1 Satellite images used – Landsat images

The scenes from Landsat 5 (30 m × 30 m resolution) in 2003 with no more than 30% cloud coverage are used. They are made available by USGS's Earth Resources Observation and Science (EROS) Centre under the public domain glovis.usgs.gov. Satellite images are mosaicked together to cover the entire Selangor state. Satellite images processing software, ERDAS Imagine 2011 geometrically assigns map coordinate to the images and radiometrically removes the error and variation of digital number over the mosaicked images. The Selangor region is then masked out for land use reclassification purpose.

A.3.2 Processing and Classification of satellite images in ArcGIS

The ESRI GIS software, ArcMAP 10.2.2 then classifies the pre-processed image. The supervised maximum likelihood classification approach is adopted to differentiate the spectral reflectance between each LU classes by manually allocating respective sample polygons. The images is classified into 10 LU classes adapted from the land cover classification standard of the IGBP [*Strahler et al.*, 1999] as shown in Table 3.2. The land use classes are selected according to the distribution of the land use in the official town plan map supplied by the Selangor Town and Country Planning Department (Jabatan Perancangan Bandar dan Desa; JPBD). The urban land use is branched out into three classes, low density residential (LDR), high density residential (HDR) and commercial/ industrial region (COM) according to the level of urbanization. An additional land use, oil palm plantation is also introduced due to its abundant presence in Selangor region [*Miettinen et al.*, 2014]. The supplement information on the land use comparison of JPBD and IGBP is given in A.3.6. During the allocation, additional class for cloud is created temporarily to avoid the confusion with other land use types with high reflectance. However, the cloud class is processed and removed in the adjustment and normalization steps in Section A.3.3

A.3.3 Normalization of land use map

In addition to the 2003 land use, land use maps for several years (1999, 2007, 2011) are separately produced. Such effort attempts to reduce the erroneous signals generated by classification and cloud coverage by ensuring the chronological change of the land use. It introduces several conditions pertinent to the general shift of land cover with time. Using Raster Calculator function, the grids from each primary maps are adjusted accordingly to that fulfil the conditions as detailed below.

1) Shrinking of natural vegetation cover including "evergreen broadleaf forest", "grasslands and shrublands" and "croplands" over years: The grid marked as the stated classes in the year-after replaces the grid not marked as the stated classes in the more recent year.

2) Shrinking of water body over years: The grid marked as “water” in the year-after replaces the grid not marked as “water” in the more recent year.

3) Growing of palm plantation coverage over years: The grids marked as "palm plantation” in the year-before replaces the grid not marked as “palm plantation” in the more recent year.

4) Growing of urban land use over years: The grid marked as “urban” in the year-before replaces the grid not marked as “urban” in the more recent year.

5) Grids that are still empty: The grid marked as “cloud” takes the land use of the year closer to it, or else it is replaced with data from original WRF LU dataset.

After the normalization process, the dataset with resolution of 30 meter is resampled by stages back into the 0.008333 meter (approximately 30’’) resolution for WRF.

A.3.4 Convert from WRF binary form to ASCII format

The original geological dataset of WRF is in the form of binary. Each binary file contains data for 10° x 10° range at 30” (arc-second) grid size. The binary file containing the fourth domain (d04) (lat: 2.5449° - 3.8830°; long: 100.8085° - 102.0138°) is identified. For ArcMAP processing, the file is converted to ASCII form with the free java source code, dmbrown[9]. After the grid and projection information are specified, the ASCII file can be read as raster file into ArcMAP for further processing.

A.3.5 Conversion back into WRF format and scripting required in index file

The land use map for Selangor is updated in the original WRF LU file in ASCII format. The raster data is then saved into TXT extension before converting back to binary format with dmbrown script. The land use entry in GEOGRID.TBL file is modified to feed in the corresponding dataset in WPS. The parameters of land use and vegetation types are updated according to the area-weighted values for new and merged land use in the land use and vegetation parameter tables (LANDUSE.TBL and VEGPARM.TBL). Parameters updated include albedo, soil moisture, surface emissivity, roughness length, thermal inertia etc.

A.3.6 JPBD data source and details

The official land use map prepared within Selangor state is used for the preparation of training sample for supervision classification in GIS and also verification of the

---

[9] The source code is provided by Daniel Brown from University of Alberta in WRF-EMS forum. Available at: http://www.wrfems.info/viewtopic.php?f=10&t=141

performance of the classification. The land use data is managed and distributed through JPBD at district levels in Selangor state with the similar land use classification standard as imposed by the central state government. JPBD town plan data is available in the form of shapefile. The Selangor state town plan map has covered all twelve local districts, including Hulu Selangor, Klang, Kuala Selangor, Sabak Bernam, MBPJ, MBSA, MPAJ, MPS, MPSJ, MPKJ, Kuala Langat, and Sepang. The former four makes up for the northern area and the remaining belongs to the central and southern region. The land use map developed by each district is valid for approximately 10 years depending on the standard set by local districts. JPBD compiles the latest land use map with the updated maps from the local authorities. The northern districts have their updates performed in 2003 whilst southern districts have updated their maps in 2007, except for Sepang district with a disparate change in 2005. In this context, the data from northern and southern region are referred for developing training samples for classification for their respective years.

The general classification of land use is recorded in *Current (Semasa)* attribute, from which it is branched out into *Activity (Activiti)* and *Activity2 (Activiti2)*. The metadata of the town plan data is referenced to re-classify JPBD land use types into MODIS-33 land use classification system (Table 3.2), as shown in Table A.1. The files are processed with ArcGIS 10.2. New field is added to the shapefile whilst conversion code in visual basic has filled it with MODIS land use code.

Table A.1: Sorting JPBD land use data according to WRF MODIS-33 category

No	Current (Semasa)	Activity (Aktiviti)	Activity2 (Aktiviti2)	Category	Code
1	Agriculture (Pertanian)	Oil Palm (Kelapa Sawit)	-	Evergreen broadleaf	2
		Rubber Trees (Getah)		Evergreen broadleaf	2
		Others		Croplands	12
2	Forest (Hutan)	Tropical Forest (Hutan Darat)	-	Evergreen broadleaf	2
		Hutan Tanah Lembap	-	Evergreen broadleaf	2
		Hutan Tanah Gambut	-	Evergreen broadleaf	2
3	Industry (Industri)			Urban-Commercial	33
4	Transportation (Pengangkutan)			Urban-Commercial	33
5	Residential (Kediaman)	Planned Housing (Perumahan Terancang)	Perumahan Strata	Urban-High Res	32
			Perumahan Bukan Strata	Urban-High Res	32
			Perumahan Kakitangan	Urban-High Res	32
			Kampung Tersusun	Urban-Low Res	31
			Kampung Felda		31
			Kampung Baru		31
			Perumahan Ladang/Estet		31
		Unplanned Housing (Perumahan Tidak Terancang)	Kampung Tradisi	Urban-Low Res	31
			Kampung Nelayan		31
			Kampung Atas Air		31
			Kampung Orang Asli		31
			Kampung Setinggan	Urban-High Res	32
6	Empty Land (Tanah Kosong)	Natural (Semulajadi)		Grasslands and Open Shrublands	10
		Man-made surface (Buatan)		Sparsely vegetated	16
7	Open and recreation land (Tanah Lapang dan Rekreasi)			Grasslands and Open Shrublands	10
8	Water Body (Badan air)			Water body	17

9	Institution and Facilities (Institusi dan Kemudahan Masyarakat)			Urban-Commercial	33
10	Infrastructure and Utilities (Infrastruktur dan Utiliti)			Urban-Commercial	33
11	Commercial and Services (Perniagaan dan Perkhidmatan)			Urban-Commercial	33
12	Farming and Aquaculture (Penternakan dan Akuakultur)	Farming (Penternakan)		Urban-Commercial	33
		Aquaculture (Akuakultur)	Salt water (Air Masin)	Water body	17
			Fresh water (Air Tawar)	Water body	17
			Mud (Air Payau)	Wetlands	11
13	Beach (Pantai)	Natural (Semulajadi)	Public beach (Pantai Awam)	Urban-Commercial	33
			Wetland (Pantai Hutan)	Wetlands	11

A.3.7 Validation with JPBD

Four year of land use maps, 1999, 2003, 2007 and 2011 are produced. Validation is performed to verify the performance of the ArcGIS land use reclassification with original WRF MODIS land use (LU) map. The official town plan map is used for the verification. As mentioned in A.3.6, the current land use information is available for different years, hence the validation performed for 2003 covers the northern region and 2007 covers the central and southern region. The entire Selangor is validated except Sepang district. The town plan for the latter district is developed for year 2005 and hence not deployed because 2005 is not one of the years of investigation. The validated map is combined and illustrated in figure below.

The original WRF LU map has consisted of more land use types as compared to the refined list of updated LU map in terms of vegetation. The similar vegetation land uses that are removed from the list are grouped together according to the standard described in Table A.1 for comparison purposes. On contrary, the new land use classification system has further diversified urban land use into 3 categories. Due to the difference of both classification system, the accuracy analysis has grouped similar LU classes for comparison compatibility. For example, the three new urban classes are returned as one urban category to compare with single urban category from original LU map.

Supplementary information on land use is included in the adjusted new land use code to merge the two lists as shown in Table A.1.

The verification has projected the town plan map onto the grid position of original and updated land use map. From which an algorithm is written to return the land use code for overlaid grids with the same adjusted land use type. In other words, the remaining grids with different land use type have returned a value of “99”. The accuracy of LU map is derived according to the number of grid count for updated LU map over actual grid count of town plan map. Accuracy improvement has compared the bias between accuracy of updated and original LU map, thus negative value indicates that original LU has better prediction. Based on the areal coverage of each LU type, the overall accuracy improvement is derived.